Washington University in St. Louis

Washington University Open Scholarship

Engineering and Applied Science Theses & Dissertations

McKelvey School of Engineering

Summer 8-15-2020

Structural Organization and Chemical Activity Revealed by New Developments in Single-Molecule Fluorescence and Orientation Imaging

Tianben Ding
Washington University in St. Louis

Follow this and additional works at: https://openscholarship.wustl.edu/eng_etds

Part of the Chemical Engineering Commons, Chemistry Commons, Electrical and Electronics Commons, and the Optics Commons

Recommended Citation

Ding, Tianben, "Structural Organization and Chemical Activity Revealed by New Developments in Single-Molecule Fluorescence and Orientation Imaging" (2020). *Engineering and Applied Science Theses & Dissertations*. 585.
https://openscholarship.wustl.edu/eng_etds/585

This Dissertation is brought to you for free and open access by the McKelvey School of Engineering at Washington University Open Scholarship. It has been accepted for inclusion in Engineering and Applied Science Theses & Dissertations by an authorized administrator of Washington University Open Scholarship. For more information, please contact digital@wumail.wustl.edu.

WASHINGTON UNIVERSITY IN ST. LOUIS

McKelvey School of Engineering

Department of Electrical & Systems Engineering

Dissertation Examination Committee:
Matthew D. Lew, Chair
Meredith Jackrel
Ulugbek Kamilov
Joseph O'Sullivan
Quing Zhu

Structural Organization and Chemical Activity Revealed by New Developments in Single-Molecule Fluorescence and Orientation Imaging

by

Tianben Ding

A dissertation presented to
The Graduate School of
Washington University
in partial fulfillment of
the requirements for the degree of
Doctor of Philosophy

August 2020
Saint Louis, Missouri

© 2020, Tianben Ding

Contents

List of Figures . . . . **v**

List of Tables . . . . **viii**

Acknowledgments . . . . **ix**

Abstract . . . . **xii**

1 Background **1**
- 1.1 Single-Molecule Fluorescence 2
- 1.2 Transition Moments and Molecular Orientation 5
- 1.3 Fluorescence Microscopy 8
  - 1.3.1 Illumination Modalities 9
  - 1.3.2 Fluorescence Detection and the Diffraction Limit 10
- 1.4 Single-Molecule Localization Microscopy (SMLM) 14
  - 1.4.1 Localization of Single Fluorescent Molecules beyond the Diffraction Limit 15
  - 1.4.2 Active Control of Emitter Concentration 18
- 1.5 Single-Molecule Image Formation by an Optical System 20
  - 1.5.1 Imaging in Refractive-Index Matched Media 21
  - 1.5.2 Imaging in the Presence of Index Mismatch 25
  - 1.5.3 Point Spread Function (PSF) Engineering 28
- 1.6 Roles of Single Fluorescent Molecules as Local Probes 30
- 1.7 Amyloid Aggregates 31
- 1.8 Scope and Contribution of Dissertation 35

2 Experimental Methods **38**
- 2.1 Dipole Basis Functions and Dipole Rotation Model 39
  - 2.1.1 Dipole Basis Functions 39
  - 2.1.2 Dipole Rotation Model 43
- 2.2 Single-Molecule Microscopy with Polarized Detection Channels 45
  - 2.2.1 Excitation Sources and Optical Components 48
  - 2.2.2 Collection Optics and Detectors 49
  - 2.2.3 Polarization-Sensitive Collection with 4f Optical System for PSF Engineering 51

2.2.4 Calibration of Liquid Crystal Spatial Light Modulator 55
2.3 Sample Preparation 59
2.3.1 Photocatalyst Preparation 59
2.3.2 Purification and Aggregation of Amyloid Peptides 60
2.4 Imaging Procedure 63
2.4.1 SMLM Procedure for Catalytic Reaction Site Imaging 63
2.4.2 SMLM and SMOLM Procedure for Amyloid Imaging 64
2.4.3 Ensemble Measurements and Other Imaging Methods 67
2.5 Single-Molecule Localization and Estimation 69
2.5.1 Background Estimation 69
2.5.2 Imaging Channel Calibration and Registration 73
2.5.3 SM Localization Based on Least-Squares Fitting 75
2.5.4 Sparsity-Promoting Maximum-Likelihood Estimator and Orientation Projection 76
2.6 Quantitative Analysis of SMLM Data 81
2.6.1 Localization Grouping across Consecutive Frames and Measuring the Length of Fluorescence Bursts 81
2.6.2 Isolation and Characterization of Regions of Interest 81
2.6.3 Coordinate-Based Colocalization (CBC) analysis 85

3 Mapping Photocatalytic Activity of Semiconductor Nanoparticles at the Nanoscale 87
3.1 Oxygen Vacancies in Tungsten Oxide Nanowires 90
3.2 SMLM for Mapping Photocatalytic Activity on Tungsten Oxide 93
3.3 Coordinate-Based Colocalization for Revealing the Role of Oxygen Vacancy in Tungsten Oxide 103
3.4 Outlook 116

4 Duo-Spot Point Spread Function for Single-Molecule Localization and Orientation Estimation 118
4.1 Design 120
4.2 Estimation Precision and Accuracy of Duo-Spot PSF in SMOLM 125
4.3 3D orientation imaging for mapping nanoscale lipid-membrane domains . . . 132
4.4 Outlook 135

5 Transient Amyloid Binding (TAB) Microscopy 136
5.1 Nanoscale Imaging of Amyloid Aggregates 138
5.2 TAB Specificity to Resolve Amyloid Structures 145
5.3 TAB Imaging across a Variety of Amyloid Structures 147
5.4 Long-Term TAB Imaging of Amyloid Dynamics 150
5.5 Outlook 156

6 TAB Single-Molecule Orientation Localization Microscopy (SMOLM) . 159
6.1 Orientation Localization Microscopy Using Polarized Standard PSF 161
6.2 Resolving Structural Heterogeneities between Amyloid Fibrils 167
6.3 Outlook 183

References 185

Vita 211

List of Figures

1.1 Simplified Jablonski diagram depicting molecular energy levels and transitions 3
1.2 Probability distributions of absorption and emission transition dipole moments 7
1.3 Transition dipole moment of Nile red molecule 8
1.4 Basic detection components in a fluorescence microscope 12
1.5 The diffraction-limited PSF 14
1.6 Example image and localization using a Gaussian function 16
1.7 Principle of single-molecule localization microscopy 19
1.8 Back focal plane intensity distributions with different SM orientations 24
1.9 Schematic diagram of an emitter at an interface and intensity distributions in back focal plane with various refractive index mismatches 26
1.10 Optical 4f system for implementing engineered PSFs 28
1.11 Structural model of a cross-β unit 32
1.12 Schematic of amyloid formation 33
1.13 Energy landscape scheme of protein folding and aggregation 34

2.1 Orientational basis images at the back focal and image planes for a molecule near a glass-air, glass-water, and glass-oil interface 42
2.2 Rotation within a cone model 44
2.3 Schematics of an epi-fluorescence microscope 46
2.4 Schematics of polarization-sensitive fluorescence microscopes 52
2.5 Representative phase masks and engineered PSFs for SM orientation measurements 55
2.6 Images of the pupil plane and SLM for verification of 4f-system alignment . . 56
2.7 Example calibration data of an SLM 58
2.8 Example residual background photons after temporal quantile filtering 70
2.9 Spatial Gaussian and wavelet filter for smooth background estimation 72
2.10 Example region of interest selection for extracting SM bursts on samples . . 82
2.11 Amyloid region of interest and backbone ridge detection 84

3.1 Structural characterization of tungsten oxide nanowires 91
3.2 Low- and high-resolution TEM images of tungsten oxide 92
3.3 SM imaging of catalytic reactions using fluorogenic probes 94
3.4 Imaging the catalytic activity of single tungsten oxide nanowires 96
3.5 Super-resolution images of APF and FA without tungsten oxide nanowires . 97

3.6 Quantitative characterization of APF blinking events on an initial tungsten oxide nanowire . . . 98
3.7 Super-resolution images of APF and FA without tungsten oxide nanowires . 99
3.8 Super-resolution fluorescence images of initial tungsten oxide nanowires . . . 100
3.9 FT-IR spectra . . . 101
3.10 Quantitative characterization of furfuryl alcohol blinking events on an initial tungsten oxide nanowire . . . 102
3.11 APF super-resolution of initial tungsten oxide nanowires before and after phosphate buffer wash . . . 105
3.12 Colocalization of hydroxyl radical generation and Lewis acid sites for tungsten oxide nanowires . . . 106
3.13 Colocalization analysis of initial tungsten oxide nanowires I . . . 107
3.14 Colocalization analysis of initial tungsten oxide nanowires II . . . 108
3.15 Colocalization analysis of initial tungsten oxide nanowires III . . . 109
3.16 Colocalization of hydroxyl radical generation and acid sites for PVP-functionalized tungsten oxide nanowires . . . 111
3.17 Colocalization analysis of PVP-functionalized tungsten oxide nanowires I . . 112
3.18 Colocalization analysis of PVP-functionalized tungsten oxide nanowires II . . 113
3.19 APF and furfuryl alcohol colocalization behavior on initial and PVP-functionalized tungsten oxide nanowires . . . 114
3.20 APF and furfuryl alcohol colocalization behavior on initial and PVP-functionalized tungsten oxide nanowires . . . 116

4.1 Basis images used in design of Duo-spot point spread function . . . 121
4.2 Imaging system degeneracy for estimating $\langle\mu_y^2\rangle$ and $\langle\mu_z^2\rangle$ second moments with various Duo-spot partitioning . . . 122
4.3 Duo-spot phase mask . . . 123
4.4 Duo-spot basis functions and PSF . . . 125
4.5 Design of Duo-spot point spread function . . . 126
4.6 Orientation sampling over a hemisphere . . . 127
4.7 The CRB of estimation of orientational second moments using various PSFs 128
4.8 Orientation estimation precision using Duo-spot PSF . . . 130
4.9 Orientation estimation bias using Duo-spot PSF . . . 131
4.10 Orientation and wobble of Nile red in single-phase SLBs . . . 132
4.11 SMOLM imaging of SMase-induced alterations of lipid composition and domain reorganization in a ternary SLB of DOPC/SPM/chol . . . 133

5.1 Transient amyloid binding microscopy . . . 140
5.2 Localization of individual ThT on amyloid aggregates and region of interest selection . . . 142
5.3 Analysis of ThT localization and blinking events in TAB microscopy 143
5.4 Imaging buffer effects on ThT blinking . . . 144

5.5 TAB SMLM imaging compared to conventional labeling methods 146
5.6 Analysis of Alexa-647 dSTORM for amyloid fibril imaging 147
5.7 TAB SMLM images of various amyloids 148
5.8 Visualization of Aβ40 structures using TAB SMLM at various aggregation stages 149
5.9 Localization rate of single ThT molecules during TAB imaging 151
5.10 Localization rate of single NR molecules during TAB imaging 152
5.11 TAB SMLM time-lapse images of Aβ42 fibril remodeling using ThT 153
5.12 Additional time-lapse ThT TAB SMLM images of Aβ42 remodeling 154
5.13 TAB SMLM time-lapse images of Aβ42 fibril growth using NR 155

6.1 Orientation measurement precision using various PSFs 163
6.2 Simulated orthogonally polarized nad Tri-spot PSFs 164
6.3 Resolvability of a fixed molecule versus an isotropic emitter using our estimator 165
6.4 Cramér–Rao bounds for estimating the 3D position of a single molecule using the polarized and unpolarized standard PSFs 166
6.5 SMOLM measurement precision for position and signal 169
6.6 SMOLM measurement bias for position and signal 170
6.7 SMOLM measurement precision for orientation 171
6.8 SMOLM measurement bias for orientation 172
6.9 SMOLM orientational measurement bias for isotropic emitters 173
6.10 TAB SMLM and SMOLM images acquired using NR 175
6.11 Fluorescence images of single Nile red molecules on fibril backbones with various orientations 176
6.12 Estimated polar orientations θ of Nile red molecules on fibrils 176
6.13 Structural heterogeneity of Aβ42 fibrils revealed by TAB SMOLM imaging . 177
6.14 Measurements of fibril widths 178
6.15 Additional fibril analysis I 179
6.16 Additional fibril analysis II 180
6.17 Estimated wobbling area of Nile red molecules on amyloid fibrils 181

List of Tables

2.1 Optical materials list for imaging APF and furfuryl alcohol 47
2.2 Optical materials list for ThT and NR TAB imaging 53

5.1 Representative experimental conditions and photon statistics of SMLM on Aβ42 141

6.1 Localization numbers, localization density, photons detected per localization, background photons per pixel, and burst on-time of Nile Red molecules on amyloid structures 174

Acknowledgments

I would like to thank the following people, without whose guidance and support I would not have been able to complete my research projects, and without whom I would not have made it through my PhD degree.

First and foremost, I would like to express my deep gratitude to my research advisor, Professor Matthew D. Lew. I feel I am really privileged to have worked with Dr. Lew, whose dedication and passion for scholarship and work ethic set an inspiring example for me throughout my PhD program at Washington University in St. Louis. Since I joined the Lew Lab in 2015 as the first PhD student in the lab, he has been continuously providing professional advice and support for my research activities including guidance on many experimental projects and constructive feedback on my research presentations and publications. I am thankful for the great amount of time he has devoted to training and mentoring me to become an independent scientist and thinker.

Thanks also to the other members of my dissertation defense committee: Professor Meredith Jackrel, Professor Ulugbek Kamilov, Professor Joseph O'Sullivan and Professor Quing Zhu. It was my pleasure to get their helpful and insightful comments based on their theoretical and experimental background.

I want to also thank the Lew Lab members who have closely worked with me, Dr. Jin Lu, Hesam Mazidi, Oumeng Zhang and Tingting Wu. I also owe thanks to all the other members of the Lew Lab and alumni with whom I have worked: Tristan Carlson, Tara Porter, Weiran Wang, Eshan King, James Jusuf, James Cevasco, Jack Hyde, and Henry Cohen.

During my PhD program, I have also greatly benefited from generous collaborators in biology and chemistry on various imaging experiments. Professor Jan Bieschke and his students Kevin Spehar and Yuanzi Sun provided some amyloid protein samples imaged in Chapter 5, and Professor Bryce Sadtler and his student Shen Meikun prepared the photocatalysts characterized in Chapter 3. Having brainstorming meetings with them and receiving feedback from them have been constant sources of inspiration for my research.

Finally, I am also deeply grateful to my parents, Shuxue Ding and Zhenhua Sun, for their endless love. I would not have had enough courage to study abroad in the US for my PhD without their support, and my recent accomplishments would not have been possible without their continuous encouragement.

Tianben Ding

Washington University in Saint Louis
August 2020

Dedicated to my parents.

ABSTRACT OF THE DISSERTATION

Structural Organization and Chemical Activity Revealed by New Developments in Single-Molecule Fluorescence and Orientation Imaging

by

Tianben Ding

Doctor of Philosophy in Electrical Engineering

Washington University in St. Louis, 2020

Professor Matthew D. Lew, Chair

Single-molecule (SM) fluorescence and its localization are important and versatile tools for understanding and quantifying dynamical nanoscale behavior of nanoparticles and biological systems. By actively controlling the concentration of fluorescent molecules and precisely localizing individual single molecules, it is possible to overcome the classical diffraction limit and achieve 'super-resolution' with image resolution on the order of 10 nanometers.

Single molecules also can be considered as nanoscale sensors since their fluorescence changes in response to their local nanoenvironment. This dissertation discusses extending this SM approach to resolve heterogeneity and dynamics of nanoscale materials and biophysical structures by using positions and orientations of single fluorescent molecules.

I first present an SM approach for resolving spatial variations in the catalytic activity of individual photocatalysts. Quantitative colocalization of chemically triggered molecular probes reveals the role of structural defects on the activity of catalytic nanoparticles. Next, I demonstrate a new engineered optical point spread function (PSF), called the Duo-spot PSF, for SM orientation measurements. This PSF exhibits high sensitivity for estimating orientations of dim fluorescent molecules. This dissertation also discusses a new amyloid imaging method, transient amyloid binding (TAB) microscopy, for studying heterogeneous organization of amyloid structures, which are associated with various aging-related neurodegenerative diseases. Continuous transient binding of dye molecules to amyloid structures generates photon bursts for SM localization over hours to days with minimal photobleaching, yielding $\sim$40% more localizations than standard immunolabeling. Finally, I augment TAB imaging to simultaneously measure positions and orientations of fluorescent molecules bound to amyloid surfaces. This new method, termed single-molecule orientation localization microscopy (SMOLM), robustly and sensitively measures the in-plane (xy) orientations of fluorophores ($\sim$9° precision in azimuthal angle) near a refractive index interface and reveals structural heterogeneities along amyloid fibrillar networks that cannot be resolved by SM localization alone.

Chapter 1

Background

Since the first optical detection of single molecules [1–3], single-molecule (SM) spectroscopy and imaging have been a versatile tools for characterizing and understanding the properties of nanoscale materials and biophysical systems. SM techniques [4,5] include single-molecule sequencing [6,7], single-molecule tracking [8–12], single-molecule fluorescence resonance energy transfer (FRET) [13–15], single-molecule force spectroscopy [16–20] and single-molecule localization microscopy (SMLM), the subject of this dissertation. In practical experiments, fluorescent probe molecules can be specifically tagged to targets of study by immunostaining, generic chemical labeling, covalent bond of protein tags, or spontaneous attachment depending on binding affinity [21,22]. By collecting and detecting emitted fluorescence in optical microscopes, the attached fluorescent molecules can resolve and convey local information of measurement targets with SM sensitivity. A key strength of the SM approaches is its ability to measure the full distributions and fluctuations of molecular phenomena under study without ensemble averaging.

The development of SMLM, awarded the Nobel Prize in Chemistry 2014 [23,24], has enabled the resolution of structural features with sizes an order of magnitude below the optical diffraction limit [25–27]. However, improving structural resolution is still insufficient to fully elucidate local organizations and mechanisms of molecular dynamics. One unifying goal of my doctoral research is to develop powerful SMLM techniques for resolving nanoscale inhomogeneity and heterogeneity within nanoparticles and biological systems. In the course of my PhD, I have utilized fluorescence properties of single fluorescent molecules, such as SM orientation, as useful tools for resolving local information of samples. Although individual fluorescent molecules only emit limited photons, appropriate imaging systems and sophisticated image processing algorithms allow precise estimation of SM properties with nanometer resolution.

This chapter is organized as follows. The key ideas of SMLM techniques are discussed after reviewing basic photophysical properties of fluorescent molecules. Next, I present a summary of a theoretical framework for SM image formation. A brief introduction of one of the main measurement targets, amyloid aggregates, is also discussed in the later part of this chapter. The chapter concludes with the scope and a list of the main contributions of the dissertation.

1.1 Single-Molecule Fluorescence

Fluorescence is a type of light-matter interaction and a two-step process that begins with the absorption of light by a molecule (photoluminescence). Figure 1.1 depicts the excitation and emission cycle of a fluorophore [21, 28, 29]. For an emissive fluorescent molecule, a photon from an incident light field is absorbed by the molecule, resulting an electronic transition from the highest occupied molecular orbital (HOMO, the electronic singlet state S_0) to the lowest unoccupied molecular orbital (LUMO, the electronic singlet state S_1) or higher energy states. A fluorophore can only emit fluorescence light from the LUMO. Hence, after excitation, the

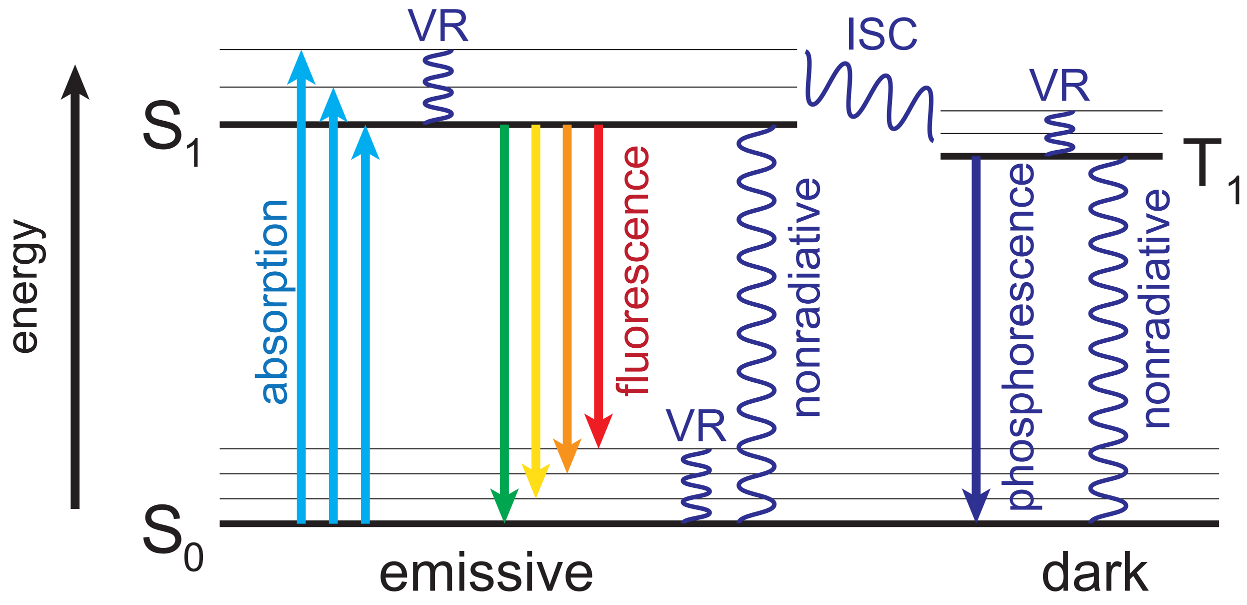

Figure 1.1: Simplified Jablonski diagram depicting molecular energy levels and transitions. In their emissive or 'bright' form, fluorescent molecules absorb an excitation photon, resulting in an electronic transition from the S_0 ground state to vibration modes of the S_1 excited state. Molecules, in their excited states, undergo vibrational relaxation (VR) and return to the S_0 state by either fluorescing or undergoing non-radiative relaxation. By electron spin-orbit coupling, there is also a nonzero probability for the excited fluorescent molecule to experience inter-system crossing (ISC) into a dark T_1 triplet state. From the T_1 state, the molecule returns to the S_0 state via non-radiative relaxation or radiative decay termed phosphorescence. Additional higher energy states and other state transitions such as triplet-triplet transitions are not shown.

molecule in higher vibrational modes of S_1 or other high-energy singlet states will undergo a fast vibrational relaxation or internal conversion to the ground state of S_1, which is a non-radiative loss of energy via vibrations or collisions. The molecule then undergoes a radiative decay back to a vibrationally excited state of S_0 with the emission of a red-shifted (Stokes shifted) photon. Finally, another fast vibrational relaxation returns the molecule into the ground state of S_0. Electron transitions from the excited state S_1 to the ground state S_0 may alternatively occur through non-radiative internal conversion.

The brightness of a fluorescent molecule is defined by two parameters, extinction coefficient ε and quantum yield Φ_{F}. The molar extinction coefficient (or absorption coefficient) is a measure of how strongly a fluorescent molecule absorbs photons to enter the excited state at a particular wavelength. Therefore, a large extinction coefficient leads to a greater probability of a photon to be absorbed by the molecule. It is an intrinsic property that is dependent upon a molecule's chemical composition and structure. A molecule's extinction coefficient ε is given by

$$\varepsilon = \frac{N_\alpha \sigma}{\ln 10}, \qquad (\mathrm{M}^{-1}\mathrm{cm}^{-1}) \tag{1.1}$$

where $N_\alpha = 6.022 \times 10^{23}\,\mathrm{mol}^{-1}$ is Avogadro's number and σ is the molecular absorption cross-section that expresses the photon-capture area of a molecule. The total absorbance A of an ensemble of molecules can be calculated by the Beer-Lambert Law as

$$A = \varepsilon l c, \tag{1.2}$$

where l is the absorption path length (thickness of the absorption medium, cm) and c is the concentration of the absorbing species in the medium (M^{-1}). Once a photon has been absorbed, the probability of a photon been emitted as fluorescence is represented as the quantum yield Φ_{F} and expressed as

$$\Phi_{\mathrm{F}} = \frac{k_{\mathrm{r}}}{k_{\mathrm{r}} + k_{\mathrm{nr}}}, \tag{1.3}$$

where k_{r} is the radiative decay (fluorescence) rate and k_{nr} is the non-radiative decay rate, which is the sum of all other conversion and transition rates without fluorescence emission. This quantity can be understood as a ratio of the number of photons emitted compared to the number absorbed and a higher yield close to unity is desirable for fluorescence microscopy.

There are multiple factors that influence the extinction coefficient and the fluorescence quantum yield, e.g., intra-molecular twists or rotations [30–33], and polarity/hydrophobicity of local dye environment [34–36]. To compare and select good fluorophores, the relative brightness of fluorophore can be computed by multiplying the extinction coefficient ε with the quantum yield Φ_{F}.

When a fluorescent molecule is in the excited state, it is possible for the spin of the excited electron to flip, causing the molecule to undergo intersystem crossing and enter into a triplet state denoted as T_1 in Figure 1.1. The lifetime of the triplet state is on the order of $10^{-6} - 10^{-3}$ s compared to the nanosecond (10^{-9} s) lifetime of the S_1 excited state. From the triplet state, the molecule will return to the ground state S_0 through non-radiative internal conversion or another type of radiative decay termed phosphorescence with a further red-shifted photon. Repeated entry to the triplet state from the excited state causes the molecule to appear to blink. In the triplet state, molecules also can undergo irreversible chemical reactions with excited oxygen species such as singlet oxygen. This process is termed photobleaching and limits the total photons emitted from a fluorescent molecule. One can effectively reduce photobleaching and increase stability of fluorescence by employing an enzymatic oxygen scavenging system or deuterated water in an imaging buffer [22, 37–41]. However, it is necessary to note that these additional chemicals may change properties of imaging targets and alter sample dynamics during fluorescence imaging.

1.2 Transition Moments and Molecular Orientation

The orientation of a single molecule can be an important sensor for probing the configuration and dynamics of molecules in its local environment. Precise measurements of SM orientations are critical for understanding a variety of nanoscale biological and chemical processes, such as the motions of molecular motors [42–44], the complex higher-order structures of DNA [20, 45,46], and reaction kinetics on the surfaces of catalytic nanoparticles [47]. The orientation of a fluorescent molecule, which will be denoted by a unit vector $\boldsymbol{\mu} = [\mu_x, \mu_y, \mu_z]^{\mathrm{T}}$ throughout the dissertation, is characterized by its transition dipole moment. The transition moment is a quantity introduced for evaluating the transition rate between the ground and excited states in quantum mechanics [28]. The displacement of charges upon the state transition described in Section 1.1 can be well approximated by the interaction between the electric field and the electric dipole moment. The absorption probability is proportional to $|\boldsymbol{\mu} \cdot \boldsymbol{E}|^2$, where $\boldsymbol{\mu}$ is the molecule's electric dipole moment and $\boldsymbol{E}$ is the local incident electric field. This relationship implies that the rate of absorption has a $\cos^2(\nu)$ dependence, where ν is the angle between the dipole moment and the polarization of the excitation field. Hence, fluorescent molecules whose moments are parallel to the electric field vector are preferentially excited (Figure 1.2A). An example of Nile red's chemical structure and its transition moment are shown in Figure 1.3.

The emission pattern of a single fluorescent emitter, on the other hand, can be calculated by solving the classical electromagnetic wave equations [29]. In the far field, that is for distances $\boldsymbol{r}$ away from the emitter such that $|\boldsymbol{r}| \gg \lambda$ (wavelength of fluorescence), the intensity of light $I(\boldsymbol{r})$ emitted along the direction specified by $\boldsymbol{r}$ is given by

$$I(\boldsymbol{r}) \propto 1 - \left(\frac{\boldsymbol{\mu} \cdot \boldsymbol{r}}{|\boldsymbol{r}|}\right)^2. \tag{1.4}$$

Therefore, the angular intensity spectrum of fluorescence emission exhibits a toroidal shape as the intensity distribution is proportional to $\sin^2(\eta)$, where η is the angle between the

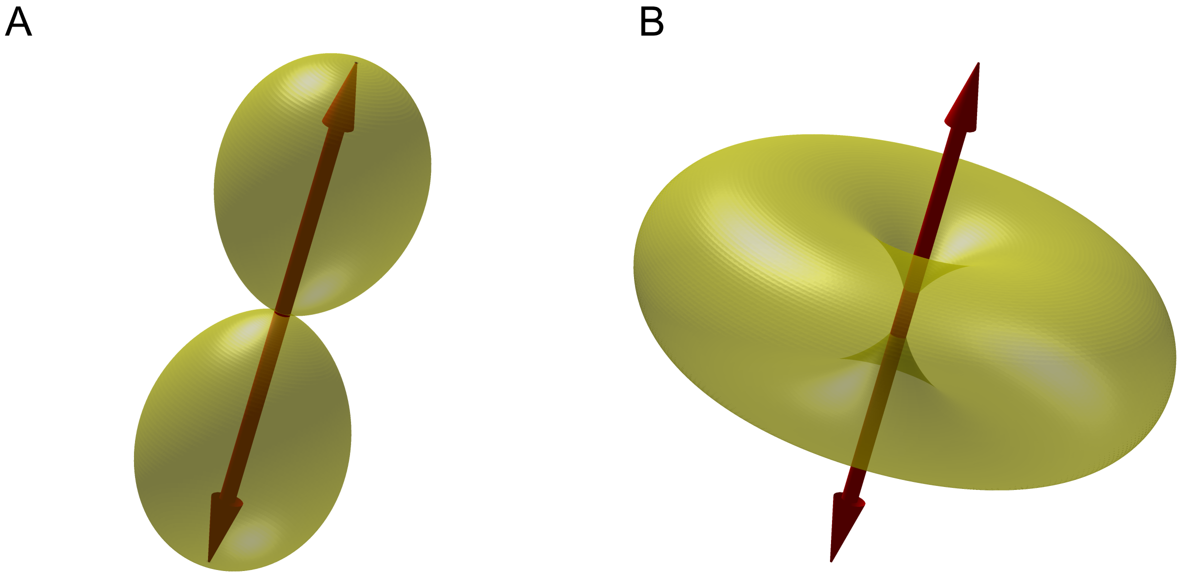

Figure 1.2: Probability distributions of absorption and emission transition dipole moments. (A) The absorption probability. When a molecule with the transition dipole (red double-headed arrow) is illuminated with light, the molecule will absorb a photon with probability proportional to $\cos^2(\nu)$ (distance from the center of the dipole to the yellow surface), where ν is the angle between the absorption dipole moment and the polarization of the excitation field. A fluorescent molecule whose moment is parallel to the electric field vector has the highest probability to absorb an excitation photon, while a molecule whose moment is perpendicular to the incident electric field cannot be excited. The resulting probability surface resembles a "dumbbell". (B) The emission probability. The far field intensity distribution of an emitting molecule is proportional to $\sin^2(\eta)$, where η is the angle between the emission dipole moment and the direction of fluorescence emission. Therefore, the majority of fluorescence emitted by a molecule propagates in a direction perpendicular to the axis of the moment, and no photon is emitted parallel to the dipole axis. This probability surface resembles a "torus".

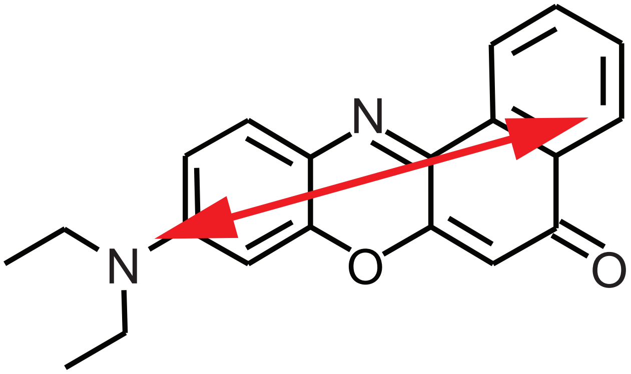

Figure 1.3: Chemical structure and transition dipole moment (red arrow) of Nile red. The dipole moment associated with the lowest energy electronic transition deviates from the longest molecular axis by $\sim 7°$ [49].

transition dipole moment $\boldsymbol{\mu}$ and the direction of fluorescence emission denoted by $\boldsymbol{r}$ (Figure 1.2B).

Note that the excitation and emission transition dipole moments are not necessarily parallel to each other. This relationship could be caused by the relaxation of the excited molecule to a different energy level in the S_0 manifold than the one from which it was originally excited. It could also be due to some interactions between the fluorescent molecule and its surrounding environment that perturb the molecular orbitals themselves during a measurement [48]. Unless stated otherwise, dipole moments $\boldsymbol{\mu}$ observed and discussed in this dissertation are emission dipoles.

1.3 Fluorescence Microscopy

Optical fluorescence microscopy has some distinct advantages over higher resolution modalities (e.g., atomic force microscopy, electron microscopy, etc.). The molecular labeling techniques provide imaging specificity with SM sensitivity and high contrast against background.

The use of fluorescence also allows relatively non-invasive imaging and compatibility with living system. However, there are several key challenges for imaging a variety samples including living cells and nanoparticles, namely noisy image acquisition caused by limited photons and the theoretical resolution barrier due to optical diffraction. What follows is an overview of the concept and limitations of conventional fluorescence microscopy.

1.3.1 Illumination Modalities

Any fluorescence microscope consists of illumination optics to excite the molecules and detection optics to collect the emitted fluorescence. As stated in Section 1.1, single fluorescent molecules only emit a limited number of photons before photobleaching. Hence, an efficient optical excitation and detection setup is essential to maximize the information from each photon. Illumination configuration is the first factor that affects image quality. For most purposes, a narrow illumination bandwidth is desirable since it facilitates filtering of any scattered or reflected light that would otherwise be collected and contribute to the background. A laser or LED source is typically used for this purpose. In a typical wide-field microscope, a large field-of-view (10 - 100 μm) is illuminated and the entire field-of-view is captured by a camera. The two most common illumination modalities employed in a wide-field fluorescence microscope are total internal reflection (TIR or TIRF) and epi-illumination [29]. In TIR, the illumination beam propagates from a high-index medium (e.g., coverslip glass) to an interface with the lower-index sample medium (e.g., water or air). An angle of incidence greater than the critical angle is chosen such that the incident beam achieves TIR at the interface, and molecules within the sample are excited by the resulting evanescent field. Since the evanescent field decays quickly with distance from the interface, only molecules near the interface, typically within ∼200 nm, are excited. TIRF illumination greatly reduces the background coming from out-of-focus fluorescent molecules.

However, the setup is limited to imaging thin samples and sacrifices one advantage of fluorescence microscopy, 3D or large volume imaging. In epi-illumination, a collimated beam perpendicular to the interface is instead incident to the sample. A Köhler lens (also known as a widefield lens) is added to the illumination path to focus the light to the back focal plane (BFP or Fourier plane) of the objective, providing collimated illumination on the imaging plane. Although the illumination configuration allows an entire volume of the target to be illuminated, it also produces out-of-focus fluorescence that increases the background and thus worsens the signal-to-background (SBR) and signal-to-noise (SNR) ratio that bound the performance of SM localization and orientation estimation.

To mitigate these drawbacks, the epi-illumination can be implemented at a severe yet sub-critical incline, often termed as pseudo-TIRF or a highly inclined and laminated optical (HILO) sheet. Light-sheet microscopy [50, 51] is another type of wide-field illumination that minimizes out-of-focus background by illuminating the sample from the side with a thin sheet of light perpendicular to the optical detection axis. Various light-sheet configurations have been proposed for reducing background in thick samples [52–56].

1.3.2 Fluorescence Detection and the Diffraction Limit

For fluorescence collection and detection, an optical relay consisting of an objective and a tube lens creates an image of a fluorescent molecule on a detection device, such as an electron-multiplying charge-coupled device (EMCCD) or scientific complimentary metal-oxide-semiconductor (sCMOS) camera (Figure 1.4). The objective lens is itself a combination of lens components specifically manufactured for minimizing aberrations from off-axis point sources at various wavelengths. The first-order performance of objective lenses is characterized by their numerical aperture (NA) and magnification. The objective magnification defines the magnifying power of an objective, typically ranging from 4× to 100×. The objective NA, on the other hand, indicates its collection efficiency and is defined by

$$\mathrm{NA} = n \sin(\vartheta_{\mathrm{obj}}), \tag{1.5}$$

where n is the refractive index of the immersion medium and ϑ_{obj} is the maximum half-angle of the cone of light that can be collected by the objective. Therefore, while a fluorescent molecule may emit light distributed over a full 4π-steradian solid angle, a typical objective only can collect about 1.2π even with a high NA ($\sim$1.4) if there is no refractive index variation between the molecule and the objective. The finite NA associated with the maximum possible collection angle also underlies the diffraction limit to be described below and therefore bounds the imaging resolution of conventional fluorescence microscopy.

An imaging system is a train of linear optical components including free space and lenses. Fourier optics, which uses linear systems theory to express arbitrary wave functions as superpositions of plane waves, is a useful and powerful framework to describe the propagation of light in imaging systems [57, 58]. One key result is that the image of a diffraction-limited shift-invariant imaging system is given by a convolution of the sample image with a system impulse response predicted by the Fraunhofer diffraction pattern of the objective BFP. Fraunhofer diffraction is a far-field approximation and is only valid if the paraxial approximation holds, i.e., the plane-wave components of the propagating light make small angles with the optical axis. The impulse response $h(u, v)$ of a shift-invariant imaging system (Figure 1.4) can be equivalently considered as the image of an isotropic monochromatic point

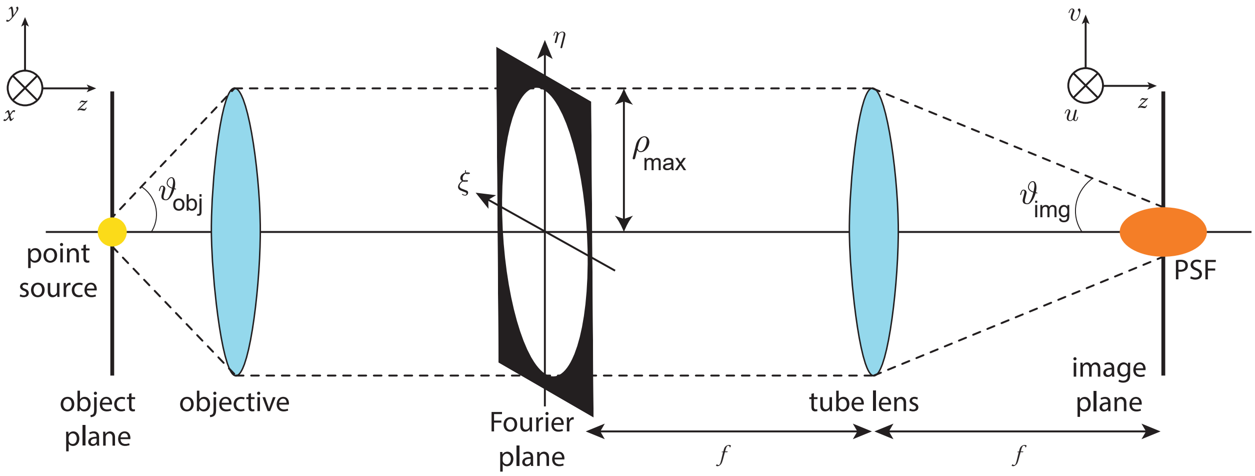

Figure 1.4: Basic detection components in a fluorescence microscope. An optical relay consisting of an objective and a tube lens projects images of fluorescent samples onto the image plane. The finite NA of the objective associated with the maximum collectable half cone angle defined by ϑ_{obj} provides finite circular support at the back focal plane (BFP, also known as the pupil) of the objective. The tube lens refocuses the light propagating through the aperture onto the image plane. The finite NA causes the image of a point source (approximation of a single molecule) to be blurred (the diffraction limit).

emitter and is given by the Fourier transform of BFP of the objective

$$h(u,v) = h_0 \iint_{-\infty}^{\infty} P(\xi,\eta) \exp\left[j2\pi(u\xi + v\eta)\right] d\xi d\eta \tag{1.6}$$

where $h_0 = \frac{j}{\lambda f}\exp(-2jkf)$, λ is the wavelength of light in the imaging system, f is the focal length of the tube lens, (ξ,η) are coordinates in the BFP, (u,v) are coordinates in the image plane and related with (x,y), which are coordinates of the point source in the object plane, by the magnification of the imaging system M such that $(u = Mx, v = My)$ (see Figure 1.4), and the pupil function $P(\xi,\eta)$ is a spatial frequency (angular spectrum) filter at the BFP of the objective. In any physically realizable optical system, light propagation is restricted to an aperture of finite extent as imposed by the limited NA of the objective lens such that

$$P(\xi,\eta) = \begin{cases} 1 : \rho \leq \rho_{\mathrm{max}} \\ 0 : \rho > \rho_{\mathrm{max}} \end{cases} \quad \text{and} \tag{1.7}$$

$$\rho = \sqrt{\eta^2 + \xi^2}, \tag{1.8}$$

where ρ_{max} is the radius of the pupil and can be calculated using the system NA and magnification M as

$$\rho_{\mathrm{max}} = f\sin(\vartheta_{\mathrm{img}}) = \frac{f\mathrm{NA}}{M}. \tag{1.9}$$

Physically, $h(u,v)$ is the complex amplitude of the electric field in the image plane produced by the optical system in response to a point source of light. Since a typical detector measures the intensity of the wavefunction, also termed as the point spread fucntion (PSF), the Fraunhofer diffraction pattern in the imaging plane is given by

$$I(u,v) = I_0\left[\frac{2J_1(2\pi\rho_{\mathrm{max}}\rho/\lambda f)}{2\pi\rho_{\mathrm{max}}\rho/\lambda f}\right]^2, \tag{1.10}$$

where I_0 is the peak intensity and $J_1(\cdot)$ is the Bessel function of order 1. This circularly symmetric pattern is known as the Airy pattern or Airy disk, and the radius of the focused central spot (from its maximum to the first zero) is given by

$$R = 1.22\lambda\frac{f}{D} = \frac{0.61\lambda}{\mathrm{NA}}M. \tag{1.11}$$

The finite size of this PSF leads to the Rayleigh resolution criterion, the minimum distance between two points which can be clearly distinguished from one another in an image (Figure 1.5A) [59,60].

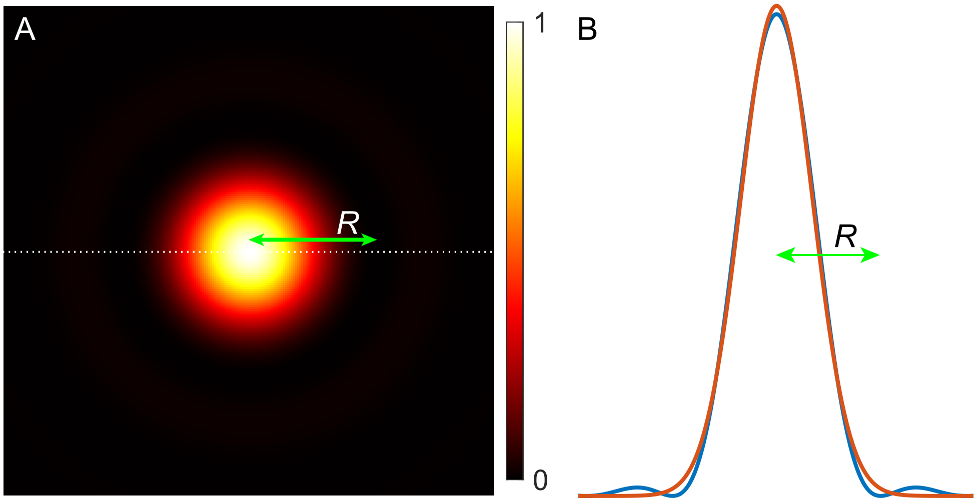

Figure 1.5: The diffraction-limited PSF. (A) The PSF associated with a fluorescence microscope with circular open aperture in BFP of the imaging system depicts the fundamental diffraction limit due to the limited NA of the objective. (B) Intensity cross-section of the diffraction patter at the location denoted by the white dashed line in A (blue) and its one-dimensional Gaussian fit (red).

1.4 Single-Molecule Localization Microscopy (SMLM)

In 2006, four research groups independently presented the concept of SMLM (also known as single-molecule super-resolution fluorescence microscopy) using different SM photoswitching and photoactivation mechanisms, namely stochastic optical reconstruction microscopy (STORM) [61], photoactivated localization microscopy (PALM) [62], fluorescence photoactivated localization microscopy (FPALM) [63], and points accumulation for imaging in nanoscale topography (PAINT) [36], respectively. These techniques leverage (1) precise localization of well-separated single molecules with nanometer precision, and (2) active control of the concentration of fluorescent molecules on imaging targets to reconstruct images with resolution beyond the diffraction limit. Although different techniques employ different chemical strategies to actively control the emissive and dark states of fluorescent molecules, the two underlying principles are common for all SMLM approaches. Here, I briefly present the idea of SMLM based on the two main principles.

1.4.1 Localization of Single Fluorescent Molecules beyond the Diffraction Limit

In Section 1.3.2, we discovered that an infinitely small point-source of light (represented by a Dirac function $\delta(x, y)$ in the object plane) forms an Airy pattern with finite width in the image plane due to the diffraction limit. Although a single fluorescent molecule is 1 - 10 nm in size and therefore its image is the convolution of an emission distribution of finite size with the diffraction-limited PSF, the intensity distribution of a rotationally mobile and focused single molecule closely resembles the Airy pattern (typical width $R_{\mathrm{obj}} = 0.61\lambda/\mathrm{NA} \sim 250$ nm) in the image plane. In addition, the Airy pattern is often approximated by a Gaussian function with a constant offset (Figure 1.5B) [64–66]

$$I_{\mathrm{Gauss}}(u, v) = a \exp\left[\frac{(u-u')^2 - (v-v')^2}{2c^2}\right] + b, \tag{1.12}$$

where a corresponds to the amplitude of the Gaussian function, which is related with the overall amount of intensity detected, (u', v') is the center position of the Gaussian function, c is the standard deviation or width of the Gaussian function, and b corresponds to the average background offset over the PSF region due to out-of-focus fluorescent molecules or any other captured photons originated from other light sources. The Gaussian model function in Eq. 1.12, therefore, may be fitted to a captured intensity distribution in the image plane using either a least square (LS) fit or maximun likelihood estimation (MLE).

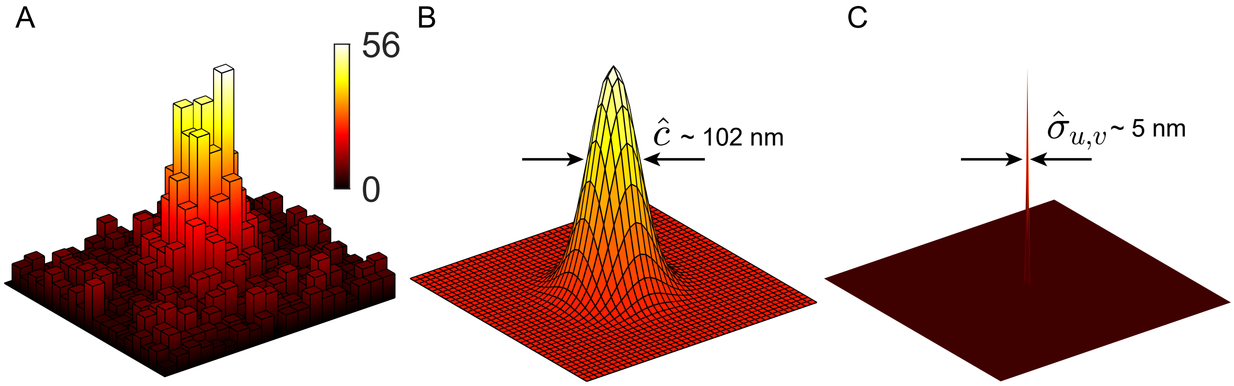

Figure 1.6: Example image and localization using a Gaussian function. (A) A synthesized example image of a single molecule in the image plane. The diffraction-limited PSF (Airy pattern) with 1,000 total photons was simulated using vectorial diffraction theory (see Sections 1.5 and 2.1.1 for details) and corrupted by Poisson-distributed photon-shot noise after adding 5 background photons per pixel. Pixel size: 58.5 nm. Color scale: photons per pixel. (B) Reconstructed two-dimensional Gaussian fit of the image in A. A Gaussian function with $\hat{c} \sim 102$ nm estimated width was fit to the photon distribution using LS minimization. (C) Histogram of 200 fits of synthesized images. The width of this histogram corresponds to a localization precision $\hat{\sigma}_{u,v} \sim 5$ nm, which is much smaller than the width of the diffraction-limited image.

The position of the molecule is determined, i.e. the molecule is localized (Figure 1.6), using the estimated values of (u, v) [67, 68].

The accuracy and precision of the estimates of a molecule's position are critical factors affecting the resolution and quality of SMLM images. If the position coordinates of a single molecule are measured multiple times, localization precision describes the spread of these estimates around the average measurement, whereas localization accuracy describes the deviation of the average measurement from the true SM coordinates [27]. The absolute localization accuracy depends upon how well the model function represents the raw SM images. A large localization bias may be introduced by failing to consider molecular orientation [65, 69–72], PSF overlapping [73–75], etc. On the other hand, the localization precision is affected by various noise processes during acquisition of SM images by a camera sensor. A camera sensor, sCMOS or EMCCD, may introduce a significant amount of noise via pixelation, thermally generated electrical charge (dark current), readout of charge, and analog-to-digital conversions (quantization). Furthermore, since single molecules are generally quite dim, where only a few hundred to a few thousands photons are detected per image acquisition, Poisson noise (or photon shot-noise) due to random photon arrivals is the fundamental source of image degradation [76]. The best possible localization precision $\sigma_{u,v}$ for a LS fit was characterized by Thompson, Larson, and Webb [77] and later slightly corrected by Mortensen et al. [9] is given by,

$$\sigma_{u,v} = \sqrt{\frac{c^2 + s^2/12}{N}\left(\frac{16}{9} + 4\tau\right)} \tag{1.13}$$

where $c^2 + s^2/12$ is the effective size of the Gaussian spot after pixelation, N is the total number of photons detected from the molecule of interest per image frame, s is the effective camera pixel size (the actual pixel size divided by the microscope magnification M), and τ roughly equals to the ratio between the background intensity and the peak intensity of the fit Gaussian function, given by

$$\tau = \frac{2\pi b(c^2 + s^2/12)}{Ns^2}. \tag{1.14}$$

This estimate of localization precision gives $\sigma_{u,v} \approx 2 - 16$ nm with a practical number of photons detected (300−5,000) with $b = 20$ background photons per pixel ($s = 58.5$ nm). This precision represents an order of magnitude improvement over the width of a diffraction-limit spot $R \sim 250$ nm. Typically, a bright SM signal is necessary for precise SM localization. Experimentally, one can achieve this by allocating the limited photons efficiently in time and spectrally filtering the fluorescence of single molecules from background autofluorescence and scattering of the excitation laser.

1.4.2 Active Control of Emitter Concentration

For applying the idea described in Section 1.4.1, SM PSFs must be well separated by a sufficient distance, such that they can be individually distinguished and localized. In practice, fluorescent molecules must be separated by a distance greater than the diffraction limit (or the Rayleigh resolution limit), generating a “sparse” image. However, in typical wide-field imaging applications, biological structures are densely labeled with fluorescent probes that emit fluorescence simultaneously, causing significant overlapping of multiple molecule images and blurring out relevant details within the structure of interest. It is, therefore, impossible to distinguish one molecule from its neighbors and localize them accurately and precisely (Figure 1.7C). A route to achieve super-resolution then is to decrease the concentration of fluorescent molecules that simultaneously emit fluorescence and then repeatedly sample random subsets of the population of fluorescent labels over time [78].

There are many fluorophores that allow microscopists to control the emissive and dark states of those fluorescent molecules over the course of an imaging acquisition [22, 79, 80]. For example, some fluorescent proteins are photoactivatable and can be “turned on” from a weakly fluorescent state to a strongly fluorescent one via stimulation of violet light [62, 63]. In contrast to this irreversible transition, many other fluorophores have the ability to reversibly switch between bright and dark states, e.g., when illuminated by a strong laser in the presence of a strong reductant (dSTORM), termed photoswitching [61,81]. Both mechanisms require activation or switching lasers in addition to longer-wavelength readout lasers. Experimenters also can employ non-optical active control mechanisms, where fluorophores are only fluorescent upon binding to specific structures with high hydrophobicity or viscosity [36, 46, 82].

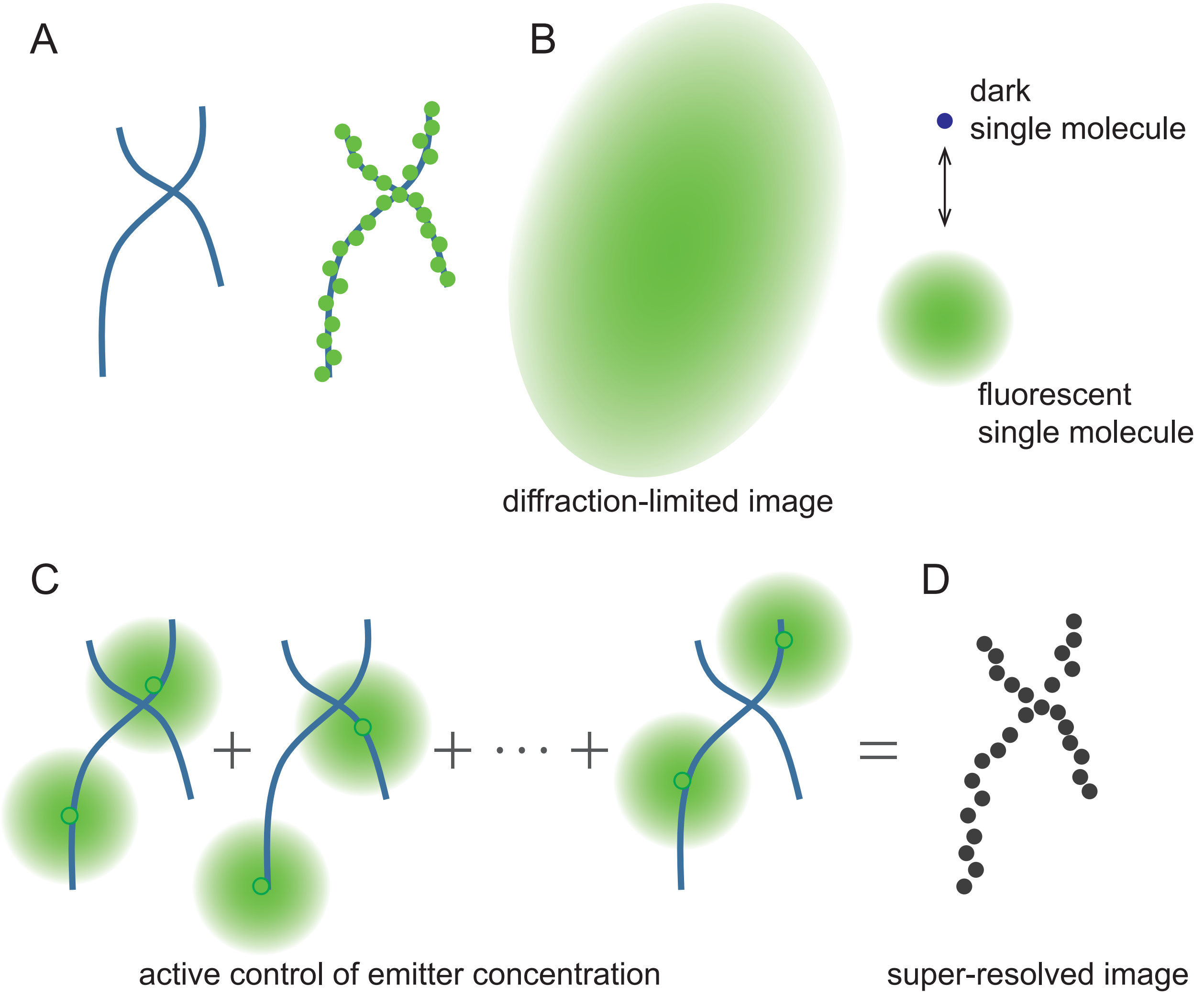
A
B
dark
single molecule
fluorescent
single molecule
diffraction-limited image
C
D
active control of emitter concentration
super-resolved image

Figure 1.7: Principle of single-molecule localization microscopy. (A) A structure of interest (left) and a dense collection of fluorescent labels (right). (B) In conventional fluorescence microscopy, all molecules emit simultaneously. The details of the structure are obscured by overlapping SM PSFs. (C) Only a sparse subset of fluorophores on the structure is activated in a time-sequential manner by active control of emitter concentration. The well-separated PSFs can be localized with precision beyond the diffraction limit. (D) From the list of localized molecules, a super-resolved reconstruction is assembled in a post-processing step.

Notably, each of these methods requires precise control of laser illumination and careful selection of laser wavelength and additive chemicals for limiting the effective concentration of fluorescent molecules in each image frame. Once only a tiny subset of molecules labeling a structure are in their emissive state at a given time point, then such molecules can be individually localized with high localization precision. This subset of fluorophores is then switched to their dark state by the chemical reductant, intersystem crossing, photobleaching, or unbinding from the sample structures. Another subset of molecules is activated or allowed to emit fluorescence subsequently. Repetition of this process and accumulation of the localized positions provides a super-resolved sample reconstruction in a "pointillist" fashion. Thus, these techniques are referred as single-molecule localization microscopy (SMLM). Note that this approach increases spatial resolution beyond the diffraction limit at the cost of temporal resolution. Although some studies examine fixed and immobilized samples, tradeoffs must be made if sample motions and dynamics are monitored during the image acquisition process [26].

1.5 Single-Molecule Image Formation by an Optical System

In Section 1.3.2 and 1.4.1, we have discussed the microscope PSF (Airy pattern) and its approximation as a two-dimensional Gaussian function. This diffraction pattern characterizes the response of an optical system to an ideal isotropic and monochromatic point emitter in its focal plane (if there really exists such an emitter [83]). In practical imaging, however, SM images captured by a highly sensitive detector are often distorted due to sample defocus, mismatched media and imaging-system aberrations, such as chromatic and spherical aberrations. In addition, the fact that single fluorescent molecules emit photons highly anisotropically (Figure 1.2) also causes dissimilar diffraction patterns in an image plane. An image-formation model taking into account these effects is necessary for precise and accurate localization of single molecules and estimation of additional SM quantities, e.g., orientation and wavelength. In this section, I describe vectorial diffraction theory for modeling the image formation of a SM dipole by a high NA microscope [29, 84–87].

1.5.1 Imaging in Refractive-Index Matched Media

The orientation of the molecule's transition dipole moment $\boldsymbol{\mu}$ (also see Section 1.2) can be parameterized using an azimuthal angle $\phi \in [0, 2\pi)$ and a polar angle $\theta \in [0, \pi/2)$ in spherical coordinates or its projection onto the Cartesian coordinates as

$$\boldsymbol{\mu} = \begin{bmatrix} \mu_x \\ \mu_y \\ \mu_z \end{bmatrix} = \begin{bmatrix} \sin(\theta)\cos(\phi) \\ \sin(\theta)\sin(\phi) \\ \cos(\theta) \end{bmatrix}. \tag{1.15}$$

Note that due to the two-fold degeneracy of a dipole moment, this unit vector is only defined over a hemisphere instead of a full sphere. The objective lens of a microscope only collects the radiation from the dipole satisfying $\vartheta \leq \vartheta_{\text{obj}}$, where ϑ is the inclination of a fluorescene ray with respect to the optical axis and ϑ_{obj} is the maximum collection angle of the objective (Figure 1.4). If a far-field (FF) point from the center of the dipole is defined by a distance vector $\boldsymbol{r}$, or by the spherical coordinates (r, φ, ϑ), such that

$$\boldsymbol{r} = \begin{bmatrix} r\sin(\vartheta)\cos(\varphi) \\ r\sin(\vartheta)\sin(\varphi) \\ r\cos(\vartheta) \end{bmatrix}, \tag{1.16}$$

then the electric fields at this point can be calculated by solving Maxwell's equations for an oriented electric dipole and expressed using Green's tensor notation [29] as

$$\boldsymbol{E}_{\mathrm{FF}}(r, \varphi, \vartheta, z) = A\exp(jn_1kz\cos(\vartheta))\boldsymbol{G}_{\mathrm{FF}}(\varphi, \vartheta)\boldsymbol{\mu}, \tag{1.17}$$

where A represents a scaling factor related to the strength of the excitation light, the molecule's absorption cross section, fluorescence quantum yield and other factors, n_1 is the refractive index of the immersion medium ($n_1 = 1.518$ for an oil-immersion objective), $k = 2\pi/\lambda$ is the wavenumber of the fluorescence, z is the distance between the molecule and the focal plane of the objective, and

$$\begin{aligned} \boldsymbol{G}_{\mathrm{FF}}(r, \varphi, \vartheta) &= \frac{\exp(jn_1kr)}{4\pi r}\big(\boldsymbol{I} - \frac{\boldsymbol{r}\otimes\boldsymbol{r}}{r^2}\big) \\ &= \frac{\exp(jn_1kr)}{4\pi r}\begin{bmatrix} 1-\cos^2(\varphi)\sin^2(\vartheta) & -\cos(\varphi)\sin(\varphi)\sin^2(\vartheta) & -\cos(\varphi)\cos(\vartheta)\sin(\vartheta) \\ -\cos(\varphi)\sin(\varphi)\sin^2(\vartheta) & 1-\sin^2(\varphi)\sin^2(\vartheta) & -\sin(\varphi)\cos(\vartheta)\sin(\vartheta) \\ -\cos(\varphi)\sin(\vartheta)\sin(\vartheta) & -\sin(\varphi)\cos(\vartheta)\sin(\vartheta) & 1-\cos^2(\vartheta) \end{bmatrix}. \end{aligned} \tag{1.18}$$

In Eq. 1.18, $\boldsymbol{r}\otimes\boldsymbol{r}$ denotes the outer product of $\boldsymbol{r}$ with itself. The exponential term in Eq. 1.17 shows the electric-field phase delay due to defocus $z \ll r$ and the scalar coefficient $\exp(jn_1kr)/4\pi r$ in Eq. 1.18 accounts for the electric field attenuation and phase-lag introduced by a wave traveling a distance r.

The interaction between an objective lens and the electric field from a dipole can be considered as follows. Any rays with $\vartheta \leq \vartheta_{\text{obj}}$ relative to the optical axis, collected from the dipole, are refracted by the lens such that they all emerge parallel to the optical axis. This transformation ensures that s-polarized component of the electric field with respect to the surface of the objective remains unchanged, whereas the p-polarized component of the electric field is rotated so that it is orthogonal to the optical axis. Each of the rays collected by the objective lens propagates parallel and in-phase with one another after this interaction until reaching the BFP of the objective. By taking into account the ray rotation, the Green's tensor notation is now given by [84, 87]

$$\begin{aligned}\boldsymbol{G}_{\text{BFP}}(\varphi,\rho) &= \frac{\exp(jn_1kf_{\text{obj}})}{4\pi f_{\text{obj}}}\sqrt{\frac{n_1}{n_0(1-\rho^2)^{1/2}}}\\ &\times\begin{bmatrix}\sin^2(\varphi)+\cos^2(\varphi)\sqrt{1-\rho^2} & \sin(2\varphi)\left(\sqrt{1-\rho^2}-1\right)/2 & -\rho\cos(\varphi)\\ \sin(2\varphi)\left(\sqrt{1-\rho^2}-1\right)/2 & \cos^2(\varphi)+\sin^2(\varphi)\sqrt{1-\rho^2} & -\rho\cos(\varphi)\\ 0 & 0 & 0\end{bmatrix},\end{aligned} \tag{1.19}$$

where f_{obj} is the focal length of the objective and replaced with r in Eq. 1.18, n_0 is the refractive index at BFP (typically air, $n_0 = 1$) and $\rho = \sin(\vartheta)$. Note that the radial coordinate ρ is normalized by f_{obj} since this quantity is not explicitly provided by objective manufacturers. The square-root term, $\sqrt{n_1}/\sqrt{n_0(1-\rho^2)^{1/2}}$ ensures energy preservation after propagation through the objective [84]. The third row vector of $\boldsymbol{G}_{\text{BFP}}$, which only contains zeros, confirms that the field emitted by a dipole on the optical axis produces a collimated plane wave in the BFP. Therefore, the electric field of BFP is simply given by

$$\boldsymbol{E}_{\text{BFP}}(\varphi,\rho,z) = A\exp\left[jn_1kz(1-\rho^2)^{1/2}\right]\boldsymbol{G}_{\text{BFP}}(\varphi,\rho)\boldsymbol{\mu}, \tag{1.20}$$

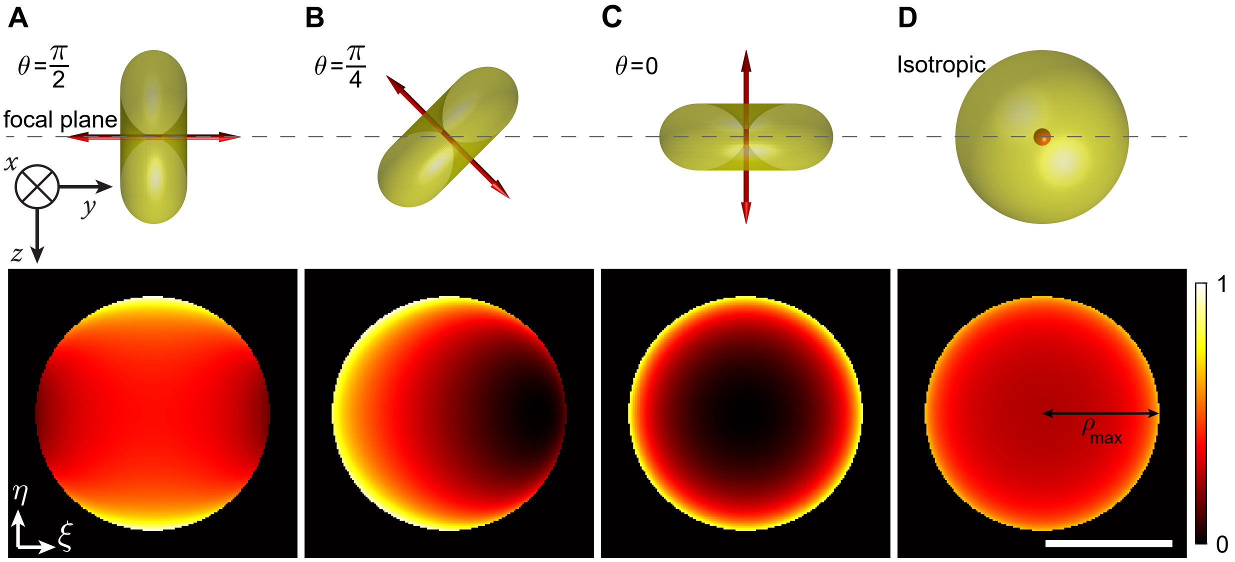

Figure 1.8: Representative intensity distributions in BFP with different fluorescent emitter orientations. (Top) orientations and emission patterns of single dipole moments with polar angles (A) $\theta = \pi/2$, (B) $\theta = \pi/4$ and (C) $\theta = 0$, and (D) isotropic emission of an ideal point emitter. (x, y, z) are coordinates in the object space as shown in Figure 1.4. (Bottom) Corresponding intensity distributions in BFP. Scale bar: one focal length f_{obj} of the objective lens. (ξ, η) are coordinates in the BFP as shown in Figure 1.4.

and the intensity distribution in BFP is calculated as

$$\boldsymbol{I}_{\text{BFP}}(\varphi, \rho, z) = \left\|\boldsymbol{E}_{\text{BFP}}(\varphi, \rho, z)\right\|^2 = \boldsymbol{E}^{\dagger}_{\text{BFP}}(\varphi, \rho, z)\boldsymbol{E}_{\text{BFP}}(\varphi, \rho, z), \tag{1.21}$$

where $\boldsymbol{E}^{\dagger}$ denotes the complex conjugate of $\boldsymbol{E}$. The effect of molecular orientation in captured intensity distribution in BFP is shown in Figure 1.8. When a molecule is oriented along the optical axis ($\theta = 0$), the majority of photons propagate away from the collection angle of the objective ($\vartheta > \vartheta_{\text{obj}}$), thus resulting a overall dimmer BFP image compared to that of a molecule oriented in the focal plane of the objective ($\theta = \pi/2$).

The electric field in the BFP is then projected into the image plane by a tube lens with focal length f (Figure 1.4). Since a typical high NA objective has a small focal length

$f_{\text{obj}} \ll f$ and thereby leading to a small ϑ_{img} (see Figure 1.4), the paraxial approximation holds and the electric field emerging from the tube lens mainly consists of plane waves perpendicular to the optical axis. Therefore, the scalar diffraction theory of Fourier optics [57] (also see Section 1.3.2) is sufficient to model light propagation through the tube lens, and the electric field distribution in the image plane is a scaled Fourier transform of the electric field in BFP of the objective, written as

$$\boldsymbol{E}_{\text{img}}(\varphi', \rho', z) = C \int_0^{2\pi} \int_0^{\rho_{\max}} \boldsymbol{E}_{\text{BFP}}(\varphi, \rho, z) \exp\left[j 2\pi \rho' \rho \cos(\varphi' - \varphi)\right] \rho d\rho d\varphi, \tag{1.22}$$

where (φ', ρ') are cylindrical coordinates in the image plane corresponding to the Cartesian coordinates (u, v) in Figure 1.4 and C is a complex constant. The intensity distribution in the image plane, that is an SM image captured by a camera, is calculated similar to Eq. 1.21 such that $\boldsymbol{I}_{\text{img}} = \left\|\boldsymbol{E}_{\text{img}}\right\|^2$.

1.5.2 Imaging in the Presence of Index Mismatch

In many practical forms of optical microscopy, samples are often imaged in the presence of index mismatch rather than in a homogeneous medium. For instance, most biological specimens have a refractive index close to that of water ($n_2 = 1.334$), while a typical objective lens with large NA requires immersion oil with refractive index matching that of glass ($n_1 = 1.518$). If a molecule emits fluorescence from a distance d above the refractive-index interface, the light rays will be refracted by the interface, resulting in a spherically aberrated image in the image plane [88,89]. On the other hand, if the refractive index of the top medium is less than that of the bottom medium and the molecule is very close to the mismatched interface such that $d < \lambda$, then the evanescent field of the molecule can couple into propagating

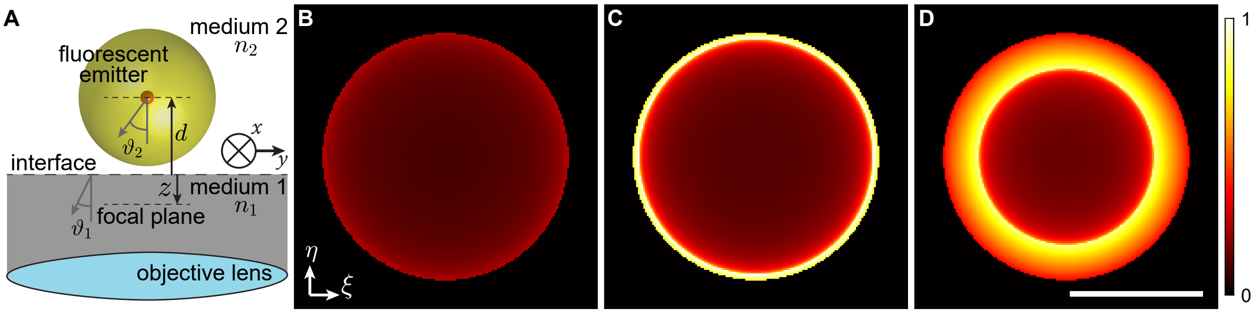

Figure 1.9: Single emitter imaging in the presence of index mismatch and intensity distributions in back focal plane with various refractive index mismatches. (A) Schematic diagram of an emitter at an interface. The distance d and z indicate the axial shift of the emitter from the interface and the depth of the interface with respect to the objective's focal plane, respectively. Due to the glass-sample geometry, d cannot be negative, and positive z means moving the objective lens away from the emitter. The angles ϑ_1 and ϑ_2 represent the polar trajectory of a given ray propagating from the molecule to the objective lens. Representative intensity distributions in BFP with an isotropic emitter at $d = z = 0$, $n_1 = 1.518$ and (B) $n_2 = 1.518$ (matched), (C) $n_2 = 1.334$ (water interface) and (D) $n_2 = 1$ (air interface). The glass-water and glass-air interfaces produce a high intensity ring in the BFP where the evanescent field has been converted to propagating waves. Scale bar: one focal length f_{obj} of the objective lens.

waves through the objective lens [86]. A modified Green's tensor is required to account for this refractive index change between the immersion media and coverslip and to simulate the electric field refraction and coupling occurring at the interface (Figure 1.9). The corrected Green's tensor $\boldsymbol{G}_{\text{BFP}}(\varphi, \rho, d)$ is given by [29, 85, 87]

$$\boldsymbol{G}_{\text{BFP}}(\varphi, \rho, d) =$$
$$\begin{bmatrix} c_3 \sin^2(\varphi) + c_2 \cos^2(\varphi)\sqrt{1-\rho^2} & \sin(2\varphi)\left(c_2\sqrt{1-\rho^2} - c_3\right)/2 & -c_1\rho\cos(\varphi) \\ \sin(2\varphi)\left(c_2\sqrt{1-\rho^2} - c_3\right)/2 & c_2\sqrt{1-\rho^2} - \left(c_2\sqrt{1-\rho^2} - c_3\right)\cos^2(\varphi) & -c_1\rho\sin(\varphi) \\ 0 & 0 & 0 \end{bmatrix}, \tag{1.23}$$

where the constants $\{c_1, c_2, c_3\}$ are defined as

$$\begin{aligned} c_1 &= \left(\frac{n_1}{n_2}\right)^2 \frac{\cos(\vartheta_1)}{\cos(\vartheta_2)} t^p(\vartheta) \exp[jkn_2 d\cos(\vartheta_2)], \\ c_2 &= \frac{n_1}{n_2} t^p(\vartheta) \exp[jkn_2 d\cos(\vartheta_2)] \quad \text{and} \\ c_3 &= \frac{n_1}{n_2} \frac{\cos(\vartheta_1)}{\cos(\vartheta_2)} t^s(\vartheta) \exp[jkn_2 d\cos(\vartheta_2)], \end{aligned} \tag{1.24}$$

where k is the wavenumber of fluorescence. The angles ϑ_1 and ϑ_2 are the polar inclination of rays traveling from the objective to the molecule and they are related to ρ in BFP by

$$\vartheta_1 = \sin^{-1}(\rho) \quad \text{and} \tag{1.25}$$

$$\vartheta_2 = \sin^{-1}\left(\frac{n_1}{n_2}\rho\right). \tag{1.26}$$

Finally, $t^p(\vartheta)$ and $t^s(\vartheta)$ are the Fresnel transmission coefficients for p- and s-polarized light and given by

$$t^p(\vartheta) = \frac{2n_2\cos(\vartheta_2)}{n_2\cos(\vartheta_1) + n_1\cos(\vartheta_2)} \quad \text{and} \tag{1.27}$$

$$t^s(\vartheta) = \frac{2n_2\cos(\vartheta_2)}{n_1\cos(\vartheta_1) + n_2\cos(\vartheta_2)}. \tag{1.28}$$

Once the Green's tensor has been calculated, the electric field in BFP of the objective lens and in the image plane can be obtained by plugging these equations into Eq. 1.20 and 1.22. This new Green's tensor accounts for the evanescent field coupling and produce high intensity rings, termed super-critical regions, in BFP of an objective lens (Figures 1.9B-C).

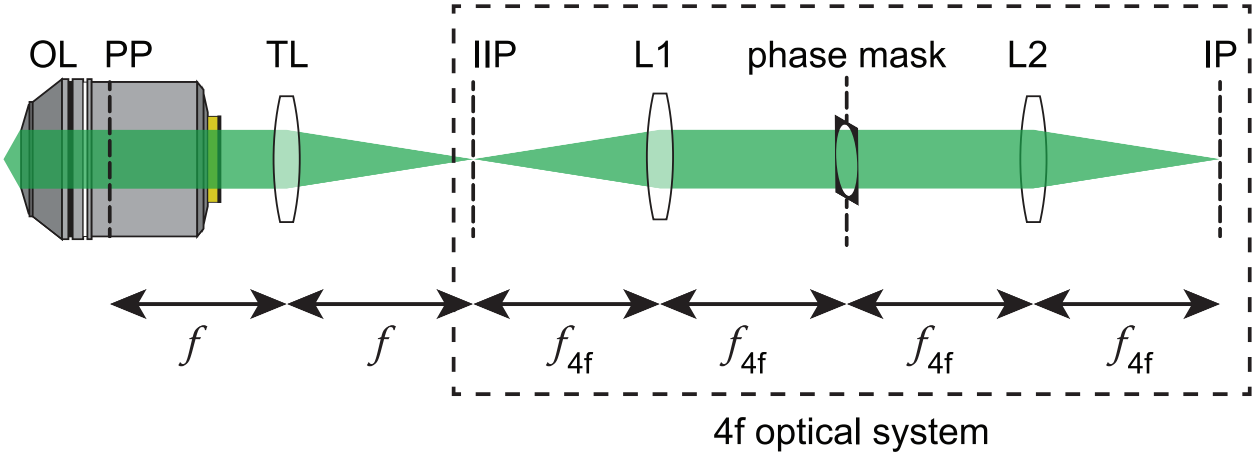

Figure 1.10: Optical 4f system for implementing engineered PSFs. The 4f system is a simple one-to-one telescope consisting of two lenses, L1 and L2, with the same focal length $f_{4\text{f}}$. The lens combination of tube lens (TL) and the first 4f lens (L1) maps the pupil (PP) of the objective lens (OL) to the Fourier plane of the 4f system, where a phase mask is placed to implement an engineered PSF. Similarly the intermediate imaging plane (IIP) generated by OL and TL projected to a second imaging plane (IP) by the 4f system optical train.

1.5.3 Point Spread Function (PSF) Engineering

Historically, design or optimization of imaging systems has involved shaping and aligning optical components, such as lenses, to produce a PSF that is aberration-free and as shift invariant as possible. However, since the early 1980s, PSF engineering or wavefront shaping has been explored as a new frontier for extending the capabilities of traditional imaging systems. PSF engineering, by definition, covers the design of non-uniform pupil functions to produce specially engineered wavefronts in the image plane. Additional physical quantities, such as axial position [90–93], wavelength [94, 95] and orientation [96–98] of an emitter, can be efficiently encoded into a PSF, typically at the expense of the lateral (xy) localization precision and emitter detectability. The physical quantities of interest are then deconvolved from the complex PSF in a custom post-processing algorithm after image acquisition.

Experimentally, engineered pupil functions are often implemented by employing a 4f optical system (Figure 1.10). A 4f system consists of two lenses of the same focal lengths f_{4f} and a separation of $4f_{\mathrm{4f}}$ between the object and image planes. The combination of tube lens and first 4f lens creates an image of the pupil of the objective lens, which is typically enclosed within the objective body and cannot be physically addressed. An additional optical element, such as spatial light modulator (SLM) or deformable mirror, is responsible for modulating the electric field in the projected pupil plane to generate an engineered PSF in the imaging plane. In general, engineered pupil functions may be designed to vary in both amplitude and phase. However, for SM approaches, it is not practical to apply amplitude modulation in the optical path, as this reduces the overall fluorescence delivered to the imaging plane and the localization precision attainable with the imaging system. Hence, functions that are perfectly transmissive, i.e., phase modulation only, are preferable in SM approaches and also considered in all engineered-PSF applications discussed in this dissertation.

The physical effect of a transmissive phase mask in the pupil is simply multiplying the BFP electric field by a spatially varying phase-lag function $\psi(\varphi, \rho)$ as

$$\boldsymbol{E}_{\mathrm{BFP}}^{\mathrm{PM}}(\varphi, \rho, z) = \exp[j\psi(\varphi, \rho)]\boldsymbol{E}_{\mathrm{BFP}}(\varphi, \rho, z). \tag{1.29}$$

By substituting $\boldsymbol{E}_{\mathrm{BFP}}^{\mathrm{PM}}$ for $\boldsymbol{E}_{\mathrm{BFP}}$ in Eq. 1.22, one can simulate the modified electric field induced by the phase mask in the image plane and obtain the engineered PSF by taking its intensity.

1.6 Roles of Single Fluorescent Molecules as Local Probes

The concept of SMLM overcomes the diffraction limit and achieves the image resolution on the order of 10 nanometers (and recently 1 nm [99]) by precisely localizing PSFs of individual single molecules. Resolving structure details by measuring each SM position, however, is not the only benefit produced by this SM approach. Generally, single molecules change their fluorescence emission (e.g., wavelength, quantum yield, fluorescence lifetime and orientation) in response to interactions with properties of their local microenvironment, e.g., solvent polarity, pH, pressure, viscosity, electric potential, intermolecular distance and local organization [28], which govern behavior and dynamics of biomolecules and chemical reactions [100–102].

Utilizing fluorescence to resolve the local environment of samples has been widely applied especially for studying biophysical systems. Fluorescence lifetime imaging microscopy (FLIM) can map intracellular viscosity by using fluorescence of molecular rotors [102–105]. Lifetime of fluorescence is also utilized to study protein interactions and conformational changes by detecting FRET, in which the excited state energy of a donor fluorophore is non-radiatively transferred to an acceptor molecule for wavelength-shifted fluorescence emission [102,106–108]. Similarly, confocal fluorescent anisotropy and fluorescence detected linear dichroism (FDLD) imaging associated with orientation of fluorophores are demonstrated to measure homogeneity of protein aggregation [109–111]. Moreover, a polarity-sensitive solvatochromic dye can encode lipid phase information into its emission color ratios [112, 113]. Despite these developments in classical fluorescence microscopy, fluorescence property extraction in addition to SM localization beyond the diffraction limit in SMLM may further elucidate hidden sample characteristics in the local environment, such as structural heterogeneity and molecular reaction kinetics, with substantially enough sampling and high resolution across individual targets.

There are several SMLM techniques investigating fluorescence properties in addition to localization of individual molecules. For example, one can study catalytic activity of nanoparticles using turnover of fluorescent molecules [114–116] and employ spectrum shifts of fluorescent molecules to map hydrophobicity of various biological structures [117,118]. In this dissertation, I will also demonstrate SMLM techniques that measure positions and properties of fluorescent molecules simultaneously. In Chapter 3, I will discuss a SMLM application to map heterogeneous photocatalytic activity of nanoparticles and reveal the role of defects in the chemical system by correlating activities of two fluorogenic catalytic reactions, in which non-fluorescent or fluorescent molecules with a low quantum yield are catalyzed to produce highly fluorescent product molecules with a high quantum yield [119, 120]. Later chapters will cover a SMLM extension using SM orientation as a key property to resolve local organizations. Structural heterogeneity of amyloid aggregates (see Section 1.7 below) will be probed by estimating SM orientations of amyloid-sensitive fluorescent molecules in Chapter 6.

1.7 Amyloid Aggregates

Amyloid aggregates and tangles are signatures of various aging-related neurodegenerative diseases (also known as amyloidoses), such as Alzheimer's disease (AD) and Parkinson's disease (PD) [121]. Neurodegeneration is a condition characterized by the progressive loss of the structure and/or function of neurons. The loss and damage of neurons in the functional

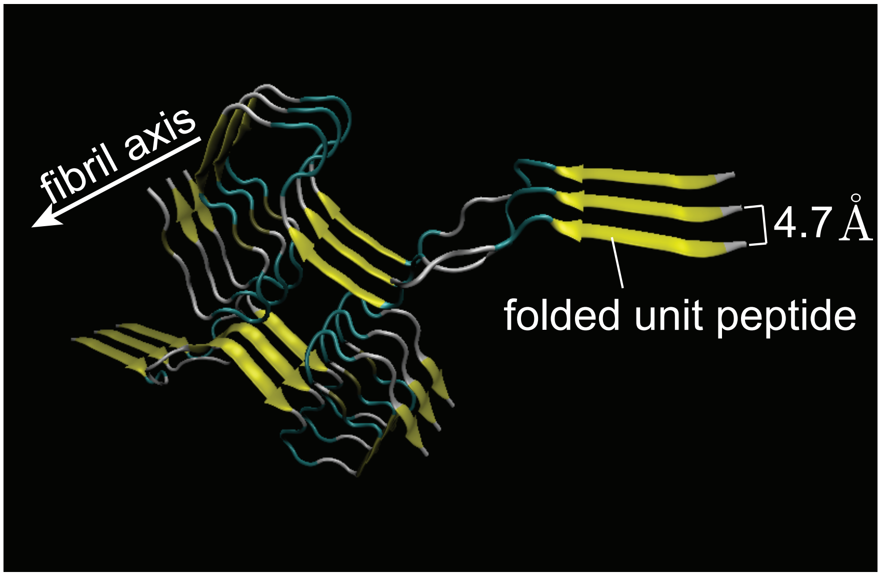

Figure 1.11: Structural model of a cross-β unit consisting of amyloid-β (1-42). The white arrow indicates the direction of the long axis of the fibril, which coincides with the direction of intermolecular backbone hydrogen bonds (cross-strand side-chains). The cross-β motif is common to all amyloid fibrils.

area of brain may lead to many different clinical symptoms, such as dementia, impairment of memory and psychological abnormalities. Although the causes and mechanisms of some neurodegenerative disorders including AD and PD are still unclear, the aggregation of small proteins (also known as peptides or amino acid sequences) into amyloid fibrils (protein aggregates characterized by a linear fibrillar morphology of $8-12$ nm in diameter), their deposition into plaques (cluster of amyloid aggregates formed in the spaces between nerve cells) and cellular uptake of aggregation intermediates are associated with these diseases [121, 122].

Amyloids are aggregates of proteins characterized by fibril formation and a β-sheet secondary structure (Figure 1.11). There are currently approximately 50 different proteins or peptides, such as amyloid-β (1-42) and α-synuclein, known to assemble into amyloid fibrils and associated with human diseases. Their native structures or precursor proteins commonly exist in our bodies. However, once they are cleaved and/or tangled, the amyloid formation

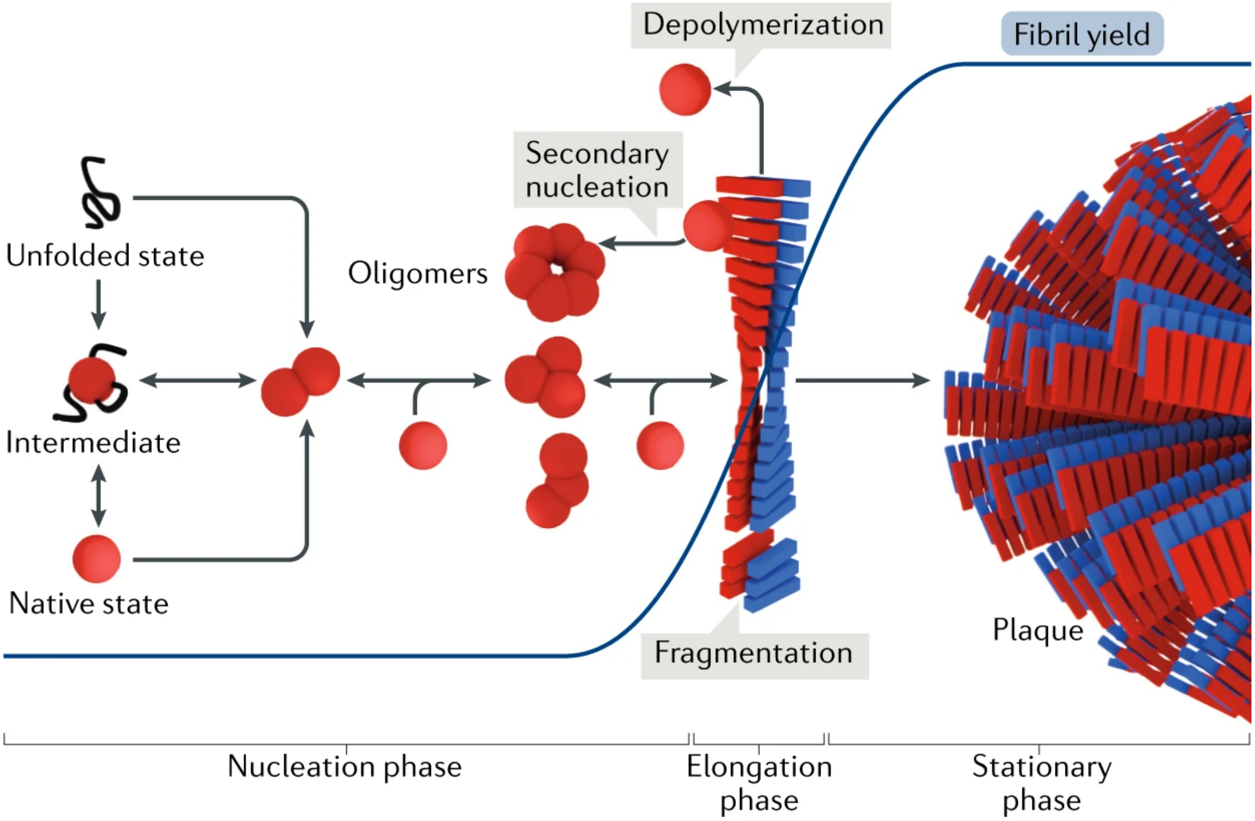
Depolymerization
Fibril yield
Secondary nucleation
Unfolded state
Oligomers
Intermediate
Native state
Fragmentation
Plaque
Nucleation phase
Elongation phase
Stationary phase

Figure 1.12: Schematic of amyloid formation. Native proteins are in dynamic equilibrium and initiate amyloid fibril formation by assembling into oligomeric species. Oligomeric structures can then further assemble to form higher-order species, which can establish a fibril nucleus and assemble into amyloid fibrils. As fibrils grow, they can fragment, yielding additional fibril ends that are capable of further elongation. This process results in an exponential growth of fibrillar material. Fibrils are dynamic and can release oligomers that may or may not be toxic. Finally, fibrils can associate with each other and form amyloid plaques. Cellular uptake of the aggregates is the hallmark of amyloidoses. Reprinted with permission from Ref. [121].

is initiated. The aggregation starts with misfolded monomeric protein structures and shares a common nucleation growth mechanism into fibril assembly regardless of the type of amyloid peptides (Figure 1.12). The fibril formation involves the assembly of oligomers, which are dynamical transient assemblies of individual monomers and intrinsically heterogeneous. Oligomers can then further aggregate into higher-order species, which can ultimately produce fibrils and plaques. Hydrogen bonds between adjacent folded unit peptides in amyloid

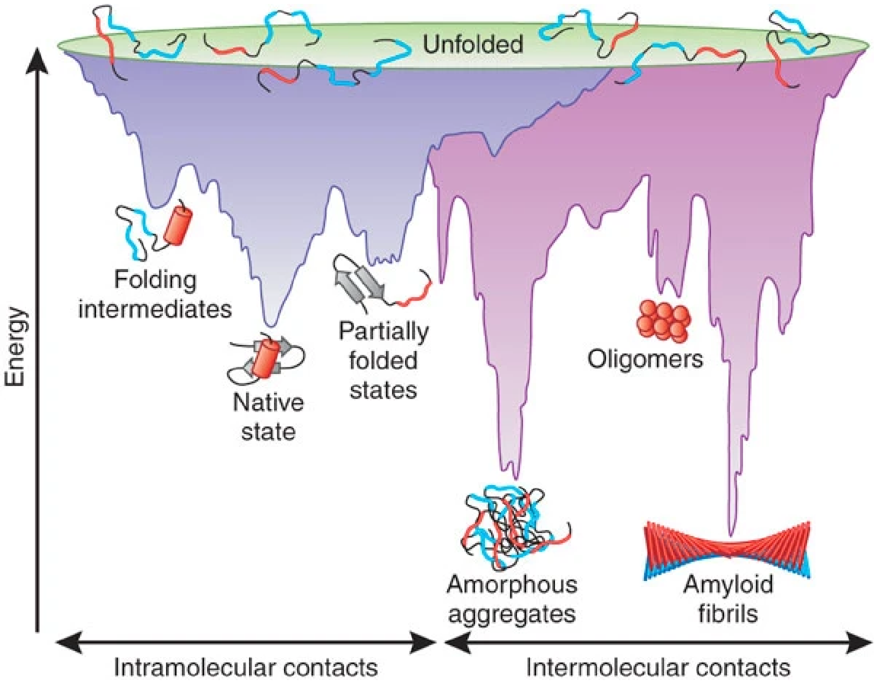
Unfolded
Energy
Folding intermediates
Native state
Partially folded states
Oligomers
Amorphous aggregates
Amyloid fibrils
Intramolecular contacts
Intermolecular contacts

Figure 1.13: Energy landscape scheme of protein folding and aggregation depicting energy changes toward the native states (left) or amorphous aggregates and amyloid fibrils (right). Reprinted with permission from Ref. [131].

fibrils construct repetitive β-sheet ladders (Figure 1.11), which forms surface-exposed side-chain grooves [32]. These grooves can serve as binding sites of amyloid-sensitive fluorescent molecules, such as Thioflavin T (ThT), for monitoring aggregation kinetics in bulk (also see Figure 5.8A) [123–125]. Although many amyloid aggregates share a common cross-β sheet structural motif that is an assembly of identical copies of amyloid peptides [121, 126], oligomers and fibrils are highly heterogeneous in terms of their structure and size [121, 127]. Typically, some small soluble oligomeric aggregation intermediates formed during amyloid fibrillation are considered to be most cytotoxic [128, 129]. However, not all aggregation intermediates are equally toxic [130].

Most proteins in our bodies need to fold into specific three dimensional structures to perform their biological functions and activities (native and functional states). The structural stability of a protein is typically defined as the free energy change between equilibrium states [131–133]. A schematic energy landscape for protein folding and protein aggregation is shown in Figure 1.13. For the protein species that form amyloid aggregates (pathological states), the natively folded protein structures are not the states with the lowest energy. They are only pseudo-stable with respect to the amyloid fibril conformation. Therefore, unfolded peptides or proteins at their native states may funneled into aggregate pathway by misfolding or destabilization of the native structures.

Amyloid aggregates, in summary, are nanoscale dynamical structures including diverse intermediate species. Since the aggregation is intrinsically heterogeneous, a bulk measurement approach cannot resolve details of individual structures. In order to fully understand mechanisms of the aggregation and cytotoxicity of individual aggregates, one needs an imaging method that enables non-averaging visualization of amyloid aggregates with nanometer resolution and long-term imaging capability for monitoring dynamics and interactions of nanoscale structures. An additional imaging capability to reveal local organizations within amyloid aggregates is also necessary for studying structural heterogeneity and elucidating nonlinear aggregation and toxicity depending on each structure. Amyloid visualization using electron microscopy [134], atomic force microscopy [123] or immunostaining fluorescence microscopy [135,136] provides high image resolution. However, it is difficult to satisfy all the requisites listed above based on these modalities.

1.8 Scope and Contribution of Dissertation

This dissertation details the applications of SMLM and its extension to orientation measurements of SM transition dipoles, termed single-molecule orientation localization microscopy

(SMOLM). SM localization and orientation estimates are utilized to probe local heterogeneity within nanoscale samples that cannot be resolved by conventional ensemble measurements. Chapter 2 describes the theoretical framework and experimental details underlying the scientific studies presented in subsequent chapters. In Chapter 3, I will report using SMLM to resolve heterogeneous catalytic activity of a semiconductor photocatalyst. The development of a new PSF for SMOLM, the Duo-spot PSF, and its application in resolving nanodomains of lipid membranes are discussed in Chapter 4. Chapter 5 presents a new versatile imaging modality, transient amyloid binding (TAB), for imaging structures of amyloid aggregates with nanometer resolution. An extension of the TAB technique to measure the orientation of single fluorescent probes on amyloids and resolve structural heterogeneities between amyloid aggregates is presented in Chapter 6.

The main contributions of this dissertation are summarized as follows.

- Introduced a temporal quantile filter for estimating background photons spatiotemporally (Section 2.5.1).
- Used coordinate-based colocalization (CBC) of chemically triggered fluorogenic probes to resolve heterogeneous catalytic activity of a semiconductor photocatalyst and to study the role of defects in the photocatalysis (Chapter 3).
- Designed a new PSF, the Duo-spot PSF, sensitive to SM orientation, and quantified its performance in SMOLM (Chapter 4, Section 4.1).
- Quantified and compared performance of various PSFs for measuring molecular orientation in SMOLM (Sections 4.2 and 6.1).
- Invented a new form of SMLM, transient amyloid binding (TAB) microscopy, for imaging amyloid structures on the nanometer scale (Chapter 5, Section 5.1).

- Demonstrated imaging specificity, less sample perturbation, versatility to visualize variety of amyloids and long-term imaging capability of the TAB imaging for studying amyloid structures (Sections 5.2 - 5.4).
- Extended the TAB SMLM to SMOLM for simultaneous imaging of SM positions and orientations on amyloid structures (Chapter 6).
- Validated that the simple polarized standard PSF provides robust and precise orientation measurements if emitters are dim and near a refractive index interface (Section 6.1).
- Revealed the main binding mode of an amyloid-sensitive molecule, Nile red, on amyloid fiber surfaces and structural heterogeneities along amyloid fibrillar networks that cannot be resolved by SM localization alone (Section 6.2).

Chapter 2

Experimental Methods

In Chapter 1, I introduced the background of photophysics of fluorescent molecules, the concept and theory behind SMLM for super-resolving samples in nanoscale. In this chapter, I present more details about the actual equipment and analysis procedures for the experimental work presented in the dissertation. Specifically, Chapter 2 starts with a discussion of dipole basis functions and a dipole rotation model. A linear decomposition of SM intensity distributions into basis functions and pre-computation of those basis functions help to rapidly generate molecule images with arbitrary dipole orientation in the objective pupil and image plane. Section 2.1 also covers the so-called "rotation-within-a-cone" model for characterizing constrained rotational diffusion of single dipole moments. In Section 2.2, I will provide a detailed optical setup for standard SMLM and some modifications of that applied in the Lew Lab for implementing engineered PSFs and performing SMOLM measurements. In addition, alignment and calibration of several key optical components in these apparatuses are discussed. The current chapter, in Section 2.3, also presents sample preparations and practical imaging procedures used in Chapters 3 - 6. Finally in Sections 2.5 and 2.6, I describe the data-handling methods utilized in post-processing of captured images for localization and orientation estimation of single fluorescent molecules.

2.1 Dipole Basis Functions and Dipole Rotation Model

In section 1.5, we covered vectorial diffraction theory that predicts distorted electric fields in the BFP and image plane of a microscope due to sample defocus, mismatched sample media and the orientation of dipole emitters. In this section, we discuss a set of basis functions that provides a simple and computationally efficient method for calculating images of SM fluorescence formed in the BFP and the image plane [137]. A "rotation-within-a-cone" model will also be introduced in this section for quantifying rotational diffusion of a dipole emitter within a camera acquisition [71, 137].

2.1.1 Dipole Basis Functions

After propagation through a microscope consisting of an objective and tube lens, the electric field emitted from an electric dipole can be calculated as follows

$$\begin{bmatrix} \boldsymbol{E}^{x}_{\text{img}}(u,v) \\ \boldsymbol{E}^{y}_{\text{img}}(u,v) \end{bmatrix} = A \begin{bmatrix} \boldsymbol{E}^{x}_{\mu_x}(u,v) & \boldsymbol{E}^{x}_{\mu_y}(u,v) & \boldsymbol{E}^{x}_{\mu_z}(u,v) \\ \boldsymbol{E}^{y}_{\mu_x}(u,v) & \boldsymbol{E}^{y}_{\mu_y}(u,v) & \boldsymbol{E}^{y}_{\mu_z}(u,v) \end{bmatrix} \begin{bmatrix} \mu_x \\ \mu_y \\ \mu_z \end{bmatrix}, \tag{2.1}$$

where $\boldsymbol{E}^{x,y}_{\text{img}}(u,v)$ are the x- and y-polarized electric fields at a given point, (u,v), in the image plane (Figure 1.4), A represents the amplitude of the electric fields and $\boldsymbol{E}^{x,y}_{\mu_{x,y,z}}(u,v)$ are the x- and y-polarized electric fields associated with an immobile dipole oriented along the x, y or z axis in the object plane. Subscripts denote the orientation of the dipole and superscripts denote the polarization of the field. Note that we have assumed negligible z-polarized electric field here due to the large magnification of the microscope's image with respect to the object of interest (i.e., $\text{NA}_{\text{img}} \ll \text{NA}$, where NA is the objective numerical aperture and $\mathrm{NA}_{\mathrm{img}}$ is the numerical aperture of the tube lens). Thus, the field emitted from an dipole with arbitrary orientation (μ_x, μ_y, μ_z) is a superposition of the electric fields of three fixed dipoles oriented along the Carteisan axes.

The x- and y-polarized intensity distribution $\boldsymbol{I}_{\mathrm{img}}^{x,y}$ in the image plane, therefore, is given by

$$\begin{aligned}\boldsymbol{I}_{\mathrm{img}}^{x,y}(u,v) = {}& \boldsymbol{E}_{\mathrm{img}}^{x,y\,\dagger}(u,v)\boldsymbol{E}_{\mathrm{img}}^{x,y}(u,v)\\ ={}&A^2\Big\{\big|\boldsymbol{E}_{\mu_x}^{x,y}(u,v)\big|^2\mu_x^2 + 2\Re\big\{\boldsymbol{E}_{\mu_x}^{x,y\,\dagger}(u,v)\boldsymbol{E}_{\mu_y}^{x,y}(u,v)\big\}\mu_x\mu_y\\ &+\big|\boldsymbol{E}_{\mu_y}^{x,y}(u,v)\big|^2\mu_y^2 + 2\Re\big\{\boldsymbol{E}_{\mu_x}^{x,y\,\dagger}(u,v)\boldsymbol{E}_{\mu_z}^{x,y}(u,v)\big\}\mu_x\mu_z\\ &+\big|\boldsymbol{E}_{\mu_z}^{x,y}(u,v)\big|^2\mu_z^2 + 2\Re\big\{\boldsymbol{E}_{\mu_y}^{x,y\,\dagger}(u,v)\boldsymbol{E}_{\mu_z}^{x,y}(u,v)\big\}\mu_y\mu_z\Big\}.\end{aligned} \tag{2.2}$$

Next, if we newly define six basis functions as

$$\boldsymbol{B}_{xx}^{x,y}(u,v) = \big|\boldsymbol{E}_{\mu_x}^{x,y}(u,v)\big|^2, \tag{2.3a}$$

$$\boldsymbol{B}_{yy}^{x,y}(u,v) = \big|\boldsymbol{E}_{\mu_y}^{x,y}(u,v)\big|^2, \tag{2.3b}$$

$$\boldsymbol{B}_{zz}^{x,y}(u,v) = \big|\boldsymbol{E}_{\mu_z}^{x,y}(u,v)\big|^2, \tag{2.3c}$$

$$\boldsymbol{B}_{xy}^{x,y}(u,v) = 2\Re\big\{\boldsymbol{E}_{\mu_x}^{x,y\,\dagger}(u,v)\boldsymbol{E}_{\mu_y}^{x,y}(u,v)\big\}, \tag{2.3d}$$

$$\boldsymbol{B}_{xz}^{x,y}(u,v) = 2\Re\big\{\boldsymbol{E}_{\mu_x}^{x,y\,\dagger}(u,v)\boldsymbol{E}_{\mu_z}^{x,y}(u,v)\big\}, \quad \text{and} \tag{2.3e}$$

$$\boldsymbol{B}_{yz}^{x,y}(u,v) = 2\Re\big\{\boldsymbol{E}_{\mu_y}^{x,y\,\dagger}(u,v)\boldsymbol{E}_{\mu_z}^{x,y}(u,v)\big\}, \tag{2.3f}$$

then Eq. 2.2 can be rewritten as

$$\boldsymbol{I}_{\text{img}}^{x,y}(u,v) = A^2 \begin{bmatrix} \boldsymbol{B}_{xx}^{x,y}(u,v) \\ \boldsymbol{B}_{yy}^{x,y}(u,v) \\ \boldsymbol{B}_{zz}^{x,y}(u,v) \\ \boldsymbol{B}_{xy}^{x,y}(u,v) \\ \boldsymbol{B}_{xz}^{x,y}(u,v) \\ \boldsymbol{B}_{yz}^{x,y}(u,v) \end{bmatrix}^{\mathrm{T}} \begin{bmatrix} \mu_x^2 \\ \mu_y^2 \\ \mu_z^2 \\ \mu_x\mu_y \\ \mu_x\mu_z \\ \mu_y\mu_z \end{bmatrix}. \tag{2.4}$$

The basis functions $\boldsymbol{B}^{x,y} = \begin{bmatrix} \boldsymbol{B}_{xx}^{x,y}(u,v) & \dots & \boldsymbol{B}_{yz}^{x,y}(u,v) \end{bmatrix}$ are independent of the emitter orientation and fully characterize the electric field propagation within the imaging system. Any measurement of $I_{\text{img}}^{x,y}$ by a camera in the image plane is a linear superposition of these functions with weighting factors determined by the emitting dipole's orientation $\boldsymbol{\mu}$.

In practical SM imaging, fluorescent probes bound to or labeled on specimens are typically not entirely immobilized in terms of orientation. We assume that molecules undergo rotational motions on timescales much faster than the camera exposure [46, 97, 139]. The effect of this rotational diffusion on the captured intensity can be modeled as

$$\boldsymbol{I}_{\text{img}}^{x,y}(u,v) = A^2 \boldsymbol{B}^{x,y} \frac{1}{t} \int_0^t \begin{bmatrix} \mu_x^2(\tau) \\ \mu_y^2(\tau) \\ \mu_z^2(\tau) \\ \mu_x(\tau)\mu_y(\tau) \\ \mu_x(\tau)\mu_z(\tau) \\ \mu_y(\tau)\mu_z(\tau) \end{bmatrix} d\tau, \tag{2.5}$$

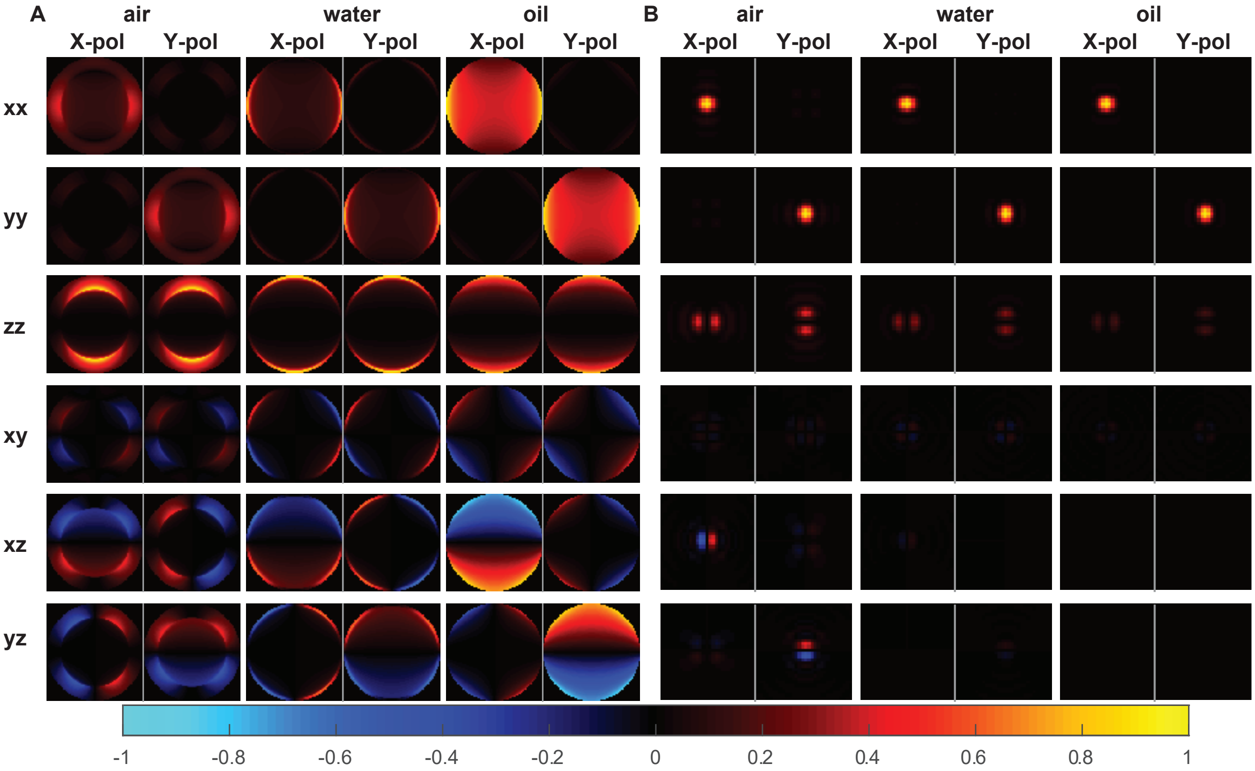

Figure 2.1: Simulated polarized orientational basis images (rows, top to bottom: $\boldsymbol{B}_{xx}$, $\boldsymbol{B}_{yy}$, $\boldsymbol{B}_{zz}$, $\boldsymbol{B}_{xy}$, $\boldsymbol{B}_{xz}$, $\boldsymbol{B}_{yz}$) at the (A) back focal plane and (B) image plane (the polarized standard PSF) of a microscope using a vectorial image-formation model (Section 1.5) [87] for a molecule at a glass-air, glass-water and glass-oil refractive index interface. Images are normalized in each column. Reprinted with permission from Ref. [138].

where t is the camera exposure time. The measured intensity distribution is the temporal average of various orientations that the dipole explores within the camera acquisition. We use $\langle\cdot\rangle$ to denote the temporal averaging operation and the forward imaging model (Eq. 2.5) can be simplified and revised as

$$\begin{aligned}\boldsymbol{I}_{\text{img}}^{x,y}(u,v) =& A^2\boldsymbol{B}^{x,y}\begin{bmatrix}\langle\mu_x^2\rangle & \langle\mu_y^2\rangle & \langle\mu_z^2\rangle & \langle\mu_x\mu_y\rangle & \langle\mu_x\mu_z\rangle & \langle\mu_y\mu_z\rangle\end{bmatrix}^{\mathrm{T}} + \boldsymbol{b}^{x,y} \\ =& s\boldsymbol{B}^{x,y}\boldsymbol{m} + \boldsymbol{b}^{x,y}, \end{aligned} \tag{2.6}$$

where s is the total intensity or the number of photons collected by the detector, $\boldsymbol{b}^{x,y}$ represents background photons due to unwanted light leakage from scattered light and/or out-of-focus fluorophores, and the second-moment vector $\boldsymbol{m}$ fully describes molecular orientation dynamics within a single camera frame. Note that the background photons $\boldsymbol{b}^{x,y}$ may or may not be uniformly distributed in the image plane (u, v) depending SMLM applications. An accurate correction of that is required for precise and accurate localization and orientation estimation (see Section 2.5.1).

The forward model of the intensity distribution in the BFP can be derived in a similar manner by considering the electric fields in the objective pupil (Figure 2.1). A key feature of this model is its linearity with respect to the orientation parameters $\boldsymbol{m}$ of interest; $\boldsymbol{B}$ is simply a linear operator or transformation from object space to image space, and the fundamental measurement sensitivity of the optical system is bounded by considering $\boldsymbol{B}$ directly. This fact will be discussed in more detail in Chapters 4 and 6.

2.1.2 Dipole Rotation Model

In the Lew Lab, we model the rotational diffusion of fluorescent molecules using the wobble-in-cone model (Figure 2.2) [71, 87, 137]. In this model, the orientational unit vector

$$\boldsymbol{\mu} = \begin{bmatrix} \mu_x \\ \mu_y \\ \mu_z \end{bmatrix} = \begin{bmatrix} \sin(\theta)\cos(\phi) \\ \sin(\theta)\sin(\phi) \\ \cos(\theta) \end{bmatrix} \tag{2.7}$$

defines the center orientation of a cone instead of individual orientations within the cone. Unless stated otherwise, hereafter the unit vector $\boldsymbol{\mu}$ refers the center orientation of the cone

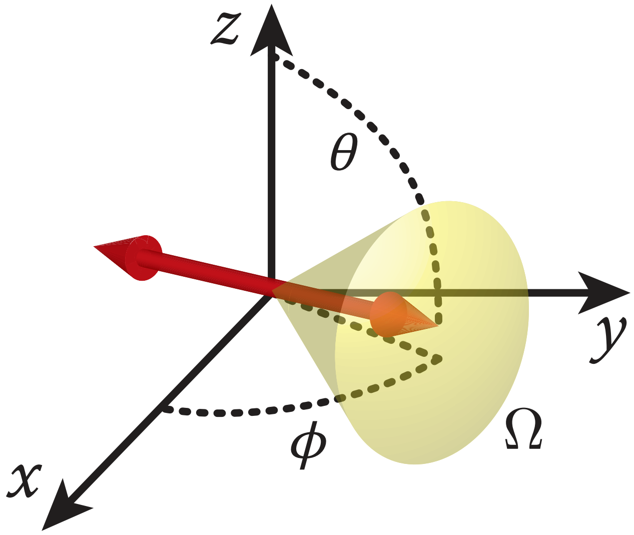

Figure 2.2: Rotation within a cone model. The orientation of a transition dipole is parameterized by an azimuthal angle $\phi \in [-\pi, \pi)$, a polar angle $\theta \in [0, \pi/2]$ and a rotational diffusion-associated wobbling area $\Omega \in [0, 2\pi]$.

throughout this dissertation. An solid angle $\Omega \in [0, 2\pi]$ specifies the "wobbling" area of the cone. If the molecule's rotational correlation time is faster than its excited state lifetime and the camera integration time [139], the second moment vector $\boldsymbol{m}$ is given by

$$\boldsymbol{m}(\phi, \theta, \Omega) = \begin{bmatrix} \langle \mu_x^2 \rangle & \langle \mu_y^2 \rangle & \langle \mu_z^2 \rangle & \langle \mu_x \mu_y \rangle & \langle \mu_x \mu_z \rangle & \langle \mu_y \mu_z \rangle \end{bmatrix}^{\mathrm{T}}, \tag{2.8}$$

$$\langle \mu_x^2 \rangle = \gamma \mu_x^2 + (1-\gamma)/3, \tag{2.9a}$$

$$\langle \mu_y^2 \rangle = \gamma \mu_y^2 + (1-\gamma)/3, \tag{2.9b}$$

$$\langle \mu_z^2 \rangle = \gamma \mu_z^2 + (1-\gamma)/3, \tag{2.9c}$$

$$\langle \mu_x \mu_y \rangle = \gamma \mu_x \mu_y, \tag{2.9d}$$

$$\langle \mu_x \mu_z \rangle = \gamma \mu_x \mu_z, \tag{2.9e}$$

$$\langle \mu_y \mu_z \rangle = \gamma \mu_y \mu_z, \quad \text{and} \tag{2.9f}$$

$$\gamma = 1 - \frac{3\Omega}{4\pi} + \frac{\Omega^2}{8\pi^2}, \tag{2.10}$$

where γ is the rotational constraint [46, 97].

2.2 Single-Molecule Microscopy with Polarized Detection Channels

This Section describes the excitation sources, optics, and detectors essential for quantitative SM imaging. I detail example optical designs used in the semiconductor study shown in Chapter 3 and the other biological system imaging discussed in Chapters 4 - 6. The section also covers how to augment a conventional epi-fluorescence microscope with necessary optical components for implementing engineered PSFs. A specific optical design with polarization-sensitive channels is presented for SM orientation imaging.

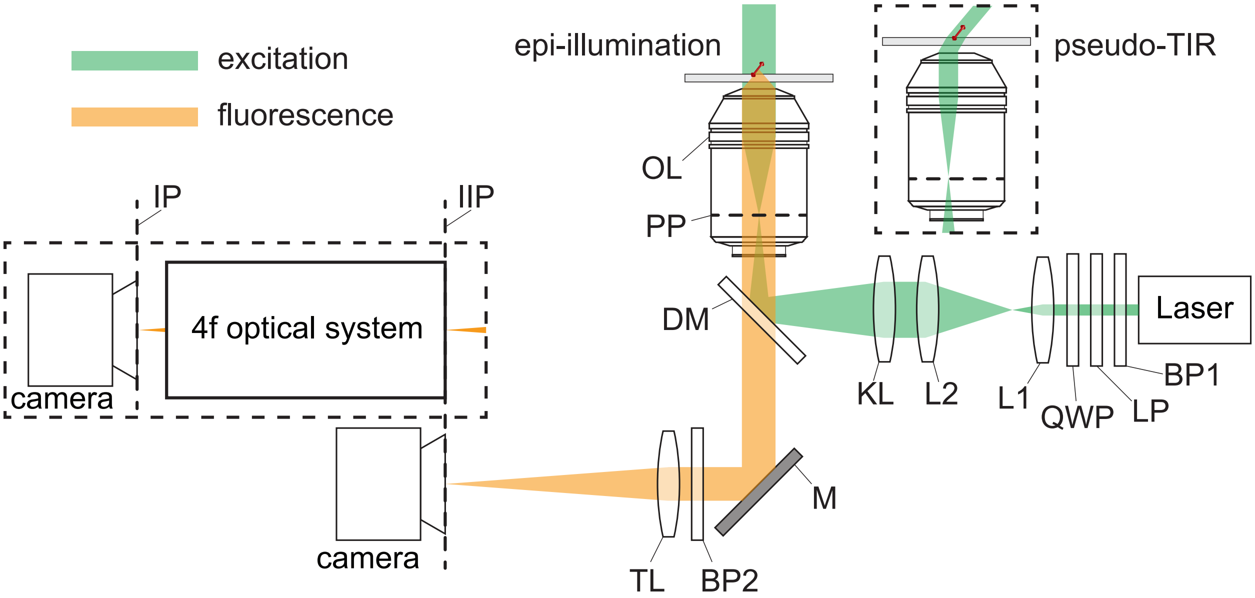
excitation
fluorescence
epi-illumination
pseudo-TIR
OL
PP
IP
IIP
DM
4f optical system
camera
Laser
KL
L2
L1
QWP
LP
BP1
camera
M
TL
BP2

Figure 2.3: Schematics of an epi-fluorescence microscope. The excitation optics include a laser, a bandpass filter (BP1), a linear polarizer (LP), and a quarter-wave plate (QWP) to generate a circular polarized excitation in the image plane. An optional telescope, consisting of lenses L1 and L2, alters the beam's diameter and provides an appropriate illumination profile for widefield imaging. A Köhler lens (KL, also known as a widefield lens) focuses the beam onto the pupil (PP) of the objective lens (OL) via reflection off of a dichroic beamsplitter/mirror (DM). Inset, top right, shows a pseudo-total internal reflection (TIR) excitation profile, in which the pumping beam is tilted with respect to the optical axis in the object plane to reduce background. The collection optics capture the fluorescence photons from the sample and filter them through DM and an additional bandpass filter (BP2) before creating an image with the tube lens (TL) to be captured by a camera. Left inset shows an additional imaging system in the fluorescence collection path, a 4f optical system, for implementing engineered PSFs. Excitation light is depicted in green; fluorescence from the sample is depicted in orange.

Table 2.1: Optical materials list for imaging oxidation of 3'-(*p*-aminophenyl) fluorescein (APF) and acid-catalyzed condensation of furfuryl alcohol (FA) in Chapter 3 [140].

Type	**Part number**	**Specification**
Microscope body	Nikon Ti-E motorized inverted optical microscope	Nikon N-STORM super-resolution microscopy system
Excitation sources[1]	Nikon, LU-NV, continuous wave coupled into fiber	405 nm, 20 mW (excitation of catalysts) 488 nm, 50 mW (excitation of fluorescein) 561 nm, 50 mW (excitation of FA oligomer)
Objective lens OL	Nikon, CFI-6-APO	100×, 1.49 NA, oil
Bandpass filter[2] BP1	Chroma, ZET405/488/561/647x	For filtering 400-410, 486-492, 559-563 and 640-658 nm lasers
Dichroic beamsplitter[2] DM	Chroma, ZT405/488/561/647rpc	For reflecting 380-414, 485-492, 558-568 and 638-659 nm lasers
Bandpass filter[2] BP2	Chroma, ZET405/488/561/647m	For filtering 423-477, 504-549, 582-625 and 677-785 nm laser
Camera	Andor iXon 897 EMCCD	512×512, EM gain 300, 16 μm pixels (corresponding to 160 nm object plane)

[1] Coupled into OL for TIR illumination in the object plane.

[2] Mounted on a C-NSTORM QUAD filter cube (405/488/561/647, CHROMA, TRF89902-NK)

2.2.1 Excitation Sources and Optical Components

The basic schematic of an epi-fluorescence microscope is depicted in Figure 2.3. The following text summarizes the functions of the optical components shown in the excitation path (green) in Figure 2.3. Single molecules are typically excited by a coherent laser source tuned near their peak absorption wavelength. Since the bandwidth of some light sources may be broad and coupled into the collection path, a narrow bandpass excitation filter (BP1) is usually used to filter out long wavelength photons leaked from the excitation source that could contributed to unwanted background. Next, a combination of a linear polarizer (LP, if necessary) and a quarter-wave plate (QWP) is applied to create a circularly-polarized beam for uniformly pumping single molecules with various azimuthal angles (ϕ) in the sample. The quarter-wave plate should match the pumping wavelength for the best-possible circular polarization ratio. Typically, a beam expansion telescope consisting of two lenses L1 and L2 is also placed before illumination into the microscope body. This controls the size of the epi-illumination beam and avoids too small or too large fields of view. The alignment of lenses and beam collimation after the telescope can be tested with a shear-plate interferometer.

The excitation light, then, can be coupled into the microscope in several different ways depending upon the sample of interest (Section 1.3.1). The most straight-forward geometry is conventional widefield epi-fluorescence excitation, in which the excitation beam is focused onto the pupil (PP) of the objective lens (OL) by a Köhler lens (KL, also known as a widefield lens). This arrangement produces a collimated excitation beam in the sample parallel with the optical axis of the objective lens. Alternatively, one can employ the total internal reflection (TIR) illumination with a tilted excitation beam beyond the critical angle and confines the excitation beam only within the evanescent field ($\sim$200 nm) for mitigating background from out-of-focus probe molecules or thick samples. Similarly, we can also excite a sample using pseudo-TIR, a illumination with a severe yet sub-critical tilt. This configuration reduces the thickness of the excitation region but still offers 2D or 3D imaging beyond the surface of a coverslip. Due to the Fourier transform relationship between pupil and sample planes, tilts of the beam in TIR and pseudo-TIR are produced by translation of the beam at the pupil of the objective (Figure 2.3 inset right). These geometries also cause the pumping beam to have a non-circular profile for creating a large dynamic range of pumping intensities in the sample.

2.2.2 Collection Optics and Detectors

The functions of the collection components depicted in Figure 2.3 orange are summarized in the following text. In a standard epi-fluorescence microscope, the objective lens (OL) plays a dual role in both excitation of the sample and collection of fluorescence emission. In the fluorescence collection, the objective is the first optical component collecting the fluorescence emission by dye molecules bound/labeled on a sample of interest. The imaging performance of each microscope objective is defined by its numerical aperture (NA) and aberration correction (Section 1.3.2). For SM imaging, it is critical to use an objective with a high NA since localization precision improves with the square root of the number of detected photons (Section 1.4.1). Other useful characteristics of objective lenses for SM imaging are infinity correction and achromatic aberration correction. Infinity correction is a standard feature of most microscope objective lenses, where the objective lens refracts collected rays such that they all emerge parallel to the optical axis and creates an image of the sample at infinity (also see Section 1.5). The collimation of rays by the objective enables optical components such as fluorescence filters, polarizers, etc. to be placed in the collection path with minimal perturbations to the objective aberration-correction and focusing performance. On the other hand, apochromat objectives are lenses corrected chromatically for three distinct wavelengths, almost eliminating chromatic aberration, and also corrected spherically for either two or three wavelengths. Therefore, it improves the alignment of color channels in multicolor localization microscopy, such as the work discussed in Chapter 3. Despite these characterization and optimization by manufacturer, it is worth to note that no objective is absolutely perfect and some of them are not necessarily optimized and corrected enough for SM purposes. Hence, when the most precise and accurate imaging is needed, careful calibration of objective lens such as by PSF characterization is needed to correct for imaging aberrations.

Additional fluorescence filters are placed in "infinity space" between the objective and tube lenses for filtering out any unwanted background and scattered photons. The dichroic mirror (DM, also known as a dichroic beamsplitter) is typically a longpass filter, allowing red-shifted fluorescence photons to pass through with minimal attenuation while reflecting shorter-wavelength excitation photons up into the microscope objective. Emission filters are used in addition to the dichroic mirror to further isolate the sample fluorescence. Generally, an additional bandpass filter (BP2) is selected, which filters out the excitation wavelength, only admits fluorescence near the peak emission wavelength of the fluorescent probe, and rejects wavelengths much longer than the desired fluorescence wavelength for attenuating autofluorescnece from glass coverslips or Raman scattering from aqueous samples.

The image of the microscope is formed by the tube lens (TL) before captured by a camera in the image plane. For creating a microscope image with the specified magnification factor printed on the objective lens, one needs to use a tube lens with a specific focal length depending upon the objective manufacturer, e.g., Olympus objectives assume a focal length of 180 mm, while Nikon microscopes uses a focal length of 200 nm. In a standard fluorescence microscope, the fluorescence photons are captured by a highly sensitive, low-noise image sensor. Typically, a 2D array detector, such as an EMCCD or sCMOS camera is used for this purpose. These detectors provide high quantum efficiency, low read-out noise, and low dark counts, which are essential for photon-limited SM imaging.

Example optical components used for the photocatalyst study discussed in Chapter 3 are listed in Table 2.1. A standard widefield fluorescence microscope with TIR illumination is used in this work for imaging catalytic activity of a semiconductor catalyst. Oxidation of 3'-(*p*-aminophenyl) fluorescein (APF) and acid-catalyzed condensation of furfuryl alcohol (FA) on the same semiconductor nanowires are imaged via an apochromat objective and a quad filter set [140].

2.2.3 Polarization-Sensitive Collection with 4f Optical System for PSF Engineering

We implement engineered PSFs using a 4f optical system (Figure 2.3 inset left). A 4f optical system is a one-to-one optical telescope of total length $4\times f_{\text{4f}}$ consisting of two lenses of focal length f_{4f} (see Section 1.5.3 and Figure 1.10). The 4f system simultaneously maps the pupil (or BFP) of the objective lens onto its Fourier plane and the intermediate image plane (IIP) created by the microscope onto its image plane (IP). Therefore, the angular spectrum of the image can be physically manipulated.

An example microscope schematic with a 4f optical system is shown in Figure 2.4. This home-built system is used in the lipid nanodomain imaging and the amyloid study discussed in Chapter 4 and Chapters 5 - 6. Samples are excited using a laser with pseudo-TIR (aligned at $\sim 30^\circ$ tilt from normal for reducing background fluorescence) through an oil-immersion objective lens. Fluorescence was collected by the same objective and filtered

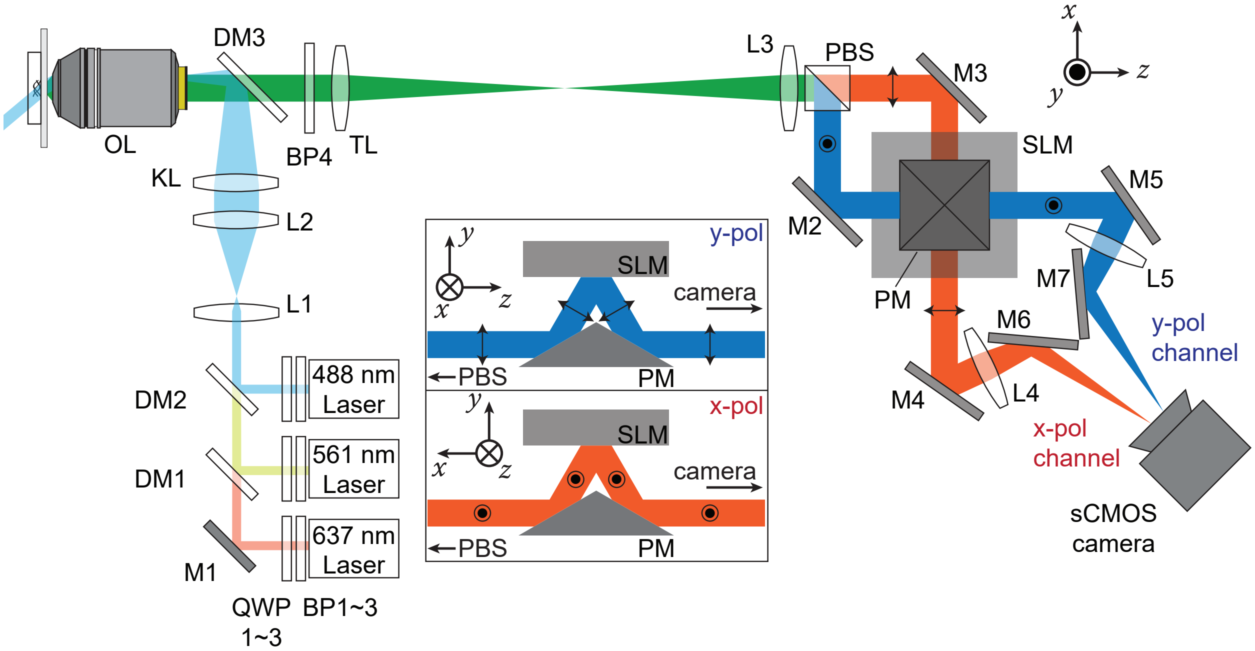
DM3
OL
BP4
TL
L3
PBS
M3
x
y
z
KL
L2
L1
SLM
M5
M2
y-pol
SLM
camera
PM
PBS
M7
L5
PM
M6
y-pol channel
DM2
488 nm Laser
561 nm Laser
637 nm Laser
DM1
M1
x-pol
SLM
camera
PBS
PM
M4
L4
x-pol channel
sCMOS camera
QWP 1~3
BP1~3

Figure 2.4: Schematics of polarization-sensitive fluorescence microscope used in transient amyloid binding (TAB) SMLM and SMOLM (Chapters 5 and 6). Circularly-polarized 488 nm, 561 nm and 637 nm lasers were used for excitation of thioflavin T (ThT) and Nile red (NR) TAB, and intrinsically/antibody-labeled imaging, respectively. After beam expansion by lenses L1 (f = 25.4 mm) and L2 (f = 76.2 mm), the excitation lasers were coupled into a 100X oil-immersion objective (OL, 1.4 NA) for highly-inclined illumination. Fluorescence was collected by the same objective and filtered by dichroic (DM3) and band-pass (BP4) filters listed in Table 2.2. Afterward, the fluorescence was split by a polarizing beam splitter (PBS) into two orthogonally-polarized channels (x- and y-polarized), and lens L3 (f = 150 mm) projects the pupil plane onto a spatial light modulator (SLM) using a square pyramidal mirror (PM). After reflection, the two channels were imaged onto different portions of an sCMOS camera by lenses L4 and L5 (f = 150 mm). An engineered phase mask can be applied at the SLM for modulation of the phase of fluorescence in the Fourier plane of polarization channels [141]. Red depicts x-polarized fluorescence channel; blue depicts y-polarized fluorescence channel.

Table 2.2: Optical materials list used in thioflavin T (ThT) and Nile red (NR) transient amyloid binding (TAB) SMLM and SMOLM (Chapters 5 and 6) [125, 138].

Type	**Part number**	**Specification**
Basics		
Microscope body	Home-built system with Physik Instrumente (PI) positioners	P-545 XYZ PI nano system M-545 XY PI travel stage C-863 Z PI motorized stage
Objective lens OL	Olympus, Uplan-SApo	100×, 1.40 NA, oil
Polarization beamsplitter PBS	Meadowlark Optics BB-100-VIS	20-mm clear aperture, $\leq \lambda/5$ wavefront distortion $\geq$500:1 p-pol, $\geq$20:1 s-pol extinction ratio
Spatial Light Modulator SLM	Meadowlark Optics HSPDM256-520-700-P8	256 XY Phase Series, 24 μm pixel size $\geq$94% reflectivity, $\leq \lambda/8$ wavefront distortion
Camera	Hamamatsu, C11440-22CU ORCA FLASH4.0v2, sCMOS	2048×2048, 16 μm pixel size (corresponding to 58.5 nm object plane)
ThT TAB		
Excitation source	Coherent OBIS 488 LX150	100 mW, 2.2 kW/cm^2 peak intensity at sample
Bandpass filter BP1	Semrock, FF01-488/6-25	single-band filter (485-491 nm)
Dichroic mirror DM3	Semrock, Di03-R488/561-t1	dual-edge filter (500 nm and 575.5 nm)
Bandpass filter BP4	Semrock, FF01-523/610	dual-band filter (503-543 nm and 584-636 nm)
NR TAB		
Excitation source	Coherent Sapphire 561 LP200	20 mW, 0.88 kW/cm^2 peak intensity at sample
Bandpass filter BP2	Semrock, FF01-561/4-25	single-band filter (559–563 nm)
Dichroic mirror DM3	Semrock, Di03-R488/561-t1	dual-edge filter (500 nm and 575.5 nm)
Bandpass filter BP4	Semrock, FF01-523/610	dual-band filter (503-543 nm and 584-636 nm)
Intrinsically/antibody-labeled imaging		
Excitation source	Coherent OBIS 637 LX140	50 mW without L1/L2 beam expansion telescope 10 kW/cm^2 peak intensity at sample
Bandpass filter BP3	Semrock, FF01-637/7-25	single-band filter (634–641 nm)
Dichroic mirror DM3	Semrock, Di02-R635	single-edge filter (655.8 nm)
Bandpass filter BP4	Semrock, FF01-676/37	single-band filter (657.5–694.5 nm)

by a dichroic beamsplitter and a bandpass filter followed by a polarization-sensitive 4f system. This type of 4f system uses a polarization beamsplitter (PBS) to split the collected fluorescence into two orthogonal polarization (x-pol and y-pol) channels, which are then reflected upward by a square pyramidal mirror (PM) to project the pupil plane of the objective onto a reflective liquid-crystal spatial light modulator (SLM) for phase modulation. The fluorescence then reflects off of the SLM and the PM to propagate parallel to the plane of the optical table. The two polarized fluorescence beams are imaged onto two separate regions of the same camera. This system efficiently modulates the two polarization channels by the same SLM without needing a half-wave plate[1]. Optical components used in this setup are listed in Table 2.2 [125, 138]. Figure 2.5 demonstrates several representative engineered PSFs (middle and bottom rows) used in this dissertation that can be produced by applying the corresponding phase masks (top row) on the SLM in the polarization-sensitive 4f system. Note that due to the symmetry of the imaging setup, the same phase masks but rotated by 90° modulate fluorescence in the x-pol channel.

In actual implementation of the 4f system, the objective pupil must be properly projected onto the mask generated by the SLM, that is, the pupil must match the size of the phase mask and should be well-aligned with the mask on the SLM. Proper implementation can be investigated by imaging the SLM surface and pupil plane using a flipping mirror to guide the fluorescence after the second 4f lens into another imaging system consisting of a lens and camera. By illuminating the SLM with fluorescence from a concentrated layer of fluorescent molecules or beads, one can validate the relative alignment of the SLM and pupil plane. The SLM is well-aligned with respect to the pupil axially and laterally if a

---

[1] A typical programmable phase-only SLM only modulates one linear polarization of its incident illumination that is parallel to the extraordinary axis of the liquid crystals in the SLM.

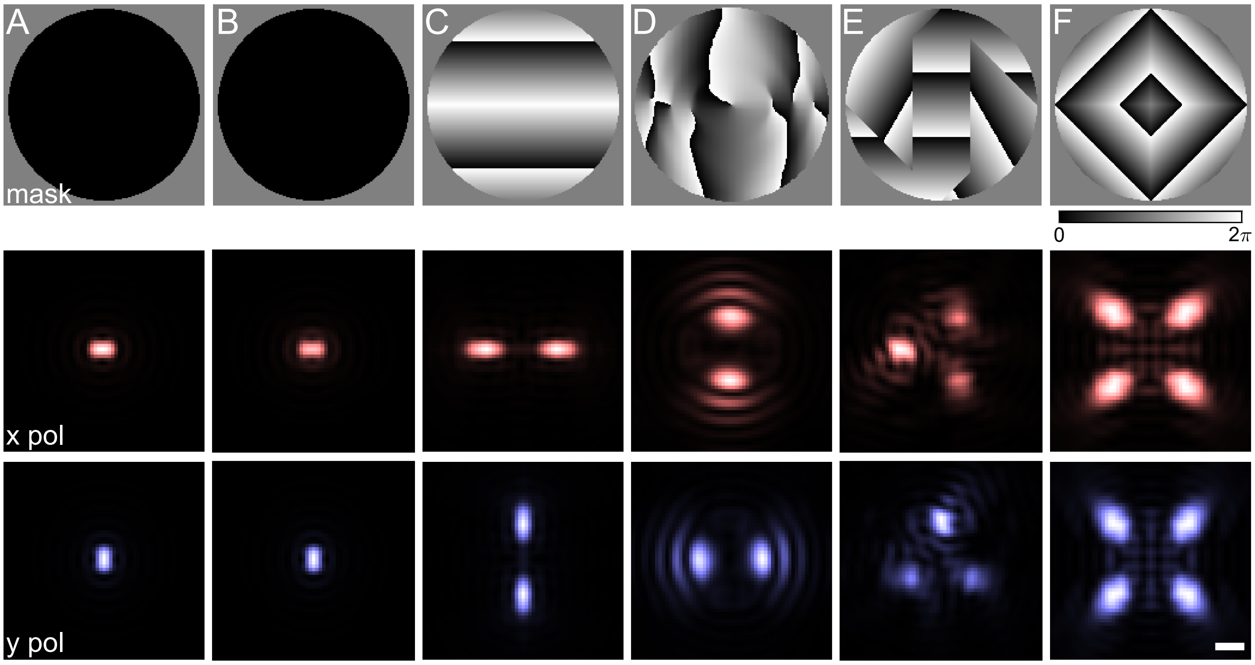

Figure 2.5: Representative phase masks (top) and corresponding engineered PSFs (middle: x-pol channel, bottom: y-pol channel) for SM orientation measurements, namely, (A) polarized standard, (B) bifocal microscope [142], (C) bisected [96], (D) double-helix [141], (E) Tri-spot [97] and (F) quadrated [98] PSF. The PSFs were simulated using vectorial diffraction theory (see Sections 1.5 and 2.1.1). An isotropic emitter at the glass-water interface was considered here. In the bifocal microscope, the two focal planes were offset by 0.2 μm by moving the focal plane of x-pol channel to the negative z direction in Figure 1.9A. Scale bar: 500 nm.

phase mask on the SLM and the pupil image are simultaneously in focus (i.e., having sharp features everywhere) and are concentric (Figure 2.6).

2.2.4 Calibration of Liquid Crystal Spatial Light Modulator

A liquid crystal SLM is fabricated with nematic liquid crystals sandwiched between a cover glass and reflective pixel electrodes. Orientations of the liquid crystals changes depending on the electric field induced by each electrode. The phase delay experienced by light traveling

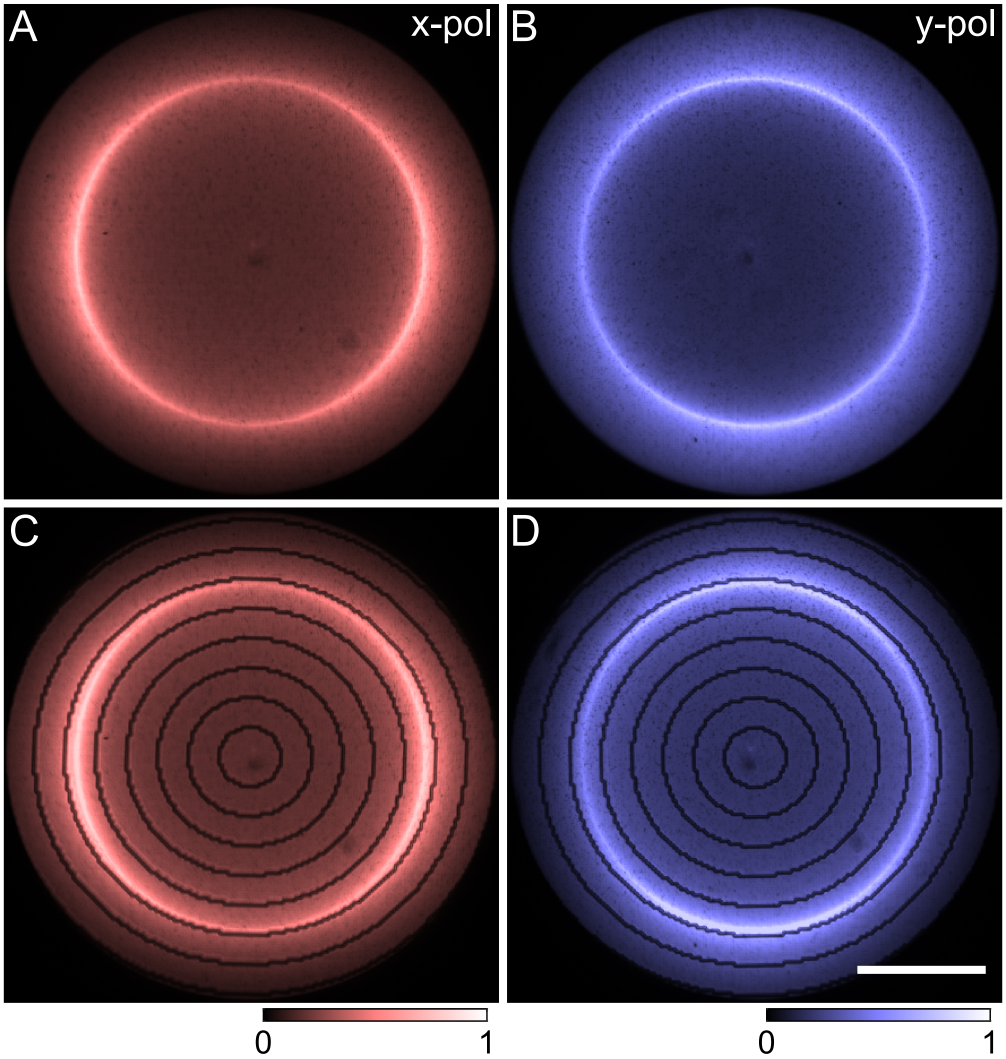

Figure 2.6: Images of the pupil plane and SLM for verification of 4f-system alignment. A well-aligned SLM with respect to the pupil (A,B) without and (C,D) with ring phase patterns on the SLM. Color scales: normalized intensities. Note that the characteristic high-intensity rings are super-critical fluorescence captured by the oil-immersion objective from fluorophores at the glass-air interface (also see Figure 1.9D) and are used to verify lateral alignment of the pupil and SLM. The ring patterns on the SLM with a known interval are also useful for measuring the size of the pupil on the SLM. Scale bar: 1 mm.

through each pixel is a function of the orientation of the liquid crystal. Therefore, nonlinear orientation response of the liquid crystals and the final phase delay with respect to applied voltage must be calibrated in advance. This subsection describes a diffraction method for calibrating the response of the SLM.

In this calibration, checkerboard patterns with a period of 32 pixels per check were used. In the test routine, the phase of one check was held constant, and the phase of the second check was varied. A collimated laser or fluorescence illuminates the surface of the SLM with a checkerboard pattern, and relative phase difference between the checks produces a diffraction pattern in the Fourier plane of the SLM imaged by a lens and camera. As checkerboard patterns with different phase shifts between the checks are loaded by the SLM, the liquid crystals in the varying SLM pixels change their orientations, resulting various diffraction patterns on the camera (Figures 2.7A-D). By monitoring the normalized intensity change of the 0th order diffraction (Figure 2.7E) and comparing that against an expected curve (Figure 2.7F), a mapping of input voltage (or gray levels of the checkerboards) to the output phase delay can be calculated. This is used to generate a look up table (LUT) that remaps input (phase values 0 - 2π converted into discretized gray scales $0 - 255$) to an output gray data set that results in a linear $0 - 2\pi$ phase shift (Figure 2.7G).

Since the phase delay is also a function of the wavelength of light illuminated on the SLM, it is important to calibrate the phase response of the SLM for actual fluorescence wavelengths. Unlike an interferometric method, this diffraction-based calibration method does not require the SLM to be removed from a 4f imaging system and set up an interferometer. Hence, it is convenient to perform the SLM calibration in a practical imaging system using wavelength-matched fluorescent beads. Note that the calibration method can take into account the extra voltage required to overcome inter-pixel cross talk by using a high frequency

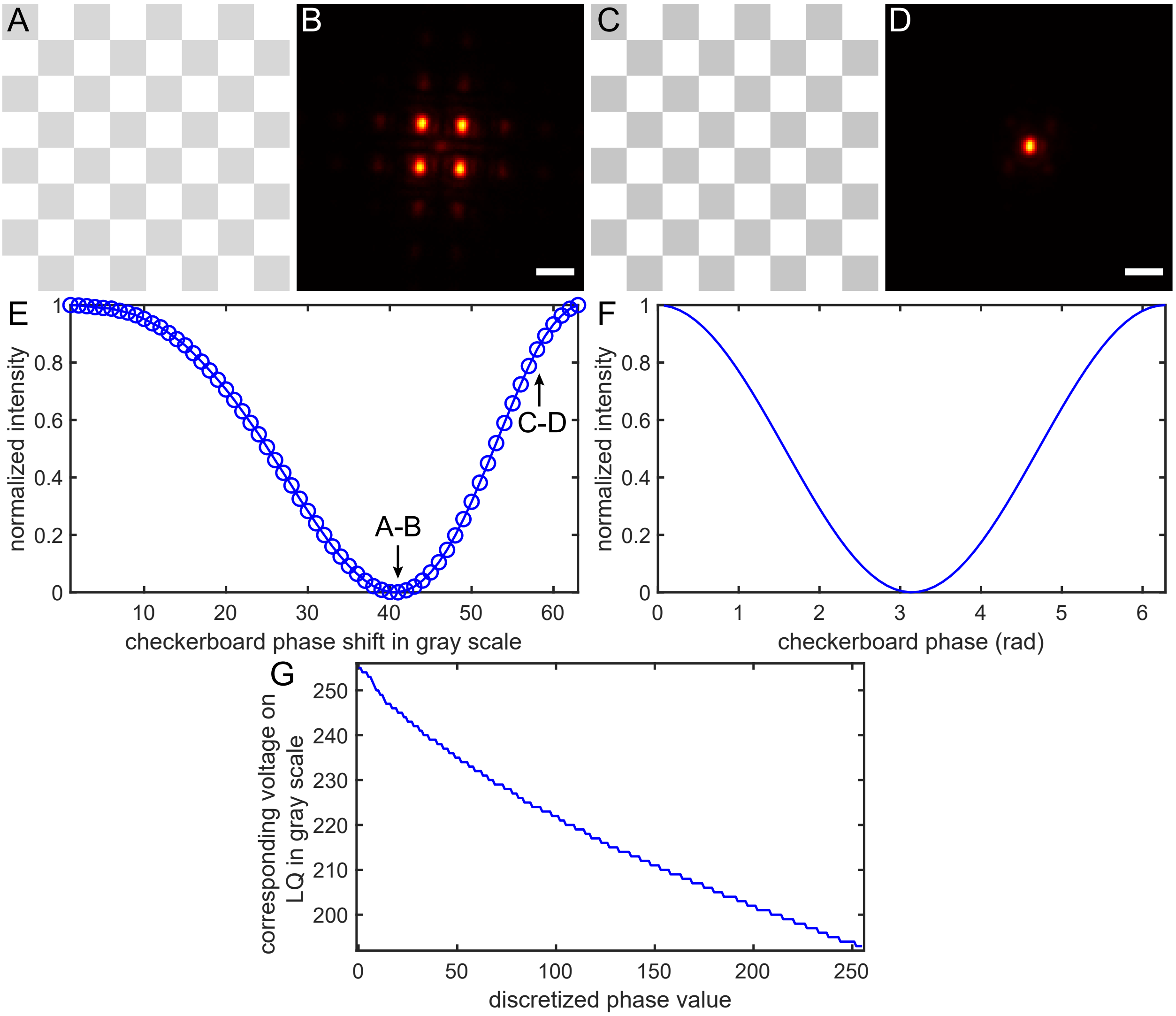

Figure 2.7: Example calibration data of an SLM. (A,C) Checkerboard patterns mounted on the SLM with different phase shifts between the two checks. (B,D) Diffraction patterns captured in the Fourier plane of the SLM with the checkerboard patterns A and C. Scale bar: 1 μm. (E) Experimentally observed and (F) simulated total intensities of the 0th order diffraction at different phase shifts of loaded checkerboards. (G) The calibrated phase response of the SLM for fluorescence wavelength $\lambda \approx 593$ nm.

checkerboard pattern, e.g., 4 pixels per check. However, the method neglects locally-varying wavefront distortion, which can be calibrated separately using an interferometric technique and corrected in software at each pixel [143].

2.3 Sample Preparation

Unless stated otherwise, all chemicals used in Capters 3-6 were purchased from Sigma-Aldrich and are ACS grade.

2.3.1 Photocatalyst Preparation

Tungsten oxide ($W_{18}O_{49}$) nanowires used in Chapter 3 were prepared using a hydrothermal method[2]. Tungsten chloride (0.040 g) and 1-butanol (40 mL) were mixed together, transferred to an acid digestion vessel, and heated at 453 K (180 °C) for 24 h. The product was washed repeatedly with ethanol and dried overnight in a vacuum oven. Oxidation of $W_{18}O_{49}$ nanowires was performed by mixing the $W_{18}O_{49}$ powder with hydrogen peroxide and 1 M sulfuric acid. The mixture was then washed repeatedly with ethanol and dried overnight. PVP functionalization of $W_{18}O_{49}$ nanowires was carried out by sonicating the $W_{18}O_{49}$ powder in an ethanolic solution of PVP. The mixture was then washed repeatedly with ethanol and dried overnight in a vacuum oven at 313 K (40 °C).

---

[2] This photocatalyst was prepared by my collaborator Meikun Shen from the lab of Prof. Bryce Sadtler.

2.3.2 Purification and Aggregation of Amyloid Peptides

Amyloid-β (1-42) and (1-40) preparation

The 42 and 40 amino-acid residue amyloid-β peptide (Aβ42 and Aβ40)[3] used for Thioflavin T (ThT) transient amyloid binding (TAB) microscopy in Chapter 5 were purified and aggregated as follows. Crude Aβ42 and Aβ40 peptide purchased from Watsonbio Sciences was purified via reverse-phase high-performance liquid chromatography (HPLC), lyophilized, then dissolved in hexafluoro-2-propanol (HFIP), and sonicated at room temperature for one hour in a water bath sonicator. After freezing in liquid nitrogen, HFIP was removed by lyophilization, and aliquots of the peptide were stored at -20 °C. To prepare unlabeled monomer, lyophilized Aβ42 and Aβ40 were dissolved in 10 mM NaOH, sonicated for 25 min in a cold water bath, and filtered first through a 0.22 μm and then through a 30 kD membrane filter (Millipore Sigma, UFC30GV and UFC5030). To prepare fibrils, we incubated 10 μM monomeric Aβ40 in PBS (150 mM NaCl, 50 mM Na_3PO_4, pH 7.4) at 37 °C with 5 seconds of shaking every 10 minutes in a non-binding 96-well black wall, clear bottom (Corning 3651) plate. 20 μM ThT was added for monitoring fibril aggregation kinetics using the ThT fluorescence in a microplate reader (Tecan, Infinite F200). Samples were removed and flash frozen in liquid nitrogen at various time points to obtain samples from different stages of Aβ40 aggregation (8 hours, 24 hours, 66 hours). Monomeric Aβ42 (60-110 μM) was aggregated at 37 °C in PBS with shaking for 24 hours under analogous conditions.

Aβ42 used for Nile red (NR) TAB imaging in Chapter 5 and Chapter 6 was synthesized and purified by Dr. James I. Elliott (ERI Amyloid Laboratory, Oxford, CT) and dissolved in hexafluoro-2-propanol (HFIP) and sonicated at room temperature for one hour. After flash freezing in liquid nitrogen, HFIP was removed by lyophilization and stored at -20 °C. To further purify the monomeric protein precursors, the same membrane filtering was applied as the purified crude peptide preparation. To prepare fibrils, we incubated 10 µM monomeric Aβ42 in phosphate-buffered saline (PBS, 150 mM NaCl, 50 mM Na_3PO_4, pH 7.4) at 37 °C with 200 rpm agitation for 42 - 50 hours.

---

[3] Aβ40 and Aβ42 amino acid sequences [144, 145]
Aβ40: DAEFRHDSGYEVHHQKLVFFAEDVGSNKGAIIGLMVGGVV
Aβ42: DAEFRHDSGYEVHHQKLVFFAEDVGSNKGAIIGLMVGGVVIA

Aβ42 monomer labeling procedure[4]

HPLC-purified synthetic Aβ42 that carried an N-terminal cysteine (Watson bio) was dissolved in 10 mM NH_4OH and sonicated on ice for 30 minutes. The dissolved Aβ42 was mixed in equal volume with a solution of 50 mM NH_4HCO_3 and 50 μM tris(2-carboxyethyl)phosphine (TCEP) with pH of 4. This final solution had pH between 7.0 and 7.5. The solution was transferred to a glass vial with stir bar. Alexa-647 C2 Maleimide (ThermoFisher Scientific, A20347) in DMSO solution (30 μL of 10 mg/mL) was added to the solution while stirring. The solution was stirred overnight at 5 °C in the dark. Afterwards, 2 µL of β-mercaptoethanol (BME) was added to the solution. The solution was then frozen in liquid nitrogen and lyophilized. The lyophilized peptide was dissolved in 1 mL formic acid, and the solution was diluted 1:1 with dH_2O before purified by high performance liquid chromatography (HPLC). The solution was then frozen in liquid nitrogen and lyophilized. Finally, the peptide was dissolved in hexafluoro-2-propanol (HFIP), and frozen in liquid nitrogen and lyophilized.

Intrinsically-labeled Aβ42 preparation[4]

Unlabeled monomeric Aβ42 (80 μg) in 100 μL of 10 mM NaOH and 0.8 nmol of monomeric Aβ42 covalently labeled with Alexa Fluor 647 C2 Maleimide in 20 μL of 10 mM

NaOH were mixed and sonicated on ice for 25 min. The mixture was filtered by centrifugation through a 0.2 μm and then through a 30 kD membrane filter. Peptide concentration and fraction of labeled monomer (4.2%) were calculated from UV-Vis absorption spectra (Implen, Nanophotometer, P330). Monomeric Aβ42 peptide (50 μM) was incubated at 37 °C for 40 hours without shaking. The fibrils were adsorbed to the coverslip as described in Section 2.4.2.

Antibody-labeled Aβ42 preparation

BSA (2%) in 200 μL of PBS with mouse anti-Aβ antibody 6E10 (Signet 9320) primary antibody (1:300 dilution) was incubated on the coverslip prepared in Section 2.4.2 for 1.5 hour. Afterwards, the coverslip was washed with 200 μL PBS for 5 times. Then 2% BSA in 200 μL of PBS with Alexa-647 labeled Goat Anti-Mouse IgG secondary antibody (1:200 dilution, Thermo Fisher Scientific, A-21236) was added to the coverslip and left for 1 hour. Afterwards, the coverslip was washed with 200 μL PBS 5 times. Note that a typical immunostaining preparation on amyloid aggregates takes more than 4 hours and includes multiple parameters need to be tuned for better SMLM performance.

α-synuclein, IAPP, tau, light chain protein preparation

Detailed purification and aggregation procedures for other amyloid samples used in Chapter 5 can be found in Supporting Information of Ref. [125][5]. Briefly, α-synuclein was expressed and purified from *Escherichia coli* as described in Ref. [146]. Lyophilized α-synuclein protein was dissolved in 10 mM NaOH and centrifuged at 50,000 RPM at 4 °C for 20 minutes. The supernatant was collected and aggregated in a phosphate buffer with a 2 mm

---

[4] Monomeric labeling and intrinsically-labeled Aβ42 used and demonstrated in Chapter 5 and Figure 5.5 were performed by my collaborator, Yuanzi Sun and Dr. Niraja Kedia, in Prof. Jan Bieschke's lab.

[5] These samples were prepared by my collaborators, Kevin Spehar, Yuanzi Sun, George R. Nahass and Dr. Niraja Kedia, in Prof. Jan Bieschke's lab.

glass bead and periodical agitation. HPLC purified 37 aa islet amyloid polypeptide (IAPP) was dissolved in hexafluoro-2-propanol (HFIP) and lyophilized afterward. The lyophilized IAPP was dissolved in 10 mM NaOH and further filtered with membrane filters before 24 h incubation in a phosphate buffer at 37 °. The wild type 2N4R tau protein (TauRD) was expressed and purified as previously described [147, 148]. Lyophilized Tau protein was dissolved into a solution consisting of dithoithreitol (DTT), NaCL and 4-(2-hydroxyethyl)-1-piperazineethanesulfonic acid (HEPES), and incubated at 20 °C for 1 hour. For fibril aggregation, the sample was further incubated at 20 ° for 17 hours after adding heparin. Immunoglobulin light chain (λ-AL-1) was purified from urine of patients suffering from light chain amyloidosis as described in Ref [124]. To form amyloid fibrils, AL protein was incubated in a glycine buffer for 7 days under permanent shaking at 37 °C.

2.4 Imaging Procedure

2.4.1 SMLM Procedure for Catalytic Reaction Site Imaging

The detailed microscope setup is shown in Section 2.2.

Glass microscope coverslips (Fisher Scientific, 12-546-2, No. 1.5) were cleaned by soaking in piranha solution (a 3:1 mixture (v/v) of concentrated H_2SO_4 and H_2O_2) for 30 minutes. The coverslips were then repeatedly rinsed with DI water and dried under N_2 flow. Next, 1 mg of the dried tungsten oxide ($W_{18}O_{49}$) nanowire powder was dispersed in 10 mL of ethanol using sonication to form a well-dispersed, colloidal suspension. 30 μL of this suspension was then spin-coated onto a cleaned coverslip. After coating with $W_{18}O_{49}$ nanowires, the coverslip was dried under N_2 flow and left in a vacuum oven at 10^{-2} atm at room temperature (21 °C) for 30 minutes to remove the residual solvent. Three laser lines were used in the study of tungsten oxide activity (Chapter 3): 405 nm (0.012 kW/cm^2), 488 nm (0.15 kW/cm^2), and 561 nm (0.34 kW/cm^2). Total 2,500 frames and 1,500 frames were captured with 50 ms exposure time for APF oxidation and condensation of furfuryl alcohol, respectively.

For imaging the oxidation of APF to produce fluorescein, a solution of 30 nM APF in PBS (pH 7.4) with 1 μM KIO_3 was dropped onto the coverslip. For this reaction, 405 and 488 nm lasers were used to photoexcite the $W_{18}O_{49}$ nanowires and fluorescein, respectively. For imaging the condensation of furfuryl alcohol, 100 μL of a solution of 10% furfuryl alcohol (v/v) in PBS was dropped onto the coverslip. A 561 nm laser was used to excite the fluorescent oligomers generated in this reaction. For both reactions, the solutions were purged with argon for 30 min before imaging. When imaging both reactions sequentially on the same set of $W_{18}O_{49}$ nanowires, the oxidation of APF was always performed prior to the condensation of furfuryl alcohol to avoid contamination from the deposition of the polymeric product. In between imaging using the two probe molecules, the coverslip was repeatedly washed with PBS.

2.4.2 SMLM and SMOLM Procedure for Amyloid Imaging

The detailed microscope setups are shown in Section 2.2.

ThT and NR TAB imaging

Eight-well cell culture chambers with optical glass coverslip bottom (Cellvis, C8-1.5H-N, No. 1.5H, 170±5 μm thickness) were cleaned using a UV Ozone Cleaner (Novascan

Technologies) for 15 minutes. Amyloid solutions were prepared as described in Section 2.3.2. The aggregated structures were adsorbed to the coverslip for 1 hour. The coverslip was rinsed with PBS (150 mM NaCl, 50 mM Na_3PO_4, pH 7.4) for maximizing adherence of the amyloid to the surfaces of glass-bottom chambers. For ThT TAB imaging, 2% (w/v) bovine serum albumin (BSA) (200 μL in distilled water) was incubated on the coverslip for 10 minutes and then rinsed off using distilled water in order to prevent unspecific binding of ThT to the glass surface. a PBS solution (200 μL) containing 1-2.5 μM ThT was pipetted into the chamber. For NR TAB imaging, A PBS solution (200 μL) containing 50 nM Nile red (Fisher Scientific, AC415711000) was placed in the amyloid-adsorbed chambers. Total 5,000-10,000 imaging frames were recorded with 20 ms camera exposure. A 488 nm or a 561 nm excitation laser was employed for excitation of ThT or NR. The peak intensities of the laser at the sample were 2.2 kW/cm^2 for the 488 nm and 0.88 kW/cm^2 for the 561 nm lasers.

Intrinsically/antibody-labeled amyloid imaging

An enzymatic oxygen-scavenging buffer containing glucose, glucose oxidase, catalase, and thiol (Table 5.1) was used to image the intrinsically-labeled and antibody-labeled Aβ42 samples (Section 2.3.2). Due to a non-uniform and sparse labeling density, only a standard diffraction-limited image could be produced from the Alexa-647 dye with 637 nm excitation (Figure 5.5A). Afterwards, the illumination was switched to the 488 nm laser, and TAB imaging was performed on the same fibril in the presence of 1 μM ThT (Figure 5.5BC). SMLM imaging was performed on the Alexa-647 labeled antibody using the 637 nm excitation laser (peak intensity: 10 kW/cm^2, Figure 5.5DE). A TAB image was taken of the Alexa-647 labeled fibril using 488 nm excitation in a similar manner as TAB imaging of intrinsically-labeled Aβ42 (Figure 5.5FG). Image stacks of 10,000 frames with 15 ms exposure were captured for Alexa-647 dSTORM (Figure 5.5H).

Time-lapse imaging of amyloid remodeling

Aβ42 fibrils were adsorbed to ozone-cleaned chambers as the standard TAB imaging, but this time without the BSA incubation for increasing reachability of epi-gallocatechin gallate (EGCG) to amyloid structures. EGCG (Taiyo International, Sunphenon EGCg) was added to an imaging buffer in the amyloid adsorbed chambers in order to remodel and dissolve structures of amyloid fibrils [123]. After variable-length incubations (as indicated in Figures 5.11 and 5.12) in the presence of 1 mM EGCG at room temperature (21 °C), the sample was rinsed and replaced with the ThT imaging buffer for TAB imaging. This procedure was repeated over 46 hours.

Time-lapse imaging of amyloid elongation

Aβ42 fibrils were needle sheared by pulling through a 25G needle ten times to form short seeds [136]. The seed sample was then adsorbed onto an ozone-cleaned coverslip (Azer Scientific, No. 1.5H, 170±5 μm thickness). A solution (10 μL) containing 20 μM monomeric Aβ42 and 500 nM NR in PBS was placed onto the coverslip. The solution was sandwiched by another coverslip from the top and sealed with wax to prevent evaporation. The sample was incubated on our microscope stage at room temperature (21 °C) without changing any buffers and meanwhile the standard NR TAB imaging was performed periodically over 21 hours (Figure 5.13).

2.4.3 Ensemble Measurements and Other Imaging Methods

While SMLM and its extension SMOLM provide SM sensitivity and relatively non-invasive imaging for resolving structural organization and chemical activity in nanoscale, classical ensemble measurements, e.g., absorption spectroscopy and fluorescence spectroscopy, and other higher resolution modalities, e.g., atomic force microscopy and electron microscopy, are still useful for characterizing and verifying general trends and morphologies of different sample groups. Further, correlation of such methods with SM approaches may leverage key properties of samples of interest that cannot be resolved by a single measurement method alone. Although details about other measurement schemes are beyond the scope of this dissertation, I briefly summarize ensemble measurement tools and other imaging methods used in Chapter 3 and Chapter 5 for quantifying and confirming tungsten oxide activity and amyloid aggregation.

Tungsten oxide and its oxygen vacancy quantification

Details about the ensemble measurements and the other imaging modalities for characterizing tungsten oxide and its oxygen vacancies in Chapter 3 can be found in Supporting Information of Ref. [140]. Briefly, x-ray diffraction (XRD) patterns were collected using a Bruker D8 Advance x-ray diffractometer. Transmission electron microscopy (TEM) and high-resolution TEM images were recorded with a FEI Tecnai Spirit transmission electron microscope operated at an acceleration voltage of 120 kV and a JEOL 2100FX transmission electron microscope operated at an acceleration voltage of 200 kV, respectively. UV-Vis absorption spectra of the $W_{18}O_{49}$ samples were recorded in transflectance mode using either a Perkin-Elmer Lambda 950 or an Agilent Cary 5000 spectrometer. Surface analysis by x-ray photoelectron spectroscopy (XPS) was performed using a Physical Electronics 5000 VersaProbe II Scanning ESCA Microprobe system. Fourier-transform infrared (FT-IR) spectra of different samples of $W_{18}O_{49}$ nanowires were obtained using a Perkin-Elmer Spectrum BX FT-IR system with a universal attenuated total reflection (UATR) accessory. Zeta potentials of different samples of $W_{18}O_{49}$ nanowires were measured using a Malvern Zetasizer Nano ZS.

Correlation of SMLM and scanning electron microscopy (SEM) images

The tungsten oxide nanowires spin-coated onto G490 round photoetched coverslips (ProSciTech, used for image correlation) were gently washed with DI water several times after the SMLM imaging using APF as a probe molecules. After water evaporation, 30 nm of gold was evaporated onto the coverslip surface using an Edwards Auto 306 thermal evaporator. Scanning electron microscope (SEM) images were recorded using a JEOL 7001LVF field-emission SEM operated at an accelerating voltage at 10 kV. In order to highlight the nanowires, the SEM image (Figure 3.7A) was denoised based on a non-local means filter (Figure 3.7B) [149] followed by Canny edge detection (Figure 3.7C) [150] using the *imnlmfilt* and *edge* functions in MATLAB (Mathworks, R2019a), respectively. The APF images were background corrected before single-molecule fluorescence bursts were localized (Figure 3.7D) as described in Section 2.5.1 and 2.5.3.

Atomic force microscopy (AFM) for amyloid morphology validation

Atomic force microscopy (AFM) used in Chapter 5 (Figure 5.8B) was performed as follows; Aliquots of Aβ aggregation time points (10 μl) were placed on a clean, freshly cleaved grade V-1 mica (Structure Probe, Inc., 01792-AB). After 10-minute adsorption, the solvent was wicked off by filter paper and the mica was washed 4 times with 20 μl of distilled water to remove salts and buffer from the sample. Samples were dried overnight, and AFM images were acquired in tapping mode on a Veeco Dimension 3100 machine (Bruker) with Bruker FESP tips.

Amyloid aggregation kinetics

Amyloid aggregation kinetics were monitored using thioflavin T (ThT) fluorescence in ensemble (Figure 5.8A). Purified 10 μM monomeric Aβ40 was incubated in PBS (150 mM NaCl, 50 mM Na_3PO_4, pH 7.4) at 37 °C with 5 seconds of shaking every 10 minites in a non-binding 96-well black wall, clear bottom plate (Corning 3651). ThT with 20 μM final concentration was added to wells for monitoring aggregation in a microplate reader (Tecan, Infinite F200). Note that, although the aggregation kinetics of different amyloids were verified in a similar manner, no fluorescent dye was added during amyloid aggregation of the samples imaged in SMLM and SMOLM in Chapter 5 and Chapter 6.

2.5 Single-Molecule Localization and Estimation

2.5.1 Background Estimation

Background correction is required for correcting weak, spatially non-uniform fluorescence arising from semiconductor nanoparticles or out-of-focus probe molecules, thereby reducing localization bias and false positive detections of single molecules. In this section, two different strategies are described.

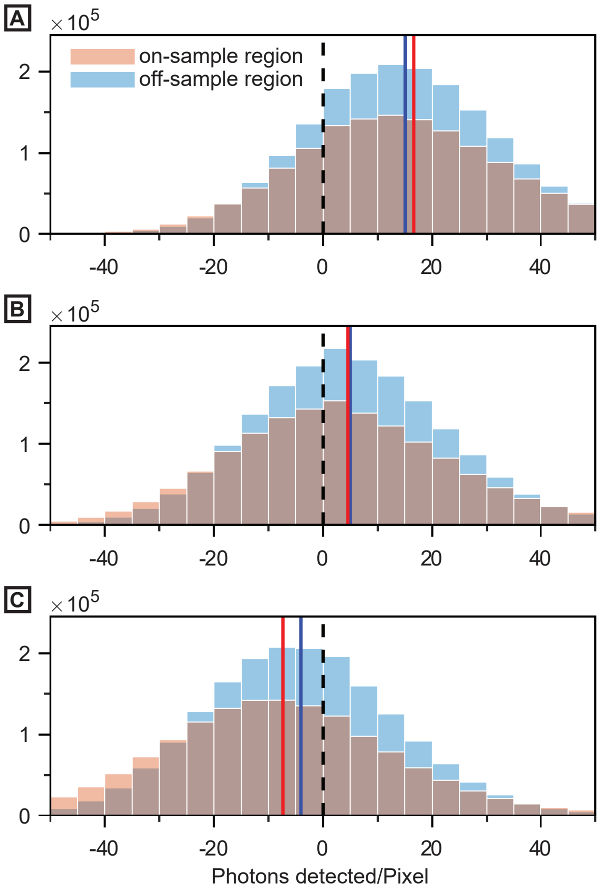

Figure 2.8: Residual background photons detected per pixel after temporal quantile filtering with (A) $q = 0.2$, (B) $q = 0.4$, and (C) $q = 0.6$ on-sample (red) and off-sample (blue) regions within an image stack shown in Figure 2.10C. Pixels corresponding to localized single molecules (5×5 pixels centered at each localization, pixel size: 160×160 nm^2) were excluded before accumulating all photons detected per pixel in each image stack. The on-sample region was extracted based on the procedure described in Section 2.6.2. The surrounding region with approximately the same area was considered as the off-sample region for the comparison. The mean residual backgrounds in each region are depicted as the vertical red (on-sample) and blue (off-sample) lines in the histograms. Adapted and reprinted with permission from Ref. [140].

Temporal quantile filter

A temporal quantile filter was introduced for estimating background photons emitted by photocatalyst nanoparticles (Chapter 3). The temporal quantile filter is an extension of conventional median filtering [151] devised to reduce systematic overestimation (or underestimation) of background by the classical median filter. First, an observed intensity $I_{u,v,t}$ at the pixel coordinate (u, v) of frame t was rescaled by the mean frame intensity over the entire frame $I_t = \left\langle I_{u,v,t} \right\rangle_{u,v}$ in order to remove spatially correlated intensity fluctuations. A temporal sliding quantile filter was then applied to the scaled intensity, $N_{u,v,t} = I_{u,v,t}/I_t$, for estimating the background intensity $\boldsymbol{b}_{u,v,t}$ as,

$$\boldsymbol{b}_{u,v,t} = I_t \times \text{quantile}\left(\left[N_{u,v,t-\frac{w}{2}}, \ldots, N_{u,v,t}, \ldots, N_{u,v,t+\frac{w}{2}} \right], q \right), \tag{2.11}$$

where w is the window size for temporal filtering, and q is the cumulative probability in the interval $[0, 1]$ denoting the quantile of the intensity data. Note that the quantile filter with $q = 0.5$ corresponds to the conventional median filtering method. The two parameters of the filtering, i.e., w and q, were optimized to minimize the mean intensity difference between sample and surrounding off-sample regions in images. The window size w has less effect on the properties of the background correction if it is significantly longer than switching events of probe molecules on an imaging target. For example, in the work described in Chapter 3, we used a window size of 200 frames on all of analysis datasets. On the other hand, the quantile q affects the localization number and the mean intensity difference significantly. A small q causes underestimation of the background, and the residual background remaining after correction increases false localizations on the regions with samples and results in a large mean intensity difference between on-sample vs off-sample regions. Conversely, a large q causes overestimation of the background, thus reducing localization number and causing

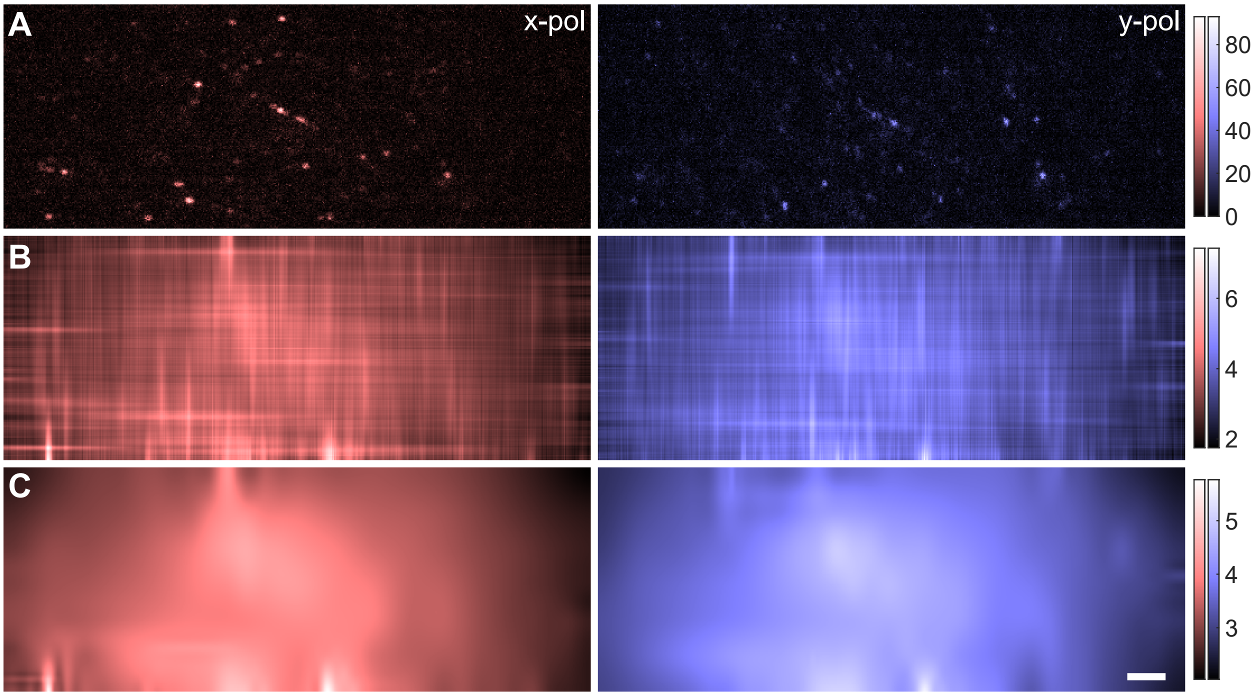

Figure 2.9: Spatial Gaussian and wavelet filter for smooth background estimation. (A) A representative raw frame captured in the polarization-sensitive fluorescence microscope shown in Figure 2.4. Nile red flashes on amyloid aggregates using the transient amyloid binding (TAB) concept were captured with a 20 ms camera exposure time. The data corresponds to the field-of-view shown in Figure 6.13A. See Section 2.4.2 and Chapters 5 and 6 for more details about the experimental setup. (B) Signal-filtered images after the temporal averaging in the sub-stack and fitting to the sum of two 1D Gaussian functions. The row-wise and column-wise fitting results were averaged and displayed for x-pol and y-pol channels, respectively. (C) The estimated background fluorescence after the wavelet filtering. Scale bar: 2 μm.

the imaging target to appear dimmer than their surroundings. Therefore, one needs to select a quantile q such that the mean intensities of the regions with and without the samples are roughly the same (Figure 2.8). In the work described in Chapter 3, $q = 0.4$ was applied on all datasets. It should be noted that a dataset with different background characteristics and SM blinking rates requires a different quantile for accurate background estimation.

Spatial Gaussian and wavelet filter

Although the temporal quantile filter provides accurate background estimation, applying the quantile filter on individual pixels with temporal sliding windows is computationally expensive for some SM analysis, especially for analyzing datasets with tens of thousands frames. In the SMOLM analysis shown in Chapters 4 and 6, we estimated background photons per pixel by combining two spatial filters. First, each raw image stack (typically several thousands in total) was split into sub-stacks, e.g., 200 frames, and a temporal average was computed for each sub-stack. The averaged images were then separated into two images for considering two polarized channels separately in the following background estimation. We fit each row and column of the images to the sum of two 1D Gaussian functions, with 6 total parameters: 2 sets of amplitudes, centroid positions and standard deviations (widths). We took the average of the two images, i.e., the row-wise and column-wise Gaussian fits, for the next spatial filtering (Figure 2.9B). Broad background fluorescence profiles in each sub-stack and channel were estimated by applying a biorthogonal wavelet filter (level 6 of 'bior6.8' as input parameters to the *wavedec2* and *wdencmp* functions in MATLAB) to the averaged results (Figure 2.9C). The estimated smooth intensity distribution was then designated as background photons in all corresponding frames within each sub-stack.

2.5.2 Imaging Channel Calibration and Registration

Registration of two probe images

In the photocatalyst activity study (Chapter 3), two probe molecules are employed for correlating and mapping catalytic activities and structural defects. An image registration is needed for resolving system drift introduced by sample washing and switching between the two probe molecules. Two-dimensional cross-correlation between the diffraction-limited images (averaged over the entire single-molecule imaging stack) of two molecules was calculated after background correction and noise reduction using rolling-ball background subtraction [152] and a 2nd order wavelet filtering [153]. The maximum position of the cross-correlation was obtained by fitting a 2D Gaussian peak function to the cross-correlation image. Similarly, the auto-correlation peak of the diffraction limited image using the first probe molecule was calculated as a reference. The lateral drift between the two probe images was extracted from the direction and the distance between the peaks in the corresponding cross-correlation and auto-correlation images. Note that, in addition to the linear translation, one may also want to consider rotation, scaling, skewing and shift-variant high order image distortion possibly introduced by the multicolor imaging and imperfection of imaging system (i.e., aberration). A finer registration based on affine or higher order transformation may provide more accurate two probe correlation.

Registration of two detection channels

A registration process is required for analyzing dual-channel images captured, for example, in the polarization-sensitive imaging system shown in Figure 2.4. In the amyloid study (Chapter 5 and 6), the geometric transformation between the two channels on a camera was first calibrated using fluorescent beads (Thermo Fisher Scientific, FluoSpheres, 0.1 μm, 505/515, F8803 for ThT TAB, and 580/605, F8801 for NR TAB) adsorbed onto an ozone-cleaned 8-well cell culture chamber. Approximately, 4,000-180,000 photons or 82,000-866,000 photons per bead were detected from the yellow-green or red fluorescent beads with 20 ms exposure time. We imaged each bead over 8-10 frames, and localized all bead positions using the ThunderSTORM plugin [154] within ImageJ [155] after subtracting dark images (see Section 2.5.3 for more details about localization). Calculated bead positions were then averaged across multiple frames for improving localization precision.

Next, all possible lines joining pairs of bead positions across the two channels were drawn. Control points for two-channel registration were selected by comparing the obtained lines, and keeping the largest ensemble of them with similar lengths and slopes. To create the two-channel registration map, coefficients of a global 2D polynomial transformation function were calculated using the control points as input to the *fitgeotrans* function included with MATLAB (Mathworks, R2019a). Although the performance of the dual-channel registration map was improved by immediate calibration after single-molecule imaging, there was still a small amount of registration error when the calibrated transformation function was applied on localized SM positions. This small and spatially-varying bias was most likely due to system drift between measurements and slightly different imaging configuration between the bead and SM imaging. We refined the registration map by re-calculating the global 2D polynomial transformation using the scheme described above, but this time using the SM localizations with high localization precision ($<$ 20 nm) as control points.

2.5.3 SM Localization Based on Least-Squares Fitting

For localization of sparse SM blinking with the standard PSF (diffraction-limited PSF), one can use a least square (LS) fit of the Gaussian model function in Eq. 1.12. ThunderSTORM [154] is an ImageJ [155] plugin and offers fast LS-based SM localization with high localization precision for low density SM image datasets [68]. The software consists of three main analysis blocks, i.e., image filtering for denoising, approximate localization for cropping pixels associated with SM bursts, and sub-pixel localization on the isolated pixel regions. For localization of fluorescent probes discussed in Chapters 3 and 5, this software plugin was employed with B-spline wavelet filter [153] for denoising and local maximum detection for approximate localization. An integrated Gaussian function instead of a standard Gaussian was fit onto SM intensity distributions to account for the effect of camera pixelation. Captured raw image stacks were offset corrected by subtracting dark images before the ThunderSTORM analysis in ImageJ. A list of estimated single-molecule positions (x, y) and point spread function (PSF) widths (σ) was produced by ThunderSTORM and loaded into MATLAB (Mathworks, R2019a) for further post-processing. Detected photons per localization were obtained by summing all photons within a region of interest (e.g., 7×7 pixels with 58.5×58.5 nm^2 pixel area) centered at the location (x, y) of each molecule. This integrated photon count was further background corrected and assigned as the detected photons for corresponding SM localizations. Additional photon and PSF width thresholding was performed to reject false localizations due to background fluorescence and low signal-to-noise ratio. For example, localizations of single molecules were only retained if: 1) the number of photons detected was larger than 100, and 2) the measured PSF widths were reasonable (50 nm $< \sigma <$ 150 nm). The estimated localization precision, or the best possible localization uncertainty for the least-squares fitting algorithm, was calculated based on the photons detected and the background as Eq. 1.13 [156].

2.5.4 Sparsity-Promoting Maximum-Likelihood Estimator and Orientation Projection

The locations and orientations of SM molecules discussed in Chapters 4 and 6 were estimated simultaneously using a sparsity-promoting maximum likelihood estimator [157]. First we define an image-formation model for this multi-parameter estimation. Based on the vectorial diffraction theory and basis function decomposition discussed in Sections 1.5 and 2.1.1, a noiseless image containing multiple SM PSFs on the image plane can be given by

$$\boldsymbol{I}(\boldsymbol{w}) = \sum_{p=1}^{P} s^p \left(\sum_{j=1}^{6} m_j^p \boldsymbol{B}_j(\boldsymbol{w} - \boldsymbol{r}^p) \right), \tag{2.12}$$

where $\boldsymbol{w} = (u, v)$ are the image plane coordinates, P is the total molecule number, $\boldsymbol{r}^p$ represents the position of pth molecule and $\boldsymbol{B}_j$ is the jth basis function after concatenating x- and y-polarized channels. We represent the object space by a rectangular lattice of N grid points with spacing equal to the camera pixel size (58.5 nm). If each grid point contains at most a single molecule parameterized by brightness, position offsets, and six orientational second moments, then Eq. 2.12 can be rewritten as

$$\boldsymbol{I}(\boldsymbol{w}) = \sum_{i=1}^{N} s^i \left(\sum_{j=1}^{6} m_j^i \boldsymbol{B}_j(\boldsymbol{w} - \boldsymbol{d}^i - \boldsymbol{\delta}^i) \right), \tag{2.13}$$

where s^i and $\boldsymbol{m}^i$ are brightness and orientational second moments associated with the ith grid, $\boldsymbol{d}^i$ denotes the position of ith grid in the coordinates and $\boldsymbol{\delta}^i$ represents a position shift of a molecule from its associated grid. Note that $s^i = 0$ if no molecule can be mapped to a point in the neighborhood of $\boldsymbol{d}^i$. By only taking the first-order Taylor approximation of Eq. 2.13, we have

$$\boldsymbol{I}(\boldsymbol{w}) \approx \sum_{i=1}^{N} \sum_{j=1}^{6} \Big(\boldsymbol{B}_j(\boldsymbol{w} - \boldsymbol{d}^i) l_j^i - \frac{\partial \boldsymbol{B}_j}{\partial x}(\boldsymbol{w} - \boldsymbol{d}^i) l_j^i \delta_x^i - \frac{\partial \boldsymbol{B}_j}{\partial y}(\boldsymbol{w} - \boldsymbol{d}^i) l_j^i \delta_y^i) \Big), \tag{2.14}$$

where $\boldsymbol{l}^i = s^i \boldsymbol{m}^i$. This image model can be interpreted as the sum of a few PSFs weighted by $\boldsymbol{f}_j = \left[\boldsymbol{l}_j, \;\; \boldsymbol{l}_j \odot \boldsymbol{\delta}_x, \;\; \boldsymbol{l}_j \odot \boldsymbol{\delta}_y \right]$ where $\odot$ represents the element-wise product. Therefore, the final imaging model can be compactly rewritten as

$$\boldsymbol{I}(\boldsymbol{w}) = \boldsymbol{\mathcal{B}}\boldsymbol{F} = \sum_{j=1}^{6} \boldsymbol{\mathcal{B}}_j \boldsymbol{f}_j, \tag{2.15}$$

where $\boldsymbol{\mathcal{B}}$ represents a linear operator corresponding to integration of $\boldsymbol{B}_j(\boldsymbol{w}-\boldsymbol{d}^i)$, $\partial \boldsymbol{B}_j/\partial x(\boldsymbol{w}-\boldsymbol{d}^i)$ and $\partial \boldsymbol{B}_j/\partial y(\boldsymbol{w}-\boldsymbol{d}^i)$ over the camera pixels. We can further model the photon count in each pixel g^i as an independent Poisson distribution [76] given by

$$g^i = \text{Poiss}\big((\boldsymbol{\mathcal{B}}\boldsymbol{F} + \boldsymbol{b})^i\big), \tag{2.16}$$

where $\boldsymbol{b}$ is the background photons in each pixel.

To robustly estimate the number of underlying molecules and their parameters in the presence of image overlap, we use a regularized maximum likelihood exploiting a group-sparsity norm to estimate the parameters of each grid point. The algorithm begins by estimating the strength (i.e., brightness) of each of the second moments $\tilde{m}_j$ independently at all object grid points. The recovery problem can be formulate as a minimization expressed as

$$\tilde{\boldsymbol{F}} = \arg\min_{\boldsymbol{F}} \big\{\mathcal{L}(\boldsymbol{F}) + \gamma \|\boldsymbol{F}\|_{2,1}\big\}, \tag{2.17}$$

where $\mathcal{L}$ is the negative Poisson log-likelihood [75] given by

$$\mathcal{L}(\boldsymbol{F}) = \sum_{i=1}^{N} \big\{(\boldsymbol{\mathcal{B}}\boldsymbol{F} + \boldsymbol{b})^i - g^i \ln{(\boldsymbol{\mathcal{B}}\boldsymbol{F} + \boldsymbol{b})^i}\big\}, \tag{2.18}$$

and the group-sparsity norm is defined by

$$\|\boldsymbol{F}\|_{2,1} = \sum_{i=1}^{N} \sqrt{\sum_{j=1}^{6} \left\{ \left(l_j^i\right)^2 + \left(l_j^i \delta_x^i\right)^2 + \left(l_j^i \delta_y^i\right)^2 \right\}}. \tag{2.19}$$

A penalty parameter γ needs to be carefully defined in order to balancing the likelihood and the group sparsity in the minimization problem.

We next pool together localizations (i.e., their brightnesses and position offsets) across the six second moments to identify the most likely molecules in the object space. Once we identify these molecules, we solve a constrained maximum likelihood to minimize systematic biases induced by the sparsity norm, yielding estimates of the brightnesses, locations, and orientations (second moments $\tilde{\boldsymbol{m}}$ of all molecules in the image). For Nile red molecule orientation estimation, we removed localizations with signal estimates less than 200 photons detected to eliminate unreliable localizations.

The estimated second-moment vectors $\tilde{\boldsymbol{m}}$ were next projected to the first-moment orientation space (azimuthal angle $\phi \in [-\pi, \pi)$, polar angle $\theta \in [0, \pi/2]$, and wobbling area $\Omega \in [0, 2\pi]$ of a transition dipole moment $\boldsymbol{\mu}$, Section 1.5) by a weighted least-square estimator:

$$(\phi, \theta, \Omega) = \underset{\phi', \theta', \Omega'}{\arg\min} \left(\tilde{\boldsymbol{m}} - \boldsymbol{m}(\phi', \theta', \Omega')\right)^{\mathrm{T}} \mathbf{FIM} \left(\tilde{\boldsymbol{m}} - \boldsymbol{m}(\phi', \theta', \Omega')\right) \tag{2.20}$$

such that satisfying Eq. 2.8-2.10. **FIM** is the Fisher information (FI) matrix [76] calculated from the basis images $\boldsymbol{B}$. Here, $\tilde{\boldsymbol{m}}$ and $\boldsymbol{m}$ denote second moment outputs of the maximum likelihood estimator and the weighted least-square estimator respectively. Here, we define the FI matrix associated with estimating the six orientational second moments $\boldsymbol{m}$ as

$$\mathbf{FIM} = \sum_{i=1}^{n} \frac{1}{I_i} \nabla I_i^{\mathrm{T}} \nabla I_i, \tag{2.21}$$

where i denotes the ith pixel of an image $I \in \mathbb{R}^n$ captured by a camera and

$$\nabla \boldsymbol{I}_i = \begin{bmatrix} \frac{\partial I_i}{\partial m_{xx}} & \frac{\partial I_i}{\partial m_{yy}} & \frac{\partial I_i}{\partial m_{zz}} & \frac{\partial I_i}{\partial m_{xy}} & \frac{\partial I_i}{\partial m_{xz}} & \frac{\partial I_i}{\partial m_{yz}} \end{bmatrix}. \tag{2.22}$$

Due to the linearity of the forward imaging model (Section 2.1.1) in terms of the second moments, the FI matrix can be further simplified as

$$\mathbf{FIM} = \sum_{i=1}^{n} \frac{s^2}{I_i} \boldsymbol{B}_i^{\mathrm{T}} \boldsymbol{B}_i, \tag{2.23}$$

where $\boldsymbol{B}_i$ represents the ith row of $\boldsymbol{B} \in \mathbb{R}^{n \times 6}$. The weighted least square estimation can be efficiently performed by pre-calculating Hadamard products of each pair of the basis images. The FI matrix assigns weights to each orientational component m_j inversely proportional to the expected measurement variance of the PSFs used in SMOLM. We performed the optimization in Eq. (2.20) using the *fmincon* function in MATLAB. If the localization was within a fibril region of interest (Section 2.6.2), in Chapter 6, then the backbone orientation of the nearest fibril section was used as the initial point of the minimization of Eq. (2.20); otherwise the eigenvector corresponding to the largest eigenvalue of the second moment matrix [137] was assigned as the initial orientation. The performance of this estimator was validated and characterized by using synthetic data (Figures 4.8, 4.9 and 6.5 - 6.9).

2.6 Quantitative Analysis of SMLM Data

2.6.1 Localization Grouping across Consecutive Frames and Measuring the Length of Fluorescence Bursts

In order to quantify the kinetics of SM fluorescence measured across multiple camera frames, we grouped localizations of SM blinking together into “bursts”. Localized single molecules in a frame were grouped with localizations in the consecutive frames by selecting the nearest neighbors within a spatial circle corresponding to 3 times the localization precision (std. dev.). Photons detected from the grouped localizations were summed and designated as total photons detected per burst. The length (or on-time) of each burst was reported as the number of frames within which localizations were successfully grouped, in units of exposure time. The time constant of a fit to an exponential decay was obtained to measure the mean of on-time of all SM bursts.

2.6.2 Isolation and Characterization of Regions of Interest

ROI selection for non-uniform SMLM reconstructions

A sample structures or chemical activities were visualized by assembling and binning all SM bursts within bins defined during post-processing. An additional region of interest (ROI) selection was needed for extracting SM activities only on targets of study. For a SMLM reconstruction with non-uniform SM burst distribution, one can select and isolate SM bursts on an imaging target based on a manually drawn structure backbone or boundary. In the photocatalyst activity study (Chapter 3), segmented lines were hand-drawn on

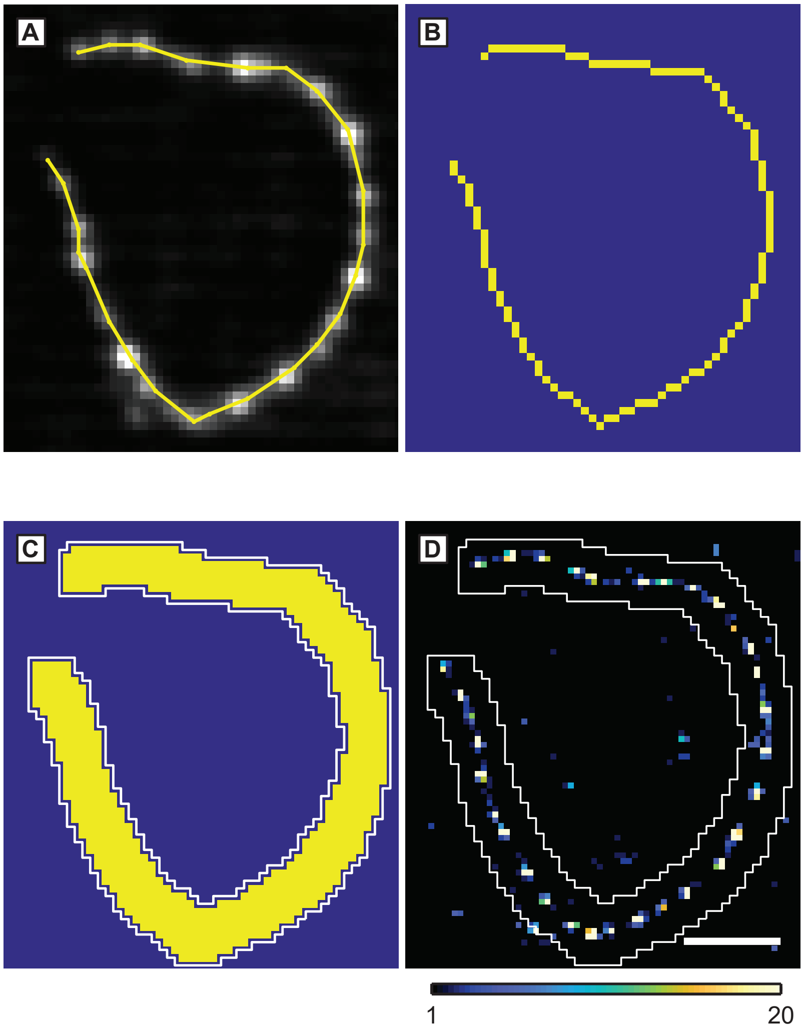

Figure 2.10: Region of interest selection for extracting SM bursts on an imaging target (tungsten oxide nanowire, see Chapter 3 for sample details). (A) A segmented line was hand-drawn on the diffraction-limited image of a nanowire for tracing the length axis of the sample. The line was then converted into (B) a binary mask image, and (C) dilated for obtaining the boundary of the sample region. (D) Localized bursts within the boundary (white line) were considered as fluorescent single molecules on the sample and used for characterization of the sample. Color scale: number of fluorescence bursts per bin (120×120 nm^2). Scale bar: 2 μm. Reprinted with permission from Ref. [140].

diffraction-limited images of imaging targets (average of an entire raw data stack without any background correction) along the length of the samples. Afterward, the lines were converted into a binary image mask using the *createMask* function in MATLAB (MathWorks, 2019a) followed by dilation of the mask to cover the entire sample. The boundaries of the sample regions were detected by *bwtraceboundary* in MATLAB, and the photon statistics of the localizations within the boundary were analyzed and reported for characterizing the SMLM images (Figure 2.10).

ROI selection for densely samples SMLM reconstructions

On the other hand, a simple ROI selection algorithm can be applied to a reconstructed image with dense SM sampling across targets of study. In the amyloid strudy (Chapter 5 and 6), the following ROI selection scheme was applied on reconstructed images of amyloid aggregates in order to extract ThT and NR blinking characteristics on the structures of interest. The SMLM image was converted into a binary image using a localization threshold of 2 localizations/bin and the largest connected structure within a field of view was identified using the *bwconncomp* function in MATLAB (Mathworks, R2019a). The boundary of the ROI was detected by *bwtraceboundary*, and on-structure localizations within the boundary were isolated by *inpolygon* in MATLAB.

Structural reference for orientation analysis

Instead of quantifying SM orientations relative to the laboratory reference frame, we select reference structures, e.g., amyloid fibril backbones, from SMLM images and evaluate the deviation of SM orientations with respect to these references in SMOLM analysis. In order to detect fibril backbones, the SMLM images of isolated amyloid aggregates were smoothed by a Gaussian filter and saved as a single tif image. The morphology of each

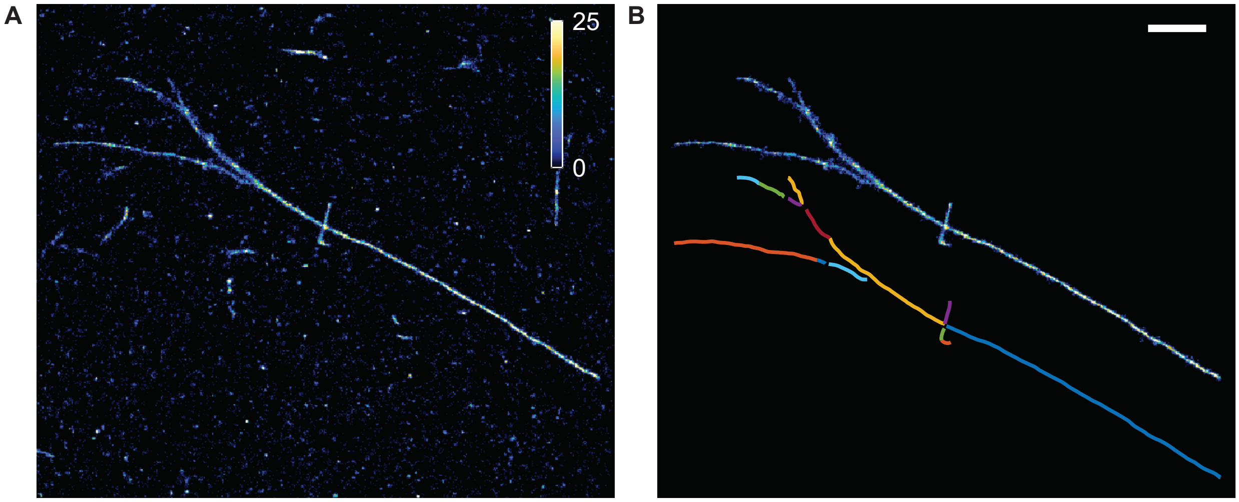

Figure 2.11: Amyloid region of interest (ROI) and backbone ridge detection. (A) SMLM image of an amyloid aggregates (Figures 6.13A-D. (B) Isolated amyloid ROI and the corresponding detected ridges (i.e., structure backbones). The ridges are individually indexed by color, but this indexing (classification) was ignored in SMLM analyses. Scale bar: 1 µm. Reconstruction bin size: 20×20 nm^2. Color bar: localizations/bin. Reprinted with permission from Ref. [138].

fibril backbone (i.e., a set of points that form a 1D curve in the xy plane) was measured using a ridge detection plugin [158] within ImageJ (Figure 2.11B). Next, the nearest section of backbone was assigned to each SM localization, which was used for both converting second-moment estimates to first-moment orientations (Section 2.5.4) and comparing SM orientations within the ROI to the fibril superstructure (see SMOLM discussion in Chapter 6 and Figures 6.13, 6.15 - 6.17).

Apparent widths of SMLM reconstructions

The full-width at half-maximum (FWHM) of each reconstructed structure was measured to characterize apparent widths of various amyloid aggregates (Chapters 5 and 6). To measure FWHM, we fit amyloid fibril cross-sections, aligned perpendicular locally to each fibril backbone, to 1D Gaussian distributions. Width measurements were performed in intervals of ∼17 nm over the entire length of each fibril, thereby building robust statistics for the morphology of the reconstructed fibrils and bundles thereof. Note that the measured apparent widths are wider than the actual widths of the fibrils due to the localization precision of the estimator used in the work.

2.6.3 Coordinate-Based Colocalization (CBC) analysis

SMLM colocalization of two probe molecules, such as Oxidation of 3'-(*p*-aminophenyl) fluorescein (APF) and furfuryl alcohol (FA) used in Chapter 3, can be performed using coordinate-based colocalization (CBC) analysis [159]. After correction of the localization positions in furfuryl alcohol data by the estimated system drift (see Section 2.5.2), the CBC analysis was performed. Briefly, this method calculates colocalization between two super-resolution datasets directly using the localized coordinates of each molecule instead of the pixelized super-resolution reconstructions. Moreover, this method is tolerant to random false positive localizations because it considers the spatial density distribution of each dataset. Specifically, the spatial density distributions, $D_{APF_i,\mathrm{APF}}(r)$ and $D_{APF_i,\mathrm{FA}}(r)$, around a localization in the APF dateset APF_i were calculated based on the neighboring localizations in both the APF and furfuryl alcohol (FA) datasets as follows,

$$D_{APF_i,\mathrm{APF}} = \frac{N_{APF_i,\mathrm{APF}}(r)}{\pi r^2} \cdot \frac{\pi R_{\max}^2}{N_{APF_i,\mathrm{APF}}(R_{\max})} \tag{2.24}$$

$$D_{APF_i,\mathrm{FA}} = \frac{N_{APF_i,\mathrm{FA}}(r)}{\pi r^2} \cdot \frac{\pi R_{\max}^2}{N_{APF_i,\mathrm{FA}}(R_{\max})} \tag{2.25}$$

where $N_{APF_i,\mathrm{APF}}(r)$ and $N_{APF_i,\mathrm{FA}}(r)$ are the numbers of APF and furfuryl alcohol localizations within the distance r around the ith APF localization APF_i. The radius r was expanded from 50 nm to 500 nm (R_{max}) with 50 nm steps in this work. Then the Spearman rank correlation coefficient of the two distributions is calculated from the covariance of rank-ordered distributions as

$$S_{APF_i} = \frac{\text{cov}\big(R_{APF_i,\text{APF}}(r), R_{APF_i,\text{FA}}(r)\big)}{\sigma_{R_{APF_i,\text{APF}}}(r), \sigma_{R_{APF_i,\text{FA}}}(r)} \tag{2.26}$$

where $R_{APF_i,\text{APF}}(r)$ and $R_{APF_i,\text{FA}}(r)$ are the ordered ranking of $D_{APF_i,\text{APF}}(r)$ and $D_{APF_i,\text{FA}}(r)$, and $\sigma_{R_{APF_i,\text{APF}}}(r)$ and $\sigma_{R_{APF_i,\text{FA}}}(r)$ represent standard deviations of these distributions. The final colocalization scoe, C_{APF_i}, assigned to the localization APF_i is calculated as

$$C_{APF_i} = S_{APF_i} \cdot \exp\left(- \frac{L_{APF_i,\text{FA}}}{R_{\text{max}}} \right). \tag{2.27}$$

Here $L_{APF_i,\text{FA}}$ is the distance from APF_i to the nearest neighbor in the furfuryl alcohol localizations. We calculated C_{APF_i} for all valid localizations in the APF data and similarly C_{FA_i} for localizations in the furfuryl alcohol dataset, with values varying from -1 for representing perfectly excluded (anti-correlated) localizations to +1 for perfectly colocalized localizations. CBC maps of APF and furfuryl alcohol data were calculated by taking median colocalization score in each reconstruction bin (120×120 nm^2, Section 3.3).

Chapter 3

Mapping Photocatalytic Activity of Semiconductor Nanoparticles at the Nanoscale

Metal oxide semiconductors are promising photocatalysts for a number of important chemical transformations including solar water splitting [160–165], CO_2 reduction [165–168], coupling of amines [169, 170], and partial methane oxidation to produce methanol [171, 172]. They can be fabricated using inexpensive, solution-phase synthesis, and they are more resistant to corrosion compared to elemental, chalcogenide, and III-V semiconductors (e.g., GaAs and InP). However, as most metal oxides possess electronic band gap energies greater than 2.5 eV (corresponding to absorption of ∼500 nm visible photons), their efficiency is limited by low absorption coefficients where incoming solar radiation is the most intense. Furthermore, due to low electron and hole mobilities, photoexcited charge carriers have a high probability of recombining before they reach the surface to oxidize or reduce adsorbed substrate molecules [165,173,174]. These limitations can be mitigated if the surface of the photocatalyst possesses sites that are highly active for the chemical transformation of interest.

The presence of structural defects, including vacancies, substitutional impurities, and unpassivated atoms, at the surface of a semiconductor can introduce surface states within the band gap that act as recombination centers and deactivate photoexcited charges. However, rather than act as recombination centers, oxygen vacancies appear to enhance catalytic activity in many metal oxide photocatalysts, including tungsten, indium, titanium, molybdenum, and zinc oxide [162–170, 175–179]. Several studies have reported higher catalytic activity in these materials as the oxygen vacancy concentration is increased through thermal or chemical treatments, although various mechanisms have been proposed to explain this observation [162–167, 169, 170, 175]. Density functional theory (DFT, a computational modeling method for predicting molecular structures within materials) calculations suggest that oxygen vacancies act as preferential adsorption sites for reactant molecules and create new states within the electronic band gap of the semiconductor [163, 169]. It is currently debated whether or not charge carriers in these localized defect states can participate in photochemical reactions [163–167, 169]. Furthermore, the plasmon resonance induced by increased free electron density increases absorption at longer wavelengths [164, 165, 180]. Currently, there is not a clear consensus as to which of these mechanisms is dominant. A major obstacle in understanding the role oxygen vacancies play in catalytic activity is that different metal oxide particles within a single batch exhibit variations in the concentration and distribution of oxygen vacancies. This heterogeneity makes it difficult to correlate specific morphological and structural features with catalytic activity when measurements are made on large groups of particles. Thus, methods are needed that can spatially map variations in activity for individual particles and correlate those variations with the specific structural features that lead to high or low activity.

SMLM has been applied to study size and shape effects in chemical reactions catalyzed by inorganic nano- and microstructures, including metal nanoparticles [114, 120, 181–188], layered and mesoporous materials [120,189–191], metal oxides [115,120,192–196], and metal-metal oxide heterostructures [120,197,198]. By localizing the positions of individual redox-active probe molecules that are chemically triggered by interfacial charge transfer, one can obtain a map of reaction events at the surface of these materials with nanoscale spatial resolution. Several studies have compared electron microscopy and single-molecule fluorescence images of the same catalyst particles to show that their activity can vary along a single-crystal facet or in the regions between groups of closely spaced particles. However, because the spatial resolution provided by this technique (typically 10 to 25 nm) still averages over many atoms on the surface of the catalyst, in most cases, the chemical structure of the active regions could not be conclusively identified [115,181–186,193–195].

In this chapter, a SMLM approach using chemically triggered molecular probes and their correlation is introduced and discussed for studying and mapping spatial variations in the catalytic activity of individual tungsten oxide ($W_{18}O_{49}$) nanowires[6]. In this work, we utilized two types of fluorogenic probes that can be catalyzed from nonfluorescent molecules into highly fluorescent products. Activation of the first probe molecule requires photoexcitation above the band gap of the semiconductor to generate hydroxyl radicals, an important intermediate in the production of chemical fuels from sunlight. The second reaction does not require photoexcitation but instead relies on the presence of either oxygen vacancies or hydroxyl groups at the surface of the nanowires. Through quantitative colocalization of the spatial distribution of the two probes, we show that the nanowires contain inactive regions dispersed among segments that are catalytically active for both transformations. The high degree of spatial correlation between the two probe reactions enabled us to elucidate the structural nature of the active regions. Segments along each nanowire that contain clusters of oxygen vacancies activate surface-adsorbed water molecules during the photocatalytic generation of hydroxyl radicals.

---

[6] I am a co-first author of this work published previously [140]. This project is a collaboration with Prof. Bryce Sadtler and graduate student Meikun Shen, experts in material chemistry and photochemistry. Meikun did all the catalyst preparation work, which included synthesis of $W_{18}O_{49}$ nanowires and their structural characterization in ensemble measurements. We did SM measurements in a microscope compatible with TIR illumination, and I have performed all the SM data analysis.

3.1 Oxygen Vacancies in Tungsten Oxide Nanowires

Tungsten oxide ($W_{18}O_{49}$) nanowires were synthesized using a solvothermal (or hydrothermal) method (see Section 2.3.1 for further details). Transmission electron microscopy (TEM) images show that the nanowires possess an average diameter of 14 ± 8 nm (average ± 1st standard deviation) and lengths of several micrometers (Figure 3.1A). A high-resolution TEM (HRTEM) image (Figure 3.1B) of a section along a single nanowire shows lattice fringes with a spacing of 3.8 Å aligned perpendicular to the nanowire length. This lattice spacing matches the *d*-spacing for the (010) plane of monoclinic $W_{18}O_{49}$, indicating that the nanowire grew along the [010] direction (addtional HRTEM images shown in Figure 3.2). An X-ray diffraction pattern of the as-synthesized sample (Figure 3.1D, black) matched the standard pattern for monoclinic $W_{18}O_{49}$ (PDF card #00-005-0392) [178, 199].

The monoclinic phase of tungsten oxide corresponding to $W_{18}O_{49}$ can accommodate variations in the W:O stoichiometry that arise due to oxygen vacancies [165, 180]. Evidence of the presence of oxygen vacancies in the as-synthesized $W_{18}O_{49}$ nanowires was provided by X-ray photoelectron spectroscopy (XPS, Figure 3.1E). The W 4f core level peaks obtained by XPS can be assigned to a mixture of W^{6+}, W^{5+}, and W^{4+} [178, 200]. Tungsten ions in the +5 and +4 oxidation states compensate the positive charge left by the removal of O^{2-}. We also observe a shoulder peak in the region for O 1s at a higher binding energy than the peak corresponding to lattice oxygen (Figure 3.1F). This peak has been previously

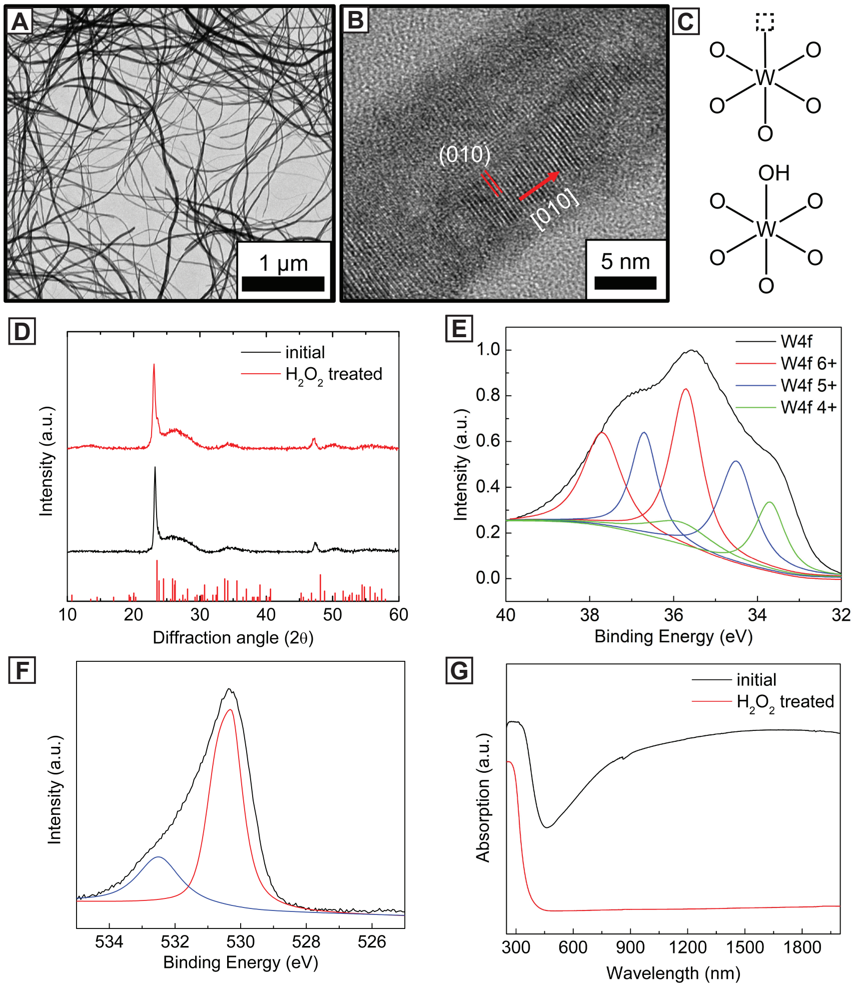

Figure 3.1: Structural characterization of $W_{18}O_{49}$ nanowires. (A) Low-magnification and (B) high-resolution TEM images of $W_{18}O_{49}$ nanowires. (C) Models for an oxygen vacancy (top) and a hydroxyl group (bottom) at the surface of $W_{18}O_{49}$. (D) X-ray diffraction patterns of tungsten oxide nanowires before (black trace) and after (red trace) oxidation with H_2O_2. The red lines at the bottom of the panel are the reflections for a standard XRD powder pattern of monoclinic $W_{18}O_{49}$ (PDF card # 00-005-0392). The monoclinic crystal structure did not change after oxidation. (E) X-ray photoelectron spectrum for $W_{18}O_{49}$ nanowires in the binding energy region for W 4f electrons. (F) X-ray photoelectron spectrum of the as-synthesized tungsten oxide nanowires showing the binding energy region for O 1s electrons. The red and blue lines show the deconvolution of the spectrum into oxygen within the $W_{18}O_{49}$ crystal (red trace) and surface adsorbed oxygen species at higher binding energy (blue trace). (G) Absorption spectrum of tungsten oxide $W_{18}O_{49}$ nanowires before (black trace) and after (red trace) oxidation with H_2O_2. Adapted and reprinted with permission from Ref. [140].

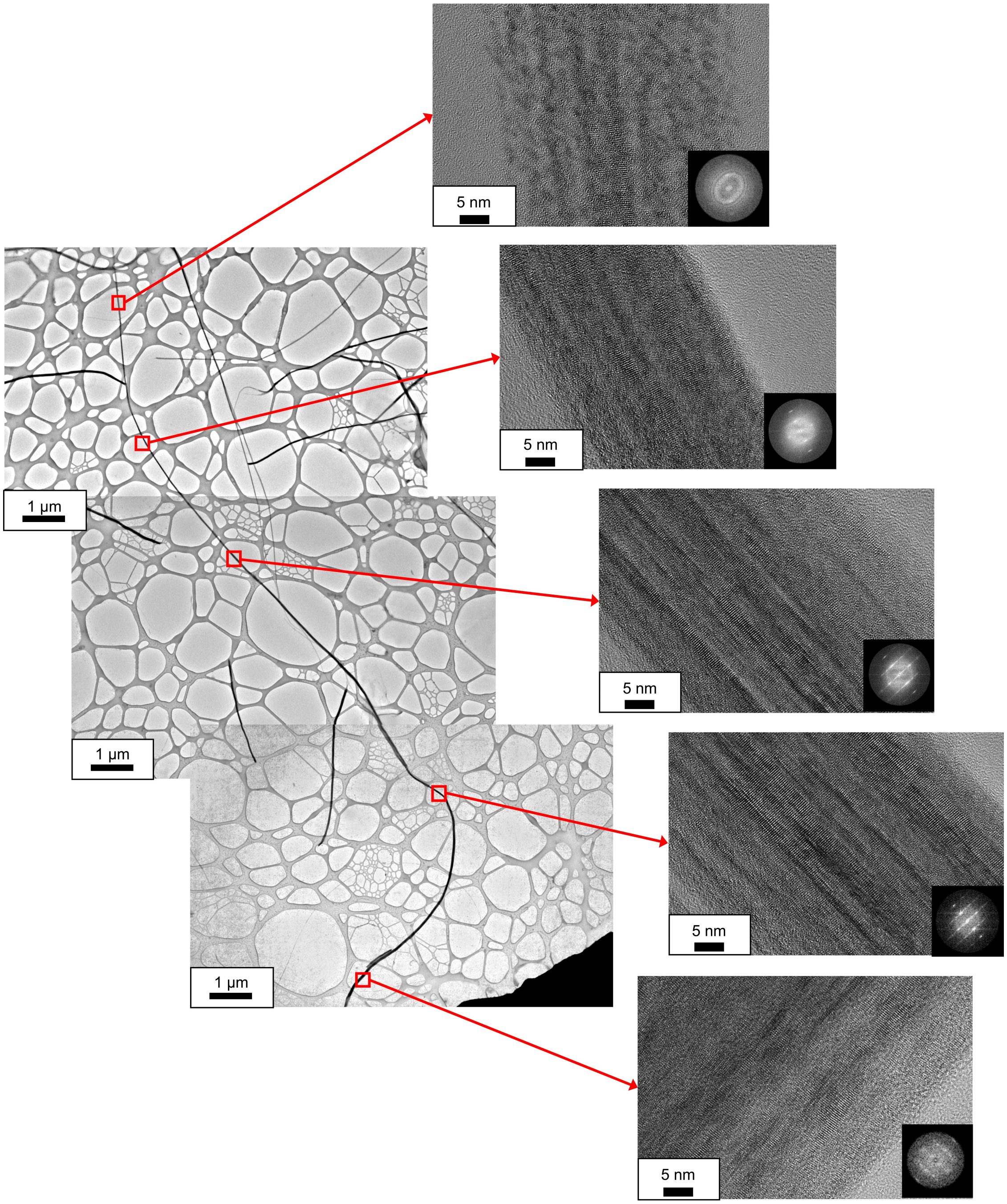
5 nm
5 nm
1 μm
5 nm
1 μm
5 nm
1 μm
5 nm

Figure 3.2: Low-magnification TEM images of a $W_{18}O_{49}$ nanowire (left) and high-resolution TEM images at different regions of the same nanowire (right). The insets show the fast Fourier transforms (FFT) of each HRTEM image. Reprinted with permission from Ref. [140].

attributed to surface-adsorbed oxygen species that bind to metal ions left exposed by oxygen vacancies [168,170,178]. Furthermore, the absorption spectruc of a film of $W_{18}O_{49}$ nanowires measured using an integrating sphere shows an absorption edge near 440 nm (Figure 3.1G, black), which corresponds to band gap excitation of tungsten oxide ($E_g = 2.8$ eV). The broad absorption at wavelengths beyond 500 nm has been previously attributed to free carrier absorption induced by surface oxygen vacancies in $W_{18}O_{49}$ [164,165,180]. Oxidation of the nanowires using either hydrogen peroxide (H_2O_2) led to the disappearance of free carrier absorption (Figure 3.1G, red). Oxidation using H_2O_2 preserved the monoclinic $W_{18}O_{49}$ phase of the nanowires (Figure 3.1D, red), enabling us to compare the catalytic activity of nanowires with and without oxygen vacancies.

3.2 SMLM for Mapping Photocatalytic Activity on Tungsten Oxide

Hydroxyl radicals (·OH) are a key intermediate in several reactions photocatalyzed by metal oxide semiconductors, including water oxidation, the degradation of environmental pollutants, and methane to methanol conversion [171,172,194,201–203]. We hypothesized that differences in the local structure of $W_{18}O_{49}$ nanowires would affect their activity for generating ·OH radicals. To image spatial variations in activity along the length of individual $W_{18}O_{49}$ nanowires, we first chose a fluorogenic probe that is activated in the presence of ·OH radicals (Figure 3.3B). Cleavage of the aminophenyl group of 3'-(*p*-aminophenyl) fluorescein (APF) by ·OH generates fluorescein [204]. Control experiments using dispersions of $W_{18}O_{49}$

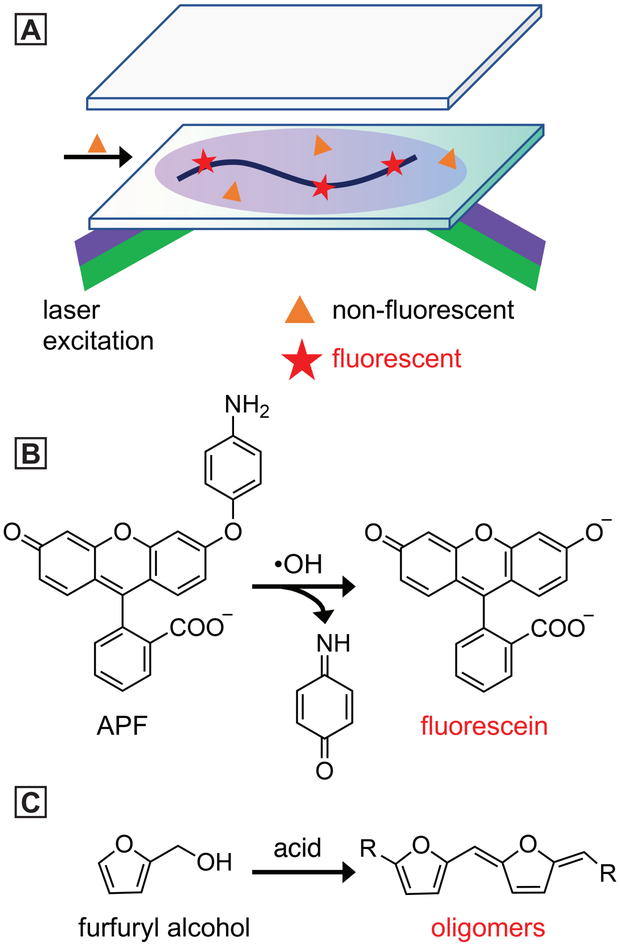
A
laser excitation
non-fluorescent
fluorescent
B
NH2
O
O
O
COO−
•OH
NH
O
O
O
O−
COO−
APF
fluorescein
C
O
OH
acid
R
O
O
R
furfuryl alcohol
oligomers

Figure 3.3: SM imaging of catalytic reactions using fluorogenic probes. (A) Experimental setup for Total Internal Reflection Fluorescence (TIRF) microscopy. One or more lasers are sent through a microscope objective at an angle such that they are internally reflected at a glass coverslip. The $W_{18}O_{49}$ nanowires catalyze the reactions shown in B and C to convert nonfluorescent substrate molecules (orange triangles) into fluorescent products (red stars). The fluorescence emission is collected through the same objective and imaged by an electron-multiplying CCD camera. (B) Oxidation of 3'-(*p*-aminophenyl) fluorescein (APF) by hydroxyl radicals produces fluorescein. (C) Acid-catalyzed condensation of furfuryl alcohol produces fluorescent oligomers. Reprinted with permission from Ref. [140].

nanowires in solution show that both nanowires containing oxygen vacancies and illumination with photon energies above the band gap of $W_{18}O_{49}$ are needed to induce this reaction at the ensemble level.

Single-molecule super-resolution microscopy was conducted using Total Internal Reflection Fluorescence (TIRF) excitation. In this imaging mode, only fluorophores activated near the surface of the coverslip are detected (Figure 3.3A) [114, 115, 181, 182, 194]. A 405 nm laser coupled into the objective of an inverted microscope was used to excite $W_{18}O_{49}$ nanowires dispersed on a glass coverslip. Simultaneous illumination with a 488 nm laser was used to excite the product fluorescein molecules. After adding a solution of APF (30 nM in a solution of phosphate buffer with pH 7.4), fluorescence intensity bursts were observed (Figure 3.4A). We attribute these fluorescence bursts to the generation of fluorescein after reaction with photogenerated ·OH radicals adsorbed on the surface of the nanowires. We performed the following control experiments to support this hypothesis. Using APF as a probe, fluorescence signals were not observed on blank coverslips (i.e., without nanowires; Figure 3.5A). Second, fluorescence signals were only observed when using both excitation beams (405 and 488 nm). Furthermore, fluorescence signals were not observed when the reaction was carried out in pure phosphate buffer solution or when dimethyl sulfoxide (DMSO) was added to the solution of APF. DMSO has been previously shown to act as a scavenger for ·OH radicals [192, 198]. Similar to the ensemble studies, very few fluorescence bursts (a number comparable to a blank sample) were observed for nanowires treated with H_2O_2 to remove oxygen vacancies. Finally, simply adding a solution of fluorescein (30 nM in phosphate buffer) to the nanowires did not produce fluorescence bursts, which indicates that fluorescein (which has a higher density of negative charge than APF) does not bind as strongly to the $W_{18}O_{49}$ surface as APF. Thus, the turn-off events are attributed to either the desorption of

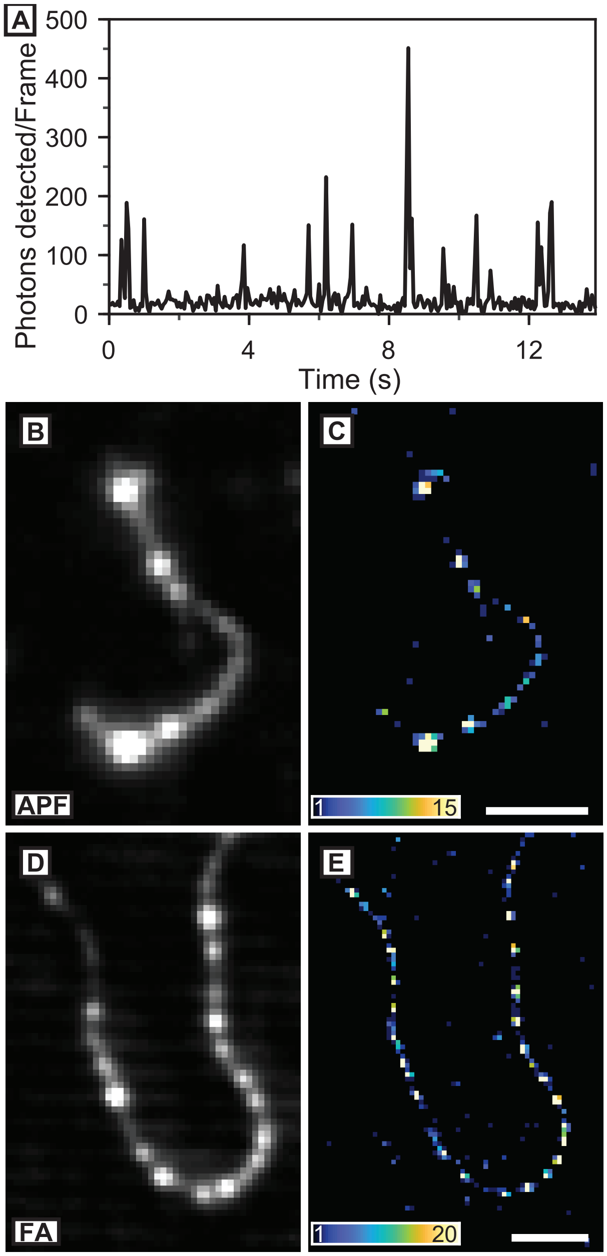

Figure 3.4: Imaging the catalytic activity of single $W_{18}O_{49}$ nanowires. (A) Trajectory of photons detected in a 1 × 1 μm region for a single $W_{18}O_{49}$ nanowire using APF as a probe molecule. (B) Diffraction-limited image of a $W_{18}O_{49}$ nanowire under the same conditions as in A. (C) Super-resolution image of the nanowire in B containing the positions of all fluorescence bursts. Color scale: number of fluorescence bursts per bin. (D) Diffraction-limited image of a $W_{18}O_{49}$ nanowire using furfuryl alcohol (FA) as a probe molecule. (E) Super-resolution image of the nanowire in d containing the positions of all fluorescence bursts. Scale bars: 2 μm. Reprinted with permission from Ref. [140].

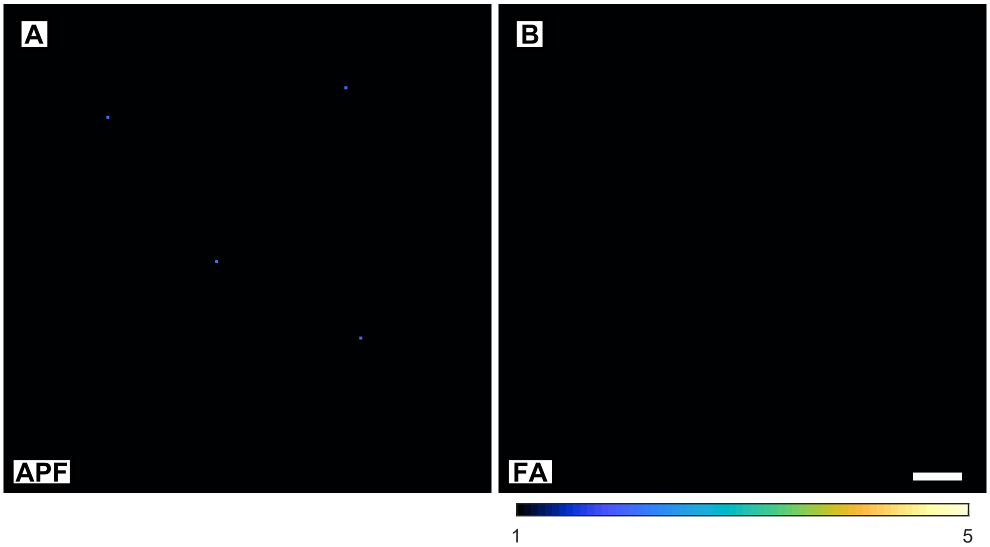

Figure 3.5: Representative blank images of APF and FA without $W_{18}O_{49}$ nanowires. Superresolution images of a blank FOV using (A) APF under the same imaging conditions as Figures 3.4A-C and (B) FA under the same conditions as Figures 3.4D and E. Color scale: number of fluorescence bursts per bin. Scale bar: 2 μm. Reprinted with permission from Ref. [140].

fluorescein from the surface of a $W_{18}O_{49}$ nanowire or its decomposition into a nonfluorescent product.

By localizing the positions of individual fluorescence bursts collected over 1,500 - 2,500 frames (50 ms camera exposure time), we acquired activity maps for single $W_{18}O_{49}$ nanowires with a localization precision of 22 nm (see Figure 3.6C for a histogram of the localization precision). The number of fluorescence bursts localized per nanowire ranged from 130 to 4,000 among the 35 nanowires analyzed for this reaction. We did not observe any obvious correlation between morphological irregularities in the nanowires imaged by electron microscopy and the variations in activity imaged by SM fluorescence (Figure 3.7). Furthermore, we kept the imaging short (typically below 5 min) to avoid photodegradation

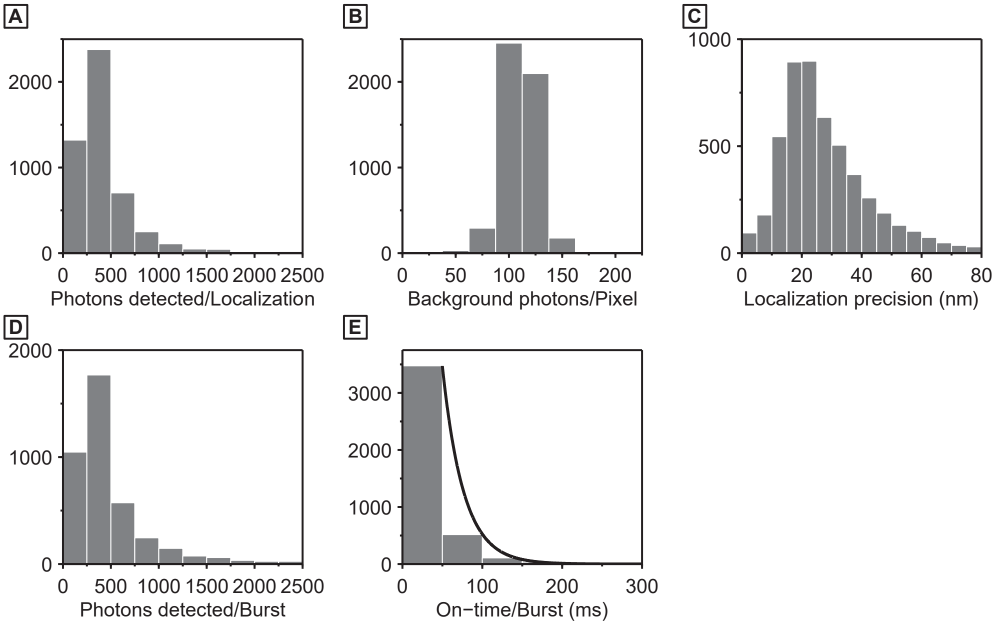

Figure 3.6: Quantitative characterization of APF blinking events on an initial $W_{18}O_{49}$ nanowire (shown in Figure 3.12A). (A) Photons detected per localization, (B) Background photons per pixel, and (C) Localization precision of APF bursts observed along a single nanowire. (D) Photons detected and (E) On-time of APF bursts after the localization grouping procedure. The black solid line in E depicts the fitting result of the on-time to an exponential decay. The median of photons detected per burst is 360 photons; the time constant of the exponential fit is 26 ms. Reprinted with permission from Ref. [140].

of the nanowires. Under the same illumination conditions used for single-molecule fluorescence (405 and 488 nm laser, buffer solution added), thin films of the nanowires showed no obvious structural changes after 5 min of irradiation. Figure 3.4C shows the activity map for photocatalytic ·OH radical generation of a representative nanowire, where the color scale indicates the number of fluorescence bursts detected in each accumulation bin (120×120 nm^2). Significant variations in activity are seen along the $W_{18}O_{49}$ nanowire, and similar variations were observed for all 35 nanowires imaged (see Figures 3.8AB for an additional example).

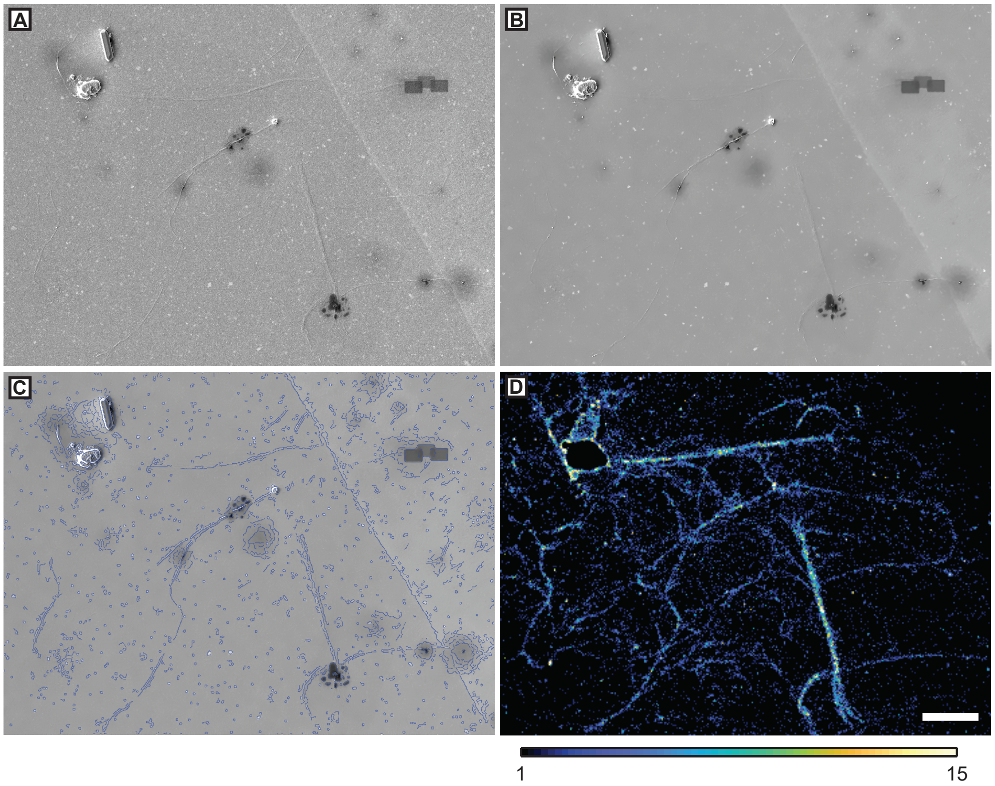

Figure 3.7: Correlation between SEM and fluorescence microscopy of APF activity of initial $W_{18}O_{49}$ nanowires. (A) The nanowires imaged by SEM. The image was (B) denoised using a non-local means filter and (C) overlaid with detected edges obtained by Canny edge detection. (D) super-resolution image of the nanowires using APF as probe molecules. Color scale: bursts per bin. Scale bar: 5 μm. The scale bar applies to A-D. Reprinted with permission from Ref. [140].

Tungsten oxide has been used as a solid-acid catalyst, similar to zeolites, due to the presence of both surface oxygen vacancies (Figure 3.1C, top), which act as Lewis acid sites (a species that accepts an electron pair and has vacant orbitals), and surface hydroxyl groups (Figure 3.1C, bottom), which act as Bronsted acid sites (a proton H^+ donor) [170, 205, 206]. Fourier-transform infrared spectroscopy (FT-IR) of chemically adsorbed pyridine indicated that dry powders of the $W_{18}O_{49}$ nanowires possessed both Lewis and Bronsted acid sites (Figure 3.9A) [206]. However, our single-molecule studies were conducted in an aqueous solution of phosphate buffer at pH 7.4. At this pH, hydroxyl groups at the surface of the

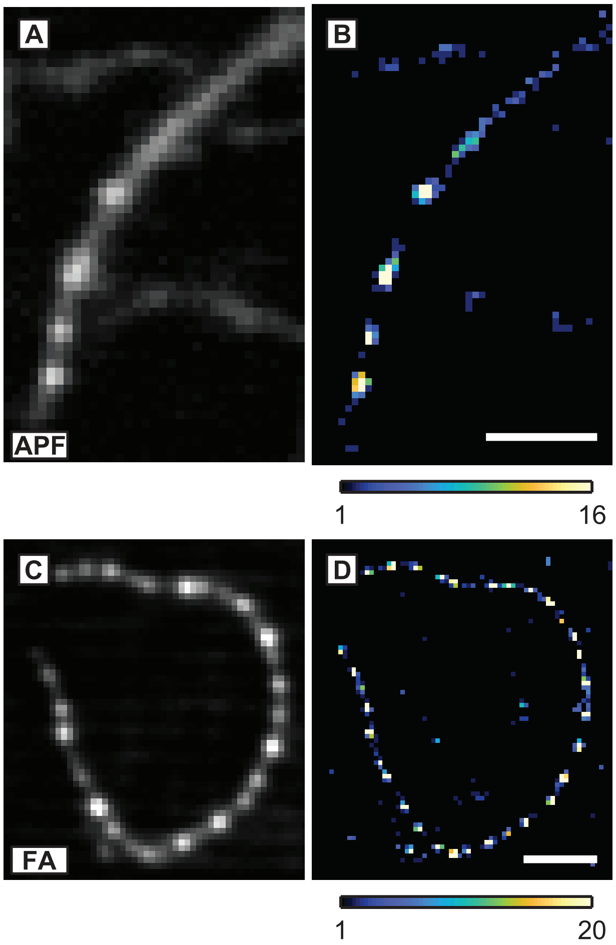

Figure 3.8: Super-resolution fluorescence images of initial $W_{18}O_{49}$ nanowires. (A) Diffraction-limited image of $W_{18}O_{49}$ nanowires under the same imaging conditions as Figures 3.4A-C. (B) Super-resolution image of the nanowires in A by localizing the positions of all fluorescence bursts. Color scale: number of fluorescence bursts per bin. (C) Diffraction-limited image of a $W_{18}O_{49}$ nanowire using furfuryl alcohol (FA). (D) Super-resolution image of the nanowire in C by localizing all furfuryl alcohol bursts. Scale bars: 2 μm. Reprinted with permission from Ref. [140].

nanowires are expected to be deprotonated due to the strong acidity of tungsten oxide (pH 0.43 at the point of zero charge), leading to a negative surface charge on the nanowires [207]. Consistent with this expectation, zeta potential measurements gave a value of -44.9 ±

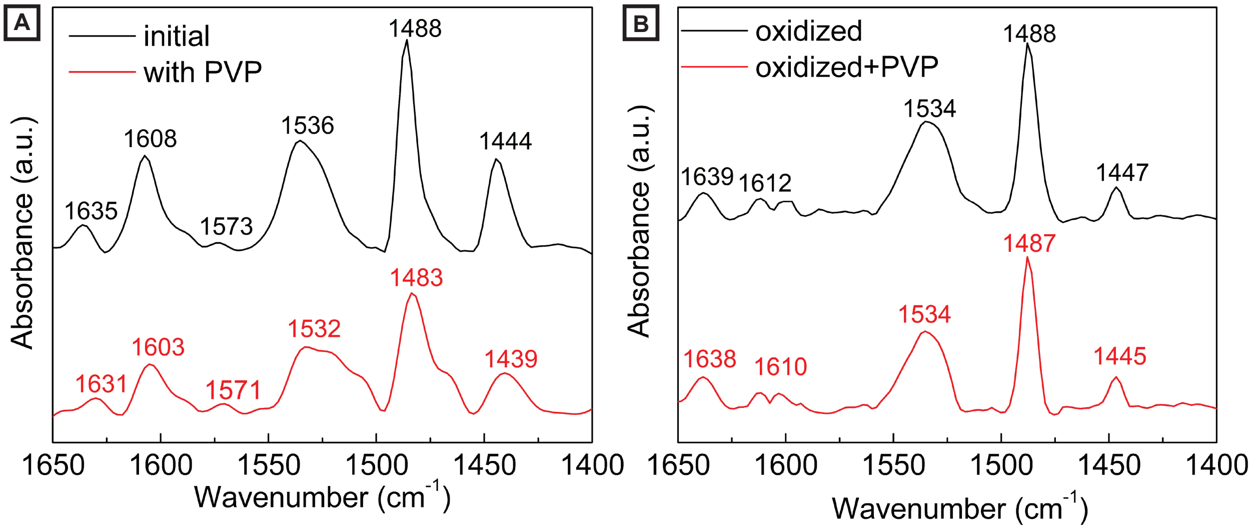

Figure 3.9: (A) FT-IR spectra after the chemisorption of pyridine on the initial (black trace) and PVP-functionalized (red trace) $W_{18}O_{49}$ nanowires. (B) FT-IR spectra after the chemisorption of pyridine on the oxidized nanowires before (black trace) and after (red trace) PVP-functionalization. The peaks near 1444 and 1608 cm^{-1} are assigned to pyridine bound to Lewis acid sites and decrease in intensity after oxidation. The peak near 1536 cm^{-1} is associated with Bronsted acid sites. Reprinted with permission from Ref. [140].

0.3 mV (average ± first standard deviation from three measurements) when the nanowires were dispersed in a buffer solution at pH 7.4.

We next selected furfuryl alcohol as a probe molecule that can undergo acid-catalyzed condensation to generate fluorescent oligomers (Figure 3.3C) [190,208]. The formation mechanism of fluorescent oligomers using both Lewis and Bronsted acids to catalyze this reaction has been previously described [209, 210], and tungsten oxide powders have been shown to catalyze the condensation of furfuryl alcohol [208]. Similar to the conditions used for APF, only Lewis acid sites are expected to be active in the as-synthesized $W_{18}O_{49}$ nanowires as surface hydroxyl groups will be deprotonated at pH 7.4. As this reaction does not require photoexcitation of the nanowires, TIRF excitation with a 561 nm laser (i.e., below the band

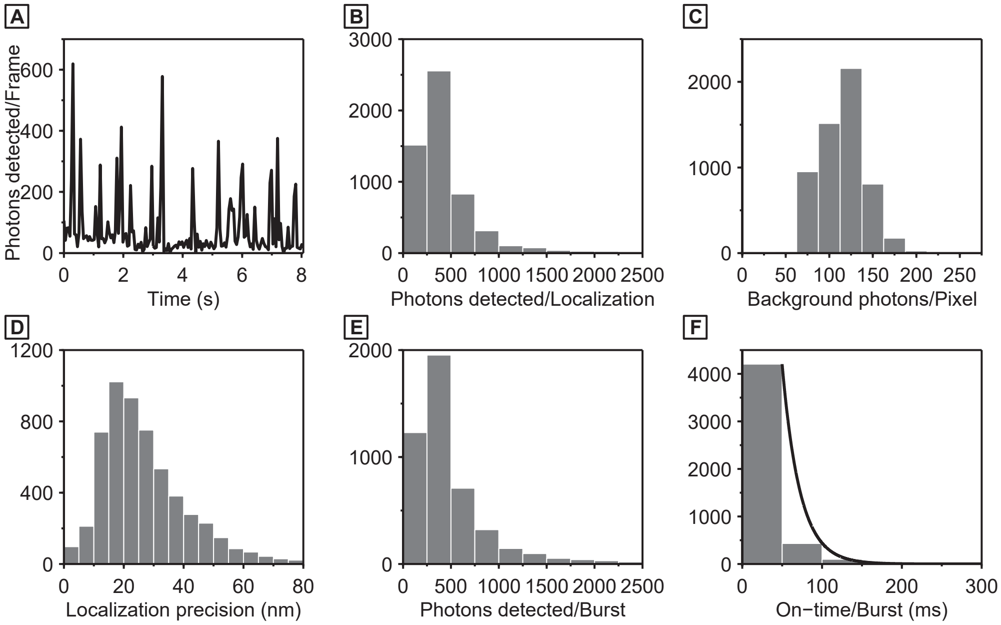

Figure 3.10: Quantitative characterization of furfuryl alcohol blinking events on an initial $W_{18}O_{49}$ nanowire (shown in Figure 3.12B). (A) Trajectory of photons detected in a 1 × 1 μm region for a single $W_{18}O_{49}$ nanowire. (B) Photons detected per localization, (C) Background photons per pixel, and (D) Localization precision of furfuryl alcohol bursts observed along a single nanowire. (E) Photons detected and (F) On-time of furfuryl alcohol bursts after the localization grouping procedure. The black solid line in F depicts the fitting result of the on-time to an exponential decay. The median of photons detected per burst is 370 photons; the time constant of the exponential fit is 22 ms. Reprinted with permission from Ref. [140].

gap energy of $W_{18}O_{49}$) was used to detect the oligomeric products. After addition of furfuryl alcohol, video recordings showed fluorescence intensity bursts similar to the case of APF (Figure 3.10A). These intensity bursts were not observed on blank coverslips in the same solution (Figure 3.5B). Figure 3.4E shows a representative activity map, revealing that the $W_{18}O_{49}$ nanowires also displayed variations in activity along their length for this acid-catalyzed reaction. Similar variations in activity were observed for all 35 nanowires imaged using furfuryl alcohol as a probe molecule (see Figures 3.8CD for an additional example).

3.3 Coordinate-Based Colocalization for Revealing the Role of Oxygen Vacancy in Tungsten Oxide

To directly correlate the active regions for photocatalytic ·OH radical generation with the distribution of Lewis acid sites, we sequentially performed single-molecule imaging with both APF and furfuryl alcohol as probe molecules on the same $W_{18}O_{49}$ nanowires (Figure 3.12A,F for APF and Figure 3.12B,G for furfuryl alcohol). Control experiments showed that APF used in the first round of imaging did not lead to fluorescence contamination during sequential imaging with the furfuryl alcohol probe (Figure 3.11). We used a coordinate-based colocalization (CBC) algorithm (see Section 2.6.3 for more details) [159] to quantify the spatial correlation of each fluorescence burst from the two probes, yielding a value ranging from -1 for anticorrelated distributions, through 0 for random, to $+1$ for perfectly correlated distributions. The colocalization maps (Figure 3.12C,D,H,I) and the distribution of the CBC score across both nanowires (Figure 3.12E,J) show that the regions of each nanowire that are more active for generating ·OH radicals are also more active for the condensation of furfuryl alcohol. Figures 3.13, 3.14 and 3.15 provide additional examples of this colocalization analysis performed on the as-synthesized $W_{18}O_{49}$ nanowires. The CBC analysis on 33 nanowires shows a high degree of colocalization between the two fluorogenic probes. Thus, not only is the catalytic activity heterogeneous along the lengths of individual nanowires, but also, to a large extent, the same segments within each nanowire are active for both reactions. Since the condensation of furfuryl alcohol probes the concentration of Lewis acid sites (or equivalently oxygen vacancies), this single-molecule colocalization reveals that regions containing oxygen vacancies are active sites for hydroxyl radical generation. This observation is consistent with previous DFT calculations showing that a H_2O molecule will preferentially bind to a tungsten ion exposed by an oxygen vacancy at the (001) surface of WO_3, which activates the H_2O molecule toward dissociation to H^+ and OH^- [211–213]. An adsorbed OH^- ion can then be oxidized to an ·OH radical using photoexcited holes in the metal oxide [214].

As regions containing surface oxygen vacancies (i.e., Lewis acid sites) are active for both hydroxyl radical generation and furfuryl alcohol condensation, changing the availability of these sites should alter the catalytic activity of the nanowires. On the other hand, the availability of Bronsted acid sites should affect only the condensation reaction. To test this hypothesis, we applied different chemical modifications to the $W_{18}O_{49}$ nanowires and measured their resulting photocatalytic activity at both the ensemble and single-particle levels. We first oxidized the $W_{18}O_{49}$ nanowires using H_2O_2 to remove oxygen vacancies, similar to a previous report [166]. The X-ray diffraction pattern of the oxidized $W_{18}O_{49}$ nanowires was indistinguishable from the original pattern (Figure 3.1D). However, the diffuse reflectance spectrum (Figure 3.1G) of the oxidized nanowires showed significantly reduced absorption at long wavelengths (600 to 2,000 nm). The FT-IR spectra measured for dry powders of the nanowires after pyridine adsorption showed a decrease in the intensity of the peaks corresponding to Lewis acid sites, while the peaks corresponding to Bronsted acid sites did not change significantly (Figure 3.9). The zeta potential after oxidation (-42.1 ± 7.32 mV) was similar to the nanowires before oxidation (-44.9 ± 0.3 mV), indicating that the density of deprotonated surface hydroxyl groups did not change significantly. Together, these ensemble results demonstrate that the oxidation of the $W_{18}O_{49}$ nanowires using H_2O_2 decreases both the concentration of oxygen vacancies and the availability of Lewis acid sites but does not significantly change the availability of Bronsted acid sites. This active-site change was further verified by negligible amount of fluorescence signal observed in our SM imaging using APF and furfuryl alcohol as the probe molecules.

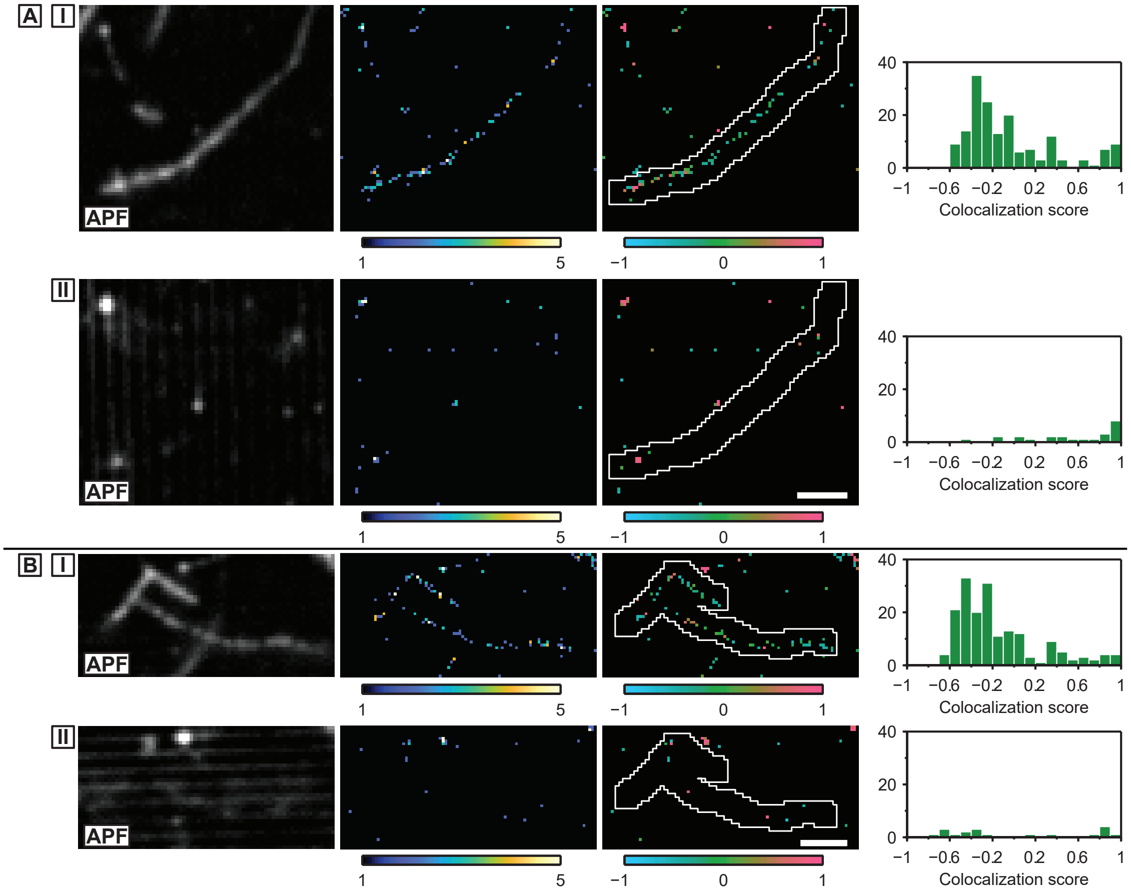

Figure 3.11: APF super-resolution of initial $W_{18}O_{49}$ nanowires before and after phosphate buffer wash. Diffraction-limited (far left), super-resolution (middle left) and coordinate-based colocalization (CBC) images (middle right), and counts of CBC scores (far right) of (A, B) two nanowires using APF (I) before and (II) after sample wash with phosphate buffer. The same 405-nm and 488-nm lasers were used as in other APF imaging. No structure was observed in II after the sample wash. Unlike other analyses in the paper, the CBC was performed using the data sets before and after the wash. Negative CBC scores in I the measurement before the wash suggest removal of APF molecules by the phosphate buffer treatment. Color scales of super-resolution images: bursts per bin. Color scales of CBC images: median of the CBC score in each bin ranging from -1 for anti-correlated to +1 for perfectly-correlated burst distributions. White lines depict boundaries of the nanowire regions. Scale bars: 2 μm. Reprinted with permission from Ref. [140].

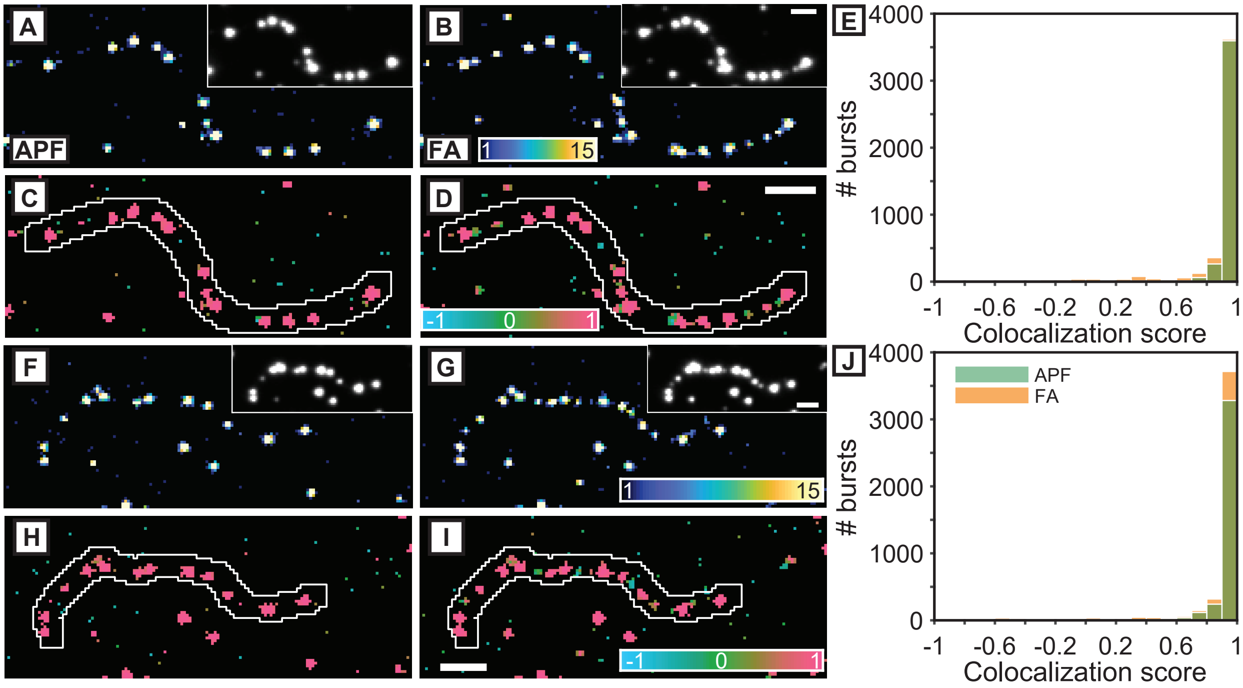

Figure 3.12: Colocalization of hydroxyl radical generation and Lewis acid sites for two representative $W_{18}O_{49}$ nanowires. Super-resolution images of the initial nanowires using (A, F) APF as a probe to detect hydroxyl radicals and (B, G) furfuryl alcohol (FA) as a probe to identify Lewis acid sites. Color scale: number of fluorescence bursts per bin. Inset: diffraction-limited images of each imaging condition. Coordinate-based colocalization (CBC) of (C, H) APF and (D, I) furfuryl alcohol bursts. Color scale: median colocalization score in each bin ranging from -1 for anticorrelated burst distributions, through 0 for random, to $+1$ for perfectly correlated burst distributions. White lines depict boundaries of the nanowire regions. All scale bars are 2 μm. The top scale bars apply to the diffraction-limited images in the insets of A, B, F, and G. The bottom scale bars apply to all super-resolution images in A-D and F-I. (E, J) CBC scores for APF (green) and furfuryl alcohol (orange) bursts within the nanowire regions. Segments of other nanowires are seen in each super-resolution image. Only fluorescence bursts detected within the white outlines are included in E and J. Reprinted with permission from Ref. [140].

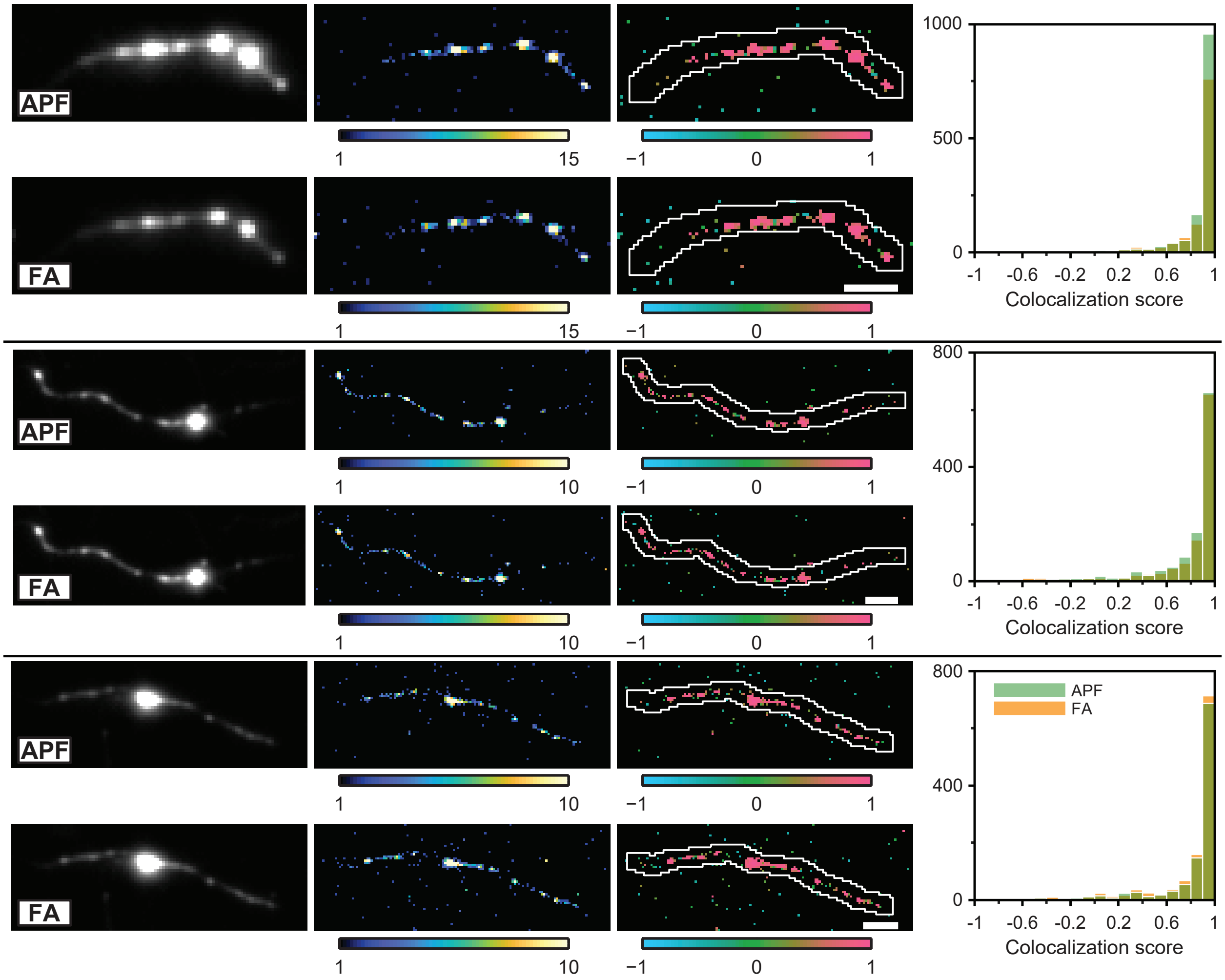

Figure 3.13: Colocalization analysis of initial $W_{18}O_{49}$ nanowires I. Diffraction-limited (far left), super-resolution (middle left) and coordinate-based colocalization (CBC) images (middle right), and counts of CBC scores (far right) of three nanowires using APF and furfuryl alcohol (FA) as probe molecules. Color scales of super-resolution images: bursts per bin. Color scales of CBC images: median of the CBC score in each bin ranging from -1 for anti-correlated to +1 for perfectly-correlated burst distributions. White lines depict boundaries of the nanowire regions. Scale bars: 2 μm. Reprinted with permission from Ref. [140].

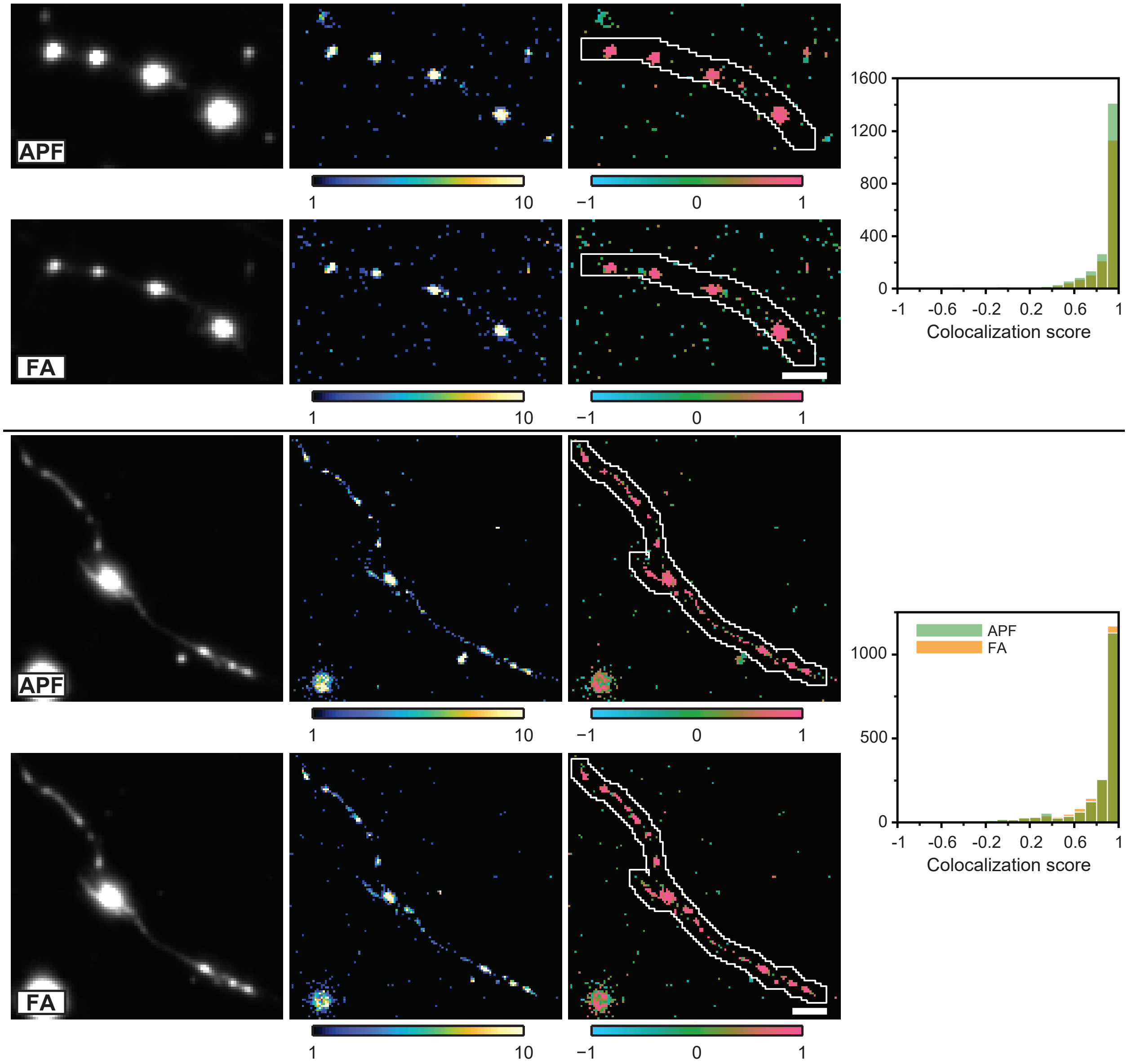

Figure 3.14: Colocalization analysis of initial $W_{18}O_{49}$ nanowires II. Diffraction-limited (far left), super-resolution (middle left) and coordinate-based colocalization (CBC) images (middle right), and counts of CBC scores (far right) of two nanowires using APF and furfuryl alcohol (FA) as probe molecules. Color scales of super-resolution images: bursts per bin. Color scales of CBC images: median of the CBC score in each bin ranging from -1 for anti-correlated to +1 for perfectly-correlated burst distributions. White lines depict boundaries of the nanowire regions. Scale bars: 2 μm. Reprinted with permission from Ref. [140].

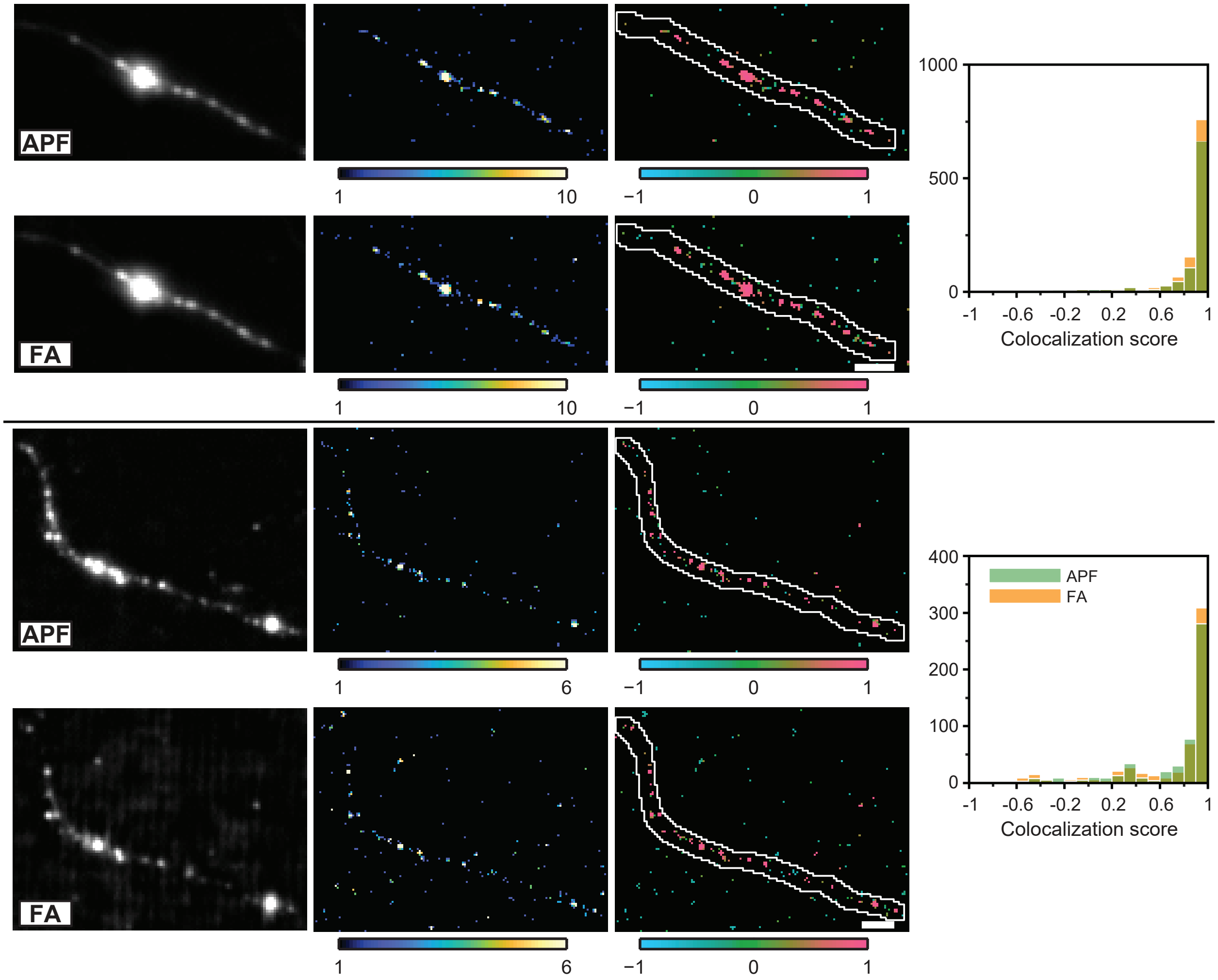

Figure 3.15: Colocalization analysis of initial $W_{18}O_{49}$ nanowires III. Diffraction-limited (far left), super-resolution (middle left) and coordinate-based colocalization (CBC) images (middle right), and counts of CBC scores (far right) of two nanowires using APF and furfuryl alcohol (FA) as probe molecules. Color scales of super-resolution images: bursts per bin. Color scales of CBC images: median of the CBC score in each bin ranging from -1 for anti-correlated to +1 for perfectly-correlated burst distributions. White lines depict boundaries of the nanowire regions. Scale bars: 2 μm. Reprinted with permission from Ref. [140].

We next treated both the initial and oxidized $W_{18}O_{49}$ nanowires with polyvinylpyrrolidone (PVP), a polymeric surfactant frequently used in the synthesis and assembly of metal and metal oxide nanoparticles [215–217]. PVP typically aids in the colloidal stability and dispersibility of metal oxide particles. Tungsten oxide nanowires with PVP on their surface have been used as photocatalysts and electrocatalysts [218, 219], but the effect of the PVP coating on their activity has not been studied. The FT-IR spectra of the PVP-functionalized nanowires after pyridine adsorption displayed weaker and broader peaks for both Bronsted acid and Lewis acid sites (Figure 3.9), indicating that PVP was bound to both sites. In aqueous solution, the binding of PVP to surface hydroxyl groups can suppress deprotonation of the Bronsted acid sites. Evidence for this suppression is provided by differences in the zeta potential of the two samples. While the zeta potential was between -42 and -45 mV for the initial and oxidized nanowires before PVP treatment, it dropped to -8.4 ± 0.7 mV (average ± first standard deviation from three measurements) for the initial nanowires and to -5.6 ± 5.6 mV for the oxidized nanowires after the functionalization of PVP. Dynamic hydrogen bonding of monomer units along the PVP polymer would allow Bronsted acid sites to still be available for the acid-catalyzed condensation of furfuryl alcohol.

The PVP-functionalization of $W_{18}O_{49}$ may affect photocatalytic activity due to the activation or deactivation of different sites on the nanowires. We next conducted the same correlative, single-molecule imaging on PVP-functionalized $W_{18}O_{49}$ nanowires using both APF and furfuryl alcohol as probes. Figures 3.16A,B,F,G show the activity maps for both ·OH radical generation and furfuryl alcohol condensation obtained by localizing all fluorescence bursts. While they are strongly correlated in the initial nanowires (Figure 3.12E,J), PVP treatment consistently reduced the correlations between APF and furfuryl alcohol localizations (Figure 3.16C-E,H-J), as reflected by a broader range of CBC scores (see Figures 3.17 and 3.18 for additional examples). Accumulating the CBC scores across all 33 initial

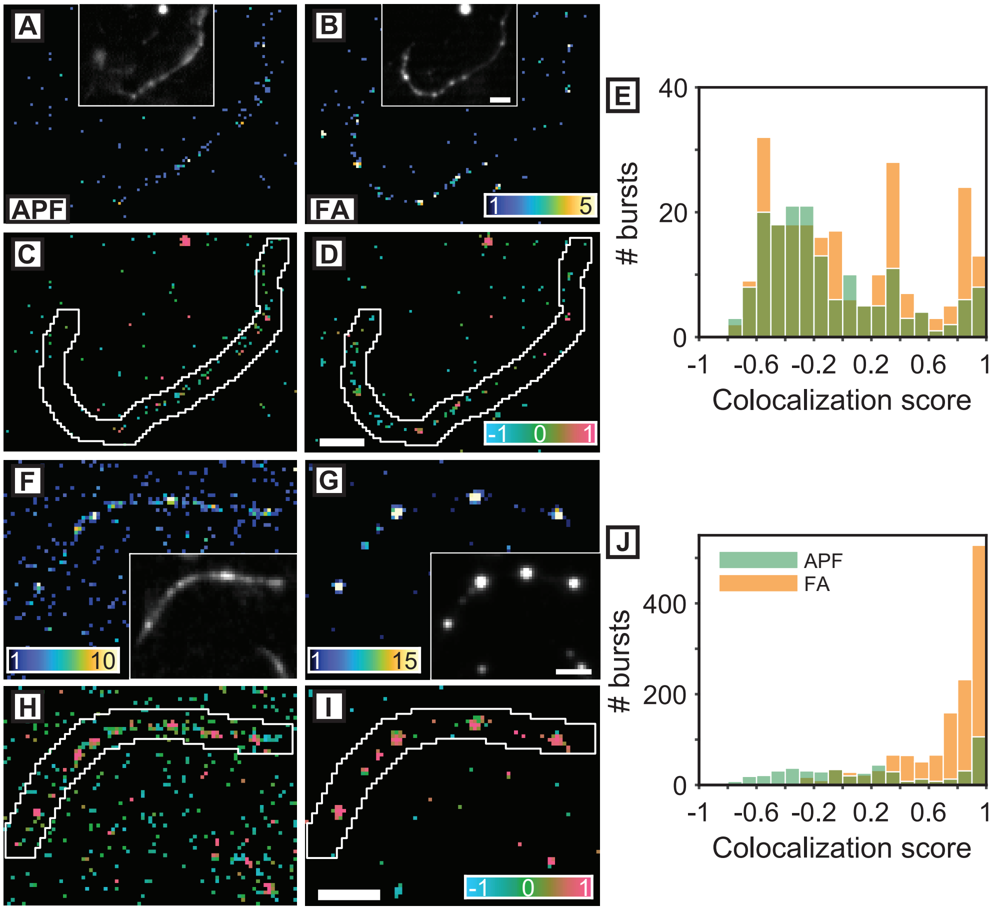

Figure 3.16: Colocalization of hydroxyl radical generation and acid sites for PVP-functionalized $W_{18}O_{49}$ nanowires. Super-resolution images of the nanowires using (A, F) APF as a probe to detect hydroxyl radicals and (B, G) furfuryl alcohol (FA) as a probe to identify Lewis and Bronsted acid sites. Color scale: number of fluorescence bursts per bin. Inset: diffraction-limited images of each imaging condition. Coordinate-based colocalization (CBC) of (C, H) APF and (D, I) furfuryl alcohol bursts. Color scale: median of the colocalization score in each bin, ranging from -1 for anticorrelated burst distributions, through 0 for random, to $+1$ for perfectly correlated burst distributions. White lines depict boundaries of the nanowire regions. All scale bars are 3 μm. The top scale bars apply to the diffraction-limited images in the insets of A, B, F, and G. The bottom scale bars apply to all super-resolution images in A-D and F-I. (E, J) CBC scores for APF (green) and furfuryl alcohol (orange) bursts within the nanowire regions. Segments of other nanowires are seen in each super-resolution image. Only fluorescence bursts detected within the white outlines are included in E and J. Reprinted with permission from Ref. [140].

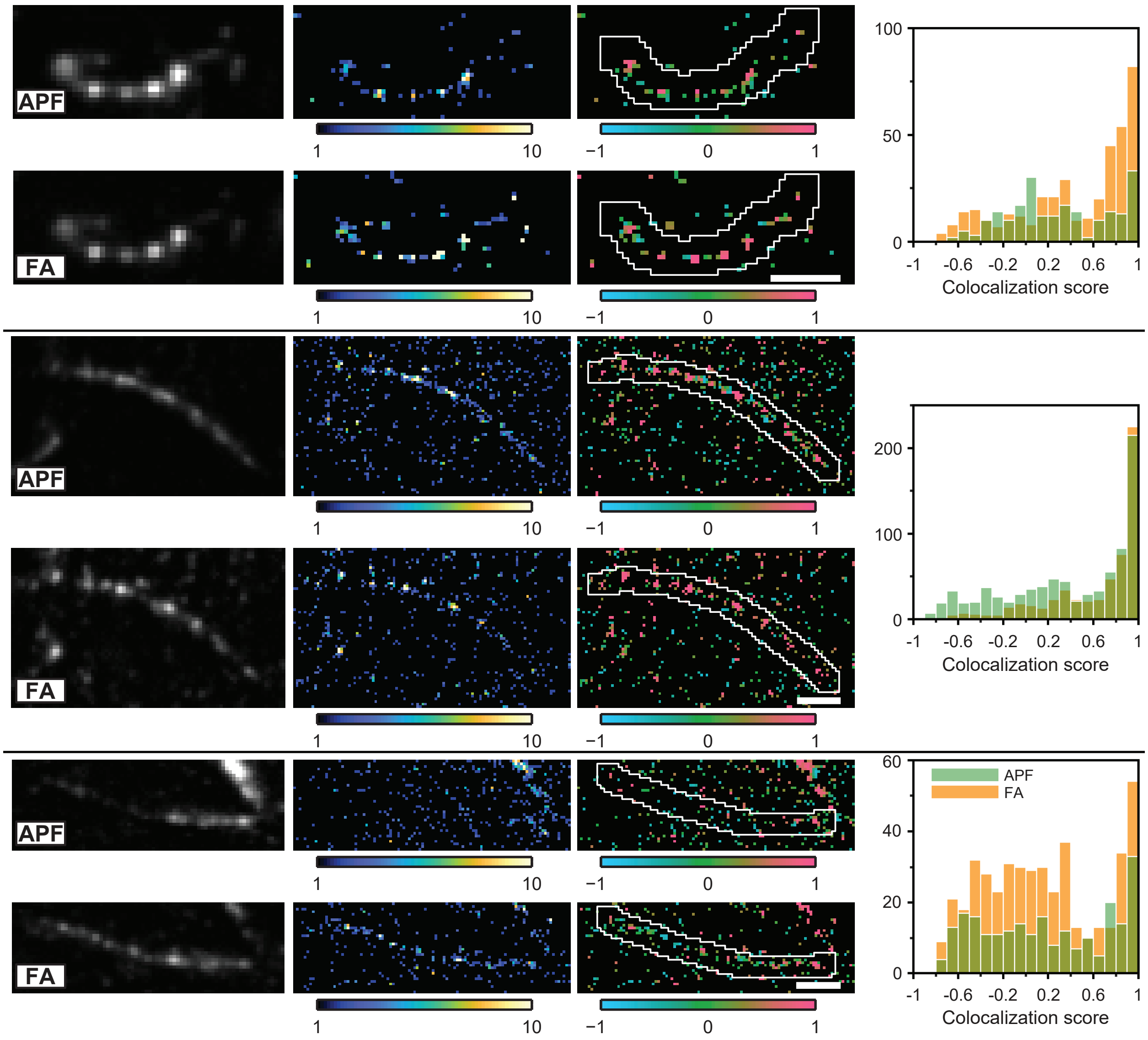

Figure 3.17: Colocalization analysis of PVP-functionalized $W_{18}O_{49}$ nanowires I. Diffraction-limited (left), super-resolution (middle left) and coordinate-based colocalization (CBC) images (middle right), and counts of CBC scores (far right) of three nanowires using APF and furfuryl alcohol (FA) as probe molecules. Color scales of super-resolution images: bursts per bin. Color scales of CBC images: median of the CBC score in each bin ranging from -1 for anti-correlated to +1 for perfectly-correlated burst distributions. White lines depict boundaries of the nanowire regions. Scale bars: 2 μm. Reprinted with permission from Ref. [140].

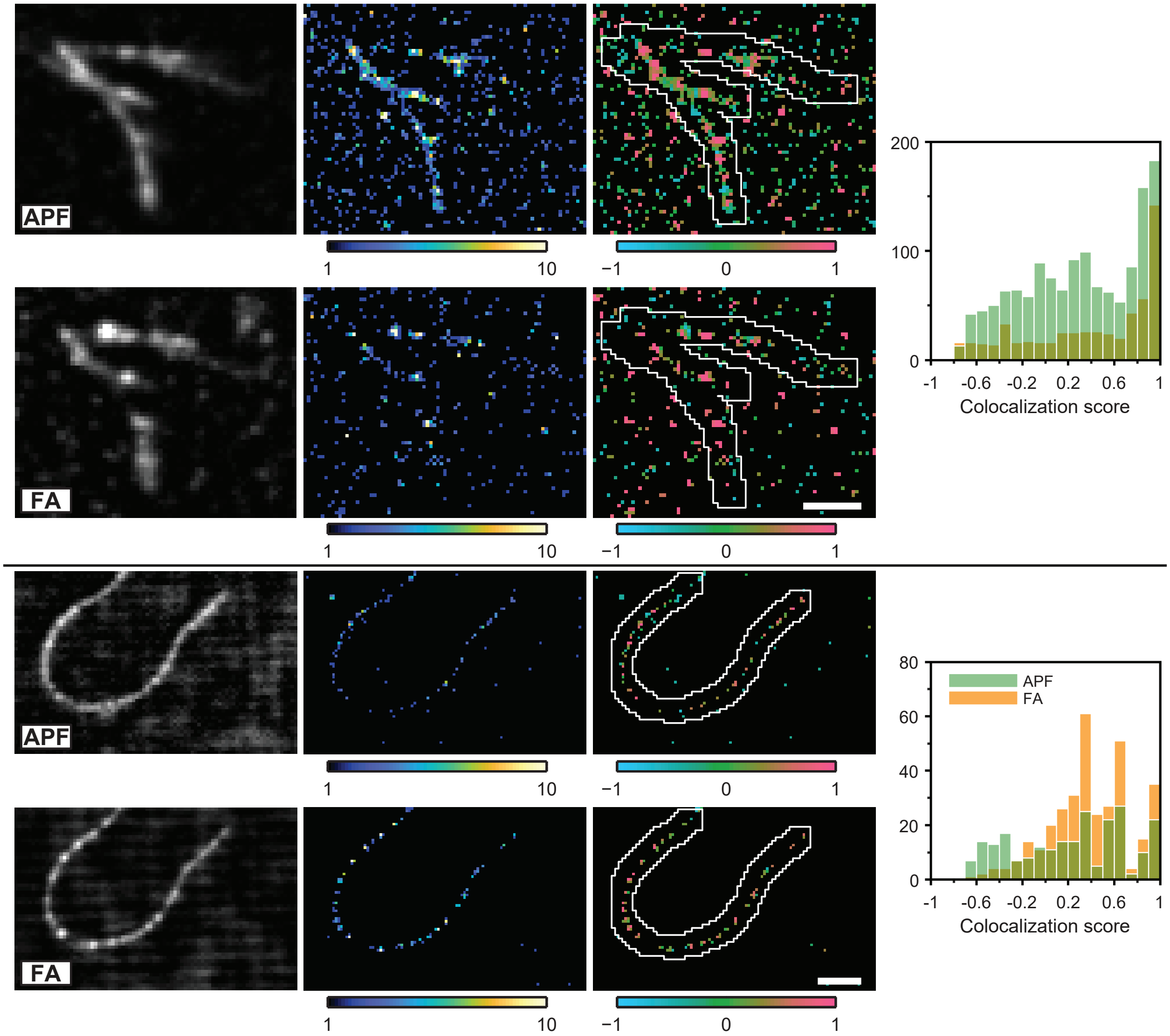

Figure 3.18: Colocalization analysis of PVP-functionalized $W_{18}O_{49}$ nanowires II. Diffraction-limited (left), super-resolution (middle left) and coordinate-based colocalization (CBC) images (middle right), and counts of CBC scores (far right) of two nanowires using APF and furfuryl alcohol (FA) as probe molecules. Color scales of super-resolution images: bursts per bin. Color scales of CBC images: median of the CBC score in each bin ranging from -1 for anti-correlated to +1 for perfectly-correlated burst distributions. White lines depict boundaries of the nanowire regions. Scale bars: 2 μm. Reprinted with permission from Ref. [140].

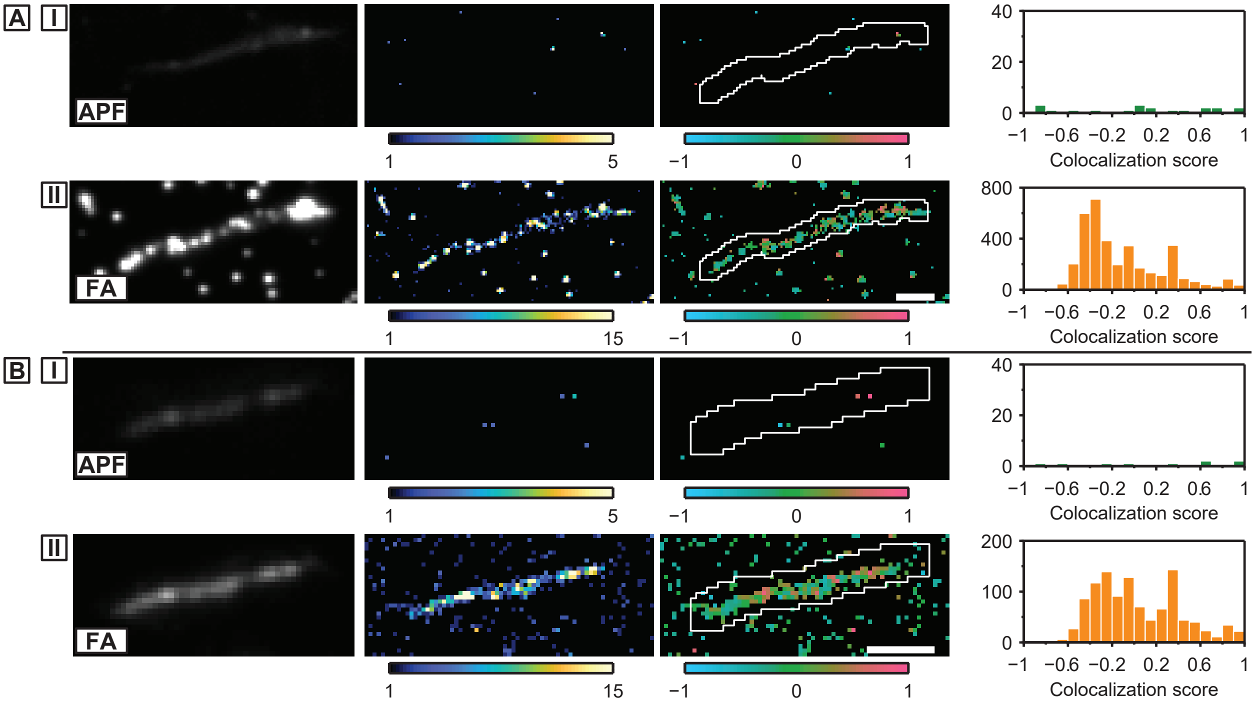

Figure 3.19: Colocalization analysis of oxidized $W_{18}O_{49}$ nanowires that were functionalized with PVP. Diffraction-limited (left), super-resolution (middle left) and coordinate-based colocalization (CBC) images (middle right), and counts of CBC scores (far right) of (A, B) two nanowires using (I) APF and (II) furfuryl alcohol (FA) as probe molecules. While condensation of furfuryl alcohol produces fluorescent bursts on the nanowires as shown in II, only a negligible number of bursts resulting from the transformation of APF can be observed in I. Color scales of super-resolution images: bursts per bin. Color scales of CBC images: median of the CBC score in each bin ranging from -1 for anti-correlated to +1 for perfectly-correlated burst distributions. White lines depict boundaries of the nanowire regions. Scale bars: 2 μm. Reprinted with permission from Ref. [140].

nanowires (Figures 3.20A,B) versus all 40 PVP-functionalized nanowires (Figures 3.20C,D) shows that PVP treatment simultaneously reduces the CBC scores for both species within each nanowire and increases the heterogeneity of CBC scores across nanowires (Figure 3.20E). Specifically, the per-nanowire CBC scores of APF (0.92 ± 0.08, average ± first standard deviation of median CBC score) and furfuryl alcohol (0.89 ± 0.13) for the initial nanowires dramatically reduce to 0.19 ± 0.33 for APF and 0.54 ± 0.37 for furfuryl alcohol for the PVP-functionalized ones (Top and right panels of Figure 3.20E). Moreover, the heterogeneous effects of PVP functionalization are evidenced by the increased variation in CBC scores across nanowires after the treatment. We also attempted colocalization analysis for the oxidized nanowires. The number of fluorescence bursts generated by the oxidized nanowires was reduced for both probe reactions to a level comparable to the background. Interestingly, after functionalizing the oxidized nanowires with PVP, the number of fluorescence bursts for the APF transformation was still low (Figure 3.19i), but the nanowires recovered their activity for furfuryl alcohol condensation (Figure 3.19ii).

Negative CBC scores seen for localizations in the PVP-functionalized nanowires represent mutually exclusive sites for $\cdot$OH radical generation and furfuryl alcohol condensation. The photocatalytic generation of $\cdot$OH radicals at Lewis acid sites is inhibited after treating the nanowires with PVP. This is because PVP inhibits activity by binding to the tungsten ions exposed by oxygen vacancies, thus blocking these sites for the adsorption of H_2O [140]. This type of binding is supported by FT-IR spectroscopy (Figure 3.9A). On the other hand, the binding of PVP to surface hydroxyl groups can suppress their deprotonation such that they become active for the acid-catalyzed condensation of furfuryl alcohol. This mode of binding is also supported by FT-IR spectroscopy and the change in zeta potential after PVP functionalization. Thus, we propose that the regions of the nanowires active for furfuryl alcohol condensation, but not active for $\cdot$OH radical generation, expose Bronsted acid

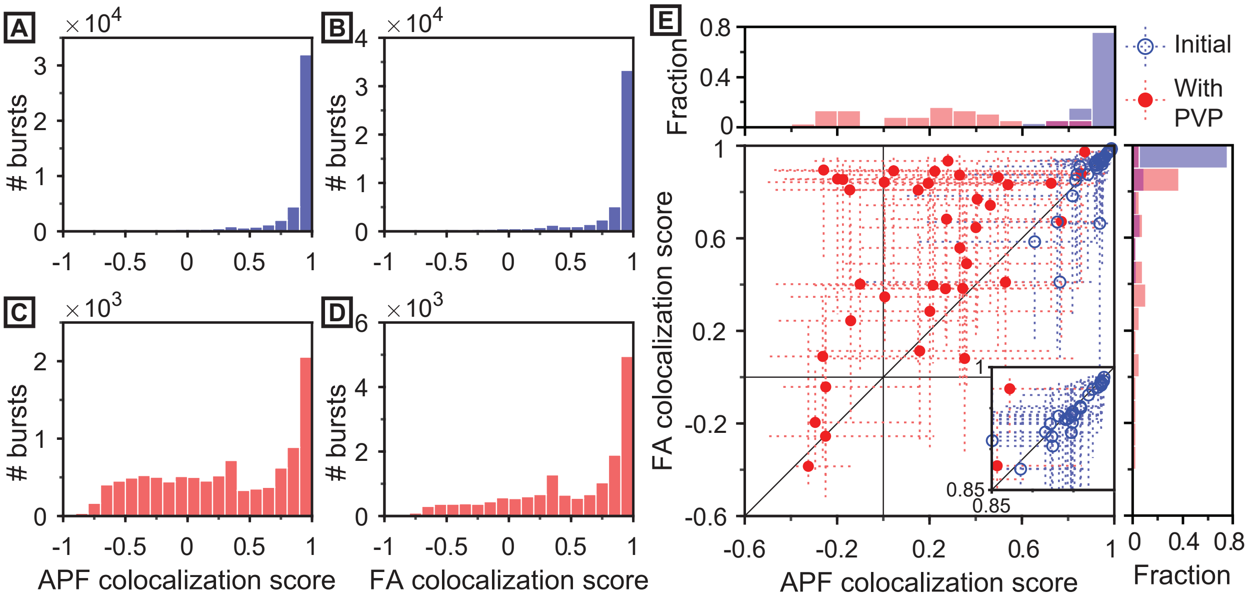

Figure 3.20: APF and furfuryl alcohol colocalization behavior on initial and PVP-functionalized $W_{18}O_{49}$ nanowires. Accumulated (A, C) APF and (B, D) furfuryl alcohol (FA) colocalization scores on 33 initial (blue) and 40 PVP-functionalized (red) nanowires. (E) Per-wire furfuryl alcohol versus APF colocalization scores for 73 initial and PVP-functionalized nanowires. Open and filled circles are the medians of the CBC scores across each nanowire. Dashed lines show CBC score ranges from 25th to 75th percentile of individual nanowires. Median APF (top) and furfuryl alcohol (right) CBC scores for each of the initial (blue) and PVP-functionalized (red) nanowires, where counts are given in fractions of the total population. Reprinted with permission from Ref. [140].

sites. Quantitative colocalization analysis of the two fluorogenic probes reveals this nanowire heterogeneity that cannot be observed at the ensemble level.

3.4 Outlook

In summary, tungsten oxide nanowires show significant spatial variations in their catalytic activity. By spatially correlating the nanoscale regions that trigger two fluorogenic probe molecules, we demonstrate that segments containing clusters of oxygen vacancies are more active for generating hydroxyl radicals. While ensemble measurements can be used to measure average changes in the catalytic activity of a sample after chemical or thermal treatments, through this quantitative colocalization, we demonstrate how new sites become active in a photocatalyst after surface functionalization (i.e., Bronsted acid sites), while others are deactivated (i.e., Lewis acid sites) heterogeneously across nanowires.

In the future, this method may be used to quantify the spatial correlation for other pairs of reactions, such as the locations of electron and hole extraction in nanostructured photoelectrodes [115]. It is also worth to note that this method can be further extended by simultaneously measuring positions and orientations of single probe molecules on catalysts (also see Chapters 4 and 6). Estimation of wobbling areas and mean orientations of individual probe molecules (Section 2.1.2 and Figure 2.2) with respect to local lattice arrangement may elucidate nanoconfinement effects in the photocatalytic activity [47] and provide new insights in design of particle morphologies and surface modification.

Chapter 4

Duo-Spot Point Spread Function for Single-Molecule Localization and Orientation Estimation

Molecular orientations are conventionally inferred from an order parameter determined via X-ray diffraction [220], infrared spectroscopy [221], nuclear magnetic resonance (NMR) [222], Raman spectroscopy [223], sum frequency generation spectroscopy [224], and fluorescence microscopy [225]. However, the order parameter is typically an ensemble average and cannot unambiguously determine 3D orientation of a single molecule within molecular assemblies [226]. Since molecular organizations in biological systems and nanomaterials are intrinsically heterogeneous and also involve complex interactions, tracking individual molecules' 3D positions and orientations is critical for understanding nanoscale morphology of supramolecular structures and functions of chemical composition.

Generally, the orientation and motion of any fluorescent probe used in fluorescence microscopy are influenced by intermolecular forces from surrounding molecules; these interactions can be strengthened by exploiting specific dye-binding modes [32] or bifunctional linkages [227,228]. Therefore, simultaneous measurements of SM locations, orientations and rotational diffusions, termed single-molecule orientation localization microscopy (SMOLM), provides a powerful measurement tool for sensing molecular interactions using any SMLM-compatible fluorescent dye.

Several technologies can estimate SM orientation with varying degrees of sensitivity and resolution. For instance, one can extract SM orientation and rotational diffusion (or simply "wobble", also see Section 2.1.2) by varying the polarization of excitation light [46, 229,230], splitting detected photons into multiple polarization channels and calculating the ratio of them [231,232], and defocusing and matching image patterns [233,234]. One can also increase the orientation sensitivity of an imaging system by implementing engineered PSFs (Section 1.5.3) [97,141]. The Lew Lab has also designed the Tri-spot PSF [97] to redistribute the photons from a single molecule into three spots per orthogonally polarized imaging channel. This system provides accurate and precise measurements of orientation and wobbling without angular degeneracy. However, this splitting of photons hampers SM detection for low signal-to-background ratios (SBRs).

In this chapter, therefore, I detail the design of a new orientation-sensitive PSF, called the Duo-spot PSF. I show that the Duo-spot PSF redistributes photons into two spots per orthogonally polarized channel for sensitive orientation measurements of dim molecules oriented out of the xy in-plane. The Cramér-Rao bound (CRB) calculation and Monte Carlo simulations indicate that the Duo-spot PSF exhibits high estimation precision. Finally, SMOLM with the Duo-spot PSF is demonstrated by resolving nanodomains of lipid membranes and monitoring *in-situ* lipid compositional changes induced by an enzyme[7].

---

[7] The work presented here was published in Ref. [235]. I am a supporting author of this work led by Dr. Jin Lu in the Lew Lab. I have designed and characterized the Duo-spot PSF, and partially contributed to implementation of estimation algorithms and data analysis.

4.1 Design

A single fluorescent molecule can be modeled as a dipole-like emitter wobbling within a cone [29, 87] (also see Sections 1.2 and 2.1.2). An orientational unit vector $\boldsymbol{\mu} = [\mu_x, \mu_y, \mu_z]^{\mathrm{T}}$ $= [\sin(\theta)\cos(\phi), \sin(\theta)\sin(\phi), \cos(\theta)]^{\mathrm{T}}$ and solid angle Ω define the center orientation and the wobbling area of the cone, respectively (Figure 2.2). Assuming that a molecule's rotational correlation time is faster than its exited state lifetime and the camera acquisition time, its orientation state can be fully characterized by a second-moment vector $\boldsymbol{m} = [\langle \mu_x^2 \rangle, \langle \mu_y^2 \rangle, \langle \mu_z^2 \rangle, \langle \mu_x \mu_y \rangle, \langle \mu_x \mu_z \rangle, \langle \mu_y \mu_z \rangle]^{\mathrm{T}}$, where each component is a time-averaged second moment of $\boldsymbol{\mu}$ within a single camera acquisition period [137]. A fluorescence microscope image $\boldsymbol{I}^{x,y} \in \mathbb{R}^n$ of such an emitter captured by an n-pixel camera can be modeled as a linear superposition of six basis images weighted by $\boldsymbol{m}$ as follows:

$$\boldsymbol{I}^{x,y} = s\boldsymbol{B}^{x,y}\boldsymbol{m} + b = s\begin{bmatrix} \boldsymbol{B}_{xx}^{x,y} & \boldsymbol{B}_{yy}^{x,y} & \boldsymbol{B}_{zz}^{x,y} & \boldsymbol{B}_{xy}^{x,y} & \boldsymbol{B}_{xz}^{x,y} & \boldsymbol{B}_{yz}^{x,y} \end{bmatrix}\boldsymbol{m} + b, \tag{4.1}$$

where s is the number of photons detected from the molecule and b is the number of background photons in each pixel. The superscripts x and y represent two orthogonally polarized detection channels separated by a polarization beam splitter (PBS, Figure 2.4). Each so-called basis image in x- and y-polarized detection channel $\boldsymbol{B}_k^{x,y} \in \mathbb{R}^{n\times 1}$ ($k \in \{xx, yy, zz, xy, xz, yz\}$) corresponds to the response of the optical system to each orientational second-moment component m_k and can be calculated by vectorial diffraction theory [85, 86, 137] (Section 2.1.1).

The Duo-spot PSF was designed to distinguish the $\boldsymbol{B}_{zz}^{y}$ basis image from $\boldsymbol{B}_{yy}^{y}$ in the y-polarized channel (or equivalently the $\boldsymbol{B}_{zz}^{x}$ basis image from $\boldsymbol{B}_{xx}^{x}$ in the x-polarized channel) for improved polar angle (θ) estimation in SMOLM. In order to achieve this goal, I

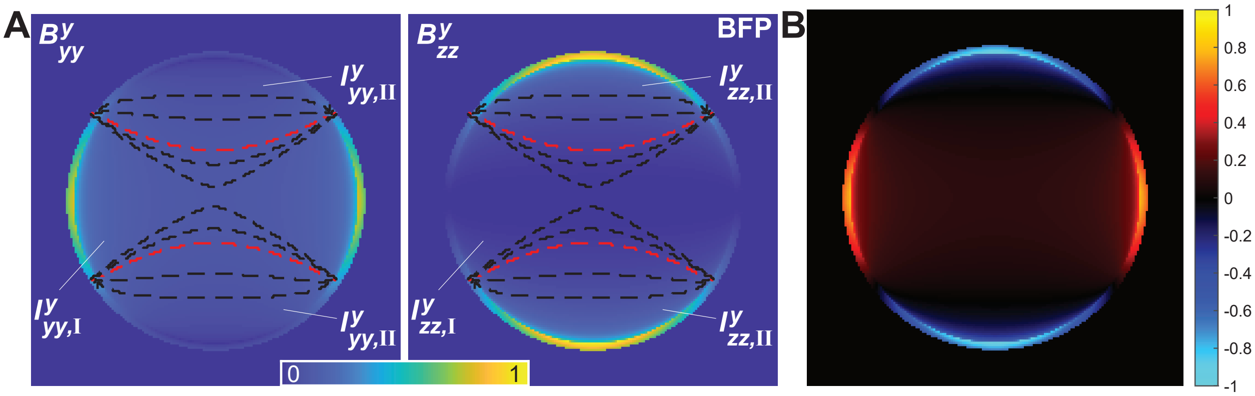

Figure 4.1: Basis images used in the design of the Duo-spot PSF. (A) Basis images at the back focal plane corresponding to orientational second-moment components $\langle\mu_y^2\rangle$ and $\langle\mu_z^2\rangle$ in the y-polarized emission channel. Dashed lines denote boundaries between Regions I and II of the Duo-spot phase mask associated with various condition numbers $\kappa(A)$. The red lines represent optimal partitioning providing the best sensitivity to $\langle\mu_y^2\rangle$ and $\langle\mu_z^2\rangle$ in the y-polarized channel. The vectorial diffraction calculations assume an emitter is located at a glass-water refractive index interface (Section 2.1.1) for mimicking SM imaging conditions in biological systems. Color bar: normalized intensity. (B) The combined basis function $\boldsymbol{B}^y_{\mathrm{comb}} = \boldsymbol{B}^y_{yy} - \boldsymbol{B}^y_{zz}$ used for finding the optimized Duo-spot boundary. Adapted and reprinted with permission from Ref. [235].

characterized the intensity distributions of the $\boldsymbol{B}^y_{yy}$ and $\boldsymbol{B}^y_{zz}$ images at the back focal plane (BFP) in the y channel (Figure 4.1A, the $\boldsymbol{B}^x_{xx}$ and $\boldsymbol{B}^x_{zz}$ basis images in x-polarized channel are similar but rotated by 90°). For achieving high estimation sensitivity to $\langle\mu_y^2\rangle$ and $\langle\mu_z^2\rangle$ in the y channel, the Duo-spot phase mask splits the BFP into two regions and separates photons distributed within Region I from the rest of photons in Region II by applying opposite phase ramps in the BFP. Note that a phase ramp at the Fourier plane corresponds to lateral displacement of intensity in the image plane. If an imaging system can perfectly separate the photons in the two regions and propagate them onto different regions of the image plane, the distributed intensity in the image plane $\boldsymbol{I}^y_{\mathrm{img}}$ is written as

$$\boldsymbol{I}^y_{\mathrm{img}} = \boldsymbol{A}\begin{bmatrix}\langle\mu_y^2\rangle \\ \langle\mu_z^2\rangle\end{bmatrix} \quad \text{and} \tag{4.2}$$

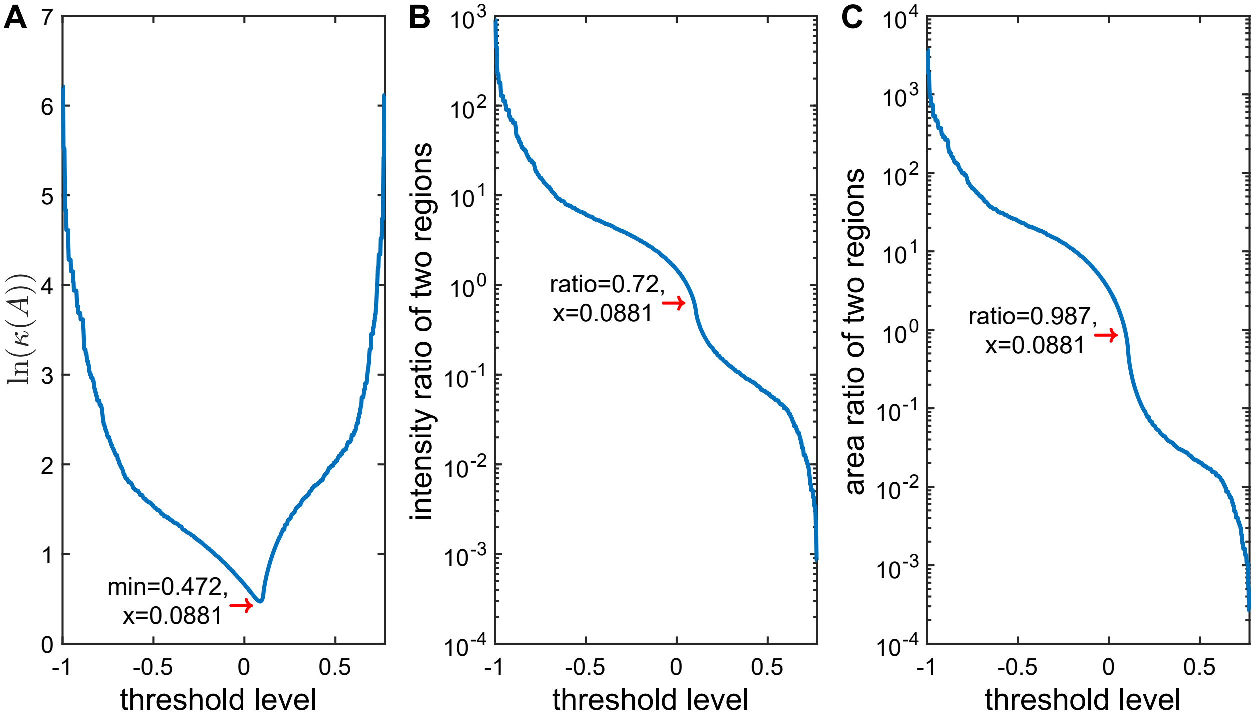

Figure 4.2: (A) Imaging system degeneracy for estimating $\langle\mu_y^2\rangle$ and $\langle\mu_z^2\rangle$ second moments with various BFP partitioning defined by threshold values χ, and corresponding (B) intensity $I^y_{\text{iso,ratio}}$ and (C) area S_{ratio} ratios of Regions I to II. Red arrows indicate the lowest degeneracy at $\chi = 0.0881$ and its associated intensity and area ratios. The BFP partitioning defined by this threshold level generates the region boundary depicted by the red lines in Figure 4.1A.

$$\boldsymbol{A} = \begin{bmatrix} I^y_{yy,\text{I}} & I^y_{zz,\text{I}} \\ I^y_{yy,\text{II}} & I^y_{zz,\text{II}} \end{bmatrix}, \tag{4.3}$$

where $I^y_{yy,\text{I}}$, $I^y_{zz,\text{I}}$, $I^y_{yy,\text{II}}$ and $I^y_{zz,\text{II}}$ represent total intensities within Region I and II of the $\boldsymbol{B}^y_{yy}$ and $\boldsymbol{B}^y_{zz}$ bases, respectively (Figure 4.1A). The sensitivity of the imaging system for estimating the two second moments can be represented as how robust the system (or the solution of the system) is against noise or perturbation to $\boldsymbol{I}^y_{\text{img}}$. The condition number κ of $\boldsymbol{A}$ defines the upper bound of error in the solution of Eq. 4.2, given by

$$\kappa(\boldsymbol{A}) = \|\boldsymbol{A}\|_2 \|\boldsymbol{A}^{-1}\|_2 = \frac{|\lambda_2|}{|\lambda_1|} \quad \text{and} \tag{4.4}$$

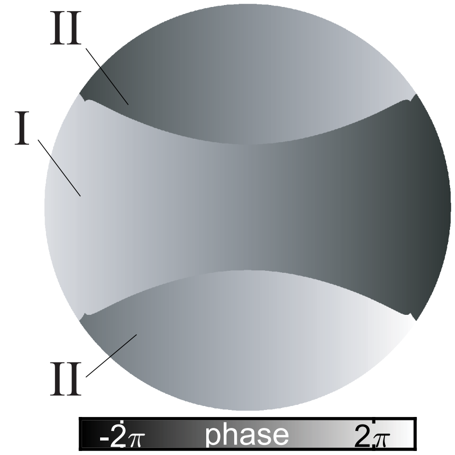

Figure 4.3: Duo-spot phase mask. Opposite phase ramps are applied to Region I and Region II with the boundary minimizing the condition number $\kappa(A)$. Color bar: phase (rad). Adapted and reprinted with permission from Ref. [235].

where λ_1 and λ_2 are the eigenvalues of $\boldsymbol{A}$ ($|\lambda_1| \leq |\lambda_2|$). A smaller condition number means high stability of the system against noise [236], and the condition number $\kappa(\boldsymbol{A})$ can also be understood as degeneracy of the system to the second moments.

To find a boundary separating Regions I and II that maximizes the PSF sensitivity for estimating the second moments, a combined basis function $\boldsymbol{B}^y_{\text{comb}}$ is defined as (Figure 4.1B)

$$\boldsymbol{B}^y_{\text{comb}} = \boldsymbol{B}^y_{yy} - \boldsymbol{B}^y_{zz}, \tag{4.5}$$

and the two regions are separated as

$$\boldsymbol{I}^y_{k,\text{I}} = \boldsymbol{B}^y_{\text{comb}} \geq \chi \quad \text{and} \tag{4.6}$$

$$\boldsymbol{I}^y_{k,\text{II}} = \boldsymbol{B}^y_{\text{comb}} < \chi, \tag{4.7}$$

where $k \in \{yy, zz\}$ and χ is a threshold level defining a boundary ($-1 \leq \chi \leq 1$). Figure 4.2A shows changes of the log of condition number $\ln(\kappa(A))$ with the threshold level χ. The boundary depicted by the red lines in Figure 4.1A defined by a threshold level ($\chi = 0.0881$) gives the lowest degeneracy of the system to the second moments. If this partitioning is applied to the intensity distribution of an isotropic emitter at the BFP (Figure 1.9C), the ratio of the total intensity within Region I to that of Region II is $I^{y}_{\text{iso,ratio}} = 0.72$ (Figure 4.2B). Similarly, the area ratio between the two regions is $S_{\text{ratio}} = 0.987$ (Figure 4.2C). The final Duo-spot phase mask with the partitioning and opposite phase ramps is shown in Figure 4.3[8]. The same direction but π-shifted phase ramp is applied to the bottom half of Region II compared to the top half of Region II for generating a well-focused $\boldsymbol{B}_{zz}$ in the image plane (Figure 4.4A). Note that the same phase mask but 90° rotated is applied to the BFP in the x-polarized channel by a practical polarization-sensitive imaging system (Figure 2.4). Due to the symmetry, the same phase mask produces a PSF exhibiting high sensitivity for estimating $\langle \mu_x^2 \rangle$ and $\langle \mu_z^2 \rangle$ in the x channel.

Although the Duo-spot PSF shows two bright spots in response to an isotropic emitter or a dipole emitter with wobble $\Omega = 2\pi$ sr (Figure 4.4), the brightness ratio between the two spots in each channel changes sensitively in response to the polar angle θ (Figure 4.5A-D) for small wobbling areas Ω (e.g., $\Omega = 0.25\pi$ sr). The Duo-spot PSF essentially produces well-focused, approximately single-spot images when molecules exhibit large or small polar angles ($\theta \approx 0°$ or $\theta \approx 90°$) and allows such molecules to be detected efficiently under low signal-to-background ratio (SBR) conditions compared to the Tri-spot PSF [97] (Figure 4.5C-F).

---

[8] Although the BFP separation based on the condition number $\kappa(\boldsymbol{A})$ gives the theoretically best sensitivity of the system (Eq. 4.2) to estimating $\langle \mu_y^2 \rangle$ and $\langle \mu_z^2 \rangle$, one must note that, in a practical imaging system, there is also intensity contribution from the other bases, i.e., $\boldsymbol{B}^{y}_{xx}$, $\boldsymbol{B}^{y}_{xy}$, $\boldsymbol{B}^{y}_{xz}$ and $\boldsymbol{B}^{y}_{yz}$, to $\boldsymbol{I}^{y}_{\text{img}}$ (Figure 4.4A). In addition, a perfect separation of photons in the image plane may not be feasible in a realistic PSF engineering due to phase singularity and discontinuity in the BFP (see intensity ripples around the main lobes in Figure 4.4).

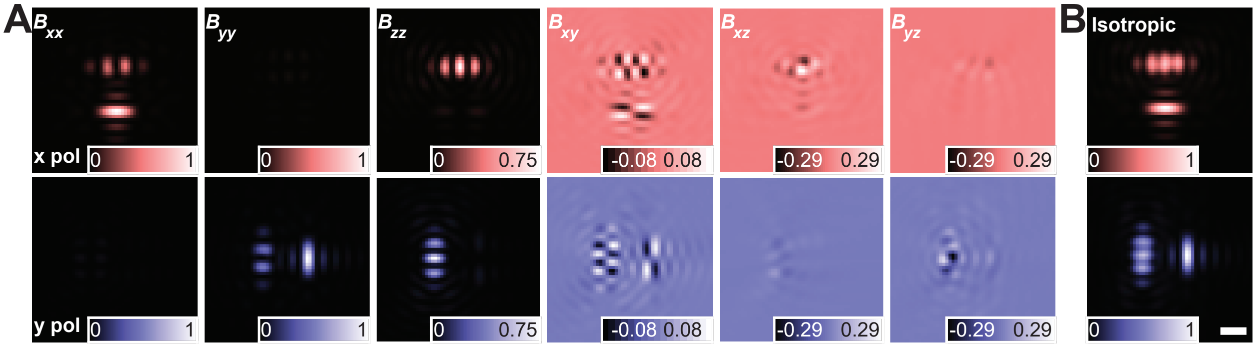

Figure 4.4: Duo-spot basis functions and PSF. (A) Duo-spot basis images corresponding to orientational second moment components $\langle\mu_x^2\rangle$, $\langle\mu_y^2\rangle$, $\langle\mu_z^2\rangle$, $\langle\mu_x\mu_y\rangle$, $\langle\mu_x\mu_z\rangle$, and $\langle\mu_y\mu_z\rangle$ in the x and y-polarized emission channels. (B) Simulated Duo-spot PSF for an isotropic emitter. Scale bar: 500 nm. Adapted and reprinted with permission from Ref. [235].

4.2 Estimation Precision and Accuracy of Duo-Spot PSF in SMOLM

To quantitatively verify its orientation estimation capabilities, I calculated the square root of the Cramér-Rao bound (CRB) of the Duo-spot PSF first. The CRB, which is the diagonal element of the inverse of a Fisher information (FI) matrix, gives a lower bound on the standard deviation (or estimation precision) of an estimator that recovers the true value of a parameter on average. The CRB is widely used as a benchmark in evaluating the precision of imaging systems [76, 238]. Since FI matrix, $\mathbf{FIM} \in \mathbb{R}^{6\times 6}$, of a set of six basis images can be expressed as Eq. 2.23 in Section 2.5.4, the CRB of each second moment is given by

$$\sigma_j^{\text{CRB}} = \sqrt{[\mathbf{FIM}^{-1}]_{jj}}, \tag{4.8}$$

where the subscript jj denotes the jth diagonal element. Here, the geometric mean of the CRB of the orientational second moments, i.e., $\text{GM}_{\text{3D}}^{\text{CRB}} = \sqrt[6]{\prod_j^6 \sigma_j^{\text{CRB}}}$, is calculated

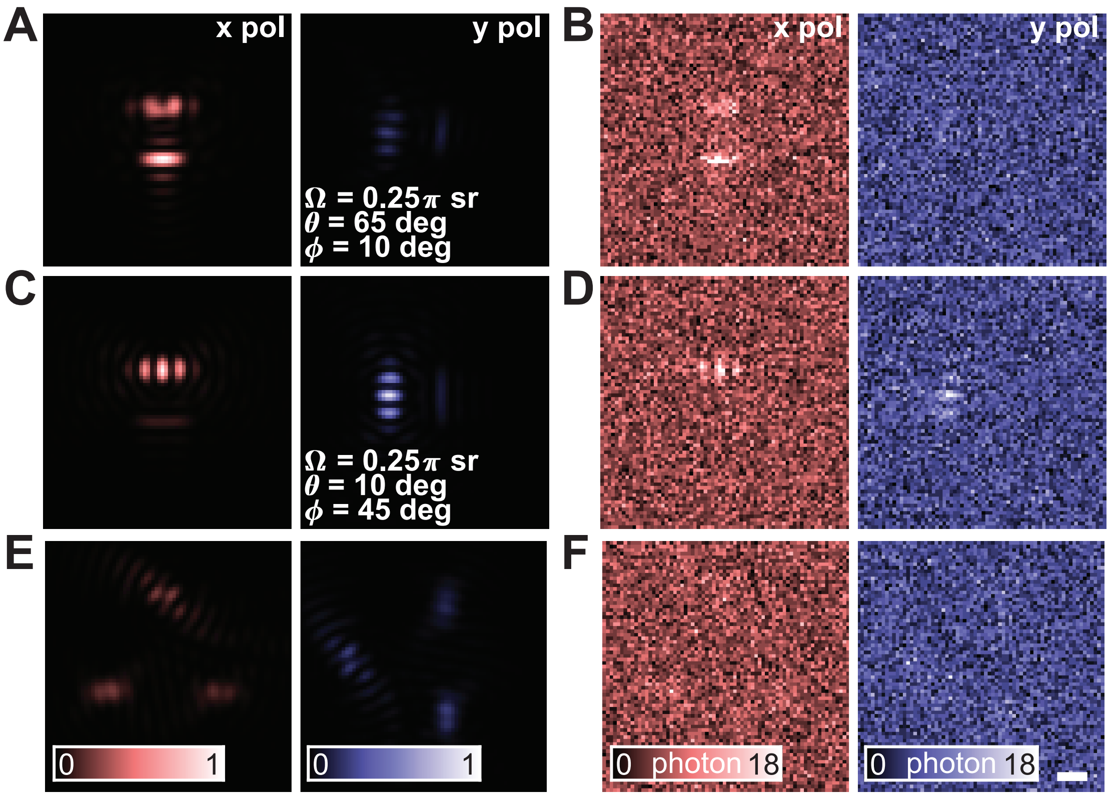

Figure 4.5: (A-D) Simulated Duo-spot PSF for a molecule (A,B) oriented at θ =65°, ϕ =10° and wobbling within Ω =0.25π sr, and a molecule (C,D) oriented at θ =10°, ϕ =45° and wobbling within Ω =0.25π sr (A,C) without and (B,D) with Poisson shot noise and background (brightness of 950 photons and background of 5 photons/pixel). (E,F) Simulated Tri-spot PSF to a molecule with the same orientation as C,D. Color bars: normalized intensity in A,C,E and brightness (photon) in B,D,F. Scale bar: 500 nm in A-F. Reprinted with permission from Ref. [235].

as a summary measure of performance of five orientation-sensing PSFs, namely the polarized standard, bisected [96], Tri-spot [97], quadrated [98] (Figure 2.5), and Duo-spot, for a molecule emitting at a glass-water interface (also see PSF performance comparison with a different SBR discussed in Section 6.1). The CRB of an imaging system is a metric measuring local precision bounds at certain imaging conditions, thus varying dramatically depending on the ground truth orientations. In order to fairly compare different PSFs, SM dipoles

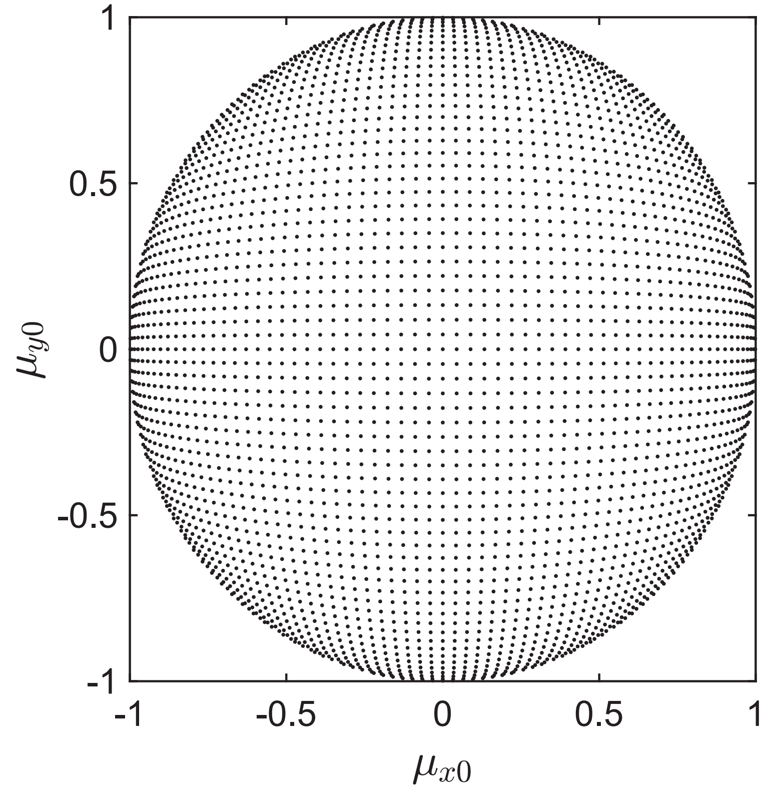

Figure 4.6: Orientation sampling over a hemisphere. The ground truth SM orientations are sampled uniformly over a hemisphere [237] for fairly evaluating CRB at various orientation situations. The subscript “0” represents the ground truth sample property considered in synthetic data.

with various orientations and wobbling areas are considered in this dissertation. SM orientations are uniformly sampled over a hemisphere (Figure 4.6) [237] for 25 different wobbling areas that are also uniformly sampled in $[0, 2\pi]$. Figure 4.7 shows the arithmetic mean of $\mathrm{GM}_{\mathrm{3D}}^{\mathrm{CRB}}$ over all of orientation space (79,325 combinations of orientations and wobbling in total). The Duo-spot PSF shows superior measurement performance, that is smaller CRB, for estimating the 3D second moments over other approaches with relatively dim molecules (Figure 4.7A). In addition, the Duo-spot PSF provides comparable estimation precision to the Tri-spot PSF for estimating orientations of brighter emitters at the glass-water interface. Notably, the Duo-spot PSF constantly exhibits better orientation sensitivity, regardless of

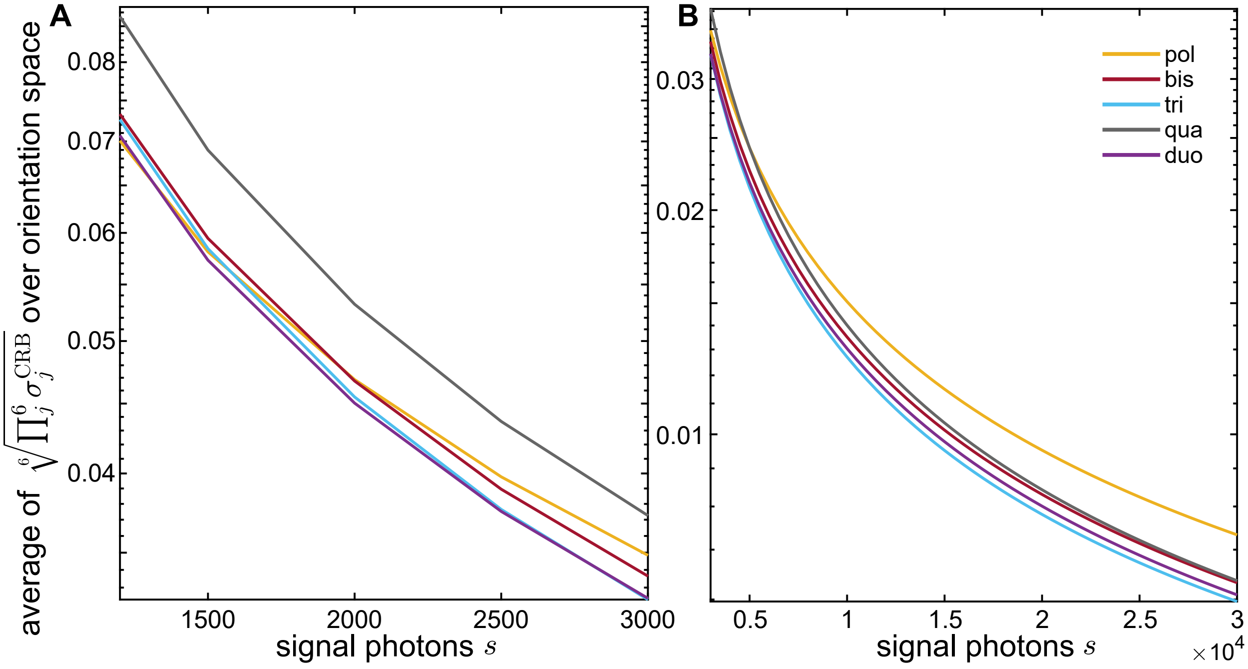

Figure 4.7: The Cramér-Rao bound (CRB) of estimation of orientational second moments using various point spread functions (PSFs). Average (arithmetic mean) of $\mathrm{GM}_{3\mathrm{D}}^{\mathrm{CRB}} = \sqrt[6]{\prod_j^6 \sigma_j^{\mathrm{CRB}}}$ over all of orientation space with a background of 5 photons/pixel, and brightnesses of (A) 1,200 - 3,000 photons and (B) 3,000 - 30,000 photons detected. Yellow: polarized standard (pol), red: bisected (bis), aqua: Tri-spot (tri), gray: quadrated (qua), and purple: Duo-spot (duo) PSF.

SBR, than the bisected PSF, which is another type of two spot PSF but with a different BFP partition.

The relative brightness of each lobe of the Duo-spot PSF is sensitive to the second moments, which fully characterize a 3D orientation state of a molecule if the molecule's rotational correlation time is faster than its excited state lifetime and the camera integration time [139] (Section 2.1.2). In a practical SMOLM, the physical orientation parameters of a SM emission dipole, the mean orientation (θ, ϕ) and wobble Ω, can be inferred via a two-step estimation method (Section 2.5.4). In the first step, the positions and six orientational second moments of SMs are estimated using using a regularized maximum likelihood estimator [157].

In the second step, the estimated second moments are projected into angular (first-moment) orientation space, thereby obtaining measurements of polar angles θ, azimuthal angles ϕ, and wobbling areas Ω (Figure 2.2) [138, 235].

Next, the measurement precision and bias of θ, ϕ and Ω using the Duo-spot PSF were evaluated by Mote Carlo simulations with the practical estimation algorithm. In this simulation, Duo-spot PSF images of dipoles at various orientations ($\theta_0 = 0° - 90°$, $\phi_0 = 0° - 360°$, $\Omega_0 = 0 - 1.5\pi$ sr) were generated via the vectorial image-formation model [87] (also see Sections 1.5 and 2.1.1). An emission wavelength of 610 nm, NA = 1.4, a spatially uniform background, a detector pixel size 58.5 × 58.5 nm^2 in object space, and a glass-water refractive-index interface were assumed to mimic an experimental conditions showing in the next section. Using the estimation algorithm (Section 2.5.4), the Duo-spot PSF yields good estimation precision ($\sigma_\theta^{\text{mean}} = 8.4°$, $\sigma_\phi^{\text{mean}} = 21.8°$, $\sigma_\Omega^{\text{mean}} = 0.16\pi$ sr) and accuracy ($|\theta - \theta_0|^{\text{mean}} = 3.5°$, $|\phi - \phi_0|^{\text{mean}} = 0.0°$, $|\Omega - \Omega_0|^{\text{mean}} = -0.11\pi$ sr) for measuring the orientation of fluorescent molecules with a brightness of 950 photons and a background of 5 photons/pixel (Figures 4.8 and 4.9, the superscripts indicate arithmetic means over the simulated orientation space). This estimation performance is comparable with that of the Tri-spot PSF with a similar condition [235]. Here, relatively dim molecules were considered since the well-focused spots of the Duo-spot PSF enable such weak emissions to be detected, contributing lower median photons detected in practical experiments.

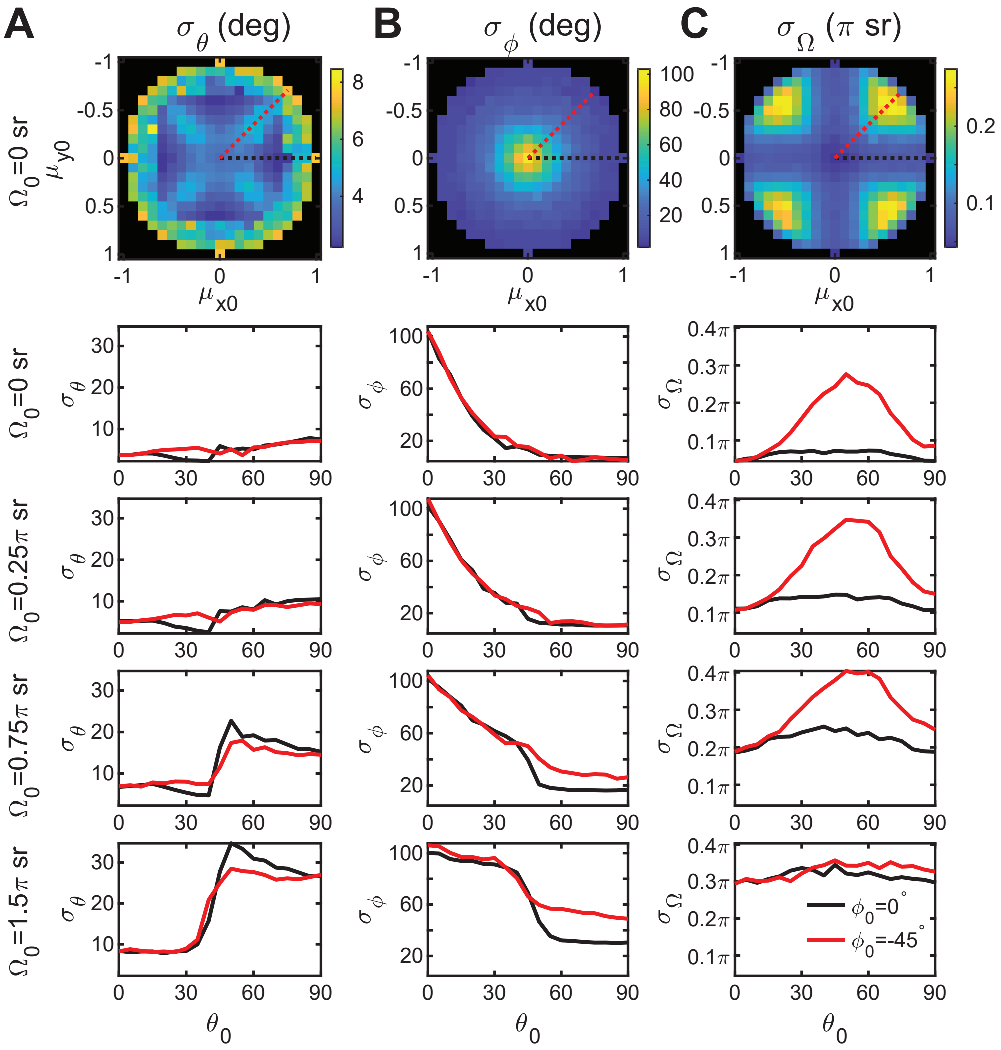

Figure 4.8: Orientation estimation precision for (A) polar angle θ, (B) azimuthal angle ϕ, and (C) solid angle Ω determined from simulated Duo-spot PSF images of dipoles at various orientations ($\theta_0 = 0° - 90°$, $\phi_0 = 0° - 360°$, $\Omega_0 = 0 - 1.5\pi$ sr, $\mu_{x0} = \sin(\theta_0)\cos(\phi_0)$, $\mu_{y0} = \sin(\theta_0)\sin(\phi_0)$). At each orientation, 1,000 independent images were generated with a brightness of 950 photons and a background of 5 photons/pixel. Orientations of simulated molecules were estimated using the maximum-likelihood estimation algorithm, and the orientation estimation precision was computed by taking standard deviation of all estimates at each orientation. Due to symmetry with respect to ϕ_0 as shown in the first row, the estimation precision is only reported at $\phi_0 = 0°$ (black) and $\phi_0 = -45°$ (red) for $\Omega_0 > 0$ sr. Reprinted with permission from Ref. [235].

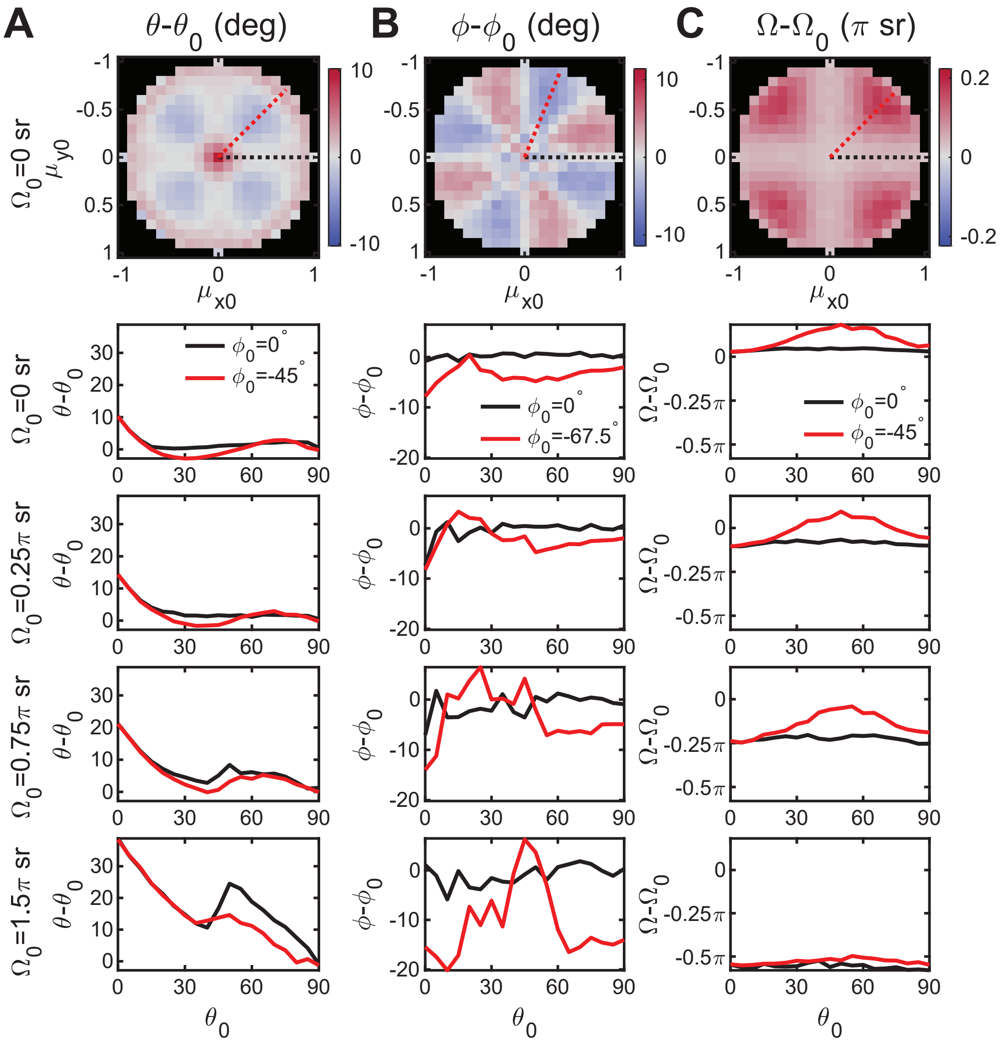

Figure 4.9: Orientation estimation bias for (A) polar angle θ, (B) azimuthal angle ϕ, and (C) solid angle Ω determined from simulated Duo-spot PSF images of dipoles at various orientations ($\theta_0 = 0° - 90°$, $\phi_0 = 0° - 360°$, $\Omega_0 = 0 - 1.5\pi$ sr, $\mu_{x0} = \sin(\theta_0)\cos(\phi_0)$, $\mu_{y0} = \sin(\theta_0)\sin(\phi_0)$). At each orientation, 1,000 independent images were generated with a brightness of 950 photons and a background of 5 photons/pixel. Orientations of simulated molecules were estimated using the maximum-likelihood estimation algorithm, and the orientation estimation bias was computed by averaging all measurement deviations at each orientation. Due to symmetry with respect to ϕ_0 as shown in the first row, the estimation bias is only reported at $\phi_0 = 0°$ (black), $-45°$ (red, for polar and solid angles) or $-67.5°$ (red, for azimuthal angle) for $\Omega_0 > 0$ sr. Reprinted with permission from Ref. [235].

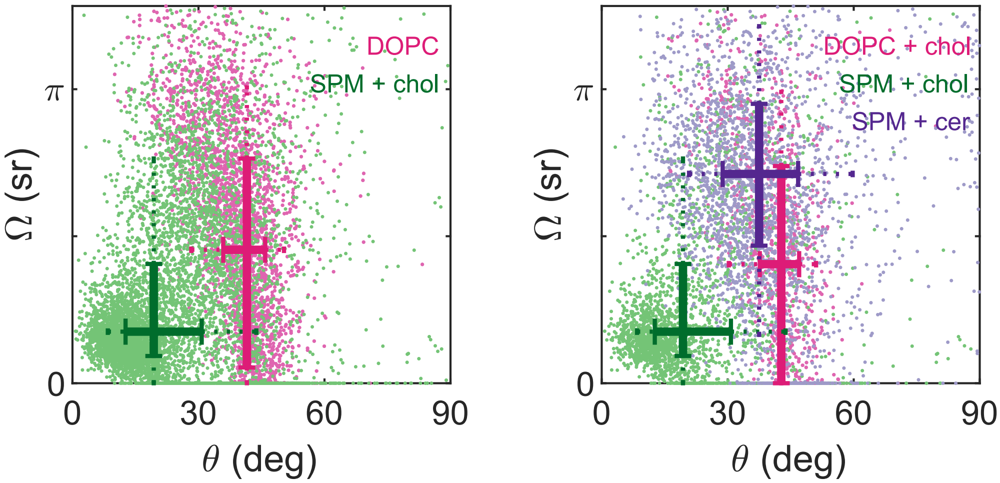

Figure 4.10: Orientation (polar angle θ) and wobble (solid angle Ω) of Nile red in the single-phase SLBs consisting of DOPC, SPM+chol, DOPC+chol, SPM+chol, and SPM+cer, imaged using the Duo-spot PSF. Adapted and reprinted with permission from Ref. [235].

4.3 3D orientation imaging for mapping nanoscale lipid-membrane domains

We next demonstrate SMOLM using the Duo-spot PSF for monitoring *in situ* enzyme-mediated lipid compositional dynamics. In the plasma membrane, the hydrolysis of palmitoyl sphingomyelin (SPM) via sphingomyelinase (SMase) generates a bioactive lipid, ceramide (cer), which selectively displaces cholesterol (chol) from liquid-ordered (Lo) domains at a 1:1 molar ratio [239], promotes lipid phase reorganization, forms a ceramide-rich ordered phase [240], and impacts cellular signaling and other vital processes [241]. Most of these nanoscopic structural details were first observed by atomic force microscopy (AFM) [240], which however is mostly limited to planar and static lipid samples and often requires other supporting imaging tools such as fluorescence microscopy for visualizing lipid dynamics [242, 243].

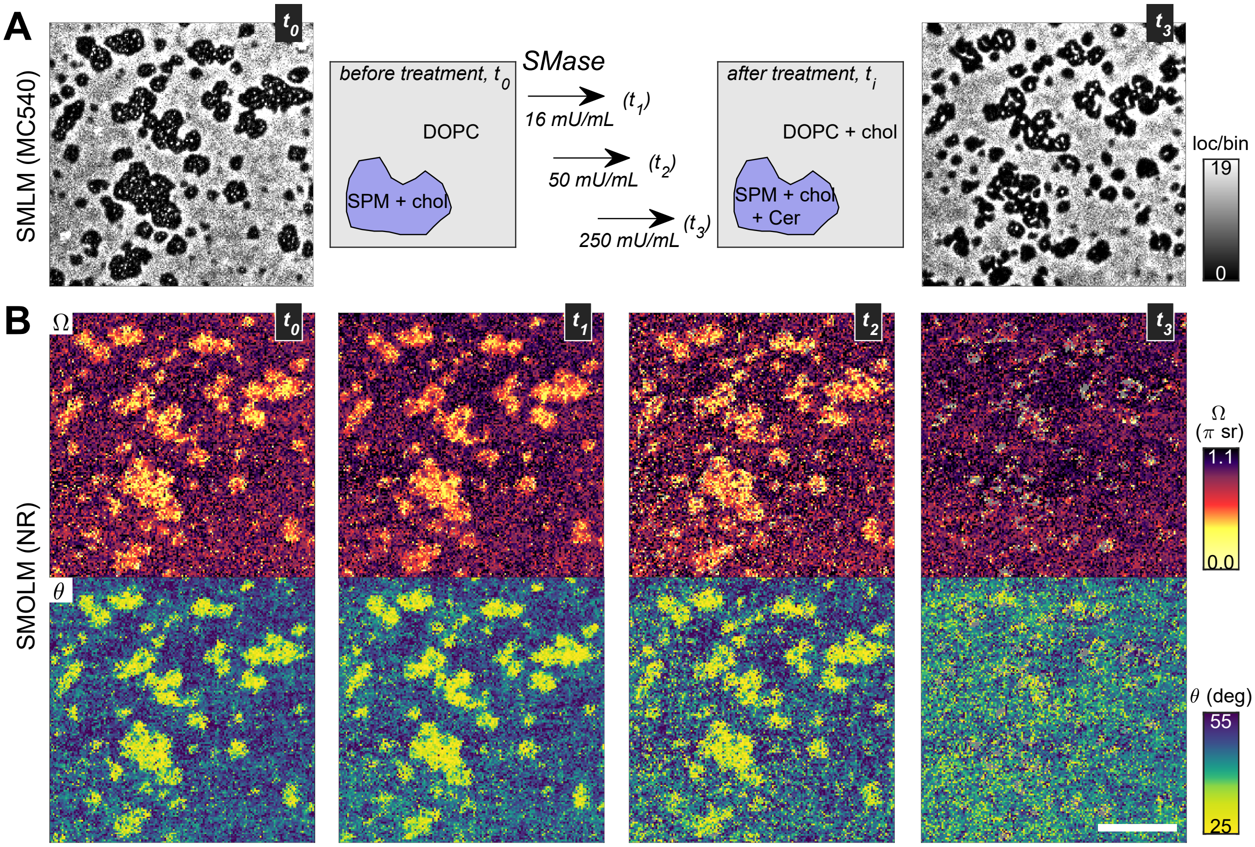
A
SMLM (MC540)
t_0
before treatment, t_0
DOPC
SPM + chol
SMase
16 mU/mL
(t_1)
50 mU/mL
(t_2)
250 mU/mL
(t_3)
after treatment, t_i
DOPC + chol
SPM + chol + Cer
t_3
loc/bin
19
0
B
Ω
t_0
t_1
t_2
t_3
SMOLM (NR)
θ
Ω (π sr)
1.1
0.0
θ (deg)
55
25

Figure 4.11: SMOLM imaging of SMase-induced alterations of lipid composition and domain reorganization in a ternary SLB of DOPC/SPM/chol. (A) Conventional MC540 SMLM image and schematic of a lipid mixture of DOPC/SPM/chol before (t_0) and after (t_3) three treatments of SMase. (B) SMOLM images (solid angle (Ω) and polar angle (θ)) of Nile red before (t_0) and after successive 5 min SMase treatments of 16 mU/mL (t_1), 50 mU/mL (t_2), and 250 mU/mL (t_3). Adapted and reprinted with permission from Ref. [235].

We applied SMOLM to monitor lipid compositional changes in ternary supported lipid bilayers (SLBs) consisting of DOPC[9]/SPM/chol and resolve the spatial redistribution of newly generated cer and displaced chol within individual Lo domains induced by low SMase concentrations, which cannot be fully observed by conventional SMLM imaging (i.e., localization density of single fluorescent molecules over different lipid domains).

---

[9] A type of phosphatidylcholine (1,2-dioleoyl-sn-glycero-3-phosphocholine, di(18:1) PC) in which two phosphatidyl acyl chains are unsaturated. See Supplementary Notes of Ref. [235] for more details about chemicals and SLB preparation as well as experimental setups.

We first confirmed that the orientation estimation of single Nile red (NR) molecules using the Duo-spot PSF has excellent sensitivity for distinguishing chol-rich Lo domains, cer domains and DOPC liquid-disordered (Ld) domains in static single-phase lipid samples (Figure 4.10). This agrees with previous fluorescence polarization observation on giant vesicles that NR molecules exhibit preferentially perpendicular orientations relative to the membrane surface in Lo phases due to constrained lipid packing and no preferential orientation in loosely packed Ld phases [113]. Next, we conducted SMOLM imaging of mixed DOPC/SPM/chol SLBs with successive 5 min SMase treatments of increasing dosage. Low SMase doses were chosen to test SMOLM sensitivity for detecting subtle enzyme activity within Lo domains (SPM+chol, Figure 4.11A, SMLM images at t_0, t_3). The SMOLM maps (Figure 4.11B) indicate a dose-dependent disappearance of chol-rich Lo domains. Before treatment (t_0), the shapes and positions of chol-rich Lo domains (small polar angle, solid angle) imaged by SMOLM match the Lo domains mapped by SMLM. SMase treatment (16 mU/mL) induced insignificant changes in the SMOLM maps (Figure 4.11B, t_1), while more regions within the Lo domains begin to lose their chol-rich signature at a larger dose (50 mU/mL SMase, t_2). After a 250 mU/mL dose, almost all the chol-rich Lo domains disappeared (Figure 4.11B, t_3); however, SMLM only reveals very minor changes in the size and shape of Lo domains (Figure 4.11A, t_3). The changes in the orientation estimation agree well with those of NR within SPM+chol and SPM+cer lipid samples and strongly indicate the generation of cer-rich, chol-poor Lo domains (Figure 4.10) [239]. SMOLM imaging using the Duo-spot PSF reveals spatially heterogeneous nanoscale SMase activity, which cannot be observed by the conventional SMLM imaging alone.

4.4 Outlook

In conclusion, the Duo-spot PSF provides sensitive and practical 3D orientation estimation in SMOLM. The well-focused footprint compared to the Tri-spot and quadrated PSFs, especially when molecules exhibit large or small polar angles, enables efficient detection of dim molecules under low SBR conditions. The narrower spread of the PSF also allows accurate and precise localization and orientation estimation without significant PSF overlap [73–75, 157]. By using the Duo-spot PSF in SMOLM, we demonstrated that individual fluorescent probes in SLBs change their polar angles and wobbling area in response to local lipid environments. This new type of nanoscale imaging spectroscopy revealed heterogeneous lipid compositional dynamics induced by enzyme activity [235].

Fundamentally, for measuring orientation with high sensitivity, the photons from each single emitter must be spread across multiple snapshots or camera pixels. However, this separation or spread of the limited photons lowers the SBR and detectability of molecules. Furthermore, performance of SMOLM analysis algorithms and translational diffusion of molecules coupled with rotational motions may impact perception of the orientation spectra. In the future, new PSFs optimized by phase retrieval [244] or machine learning [245] accompanied with CRB or a global bound [138] as a metric could balance these trade-offs and further improve SMOLM's spatiotemporal resolution for capturing faster biological processes.

Chapter 5

Transient Amyloid Binding (TAB) Microscopy

Amyloid diseases, such as Alzheimer's disease (AD), Parkinson's disease (PD) and type II diabetes are the most prevalent, yet incurable, aging-related diseases. Protein misfolding and amyloid formation underlie their disease progression [121, 246]. The 42-residue amyloid-β peptide (Aβ42) is the main component of extracellular plaques in the brains of AD patients [247,248]. Nanometer-sized aggregation intermediates, oligomers, are the main culprits in amyloid toxicity [122,128,129]. Amyloid aggregation, including the formation of oligomers and the assembly of oligomers into linear fibrillar structures, is dynamic, transitory, and heterogeneous, and its mechanisms are still not fully understood. A new imaging methodology with single-molecule sensitivity and long-term measurement capability is required for quantitatively studying the nanometer-scale inhomogeneities and dynamics of these aggregates.

Conventional fluorescence microscopy is ubiquitous in studies of dynamics in living systems due to the specificity of its molecular tags and its ability on imaging living cells due to its use of non-ionizing radiation. Both aggregation [249–252] and destruction [253, 254] of amyloid assemblies have been observed using fluorescence microscopy. However, the physical resolution barrier, optical diffraction, bounds its resolution to approximately 250 nm given by the Abbe diffraction limit $\lambda/2\text{NA}$ [25]. SMLM techniques, such as (f)PALM [62, 63] and (d)STORM [61, 81], overcome this physical limitation by actively switching densely labeled molecules between bright and dark states to reduce the concentration of emitters within a sample. The states of molecules can be switched by using a variety of mechanisms including photoactivation and chemical-induced photoswitching [15, 22]. A related SMLM technique, called PAINT [36], uses combinations of fluorophore binding and unbinding, diffusion into and out of the imaging plane, and/or spectral shifts upon binding to generate flashes of SM fluorescence. It was first demonstrated for imaging lipid bilayers using Nile red as an imaging probe. Regardless of how molecules are turned on and off, many blinking events are recorded over time, and image-processing algorithms [68] measure the position of each bright molecule with high precision. A super-resolution (SR) image can be reconstructed by collecting the locations of these single fluorophores [23, 24, 255] (see more details in Section 1.4).

SMLM commonly leverages tagging techniques that involve covalent attachment [81, 135, 256, 257] or intrinsic intercalation [258] of a fluorophore to the biomolecule of interest. To produce high-resolution images, biological targets must be densely labeled with fluorescent molecules [259, 260], which can potentially alter the structure of interest. Furthermore, photobleaching of tagged fluorescent molecules limits measurement time and prevents long-term imaging of targets. Recently, following the development of PAINT, binding-activated or transiently binding probes have expanded the scope of SR imaging to functional studies [261–263]. When in the immediate vicinity of their target, these probes either become fluorescent, temporarily bind to the target, or both, thereby creating a “flash” of fluorescence that is used to locate the target of interest. Amyloidophilic dyes such as thioflavin T (ThT), thioflavin S, and Congo Red specifically bind to amyloid structural motifs, cross-β sheets [32, 33]. Their absorbance and fluorescence have been used for close to 100 years in the histological staining of amyloid structures and in resolving aggregation kinetics in vitro [249–254].

In this chapter, I describe and characterize a technique to image amyloid structures on the nanometer scale, called transient amyloid binding (TAB) microscopy/imaging[10]. TAB imaging uses standard amyloid dyes such as ThT, without the need for covalent modification of the amyloid protein or immunostaining. The technique mates SMLM with histological staining techniques and is compatible with epi-fluorescence and TIRF microscopy for monitoring amyloid structures. This chapter also shows the use of Nile red (NR) as a TAB imaging probe and the advantage of TAB imaging for studying dynamics of amyloid structures [264].

5.1 Nanoscale Imaging of Amyloid Aggregates

The fluorescence of ThT increases upon binding to amyloid proteins, transforming dark ThT in solution into its bright state [32, 265]. The molecules emit fluorescence until they photobleach or dissociate from the structure. These transient binding dynamics enabled us to record movies of "blinking" ThT molecules, localize their positions with high precision, and reconstruct the underlying amyloid structure. To demonstrate the concept of TAB imaging, we imaged Aβ42 fibrils adsorbed to an imaging chamber by using an epi-fluorescence microscope with a highly inclined 488-nm excitation laser (Figure 5.1A, also see Figure 2.4 and Table 2.1 in Section 2.2 for detailed imaging setups and a list of optical equipment used in this work). An imaging buffer containing 1–2.5 mm ThT was pipetted into the chamber

---

[10] The work presented here was first published in Ref. [125]. I am a co-first author of this collaboration work with Prof. Jan Bieschke and his student Kevin Spehar. Kevin and I prepared amyloid imaging samples with the help of Yuanzi Sun, George R. Nahass and Dr. Niraja Kedia. We conducted TAB imaging in two pseudo-TIRF microscopes and I have performed the SM data analysis for showing sensitivity and utility of TAB microscopy in the amyloid imaging.

(Section 2.4.2, Table 5.1), and 5,000–10,000 imaging frames were recorded with 20 ms camera exposure. The image sequence (Figure 5.1B) and temporal trace of photons detected (Figure 5.1D) demonstrate the blinking of single ThT molecules. A SMLM image with 20×20 nm^2 bin size (Figure 5.1C) was reconstructed from multiple blinking events by using ThunderSTORM [154] and a custom post-processing algorithm (Figure 5.2, Section 2.5). We found that each blinking event lasted on average 12 ms (Figure 5.3, Section 2.6.1). The measured full-width at half-maximum (FWHM) of the reconstructed Aβ42 fibril over the length of the fibril is 60 ± 10 nm. Typical amyloid fibrils have diameters of 8–12 nm [266]. The measured width of the fibril likely arises from our localization precision [67] of 17 nm (FWHM: 40 nm), corresponding to a median of 296 photons detected per ThT localization and a median of 35 background photons per pixel (Figure 5.3, Table 5.1).

The blinking characteristics of ThT are determined by the binding and photobleaching kinetics of the dye. Binding affinity and specificity can be affected by hydrophobic interactions [267]. Therefore, we varied the NaCl concentration and pH as well as the ThT concentration of the buffer to test their influence on ThT blinking (Figure 5.4). We found that the NaCl concentration (10–500 mm) and pH of the imaging buffer (6.0–8.6) had little effect on the blinking of ThT on Aβ42 fibrils. However, a high NaCl concentration (500 mm) and low pH (6.0) lowered the fluorescence background of unbound ThT in the imaging buffer. This corresponds to less fluorescence signal occurring off the amyloid fibril, thus improving TAB imaging performance. On the other hand, we also found that the blinking rate of ThT, and thus the rate of localizations per time, is approximately proportional to ThT concentration. In the TAB microscopy with ThT as a probe molecule, the ThT concentration was chosen to maximize the localization rate of ThT binding events while avoiding too much fluorescence background. These results demonstrate that TAB imaging of amyloid structures

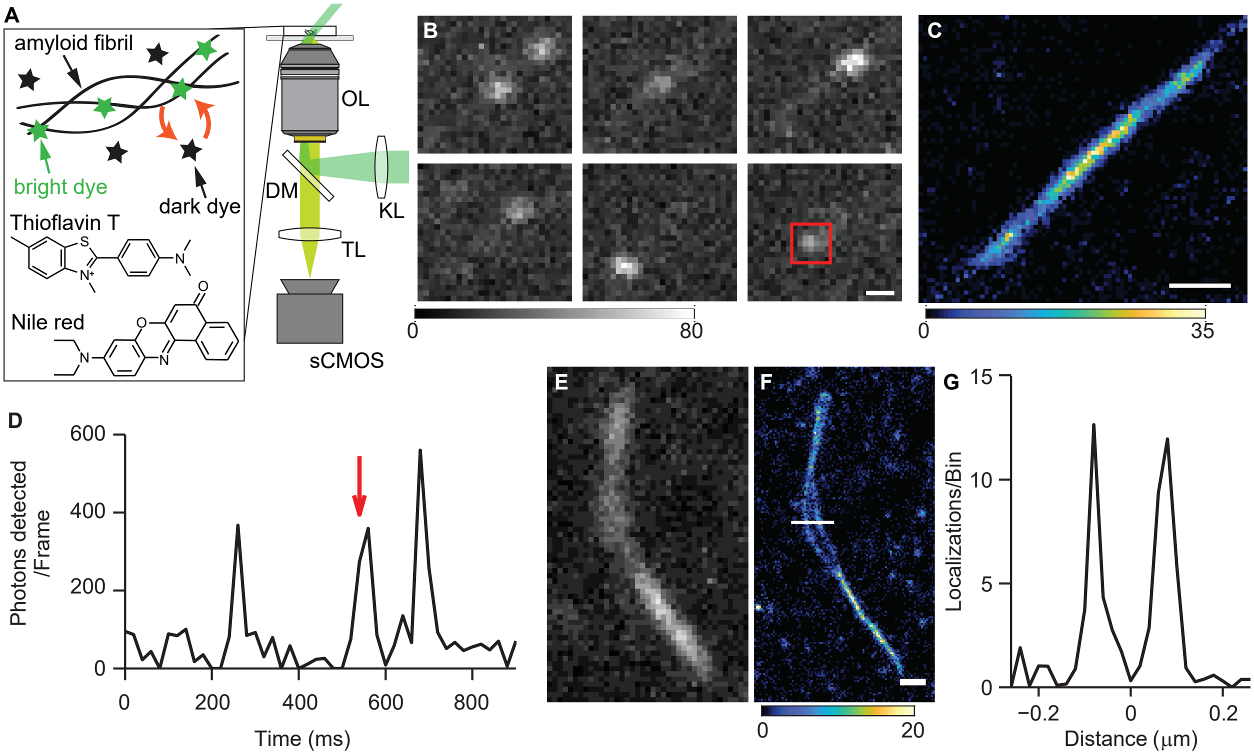

Figure 5.1: Transient amyloid bindging (TAB) microscopy. (A) Pseudo-TIRF illumination excites fluorophores within the sample, and collected fluorescence is imaged onto a camera. KL: widefield lens, OL: objective lens, DM: dichroic mirror, TL: tube lens. Inset: transient binding, fluorescence activation, and unbinding of TAB probe molecules and the chemical structures of thioflavin T (ThT) and Nile red (NR). (B) ThT blinking on an Aβ42 fibril. Gray scale: photons per pixel. (C) ThT TAB SMLM image of the Aβ42 fibril. Color scale: localizations per bin. (D) Integrated photons detected over time within the red square in B. The red arrow indicates the frame containing the square in B. (E) Diffraction-limited image using NR of another fibril field of view. (F) NR TAB SMLM image of the fibril in E. Color scale: photons per pixel. (G) Cross-section of the white line across the fibril in F. Scale bar: 300 nm. Adapted and reprinted with permission from Ref. [125, 264].

Table 5.1: Representative experimental conditions and photon statistics of SMLM on Aβ42

	Figure 5.1 BD	 5.1 F	 5.5 C	 5.5 D[1]	 5.5 F	 5.11 Pre-EGCG	 5.11 46 h	 5.13 2 h	 5.13 21 h
Imaging buffer									
Fluorophore	ThT	NR	ThT	Alexa647	ThT	ThT	ThT	NR	NR
TAB probe concentration (μM)	1	0.05	1	-	1	2.5	2.5	0.5	0.5
pH	8.6	7.4	8.6	8.3	8.3	7.4	7.4	7.4	7.4
NaCl (mM)	500	150	500	-	-	150	150	150	150
Na_3PO_4 (mM)	20	50	20	-	-	20	20	50	50
GLOX+MEA[2]	-	-	-	+	+	-	-	-	-
Statistics									
Photons detected /localization[3]	296	336	425	3718	675	424	370	251	265
Background photons/pixel[3]	35	6	54	71	63	47	36	21	15
Localization precision (nm)[3]	17	9	19	6	15	16	17	23	17

[1] See Section 2.3.2 for dSTORM preparation.

[2] Enzymatic oxygen scavenger (GLOX, glucose oxidase with catalase) and thiol buffer (MEA, β-mercaptoethylamine) [156] consists of two solutions. Solution A: Tris (50 mM, pH 8.3), NaCl (10 mM), glucose (10% w/v), and MEA (Sigma-Aldrich, 30070, 10 mM). Solution B: glucose oxidase (Sigma-Aldrich, G2133, 8 mg), and catalase (Sigma-Aldrich, C100, 38 μL, 21 mg/mL) in PBS (160 μL). The solutions A and B were mixed at the ratio of 99:1 (v/v) immediately before use. + or - refers to the presence or absence of the oxygen scavenger and thiol buffer.

[3] Median of each statistic.

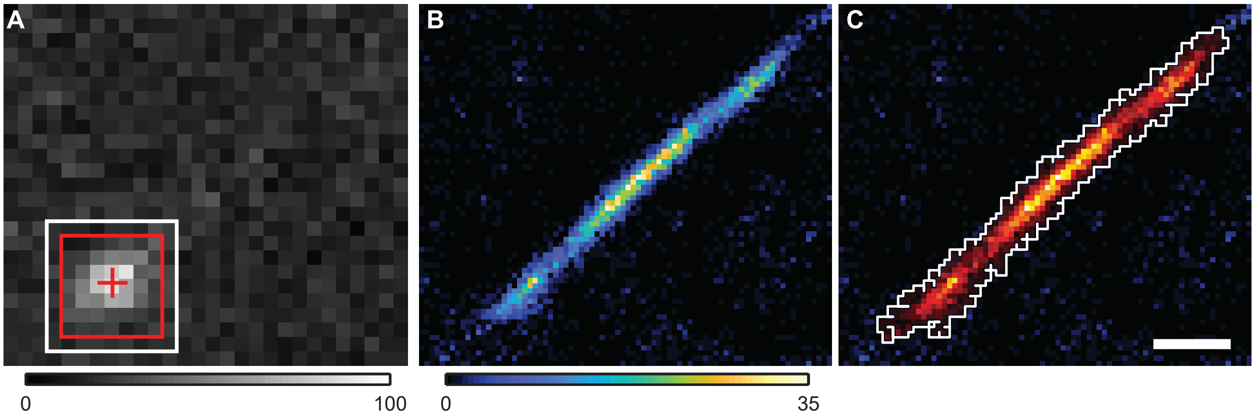

Figure 5.2: Localization of individual ThT on amyloid aggregates and region of interest selection. (A) A captured ThT blinking event on an Aβ42 fibril. Gray scale denotes the number of photons detected per pixel. Detected photons per localization were calculated by integrating all photons within a region of interest (red square) centered at the location output by ThunderSTORM (red cross). The integrated photon number was then background corrected using the average photons within the surrounding pixels between the red and white squares. (B) ThT TAB super-resolution image of the Aβ42 fibril after the filtering and the two channel registration process described in Section 2.5. The color scale denotes the number of localizations per bin. (C) Region of interest (ROI) selection (Section 2.6.2). The hot color scale shows the region of interest associated with the fibril, while the white line depicts the boundary of this ROI. Scale bar: 300 nm. This data corresponds to the fibril shown in Figure 5.1B-D. Adapted and reprinted with permission from Ref. [125].

is amenable to a wide variety of buffer conditions. The TAB imaging relies onto the fluorescence increase and the transient binding dynamics of individual probe molecules on amyloid aggregates. Hence, unlike SR methods that employ photoswitching of organic dyes [81], TAB does not require the addition of specific reducing agents or oxygen scavengers [135] to the buffer (Table 5.1).

In addition to ThT, we also used NR as a TAB probe [264]. The binding affinity of NR to amyloid structures has been used to map the hydrophobicity of amyloid structures [118]. An improved signal-to-background ratio (336 median photons per NR localization and 6 median background photons per pixel) allows TAB to achieve 9 nm localization precision, leading to ∼30 nm amyloid fibril resolution (Figures 5.1F and G, also see Figure 6.14 and

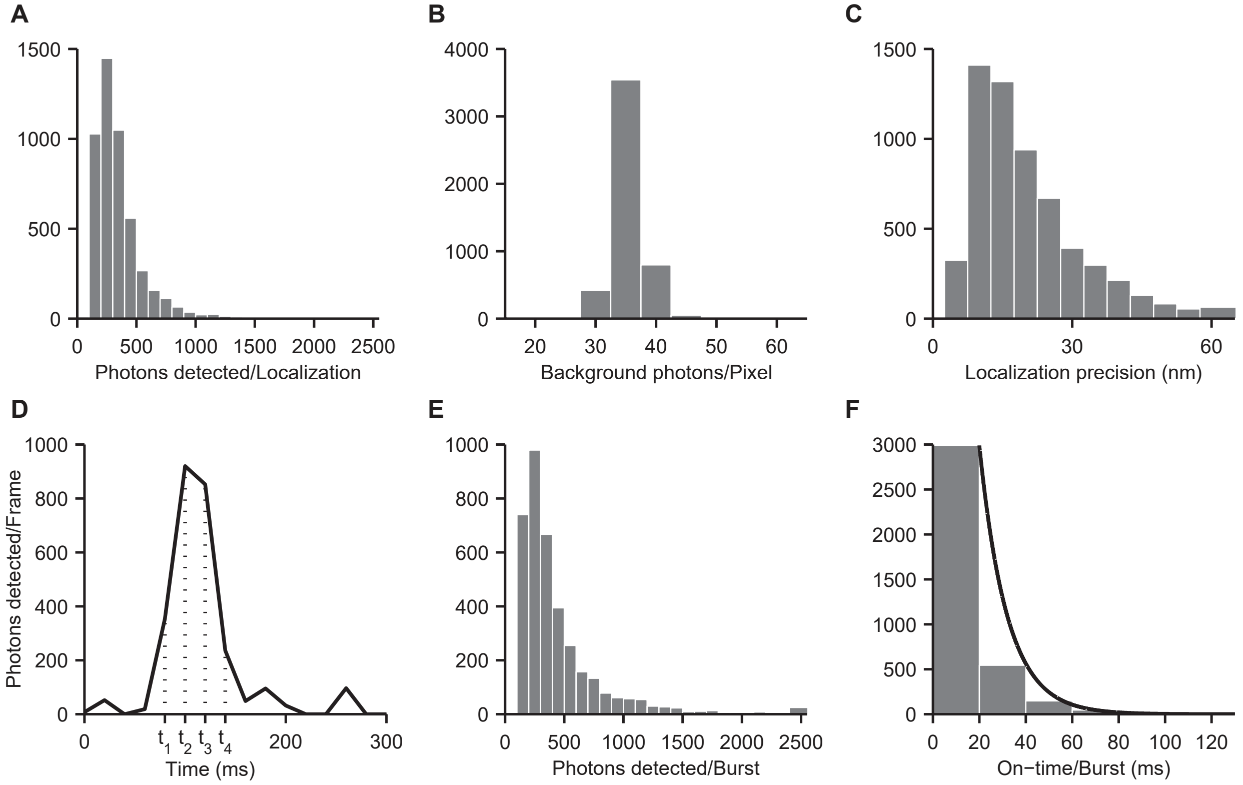

Figure 5.3: Analysis of ThT localization and blinking events in TAB microscopy. (A-C) Histograms of photons detected/localization, background photons/pixel, and the localization precision of ThT bursts observed in the image stack (5000 frames, 100 s) within the ROI. (D) Photons detected over time in the red square in Figure 5.2A. Localizations over consecutive frames (t_1-t_4) were grouped together as a single "burst", and the detected photons from each ThT burst were analyzed after the localization grouping process (Section 2.6.1). (E, F) Histograms of photons detected and the on-time of ThT bursts after the localization grouping process. Black solid line in I depicts the fitting result to an exponential decay. The median of photons detected per burst was 319; the time constant of the exponential fit was 12 ms. This data corresponds to the fibril shown in Figure 5.1B-D. Adapted and reprinted with permission from Ref. [125].

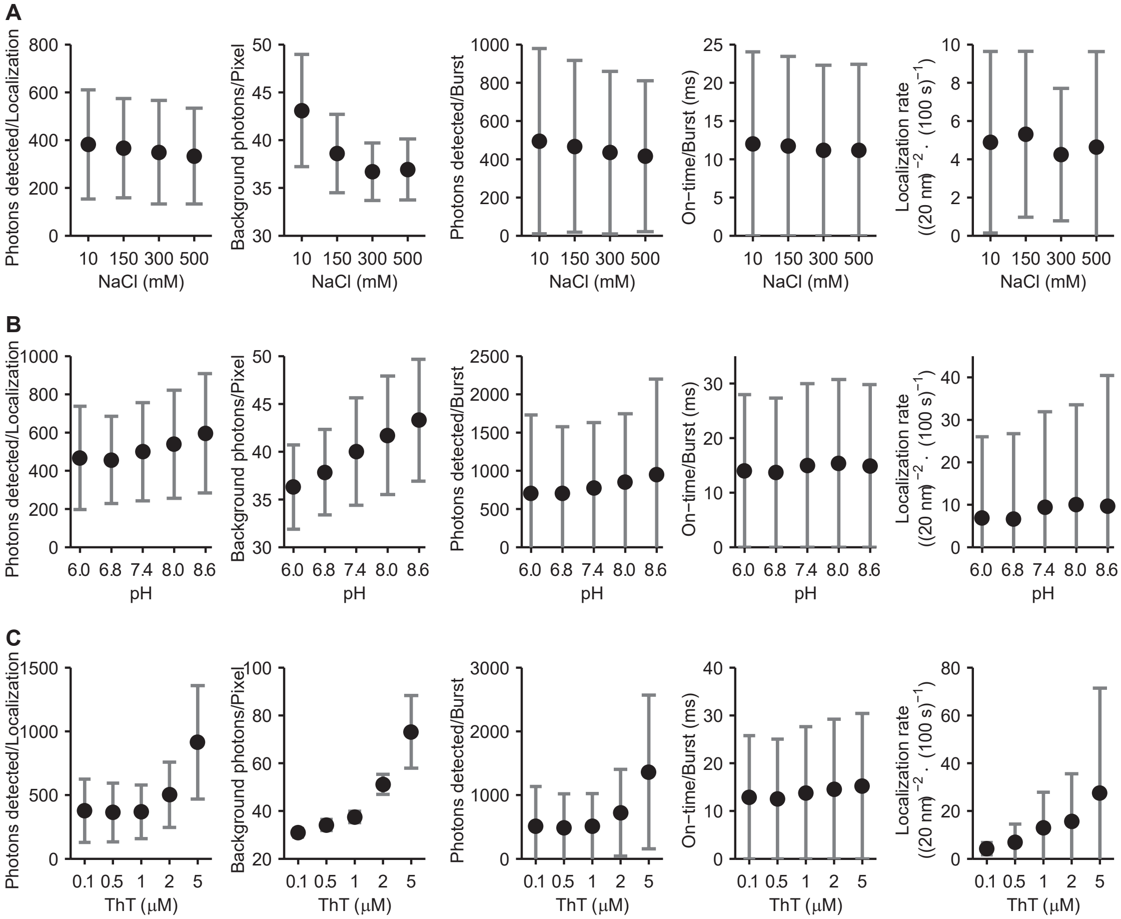

Figure 5.4: Imaging buffer effects on ThT blinking. ThT blinking characteristics were measured under varying (A) NaCl concentration (10–500 mM), (B) pH (6.0–8.6), and (C) ThT concentration (0.1–5 μM). NaCl concentration and pH appear to have limited effect on the blinking of ThT on fibrils. However, reduced background photons/pixel were observed under high NaCl concentration and low pH conditions. On the other hand, the blinking rate of ThT, and thus the rate of locations per time, and background photons rise with increasing ThT concentration. The high blinking rate at 5 μM ThT causes images of overlapping molecules, which leads the number of photons detected and background photons per localization to rise significantly. Dots represent the mean across experiments, error bars represent standard deviations. Negative error bars are truncated at zero. Unique 12 Aβ42 fibrils per condition were imaged for NaCl comparison with 20 mM Na_3PO_4, 1 μM ThT, pH 8.6. Similarly, 5 identical Aβ42 fibrils with 20 mM Na_3PO_4, 500 mM NaCl, 1 μM ThT, and 3 long identical fibrils with 20 mM Na_3PO_4, 150 mM NaCl, pH 7.4 were imaged for the comparison of pH and ThT concentration, respectively. The imaging buffers were exchanged completely between each imaging acquisition in a random order. Reprinted with permission from Ref. [125].

its related discussion in Chapter 6). This nanoscale resolution helps to resolve twisted fibril structures in Figure 5.1F that cannot be visualized in the diffraction-limited image (Figure 5.1E).

5.2 TAB Specificity to Resolve Amyloid Structures

We verified that TAB SR imaging faithfully reproduces the structure of Aβ fibrils by comparing TAB images to those produced with conventional fluorescent tags. First, Aβ42 fibrils were intrinsically labeled with Alexa-647 (Section 2.3.2) and imaged by using a conventional epi-fluorescence microscopy. Their morphology matched the TAB SR image of the same fibril (Figures 5.5A-C). Next, we directly compared SR TAB images to dSTORM imaging. Aβ42 fibrils were tagged with monoclonal anti-Aβ antibody 6E10 and Alexa-647 labeled goat anti-mouse secondary antibody (Section 2.3.2), and imaged by dSTORM of the Alexa-647 dye, followed by TAB imaging of the ThT dye. Typical dSTORM imaging with Alexa-647 gives a localization precision of 6 nm (FWHM: 14 nm) that corresponds to 3,700 photons detected per localization (Figure 5.6 and Table 5.1). Both dSTORM and TAB imaging reveal a thin and uniform fibril structure (Figures 5.5D-G). Reconstructed images from SR TAB microscopy gave comparable or better resolution than the conventional label-based SR technique. The measured FWHM of the reconstructed Aβ42 fibril with Alexa-647 was (80±30) nm (Figure 5.5D), whereas the TAB reconstruction on the same fibril yielded a FWHM of (60±10) nm (Figure 5.5F). This resolution is comparable to apparent fibril widths of 40–50 nm reported for dSTORM imaging of covalently modified Aβ [135]. A resolution of 14 nm was reported for synuclein fibrils that were imaged by binding-activated fluorescence using a conjugated oligothiophene *p*-FTAA [261]. However, this resolution was achieved

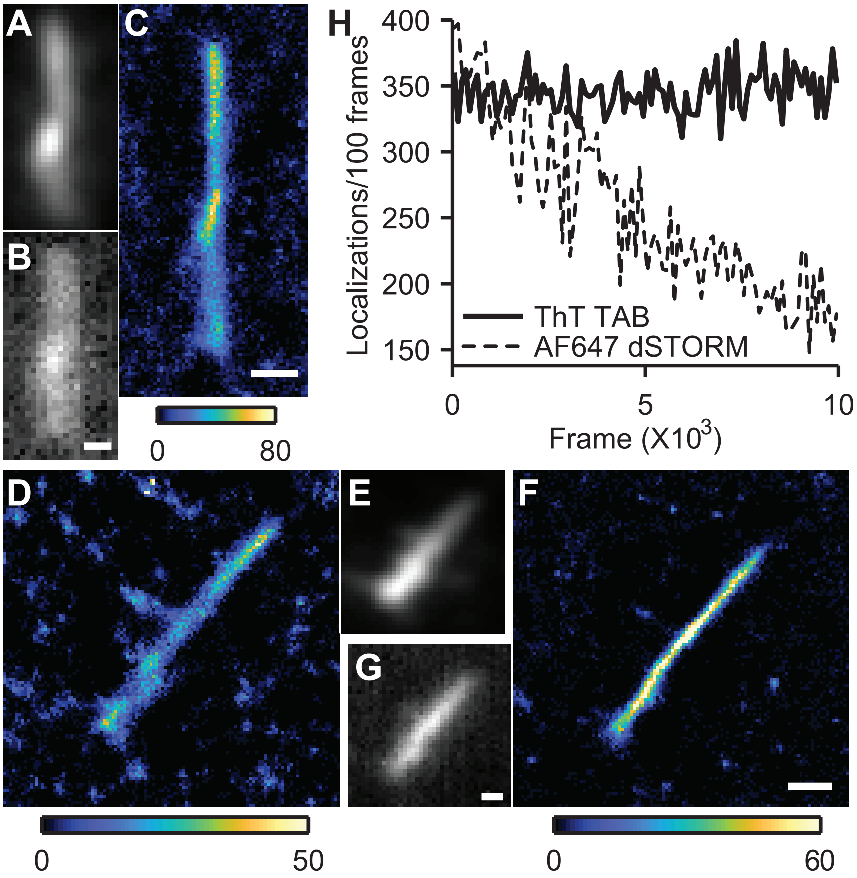

Figure 5.5: TAB SMLM imaging compared to conventional labeling methods. (A) Diffraction-limited image of an intrinsically labeled Aβ42 fibril (4.2%, Aβ42-Alexa 647). (B) Diffraction-limited ThT and (C) TAB SMLM images of the fibril in A. (D) Conventional SMLM image of an Aβ42 fibril with Alexa-647 antibody staining. (E) Diffraction-limited image of D with Alexa-647. (F) TAB SMLM image of D. (G) Diffraction-limited ThT image of D. Color bars: localizations per bin, scale bars: 300 nm. (H) Localizations per 100 frames over time for TAB and dSTORM imaging. Adapted and reprinted with permission from Ref. [125].

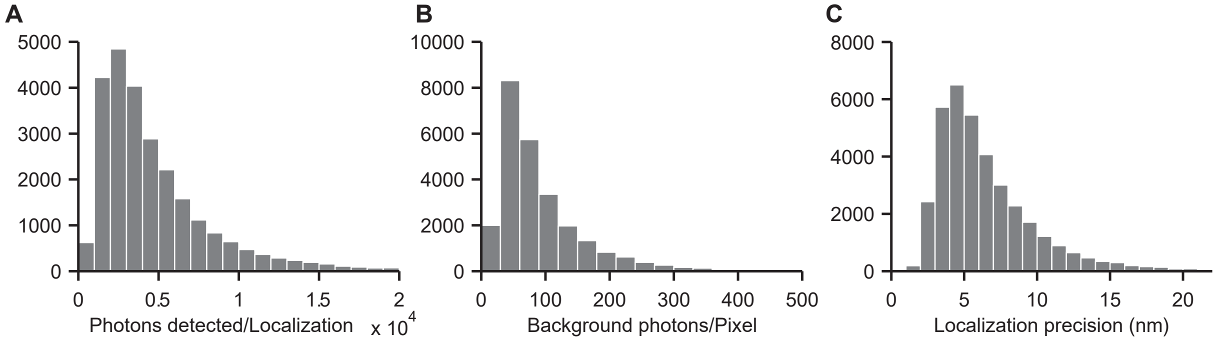

Figure 5.6: Analysis of Alexa-647 dSTORM for amyloid fibril imaging. (A-C) Histograms of photons detected/localization, background photons/pixel, and localization precision of Alexa-647 bursts observed in the image stack (10,000 frames, 150 s). Reprinted with permission from Ref. [125].

at the expense of limited observation times. Our results also demonstrate that the TAB technique relaxes the challenges stemming from the high labeling density and uniformity requirements [260] of conventional SR methods.

5.3 TAB Imaging across a Variety of Amyloid Structures

We next explored the versatility of ThT as a probe for TAB imaging of various amyloid structures. We prepared fibrils of Aβ40 (AD associated), α-synuclein (PD associated), islet amyloid polypeptide (IAPP, Type II diabetes associated), tau protein (AD associated) and light-chain (AL, light-chain amyloidosis associated) amyloid (Section 2.3.2), adsorbed them to glass surfaces, and imaged them. We were able to reconstruct images with apparent fibril widths of 40–80 nm for all polypeptides (Figure 5.7); this experiment demonstrates that ThT can be used for SR imaging across a wide variety of targets. Some amyloids

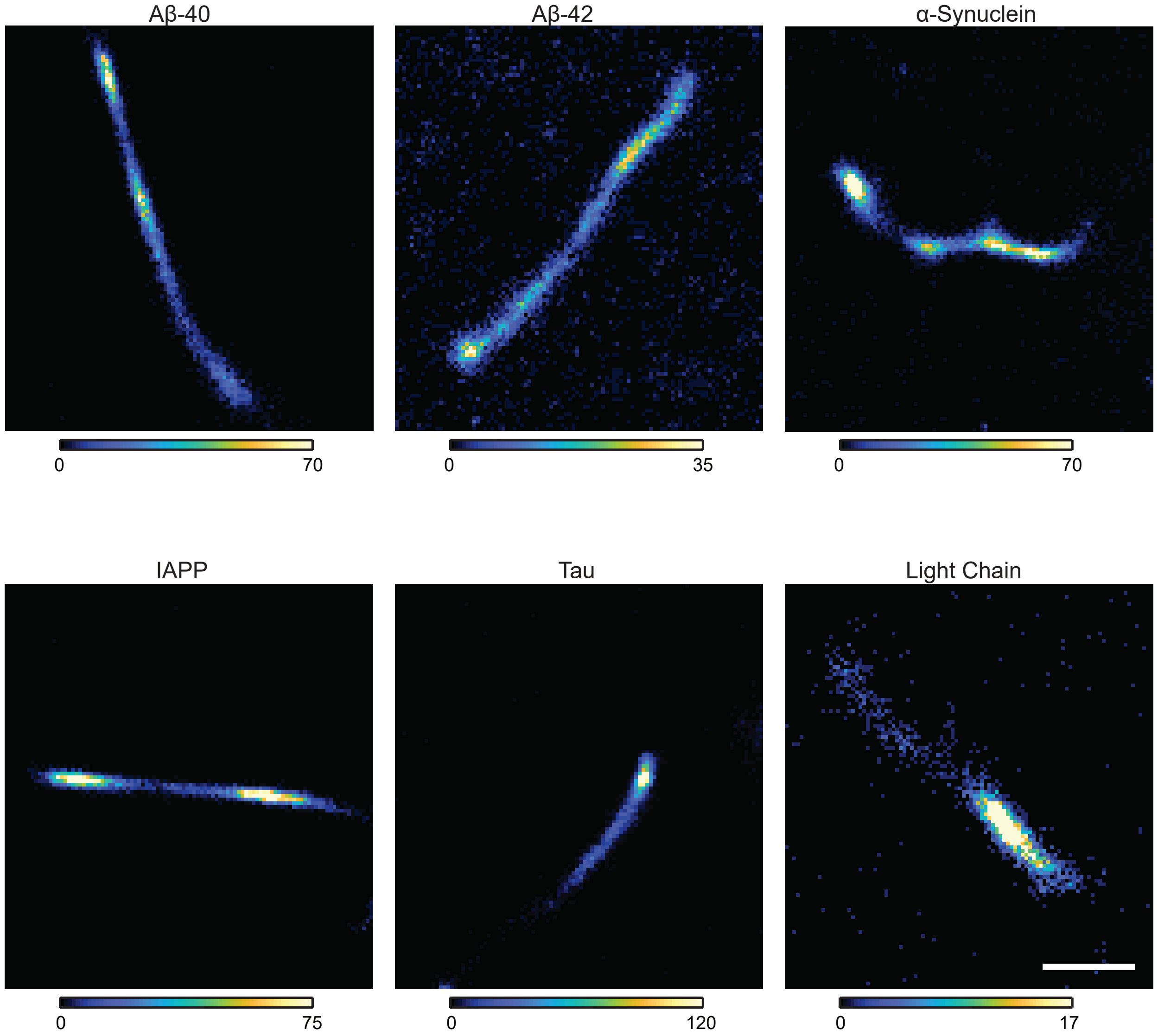
Aβ-40
Aβ-42
α-Synuclein
0
70
0
35
0
70
IAPP
Tau
Light Chain
0
75
0
120
0
17

Figure 5.7: TAB SMLM images of Aβ40, Aβ42, α-Synuclein, IAPP, Tau, and Light Chain. Scale bar: 500 nm. Color bars in units of localizations/bin. Reprinted with permission from Ref. [125].

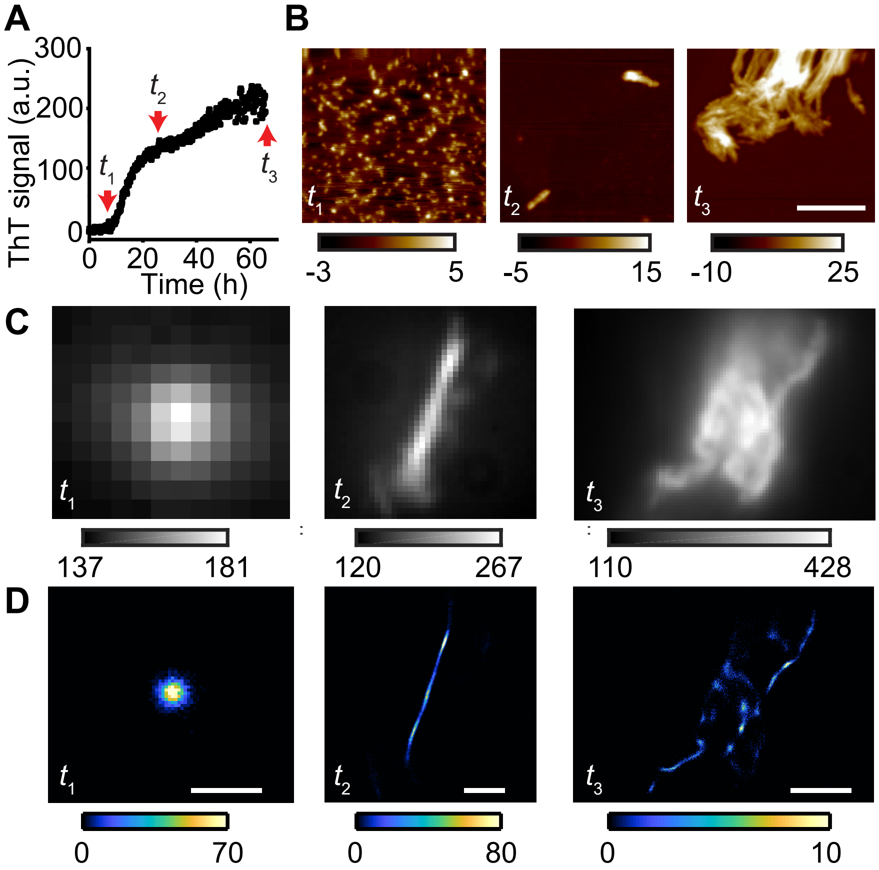

Figure 5.8: Visualization of Aβ40 structures using TAB SMLM at various aggregation stages. (A) Aggregation kinetics of Aβ40 measured by ThT fluorescence in bulk. t_1 (8 h), t_2 (24 h), and t_3 (66 h) represent oligomers, early fibrils, and late fibril clusters, respectively. (B) AFM images of Aβ40 at t_1, t_2, and t_3. Color bar in nm, scale bar: 350 nm. (C) Diffraction-limited images of Aβ40 aggregates using ThT fluorescence at t_1, t_2, and t_3. (D) TAB SMLM images of the structures in C. Fluorescence from out-of-focus structures decreased localizations in t_3. Scale bars: 0.5 (t_1), 1 (t_2), and 2.5 mm (t_3). Reprinted with permission from Ref. [125].

produced reconstructions with wider apparent fibril widths than others; this inhomogeneity might reflect differences in the binding affinities and the quantum yields of ThT on different fibrillar structures [32, 268]. The synthesis and characterization of new dyes with different affinities [33] could improve TAB image quality on such amyloids in the future.

Thioflavin T is well-known to bind to mature amyloid fibrils. However, it would also be valuable to image intermediates of the aggregation pathway. We therefore explored whether TAB imaging could visualize different stages of the amyloid aggregation process. We generated Aβ40 aggregates from the late lag phase (t_1, 8 h), the growth phase (t_2, 24 h), and the late plateau phase (t_3, 66 h) of ThT kinetics (Figure 5.8A) and verified aggregate morphologies by atomic force microscopy (AFM; Figure 5.8B). Aggregates from t_1 corresponded to spherical oligomers, t_2 to single fibrils, and t_3 to fibril clusters, respectively.

We performed TAB imaging of the Aβ40 aggregates in a pseudo-TIRF microscope. Strikingly, TAB imaging was able to reconstruct spherical Aβ40 structures from an early stage of aggregation (Figure 5.8D). These structures were measured to have dimensions of 4–5 nm by AFM, and therefore constitute typical Aβ40 oligomers [123]. Being able to accurately image oligomeric structures is important to capturing the dynamics of Aβ aggregation and could open the door for future applications in cellular imaging of oligomeric structures for studying their cytotoxicity.

5.4 Long-Term TAB Imaging of Amyloid Dynamics

To image the dynamics of amyloid formation, it is essential to have a robust tool that can follow the structure of a single aggregate over hours or more. We analyzed the stability of

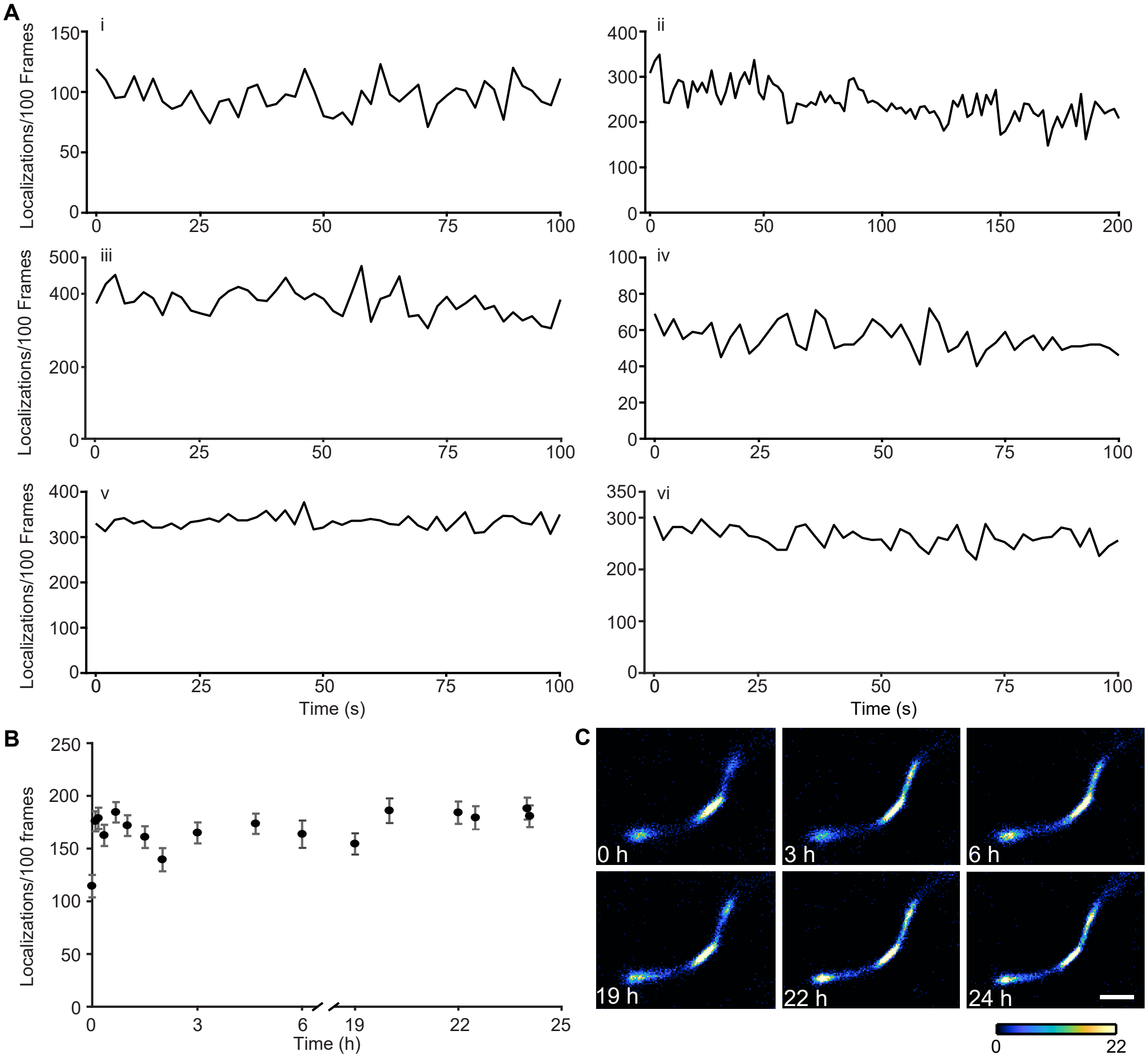

Figure 5.9: The localization rate of single ThT molecules during TAB imaging. (A) Localizations per 100 frames (2 s) over time during the acquisition of imaging stacks for (I) Figure 5.1D, (II) Figure 5.5C, (III) Figure 5.5F, (IV) Figure 5.8 t_1, (V) Figure 5.8 t_2 and (VI) Figure 5.8 t_3. Localizations over time were approximately constant over time with no evidence of photobleaching. (B) The localization rate of ThT molecules for multiple TAB images over an extended observation time. 17 time-lapse TAB image stacks were taken on an Aβ42 fibril over 24 h without changing ThT imaging buffer. The stable localization numbers show that long-term TAB imaging is feasible. (C) TAB image reconstructions at select time points from the plot in B. Images show consistent reconstruction quality of the same fibril over 24 hours. Scale bar: 500 nm. Color bar in units of localizations/bin. Reprinted with permission from Ref. [125].

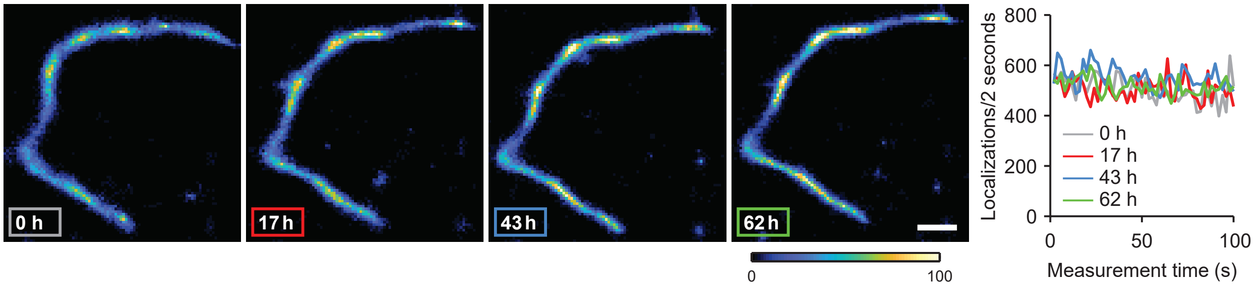

Figure 5.10: The localization rate of single NR molecules during TAB imaging. Time-lapse NR TAB imaging of an Aβ42 fibril and localization per 2 seconds in each image acquisition. The continuous replenishment of NR dye molecule to the amyloid surface gives robust localization numbers over the extended observation times. Note that the NR imaging buffer was not refilled over the measurements.

TAB imaging over time in four ways. First, we tested whether the localization rate remained constant within a single imaging experiment. We counted localization events in blocks of 100 frames (2 s) across fibrils of various sizes and observed that the number of localizations did not change during the acquisition of an image stack (typically 1.5–3.5 min, Figures 5.5H and 5.9A). In contrast, the localization rate of Alexa-647 in dSTORM dropped to less than half of its initial value in a similar time frame.

Further, we tested whether the localization rate remained constant over extended observation times. We imaged an Aβ42 fibril 17 times over 24 h, and counted localization events in blocks of 100 frames (2 s) for each acquisition. We observed that the TAB reconstructions and the number of localizations remained approximately constant over the 24-hour acquisition (Figures 5.9B and C). Therefore, TAB imaging with ThT is resistant to photobleaching and capable of producing multiple time-lapse SR images, which can involve the localization of over 100,000 ThT molecules on a single fibril. TAB's robustness against photobleaching using NR as a probe molecule has also been validated in a similar way (Figure 5.10). We observed approximately sustained NR TAB reconstructions and the rate of localization in each 5,000-frame stack (100 s image stack acquisition) over the 62-hour

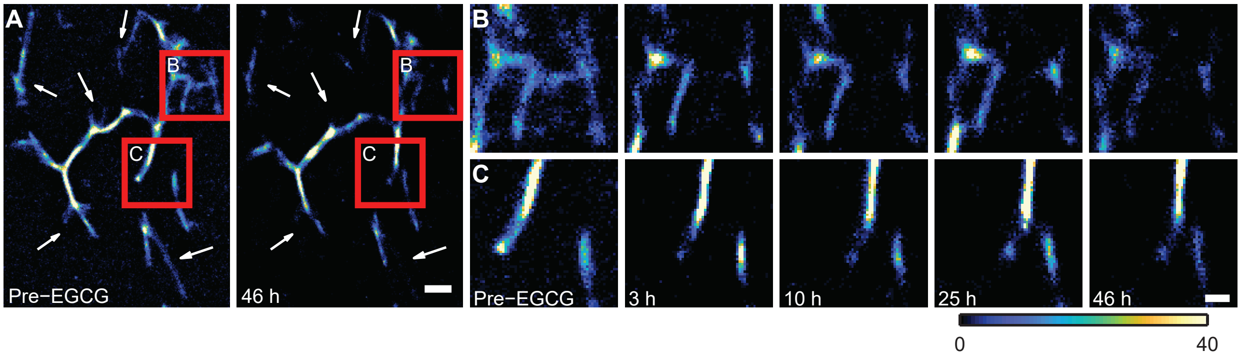

Figure 5.11: TAB SMLM images of Aβ42 fibril remodeling using ThT as the imaging probe. (A) Aβ42 before and after a 46-hour reaction with EGCG (1 mM). White arrows denote regions with distinct changes. Scale bar: 500 nm. (B, C) Time-lapse TAB images of regions denoted by red squares in A, recorded before and 3, 10, 25, and 46 h after adding EGCG. Color bar denotes localizations per bin, scale bar: 200 nm. Reprinted with permission from Ref. [125].

time-series experiment. These results also imply that the binding of TAB probe molecules on amyloid surfaces is transient and continuous binding and unbinding of dye molecules allow replenishment of fluorescence flashes and SM localizations for resolving amyloid structures over hours to days.

We next validated the capability of TAB for SR imaging over the course of hours to days. The time-lapse images (Figures 5.11 and 5.12) show the dissolution and remodeling of Aβ42 fibrils by epi-gallocatechin gallate (EGCG) [123]. Remarkably, TAB imaging captured the structural dynamics of amyloid fibrils for ∼2 days, thus allowing us to observe remodeling over tens of micrometers with ∼16 nm precision. In this experiment, we observed dynamics that were slower than at 37 °C in solution [123], most likely due to the lack of agitation of fibrils that were adsorbed to the glass surface and to incubation at room temperature (∼21°C). It should also be noted that the fluorescence background increased in the presence of EGCG. This increase is most likely a result of reduced photobleaching, because EGCG is a

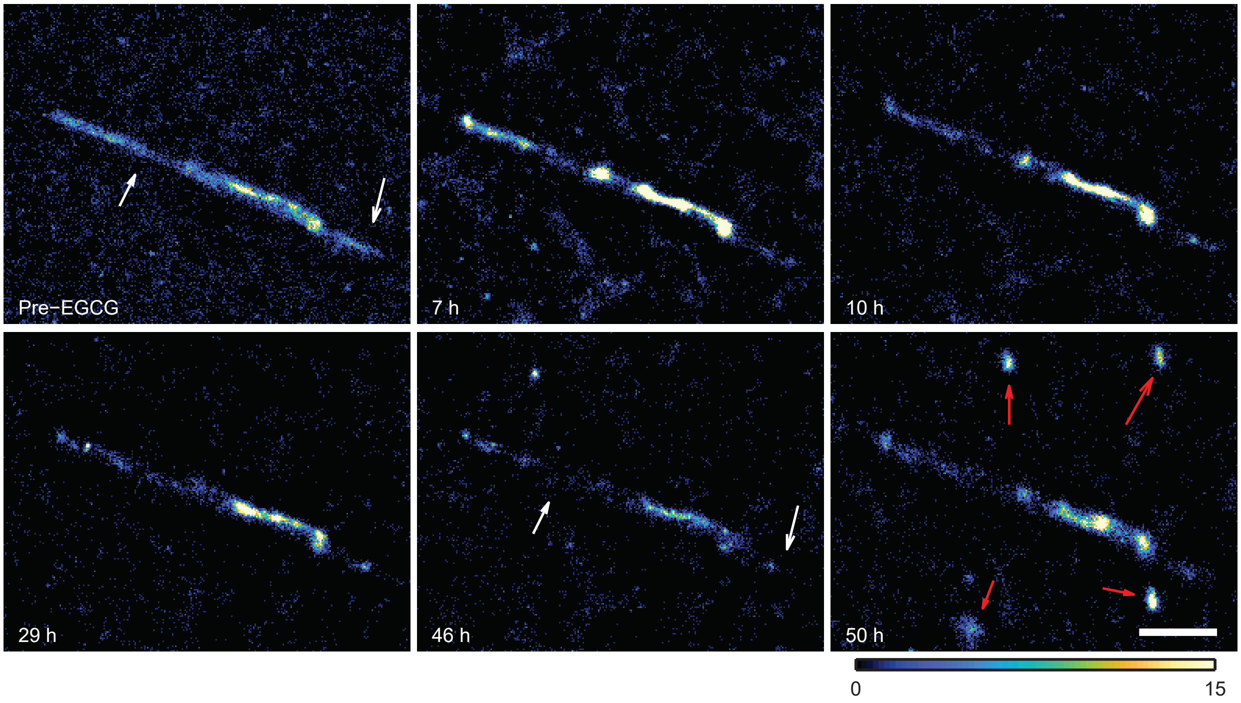

Figure 5.12: Additional time-lapse ThT TAB SMLM images of Aβ42 before and 7, 22, 29, 46, 50 h after adding EGCG. The fibril was incubated with 1 mM EGCG at room temperature (~21°C) except for the final incubation during 46-50 h. More concentrated EGCG was added to make an 8 mM EGCG buffer during this period in order to accelerate fibril remodeling. Gradual fibril dissolution was observed in the first 46 h incubation with 1 mM EGCG (white arrows), and some spherical assemblies were observed after the 4 h incubation in the presence of 8 mM EGCG (red arrows). Similar spherical structures were previously reported using AFM and bulk incubation [123] Scale bar: 1 μm; color bar in units of localizations/bin. Reprinted with permission from Ref. [125].

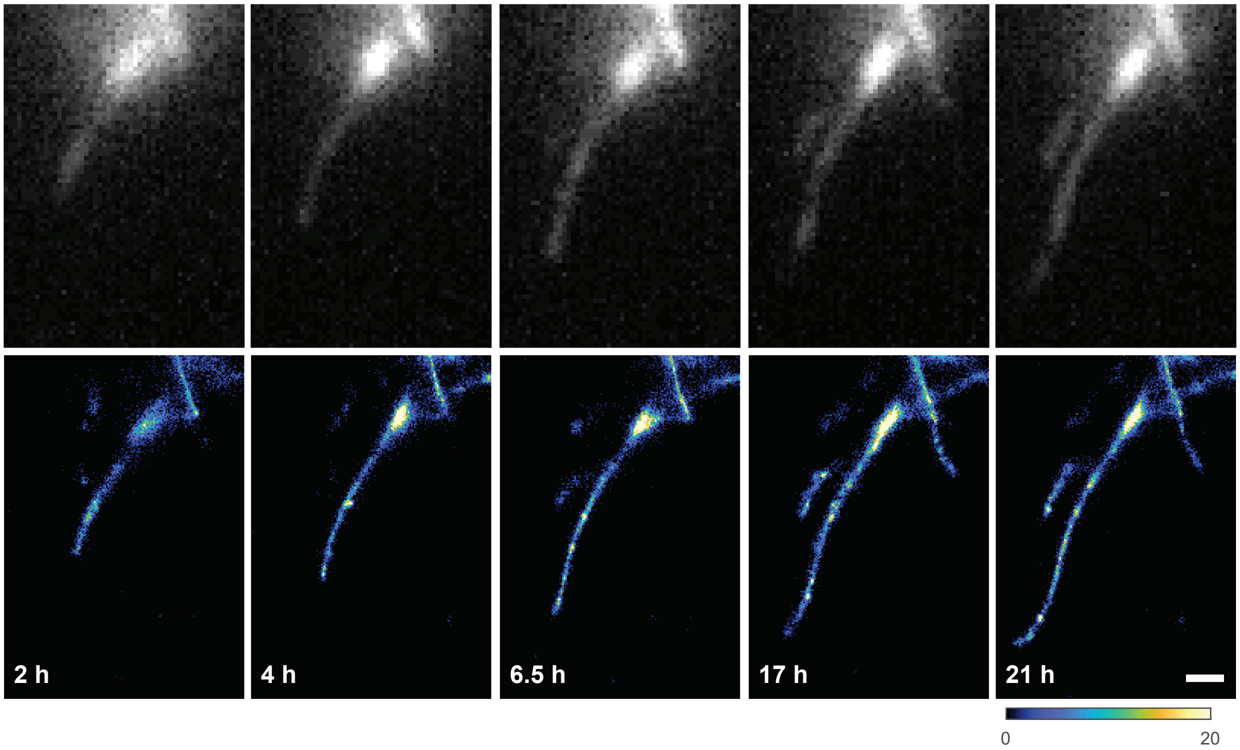

Figure 5.13: TAB SMLM images using NR of Aβ42 fibril growth, recorded 2, 4, 6.5, 17, and 21 hours after placing needle-sheared Aβ42 fibrils on our microscope stage with 20 μM monomeric Aβ42 at room temperature (21 °C). Top row: diffraction-limited images. Bottom row: corresponding NR TAB SMLM images. Color bar denotes localizations/bin. Scale bar: 300 nm. This figure is modified with permission from [264].

potent antioxidant and might affect fluorescent dyes in a manner similar to other antioxidants such as ascorbic acid [37].

Finally, we imaged amyloid elongation on our microscope stage using NR TAB imaging. The time-lapse TAB images (Figure 5.13) show non-linear growth of amyloid fibrils over time that cannot be clearly resolved in the corresponding diffraction-limited images. TAB's robustness against photobleaching allowed us to observe transitions between active elongation and arrested growth with nanoscale resolution.

The success of these experiments demonstrates the ability of TAB imaging to follow the dynamics of amyloid structures with nanometer resolution and approximately minute temporal resolution over extended periods. This capability will be essential for visualizing drugs acting on amyloid structures in order to gain insight into their molecular-scale interactions with these structures.

5.5 Outlook

The photobleaching of dyes limits observation times in conventional SR techniques [81]. Previous studies have imaged ThT binding to dried amyloid samples through photoactivation in a dSTORM manner [258]. One may also resolve amyloid fibrils using other binding-activated probe molecules [261]. However, a fixed number of fluorophores labeled on amyloid aggregates and irreversible binding mechanisms of the probe molecules limit observation times for monitoring amyloid dynamics. We report SR imaging of a wide variety of fibrils and aggregation intermediates by using transient binding of ThT, one of the most widely used amyloid dyes, and NR, a classic solvatochromic dye; because TAB generates blinking by transient molecular binding, the technique is inherently resistant to photobleaching and allows extended observation times compared to dSTORM and similar techniques. Although the use of binding dynamics of novel amyloid dye molecules might increase photon yield [269], the ubiquity and versatility of ThT and NR in amyloid staining should facilitate its adoption in nanoscopic imaging. We therefore expect that the use of TAB imaging could be expanded easily to a variety of substrates and conditions.

A critical challenge in preparing samples for SR microscopy is the need for high labeling density and uniformity, which necessitate a large number of covalent modifications of, or antibodies attached to, the biomolecule of interest. Transient binding strategies, like PAINT and TAB imaging, reduce the complexity of sample preparation but potentially at the cost of requiring specific buffer conditions for efficient single-molecule blinking. Further, some transient labeling strategies, in which the fluorophores emit fluorescence regardless of their binding state, require TIRF illumination to reduce the background fluorescence for single-molecule imaging. Our results demonstrate that TAB SMLM maintains the simplicity of transient labeling methods while remaining robust to a wide variety of imaging conditions. ThT blinking is readily detectable across a range of pH and salt concentrations. TAB SMLM performs well with both widefield epi-fluorescence and TIRF illumination strategies because TAB probes become much brighter when bound to amyloid than in its unbound state. This flexibility and robustness allow TAB imaging to work in tandem with other dyes or molecules that probe specific proteins or biomolecules. TAB SMLM can also provide continuous imaging for long periods of time without image degradation due to photobleaching, a major advantage over conventional SR techniques.

In summary, TAB microscopy is a flexible imaging technique that can provide images of amyloid structures with nanometer resolution over observation times of hours. It is capable of imaging various stages of amyloid aggregation as well as dynamic imaging of structure elongation and fibrillar remodeling induced by an antiamyloid drug.

TAB microscopy detects and localizes fluorescence flashes of single molecules on amyloids. Since binding of TAB probe molecules occurs spontaneously relying on binding affinity of the molecules to amyloid aggregates, we believe the flashes contain more information regarding underlying local amyloid assemblies beyond simple dye positions. In the next chapter, we extend the TAB microscopy to simultaneously measure positions and orientations of TAB molecules on amyloid structures. We demonstrate that the orientation estimates infer local organization of amyloid β-sheet assemblies and resolve structural heterogeneity that cannot be observed by SM localization alone.

Chapter 6

TAB Single-Molecule Orientation Localization Microscopy (SMOLM)

Going beyond standard SMLM to measure SM position and orientation simultaneously provides critical insight into a variety of nanoscale biological and chemical processes [20, 42–45, 47]. To perform these measurements, molecular position and orientation must be encoded within the shape of the image produced by a microscope [270], i.e., its PSF (also see Sections 1.5.3 and 2.1.1). However, balancing the need to resolve various orientations with high estimation precision and the need to detect SMs efficiently remains a challenge that limits the adoption of single-molecule orientation localization microscopy (SMOLM) for biological and chemical applications; existing techniques either cannot discriminate between similar types of molecular motions or cannot detect weak fluorescent emitters.

In order to design or select a PSF for measuring molecular orientation, one must have a figure of merit for comparison. The Cramér-Rao bound (CRB), which is the best-possible precision achievable by an unbiased estimator, has been used extensively for evaluating [238] and optimizing [271, 272] SMLM techniques. Similarly, estimation precision of molecular orientation can be evaluated by the CRB for each specific orientation locally.

In this chapter, the performance of various PSFs is quantified and compared for measuring molecular orientation. By illuminating why a particular method performs well or poorly in a certain situation, CRB characterization shows that a microscope with two polarized detection channels, exhibiting a polarized (standard) PSF, provides superior measurement precision especially when molecules are near a refractive index interface and lie perpendicular to the optical axis. This conventional method of measuring molecular orientation has poor performance in index-matched samples unless a perturbation, such as defocus, is added to the optical system [233]. To demonstrate, we use TAB (Chapter 5) [125] and a maximum likelihood estimator that promotes sparsity (Section 2.5.4) [157] to measure the position and orientation of fluorescent molecules transiently bound to amyloid fibrils. For the first time to our knowledge, SMOLM reveals the orientation and rotational diffusion of Nile red (NR), a fluorescent molecule whose quantum yield increases when exposed to a non-polar environment [35, 36], when bound to fibrils at the single-molecule level. We show that SMOLM probes structural heterogeneities between these amyloid aggregates that are not detectable by standard SMLM[11].

---

[11] I am a co-first author of this work, published previously in Ref. [138]. In this project, Tingting Wu developed a performance metric, termed variance upper bound (VUB), that globally bounds the CRB to quickly evaluate any optical method for measuring molecular orientation. We demonstrated superior measurement precision and SM detectability of the polarized standard PSF for molecules near a refractive index interface. I have performed all amyloid imaging and data analysis for resolving orientation of NR molecules on surfaces of amyloid aggregates and probing heterogeneities between these structures.

6.1 Orientation Localization Microscopy Using Polarized Standard PSF

To begin, we model a fluorescent molecule as a dipole-like emitter [29, 83, 273] with an orientational unit vector $\boldsymbol{\mu} = [\mu_x, \mu_y, \mu_z]^{\mathrm{T}}$, or equivalent angles (ϕ, θ) in spherical coordinates (also see Section 1.2 and 1.5). Assuming that a molecule's rotational correlation time is faster than its excited state lifetime and the camera integration time [139], its orientation trajectory can be modeled by a second-moment vector $\boldsymbol{m} = [\langle \mu_x^2 \rangle, \langle \mu_y^2 \rangle, \langle \mu_z^2 \rangle, \langle \mu_x \mu_y \rangle, \langle \mu_x \mu_z \rangle, \langle \mu_y \mu_z \rangle]^{\mathrm{T}}$, where each entry is a time-averaged second moment of $\boldsymbol{\mu}$ [87, 137]. These orientational second moments contain information on both the orientation of a molecule and its "wobble" or rotational diffusion, represented by the solid angle $\Omega \in [0, 2\pi]$ sr, within a camera frame (see Section 2.1.2 and Figure 2.2). Fluorescence photons collected from such an emitter are projected to a microscope's image plane with an n-pixel intensity distribution that can be modeled as a linear superposition of six basis images weighted by $\boldsymbol{m}$, i.e.,

$$\begin{aligned} \boldsymbol{I} &= s\boldsymbol{B}\boldsymbol{m} + \boldsymbol{b} \in \mathbb{R}^{n\times 1}, \\ &= s\begin{bmatrix} \boldsymbol{B}_{xx} & \boldsymbol{B}_{yy} & \boldsymbol{B}_{zz} & \boldsymbol{B}_{xy} & \boldsymbol{B}_{xz} & \boldsymbol{B}_{yz} \end{bmatrix} \boldsymbol{m} + \boldsymbol{b}, \end{aligned} \tag{6.1}$$

where s is the number of photons collected by the detector, and $\boldsymbol{b}$ is the number of background photons in each pixel. Each so-called basis image $\boldsymbol{B}_j \in \mathbb{R}^{n\times 1}$, corresponding to the response of the optical system to each orientational second-moment component m_j, can be calculated by vectorial diffraction theory (Section 1.5 and 2.1.1) [85, 87, 137, 274], and various optical elements, such as phase masks, polarizers, and waveplates, can be used to encode orientation information within $\boldsymbol{B}_j$ more efficiently.

We next quantify the Fisher information (FI) contained in the basis images, i.e., the amount of information that the basis images contain about each of the orientational second moments. A larger FI corresponds to a smaller CRB and higher sensitivity for measuring $\boldsymbol{m}$. Given our linear imaging model, the FI matrix $\mathbf{FIM} \in \mathbb{R}^{6\times 6}$ for the orientational second moments can be written as (Section 2.5.4)

$$\mathbf{FIM} = \sum_{i=1}^{n} \frac{s^2}{I_i} \boldsymbol{B}_i^{\mathrm{T}} \boldsymbol{B}_i, \tag{6.2}$$

where $\boldsymbol{B}_i \in \mathbb{R}^{1\times 6}$ is the ith row of $\boldsymbol{B}$. Note that $\mathbf{FIM}$ is a function of $\boldsymbol{m}$ and may vary dramatically for different molecular orientations. The CRB of each second moment is then related to the diagonal elements of the inverse of matrix $\mathbf{FIM}$ as

$$\sigma_j^{\text{CRB}} = \sqrt{[\mathbf{FIM}^{-1}]_{jj}}, \tag{6.3}$$

where the subscript jj denotes the jth diagonal element.

We calculated the geometric mean of the CRB, i.e., $\text{GM}_{\text{3D}}^{\text{CRB}} = \sqrt[6]{\prod_j^6 \sigma_j^{\text{CRB}}}$, as a summary measure of performance of eight orientation-sensing PSFs, namely unpolarized standard, polarized standard, bifocal microscope [142], bisected [96], double helix [141], Duo-spot [235], Tri-spot [97], and quadrated [98] (see Chapter 4 for the Duo-spot PSF and Figure 2.5 for the other PSFs), for a molecule emitting at a glass-water interface (typical imaging configuration for TAB imaging, Figure 6.1). Figure 6.1A shows the minimum/average/maximum value of $\text{GM}_{\text{3D}}^{\text{CRB}}$ over all of orientation space (79,325 orientation situations in total, Figure 4.6 and Section 4.2). While the polarized standard PSF doesn't show the best CRB, its FI (in terms of $[\mathbf{FIM}]_{jj}$) is large for the first four second moments (Figure 6.1B), implying its superior sensitivity to these rotational motions. Therefore, the

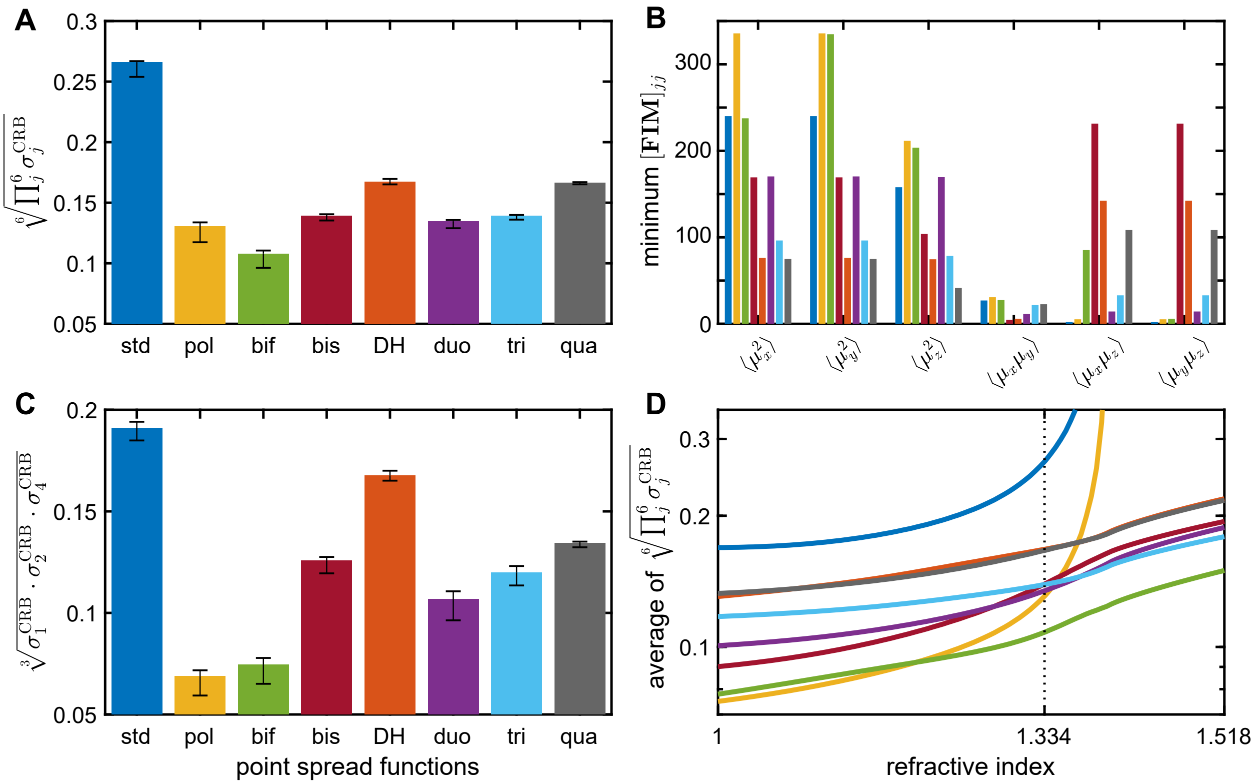

Figure 6.1: Orientation measurement precision using various point spread functions (PSFs) for 380 signal photons and 2 background photons per pixel. (A) Average (arithmetic mean) of $\mathrm{GM}_{\mathrm{3D}}^{\mathrm{CRB}} = \sqrt[6]{\prod_j^6 \sigma_j^{\mathrm{CRB}}}$ over all of orientation space for various PSFs. Blue: unpolarized standard (std), yellow: polarized standard (pol), green: bifocal microscope (bif), red: bisected (bis), orange: double helix (DH), purple: Duo-spot (duo), aqua: Tri-spot (tri), and gray: quadrated (qua) PSFs. Bars indicate the maximum/minimum of $\mathrm{GM}_{\mathrm{3D}}^{\mathrm{CRB}}$ over all of orientation space. (B) Fisher information (FI) lower bound $[\mathbf{FIM}]_{jj}$ of each orientational second moment m_j. (C) Average (arithmetic mean) of $\mathrm{GM}_{\mathrm{2D}}^{\mathrm{CRB}} = \sqrt[3]{\sigma_1^{\mathrm{CRB}} \cdot \sigma_2^{\mathrm{CRB}} \cdot \sigma_4^{\mathrm{CRB}}}$ over all of orientation space for comparison of in-plane (xy) orientation sensitivity. Bars indicate the maximum/minimum of $\mathrm{GM}_{\mathrm{2D}}^{\mathrm{CRB}}$ over all of orientation space. (D) Average of $\mathrm{GM}_{\mathrm{3D}}^{\mathrm{CRB}}$ for various refractive indices. Dotted line: refractive index of water.

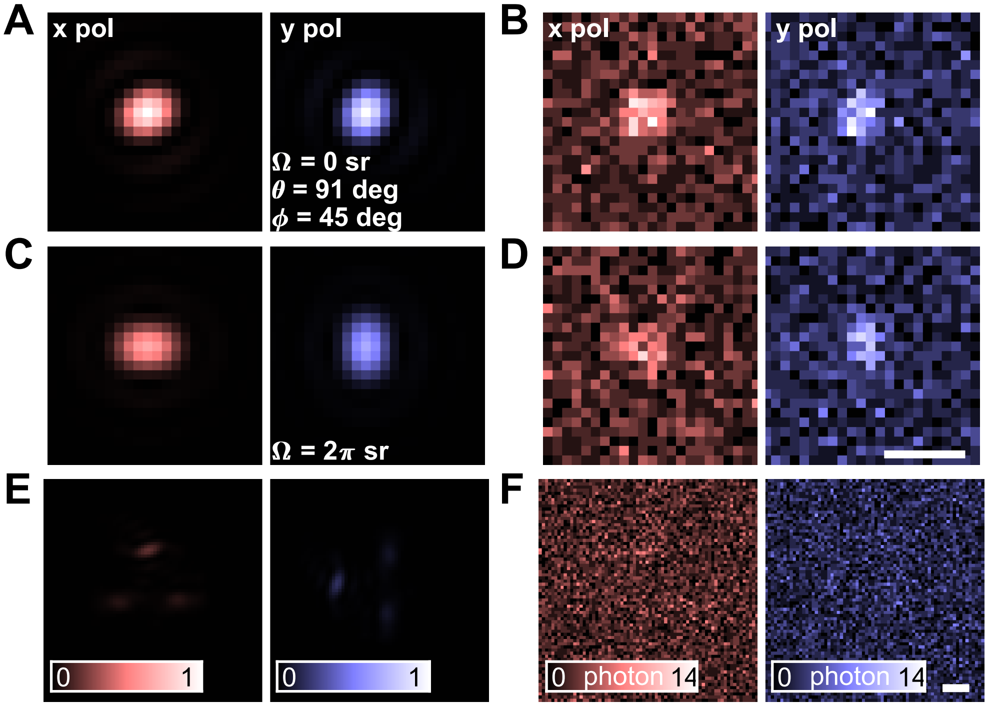

Figure 6.2: Simulated noiseless orthogonally polarized images of (A) a fixed molecule with orientation ($\theta = 90°$, $\phi = 45°$) and (C,E) an isotropic emitter using (C) the polarized PSF and (E) the Tri-spot PSF. (B,D,F) Photon shot-noise perturbed images corresponding to A, C, E with 380 signal photons and 2 background photons per pixel. Scale bars: 500 nm.

polarized PSF can estimate the in-plane (xy) orientations of fluorescent molecules with excellent precision (Figure 6.1C).

To explore the effect of refractive index (RI) mismatch, we evaluated $\text{GM}_{\text{3D}}^{\text{CRB}}$ for sample media ranging from air (RI = 1) to oil (RI = 1.518). When the RI is low, the polarized standard PSF surprisingly show superior measurement performance for the 3D second moments (Figure. 6.1D). This insight is confirmed by our observations that a molecule at a glass-air interface produces basis images $\boldsymbol{B}_j$ with vastly superior contrast (energy) compared to one within matched media (Figure 2.1). On the other hand, for samples with RI near that of oil, PSF engineering clearly provides increased orientation precision over other approaches.

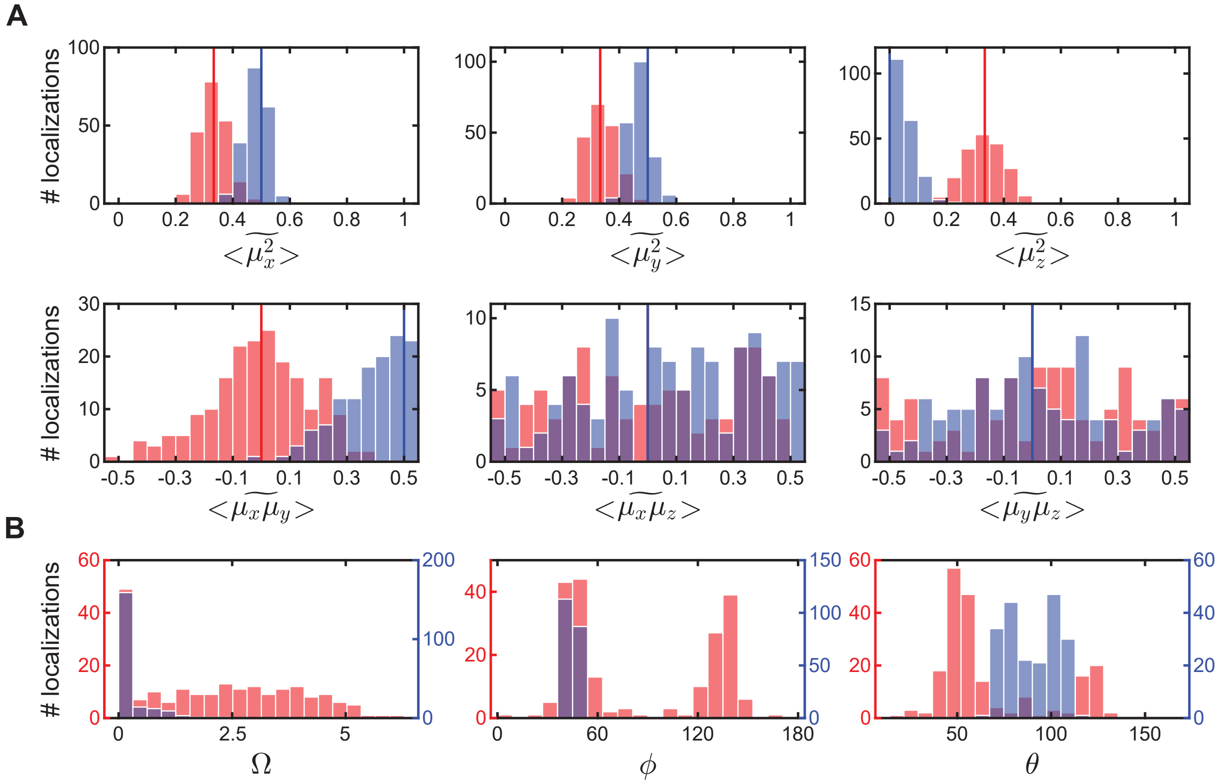

Figure 6.3: Resolvability of a fixed molecule versus an isotropic emitter using the maximum likelihood estimator followed by a weighted least-square estimator. (A) Estimated second moments $\tilde{m}$ using the polarized standard PSF and the maximum likelihood estimator described in Section 2.5.4 for a fixed molecule with orientation (blue, $\Omega_0 = 0$ sr, $\theta_0 = 90°$, $\phi_0 = 45°$, Figure 6.2B) and an isotropic emitter (red, $\Omega_0 = 2\pi$ sr, Figure 6.2D). At each orientation, 200 independent images were generated with $s_0 = 380$ signal photons, $b_0 = 2$ background photons/pixel. The vertical lines depict the ground truth second moments ($\boldsymbol{m}_0$) for the fixed molecule (blue) and the isotropic emitter (red). The estimator allows the cross terms ($\langle\widetilde{\mu_x\mu_y}\rangle, \langle\widetilde{\mu_x\mu_z}\rangle, \langle\widetilde{\mu_y\mu_z}\rangle$) to have non-physical values (e.g., $\langle\widetilde{\mu_x\mu_y}\rangle < -0.5$ or $\langle\widetilde{\mu_x\mu_y}\rangle > 0.5$). Note that the estimator gives unbiased and precise measurements of the first four second moments but wide distributions for the last two moments. This behavior is consistent with the discussion in Figure 6.1; the polarized standard PSF contains little sensitivity to $\langle\widetilde{\mu_x\mu_z}\rangle$ and $\langle\widetilde{\mu_y\mu_z}\rangle$. (B) Projected mean orientation (ϕ,θ) and wobbling area (Ω) of each estimate obtained from $\tilde{m}$ using the weighted least-square estimator for the fixed in-plane molecule (blue) and the isotropic emitter (red). Although Ω estimates of the isotropic emitter show unavoidable bias and low precision due to photon shot noise (Figure 6.9A) [275], the estimates demonstrate that the fixed molecule and isotropic emitter are easily resolved by our method. Note that measurements of θ and ϕ have little significance for the isotropic emitter (red). Reprinted with permission from Ref. [138].

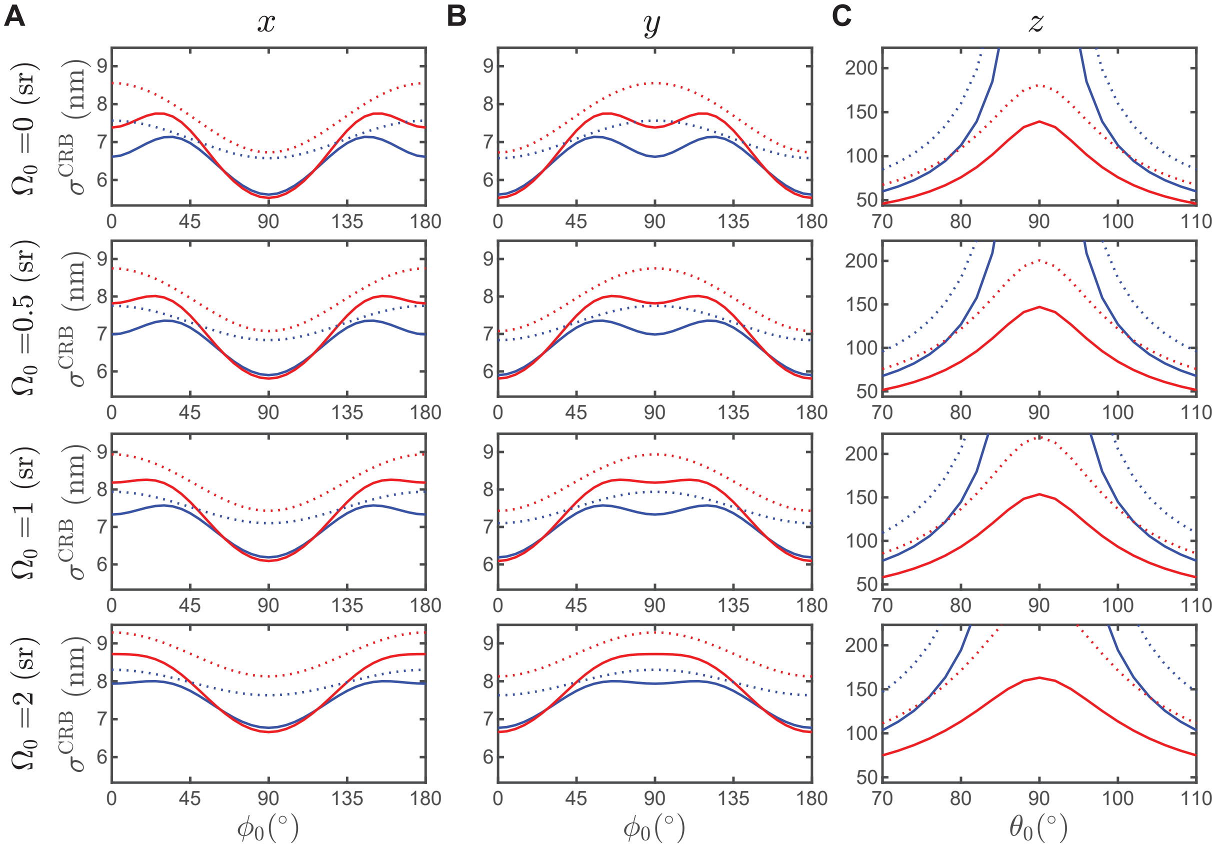

Figure 6.4: Cramér–Rao bounds for estimating the 3D position along (A) x, (B) y, and (C) z of a single molecule using the polarized (solid) and unpolarized (dashed) standard PSFs. The bounds are computed for a focused molecule ($z = 0$ nm) at various orientations ($\Omega_0 = 0 - 2$ sr , $\phi_0 = 0 - 180°$, $\theta_0 = 70 - 110°$) within a matched medium (RI = 1.518, blue) and at a mismatched refractive index interface (RI = 1.334, red). Calculations were performed for $s_0 = 380$ signal photons and $b_0 = 2$ background photons/pixel. Note that the square root of the CRB for x and y estimations were averaged over all simulated θ_0 since the estimation precisions are mostly constant for the range of θ_0 examined here. Similarly, the square root of the CRB for z estimation was averaged over all ϕ_0. Reprinted with permission from Ref. [138].

In addition to high orientation measurement precision, PSFs must be easily detectable under low SBRs in order to be practical for SMOLM. Using the polarized standard PSF, a fixed molecule ($\theta = 90°, \phi = 45°$) and an isotropic emitter can be distinguished from one another with only 380 photons detected (Figures 6.2A-D, 6.3). Note that distinguishing these two types of emitters is nearly impossible under matched RI conditions; it is the RI mismatch and the associated supercritical fluorescence collected from fluorophores near the interface that enables this remarkable sensitivity. However, the Tri-spot PSF, despite its superior CRB, cannot detect the same isotropic emitter due to the splitting of photons into three spots in each polarization channel (Figures 6.2E,F). The RI mismatch also improves 3D localization precision with various dipole orientations (Figure 6.4). These observations suggest that the polarized standard PSF should be practical for measuring the positions and orientations of single fluorescent molecules precisely and sensitively. Similar PSF characterization and comparison can be performed by using variance upper bound (VUB). VUB is a global bound of the CRB of the six orientational second moments. While VUB overestimates the mean variance of an orientation measurement by 37%, computing the VUB is $\sim$1000 times faster than evaluating the average CRB across orientation space with sufficient sampling. See more details regarding VUB in Ref. [138].

6.2 Resolving Structural Heterogeneities between Amyloid Fibrils

Next, we explore using SMOLM with the polarized standard PSF and Nile red (NR) for detecting the structural heterogeneity of amyloid fibrils. NR has been used as a surface hydrophobicity sensor for individual protein aggregates by measuring its emission wavelength while transiently and spontaneously bound to fibrils and proto-fibrils [117,118]. In this work, we characterize NR's binding orientation as a method of mapping the organization of β-sheets within amyloid aggregates.

We prepared fibrils of amyloid-β peptide (Aβ42) adhered to cleaned glass-bottom imaging chambers (Sections 2.3.2 and 2.4.2). By adding 50 nM NR and illuminating with a circularly polarized 561-nm laser, we captured isolated fluorescence bursts corresponding to individual NR molecules transiently bound to the amyloid aggregates (Chapter 5) [125,264]. Note that the circularly polarized illumination preferentially pumps NR molecules lying mostly parallel to the coverslip–precisely those molecules for which the polarized PSF has the best sensitivity for measuring orientations and wobbling areas (Figures 2.4 and 6.1C). The brightness (s), 2D position (x, y) and second-moment vector ($\boldsymbol{m}$) of individual NRs within each frame were jointly estimated by using a sparsity-promoting maximum-likelihood estimator [157], followed by a weighted least-square estimator for projecting the estimated second moments to angular coordinates (ϕ, θ, Ω) (Section 2.5.4). For simulated images of NR using the polarized PSF, the estimator shows good accuracy and precision for both localization and orientation measurements, especially for molecules approximately parallel to the coverslip (Figures 6.5-6.9).

The concentrated photon distribution of the polarized PSF enables our estimator to detect relatively dim molecules, providing ∼2.3 localizations/nm on amyloid aggregates over ∼3 min measurement time (Table 6.1). Figure 6.10A shows a super-resolved fibril network. We estimate our localization precision to be 9 nm (std. dev., Figure 6.5, Table 6.1). NR molecules exhibit strikingly different polarized PSFs depending on the long axis of the underlying fibrils (Figure 6.11). Our orientation measurements show mostly in-plane polar angles ($\theta \approx 90°$, Figure 6.12) and azimuthal orientations (ϕ) aligned to the long axis of amyloid

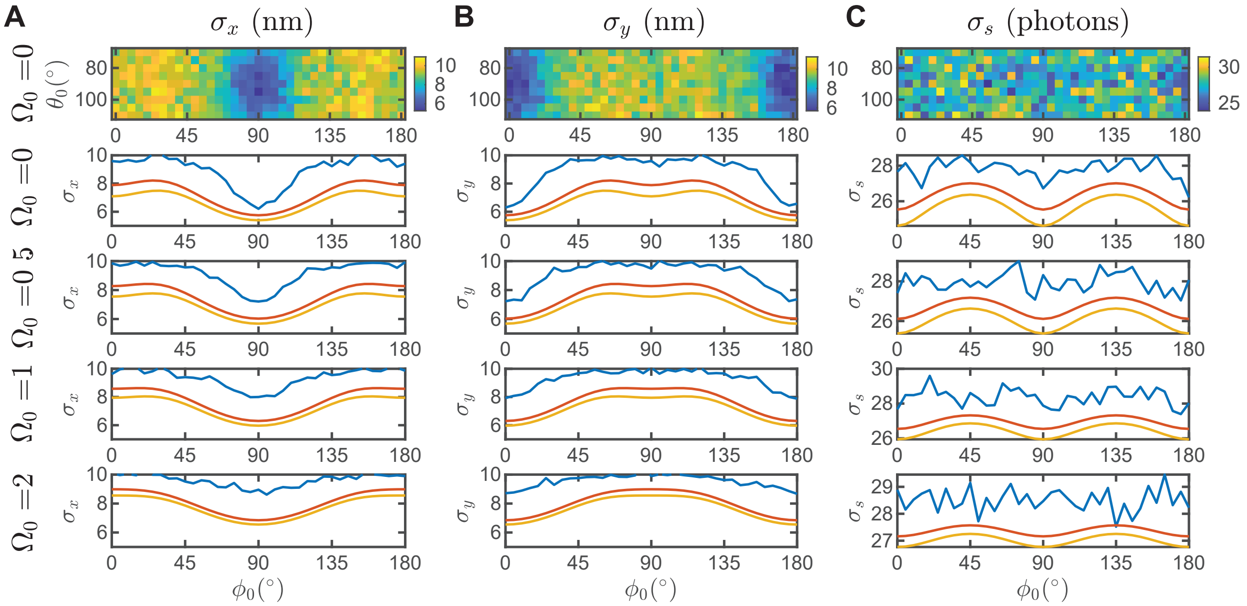

Figure 6.5: SMOLM measurement precision for 2D position (A) σ_x and (B) σ_y and (C) brightness σ_s determined by repeatedly localizing dipoles at various orientations ($\Omega_0 = 0 -$ 2 sr, $\phi_0 = 0 - 180^\circ$, $\theta_0 = 70 - 110^\circ$) in synthesized polarized standard PSF images. At each orientation, 200 independent images were generated with $s_0 = 380$ photons, $b_0 = 2$ background photons/pixel (a total of 266,400 images across 1,332 different orientations). Positions and photons of simulated molecules were estimated as described in Section 2.5.4, and the measurement standard deviation was computed for each ground-truth orientation. Note that the estimator detects all emitters at this SBR, since the localization and signal estimation precisions have little correlation with θ_0, estimation performance was accumulated over all simulated θ_0 and compared against ϕ_0 and Ω_0 (blue lines in the bottom 4 rows). The square root of the CRB for x, y, and s estimations are shown for (red) 20° out-of-plane ($\theta_0 = 70^\circ, 110^\circ$) and (orange) in-plane ($\theta_0 = 90^\circ$) orientations. Reprinted with permission from Ref. [138].

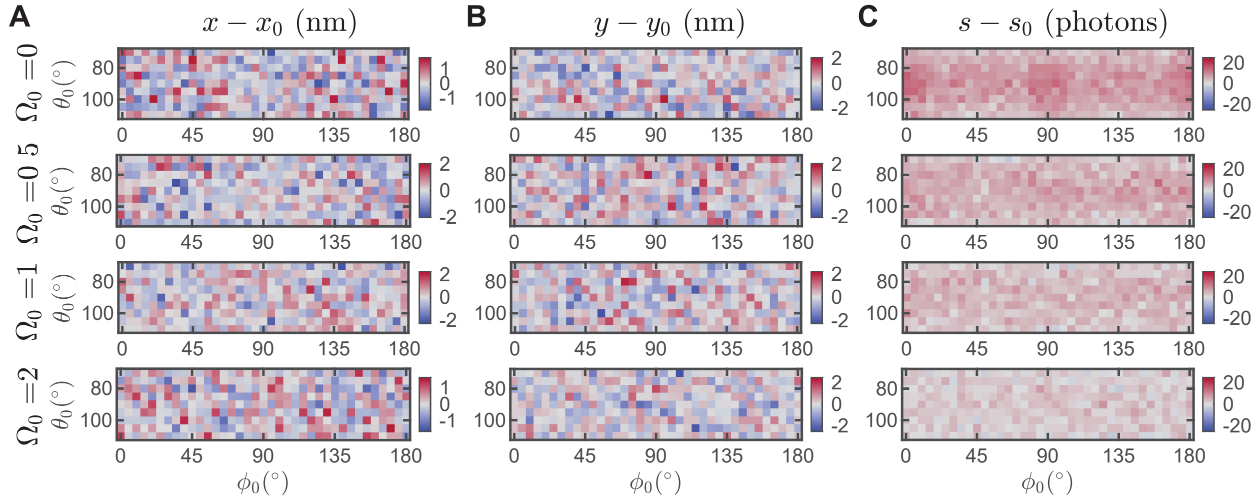

Figure 6.6: SMOLM measurement bias for 2D position (A) $x - x_0$ and (B) $y - y_0$ and (C) brightness $s - s_0$ determined by repeatedly localizing dipoles at various orientations ($\Omega_0 = 0 - 2$ sr, $\phi_0 = 0 - 180^\circ$, $\theta_0 = 70 - 110^\circ$) in synthesized polarized standard PSF images. At each orientation, 200 independent images were generated with $s_0 = 380$ photons, $b_0 = 2$ background photons/pixel (a total of 266,400 images across 1,332 different orientations). Positions and photons of simulated molecules were estimated as described in Section 2.5.4, and the measurement bias was computed by averaging the measurement errors at each ground-truth orientation. Reprinted with permission from Ref. [138].

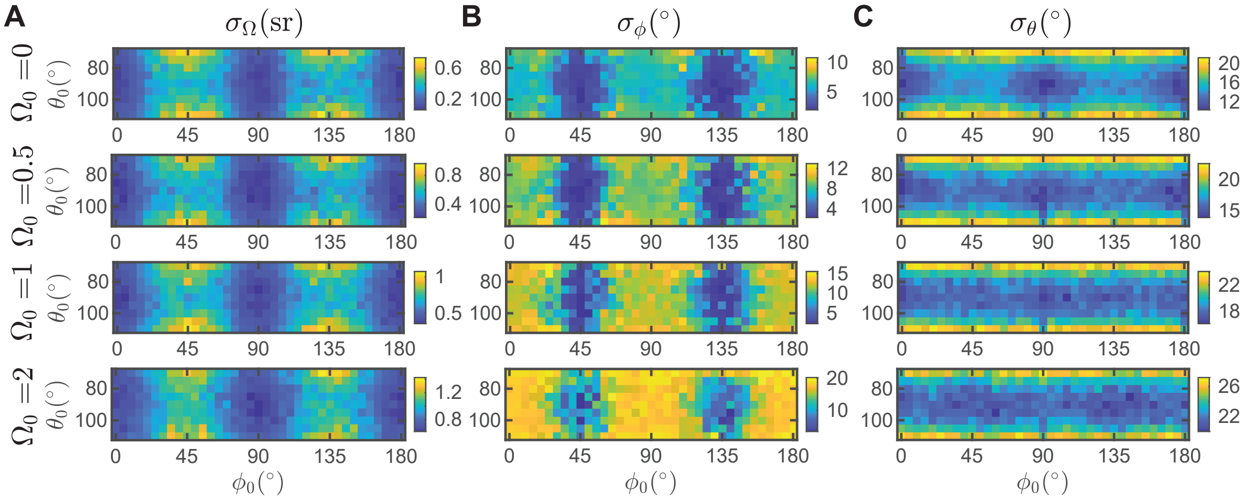

Figure 6.7: SMOLM measurement precision for (A) wobbling area σ_Ω, (B) azimuthal orientation σ_ϕ, and (C) polar orientation σ_θ determined by repeatedly localizing dipoles at various orientations ($\Omega_0 = 0 - 2$ sr, $\phi_0 = 0 - 180°$, $\theta_0 = 70 - 110°$) in synthesized polarized standard PSF images. At each orientation, 200 independent images were generated with $s_0 = 380$ photons, $b_0 = 2$ background photons/pixel (a total of 266,400 images across 1,332 different orientations). Orientations of simulated molecules were estimated as described in Section 2.5.4, and the measurement standard deviation was computed at each ground-truth orientation. Reprinted with permission from Ref. [138].

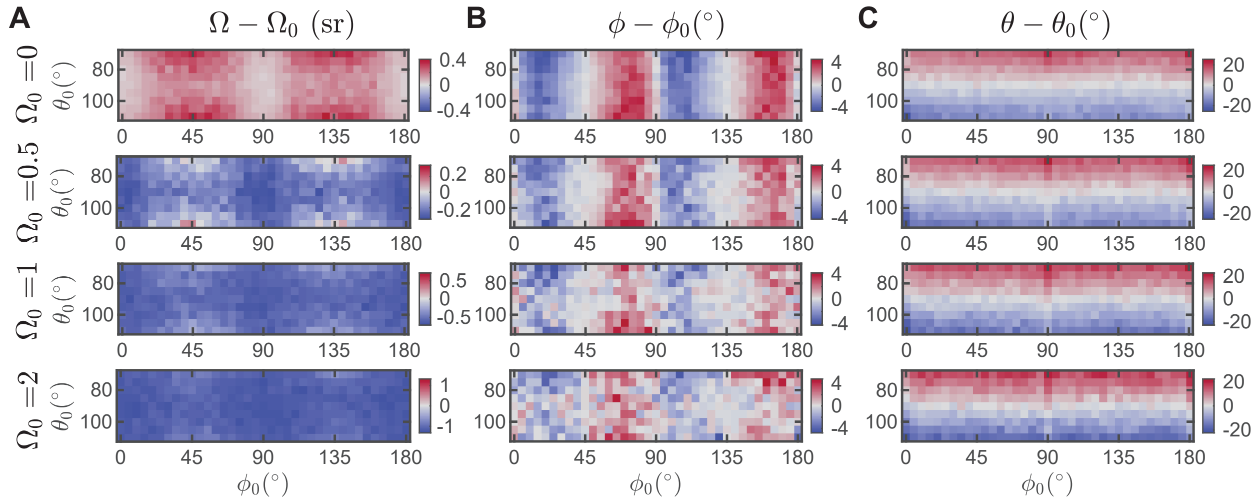

Figure 6.8: SMOLM measurement bias for (A) wobbling area $\Omega - \Omega_0$, (B) azimuthal orientation $\phi - \phi_0$, and (C) polar orientation $\theta - \theta_0$ determined by repeatedly localizing dipoles at various orientations ($\Omega_0 = 0 - 2$ sr, $\phi_0 = 0 - 180°$, $\theta_0 = 70 - 110°$) in synthesized polarized standard PSF images. At each orientation, 200 independent images were generated with $s_0 = 380$ photons, $b_0 = 2$ background photons/pixel (a total of 266,400 images across 1,332 different orientations). Orientations of simulated molecules were estimated as described in Section 2.5.4, and the measurement bias was computed by averaging the measurement errors at each ground-truth orientation. Reprinted with permission from Ref. [138].

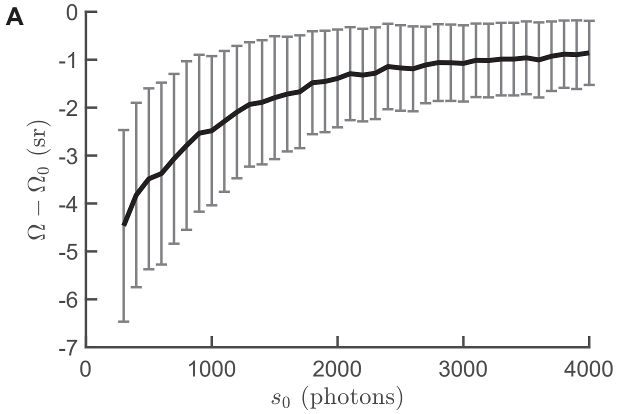

Figure 6.9: SMOLM measurement bias for (A) wobbling area $\Omega - \Omega_0$ and (B) brightness $s - s_0$ determined by repeatedly localizing isotropic emitters ($\Omega_0 = 2\pi$ sr) with various brightnesses ($s_0 = 200 - 4000$ photons) in synthesized images. At each brightness, 5,000 independent images were generated with $b_0 = 2$ background photons/pixel (a total of 195,000 images). The wobbling areas and brightnesses of simulated molecules were estimated as described in Section 2.5.4, and the estimation bias was computed by averaging the measurement errors at each brightness condition s_0. Error bars represent standard deviations of the estimates. Systematic underestimation of the wobbling area, i.e., apparent rotational diffusion that is smaller than the ground truth, is attributed to Poisson shot noise and is consistent with theoretical models [275]. Overestimation of the brightness at 200 photons is due to the filtering (removal) of weak localizations with less than 200 photons detected. Reprinted with permission from Ref. [138].

Table 6.1: Localization numbers, localization density, photons detected per localization, background photons per pixel, and burst on-time of Nile Red molecules on amyloid structures

	Localizations number	Fibril length (µm)	Localizations/µm (per fibril length)	Photons/loc[1] s	Background photons/pixel[1] b	On-time (ms) τ_{on}
FIG. 6.10	88748	37.39	2373	481	2.4	14
FIG. 6.13 a-d	34352	14.51	2368	600	2.2	13
FIG. 6.13 e-h	13351	9.04	1477	460	1.4	17
FIG. 6.15	17425	6.68	2607	566	2.5	14
FIG. 6.16	3466	1.89	1833	443	2.0	13

[1] Median of each statistic.

fibrils (Figures 6.10B-6.10F). These observations confirm that NR molecules preferentially bind to surfaces of β-sheets with their transition dipoles parallel to the fibril backbones (Figure 6.10B inset), similar to the binding behavior of Thioflavin T [258, 276]. NR may bind transiently to grooves formed by adjacent amino acid side chains [32].

Although we observed most NR orientations to be parallel to the fibril backbones, these orientations are not always aligned with one another, even in neighboring structures. For example, two small aggregation limbs shown in Figure 6.10G exhibit substantial differences in the standard deviation of azimuthal orientations (σ_ϕ) and median wobbling area (Ω_{med}), despite looking quite similar in the standard SMLM image. We speculate that this variation arises from structural dissimilarity between these regions, i.e., one of the limbs (Figure 6.10GI) could be a relatively new deposit with disordered binding sites (leading to diverse mean orientations and large wobble), while the other (Figure 6.10GII) is a relatively well-ordered secondary nucleation of a new fibril branch [121, 251]. These structural details of amyloid aggregates cannot be detected by standard SMLM.

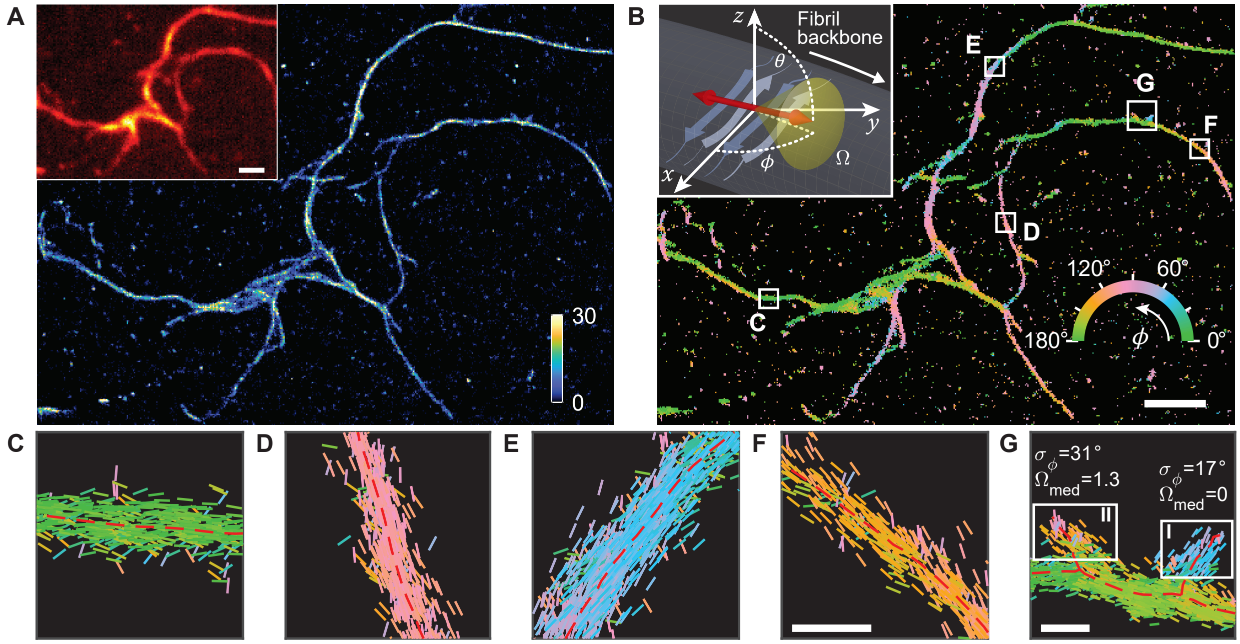

Figure 6.10: Transient amyloid binding (TAB) SMLM and SMOLM images acquired using Nile red (NR). (A) SMLM image of a network of Aβ42 fibrils. Color bar: localizations per bin (20×20 nm^2). Inset: diffraction-limited image. (B) TAB SMOLM image, color-coded according to the mean azimuthal (ϕ) orientation of NR molecules measured within each bin. Inset: Main binding mode of NR to β-sheets, i.e., dipole moments aligned mostly parallel to the long axis of a fibril (its backbone). (C-G) All individual orientation measurements localized along fibril backbones within the white boxes in B. The lines are oriented and color-coded according to the direction of the estimated ϕ angle. Red dashed lines depict fibril backbones estimated from the SMLM image. Scale bars: A,B 1 µm, F,G 100 nm. Adapted and reprinted with permission from Ref. [138].

To further correlate the orientations of single-molecule probes with the structural organization of amyloid aggregates, we imaged an amyloid aggregate containing obvious fibril bundles (Figure 6.13A). The intertwined structures are evidenced by their branching architecture and their at least twice larger width (purple) compared to thinner structures (green) in the field of view (Figure 6.14). We observed NR to be mostly parallel to the backbone (Figures 6.13BI, 6.13CI) of the thin fibrils, whereas thicker bundles cause NR to bind with relatively disordered ϕ angles (Figures 6.13BII, 6.13CII). Since NR binds to specific grooves along the stacked β-sheet aggregate, these orientation measurements indicate

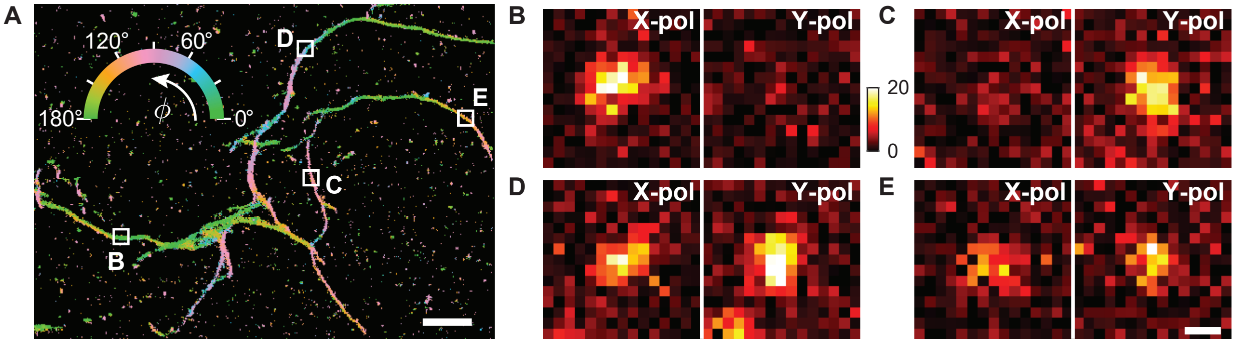

Figure 6.11: Fluorescence images of NR molecules on fibrils. (A) TAB SMOLM image, color-coded according to the mean azimuthal (ϕ) orientation of the NR molecules measured within each bin (20×20 nm^2). (B-E) Representative fluorescence raw images of single NR molecules on the fibril network shown in Figure 6.10. The observed polarized images of NR molecules exhibit substantial differences depending on the orientation of the underlying fibril structures [B $\phi_{\text{avg}} = 176°$, C $\phi_{\text{avg}} = 108°$, D $\phi_{\text{avg}} = 50°$, and E $\phi_{\text{avg}} = 140°$]. Color bar: photons/pixel. Images contain B 290, C 334, D 523, and E 336 detected photons across both polarized images. Scale bars: A 1 µm, E 200 nm. Reprinted with permission from Ref. [138].

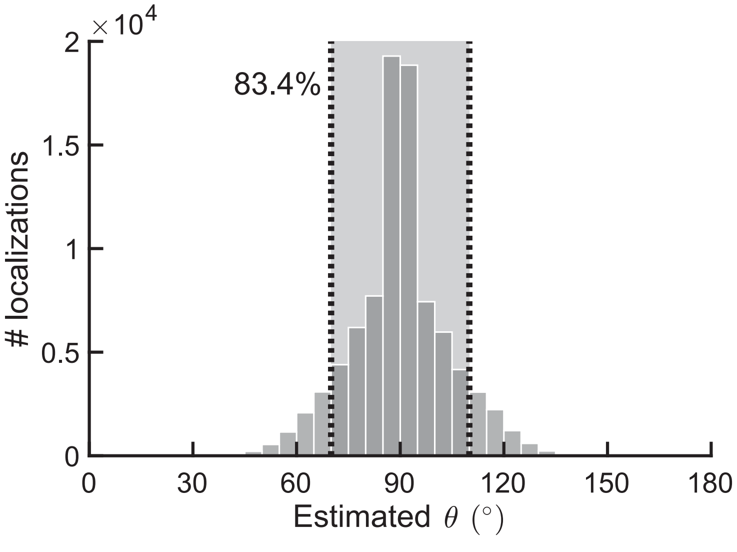

Figure 6.12: The estimated polar orientations θ of Nile red molecules on fibrils show small out-of-plane angles. NR molecules with near in-plane polar orientations ($70° < \theta < 110°$) dominate ($> 83\%$) the distribution. These data correspond to the fibrils shown in Figure 6.10. Reprinted with permission from Ref. [138].

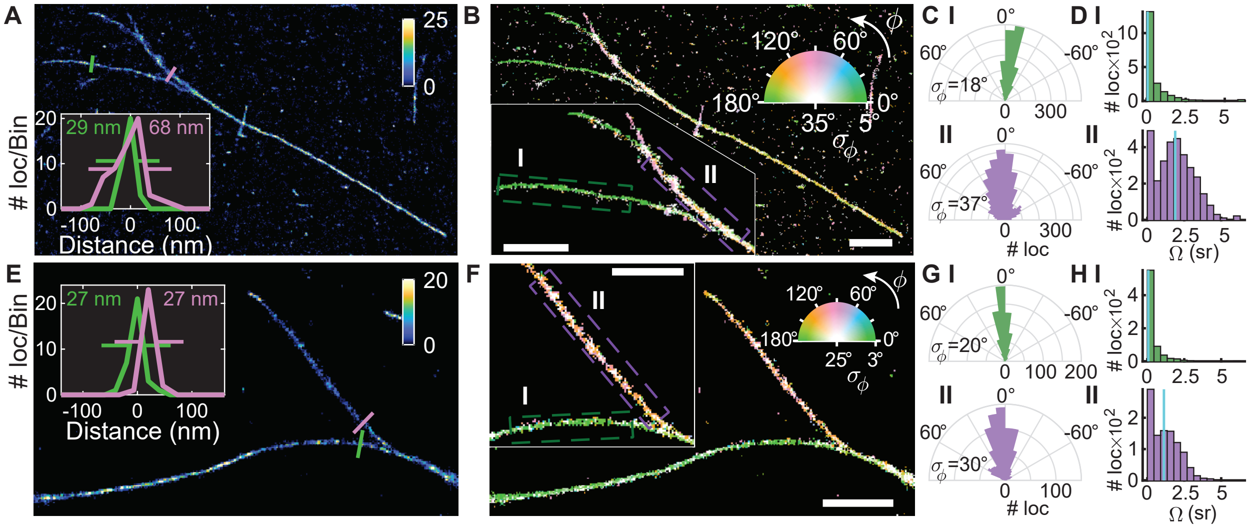
A
25
0
# loc/Bin
20
10
0
29 nm
68 nm
-100
0
100
Distance (nm)
B
ϕ
120°
60°
180°
0°
35°
5°
σ_ϕ
I
II
C I
0°
60°
-60°
σ_ϕ=18°
0
300
II
0°
60°
-60°
σ_ϕ=37°
0
300
# loc
D I
# loc×10^2
10
5
0
0
2.5
5
II
# loc×10^2
4
2
0
0
2.5
5
Ω (sr)
E
20
0
# loc/Bin
20
10
0
27 nm
27 nm
-100
0
100
Distance (nm)
F
II
I
ϕ
120°
60°
180°
0°
25°
3°
σ_ϕ
G I
0°
60°
-60°
σ_ϕ=20°
0
100
200
II
0°
60°
-60°
σ_ϕ=30°
0
100
# loc
H I
# loc×10^2
4
2
0
0
2.5
5
II
# loc×10^2
2
1
0
0
2.5
5
Ω (sr)

Figure 6.13: Structural heterogeneity of Aβ42 fibrils revealed by TAB SMOLM imaging. (A) SMLM image of fibril bundles. Color bar: localizations per bin (20×20 nm^2). Inset: fibril cross-sections at the locations denoted by green and purple lines with measured full-width at half-maximum (FWHM) thicknesses. (B) TAB SMOLM image corresponding to A, color-coded according to the mean (ϕ) and standard deviation (σ_ϕ) of the azimuthal orientation measured within each bin. Inset: zoomed (I) thin and (II) thick fibril regions isolated from background structures. (C) Histograms of measured azimuthal orientations relative to the fibril backbone within the regions denoted in B, showing standard deviations (σ_ϕ) of I 18° and II 37°. (D) Measured wobbling areas (Ω) corresponding to the localizations in C, yielding median wobbling areas (Ω_{med}, cyan) of I 0.07 sr and II 1.89 sr. (E-H) TAB SMLM and SMOLM images of another fibril field of view, as in A-D. Although fibril regions I and II in the inset of F show little difference in apparent width, the measured orientation distributions contain significant differences. The standard deviations of azimuthal angles σ_ϕ are I 20° vs II 30°, and the median wobbling areas (Ω_{med}, cyan) are I 0.07 sr vs II 1.12 sr. Scale bars: 1 µm. Reprinted with permission from Ref. [138].

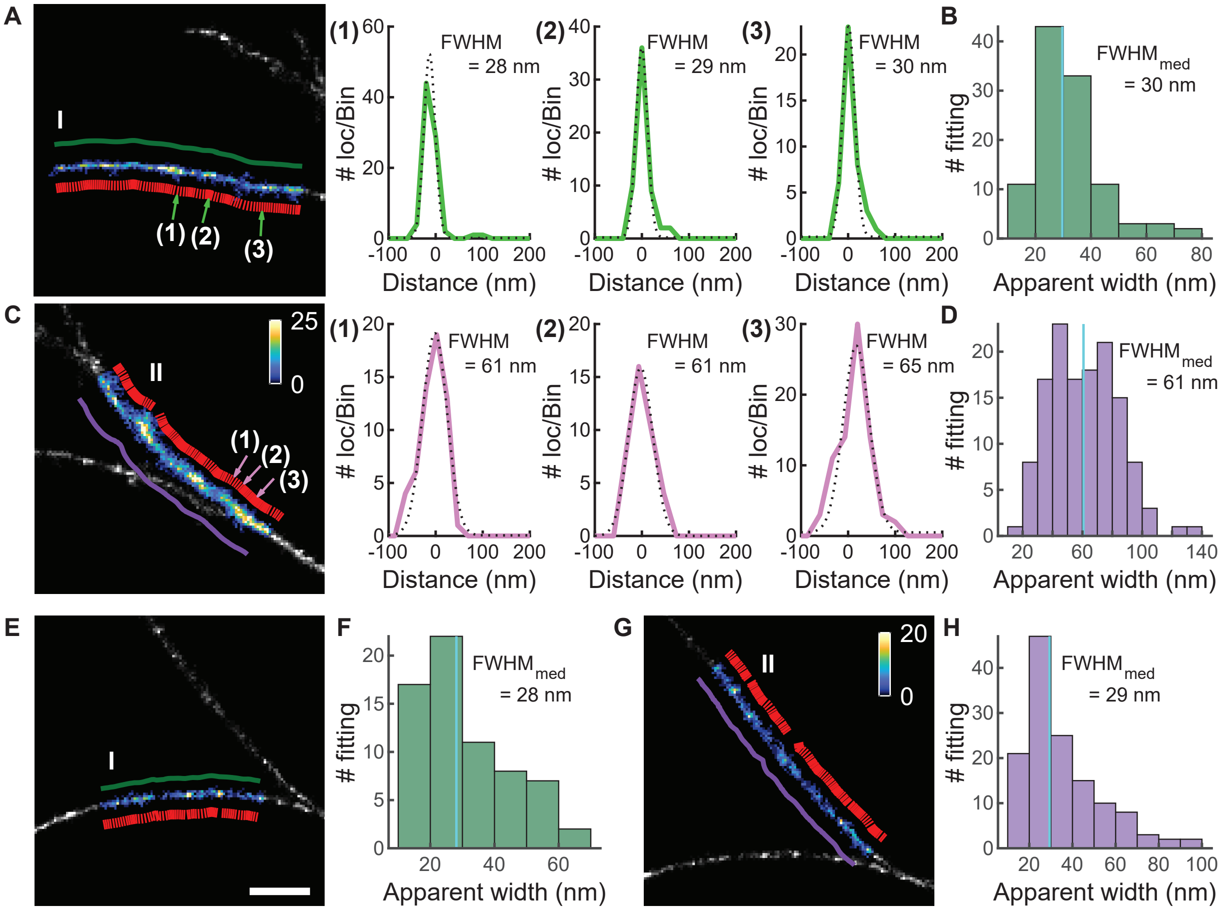

Figure 6.14: Measurements of fibril apparent widths for the regions in Figure 6.13. (A) Zoomed-in SMLM image of the fibril shown in Figures. 6.13A-DI. The green line depicts the detected backbone in this region. The red lines represent each cross-sectional profile aligned perpendicular to the ridge. Three representative width profiles (green) and their Gaussian fits (dotted black) are shown in (1-3) with the estimated FWHM. (B) All apparent fibril widths within the region shown in A. The median FWHM is 30 nm. (C) Zoomed-in SMLM image of the fibril bundle shown in Figures 6.13A-DII and its representative cross-sectional profiles. (D) All apparent fibril widths within the region shown in C. The median FWHM is 61 nm. (E-H) Zoomed-in SMLM images of the fibrils shown in Figures 6.13E-HI and II, and the distribution of fitted FWHMs in the two regions. The median apparent widths are I 28 nm and II 29 nm respectively. Scale bar: 500 nm. Color bars: localizations/bin. Reprinted with permission from Ref. [138].

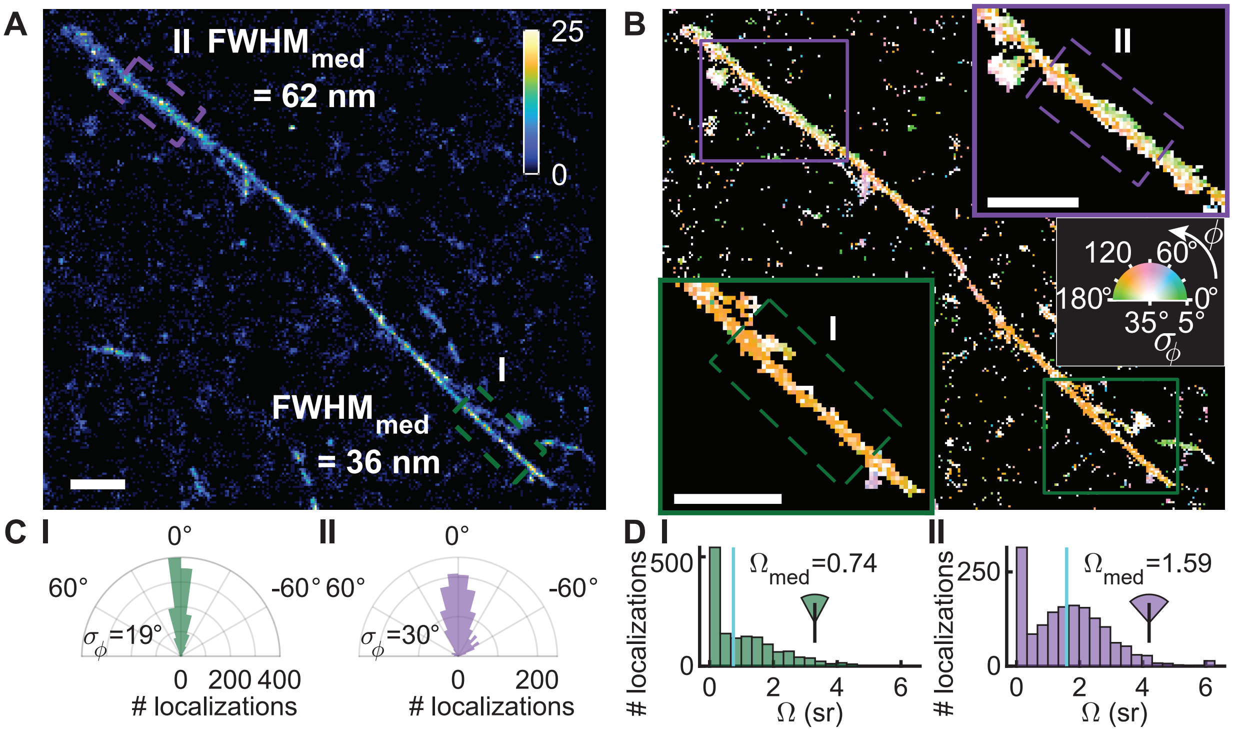

Figure 6.15: Structural heterogeneity of Aβ42 fibrils revealed by TAB SMOLM imaging I. (A) SMLM image of a fibril. Color bar: localizations per bin (20×20 nm^2). Apparent fibril widths represented by FWHM are (I) 36 nm and (II) 62 nm in the regions denoted by (I) green and (II) purple boxes. (B) TAB SMOLM image corresponding to A, color-coded according to the mean azimuthal angle (ϕ) and standard deviation of the orientations (σ_ϕ) measured within each bin. Insets: zoomed (I) thin and (II) thick fibril regions isolated from background structures. (C) Distributions of NR azimuthal orientations relative to the fibril backbone within the regions denoted in B. The standard deviations (σ_ϕ) in relative backbone angle are I 19° and II 30°. (D) Histograms of the measured wobbling area (Ω) corresponding to the localizations in C. The median wobbling areas (Ω_{med}) are I 0.74 sr and II 1.59 sr. Scale bars: 500 nm. Reprinted with permission from Ref. [138].

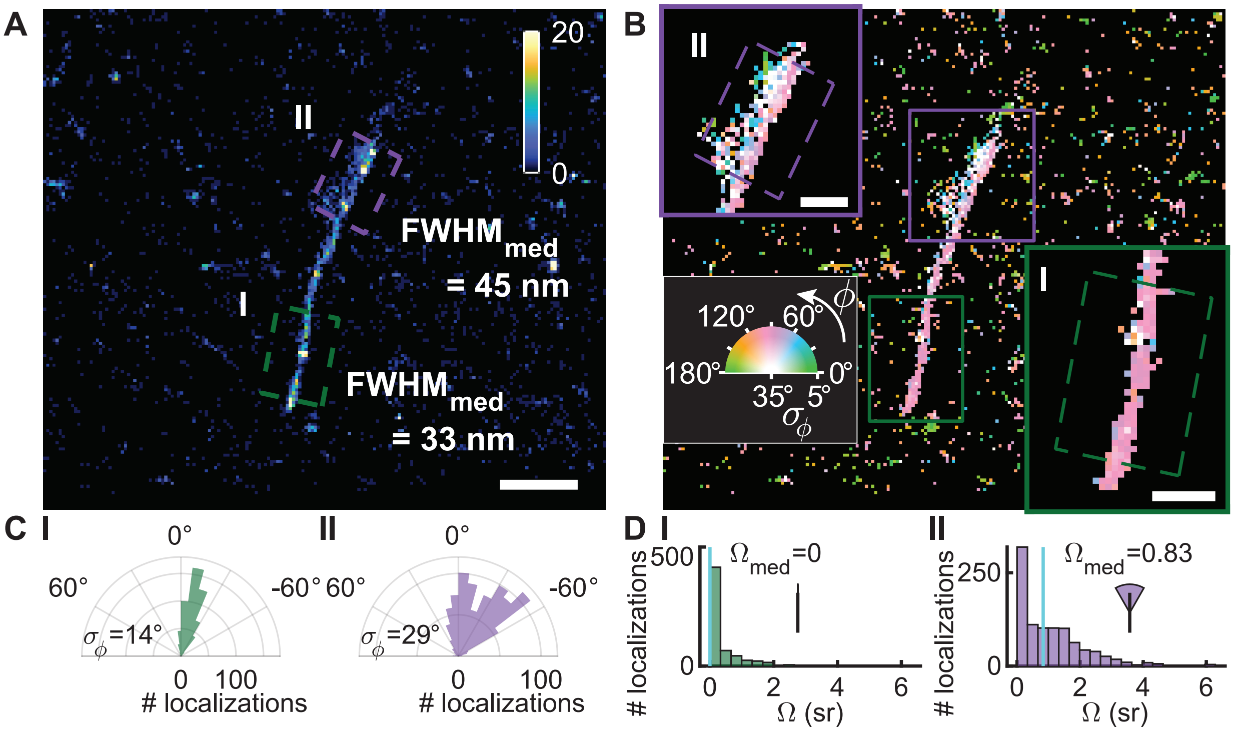

Figure 6.16: Structural heterogeneity of Aβ42 fibrils revealed by TAB SMOLM imaging II. (A) SMLM image of a fibril. Color bar: localizations per bin (20×20 nm^2). Scale bar: 500 nm. Apparent fibril widths represented by FWHM are (I) 33 nm and (II) 45 nm in the regions denoted by (I) green and (II) purple boxes. (B) TAB SMOLM image corresponding to A, color-coded according to the mean azimuthal angle (ϕ) and standard deviation of the orientations (σ_ϕ) measured within each bin. Inset: zoomed (I) thin and (II) thick fibril regions isolated from background structures. Scale bars: 200 nm. (C) Distributions of NR azimuthal orientations relative to the fibril backbone within the regions denoted in B. The standard deviations (σ_ϕ) in relative backbone angle are I 18° and II 29°. (D) Histograms of the measured wobbling area (Ω) corresponding to the localizations in C. The median wobbling areas (Ω_{med}) are I 0 sr and II 0.83 sr. Reprinted with permission from Ref. [138].

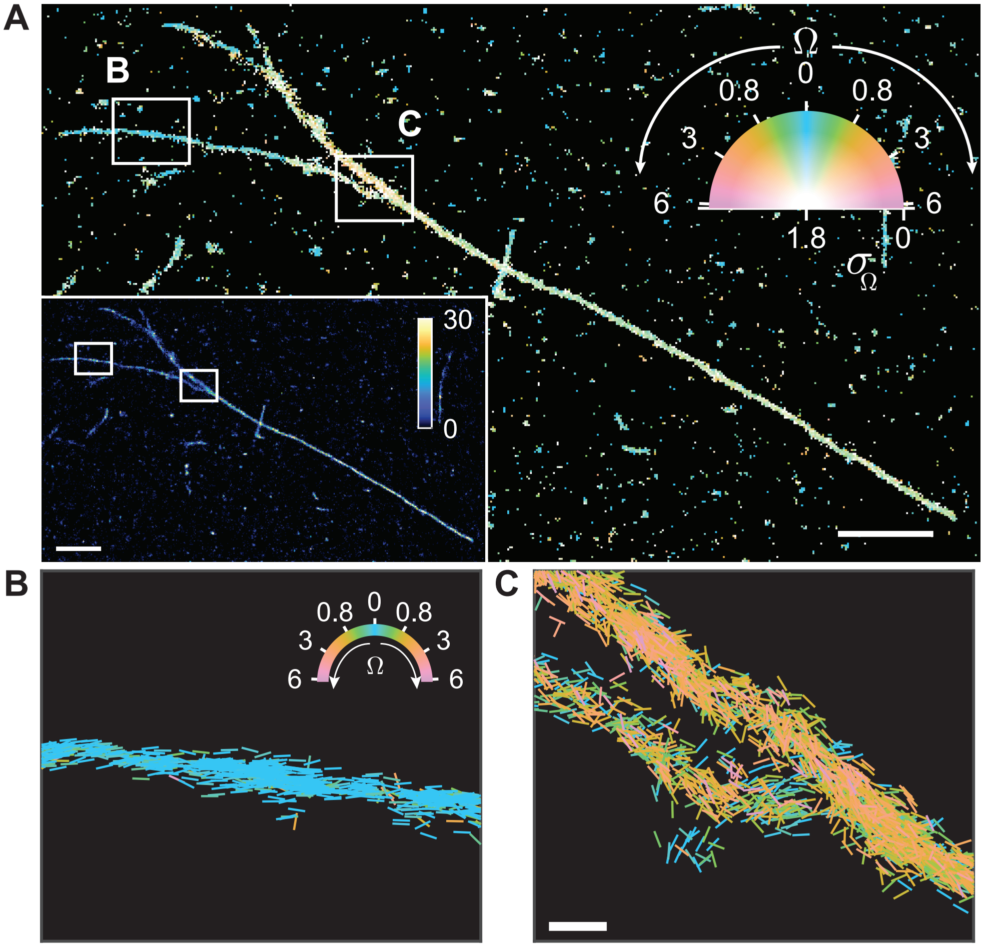

Figure 6.17: Estimated wobbling area Ω of NR molecules on amyloid fibrils. (A) TAB SMOLM image, color-coded according to the mean wobbling area (Ω, sr) and standard deviation of the rotational diffusion (σ_Ω) measured within each bin. Inset: SMLM image of the fibril bundles. Color bar: localizations per bin (20×20 nm^2). Scale bar: 1 µm. (B,C) All individual wobbling measurements localized along fibril backbones within the white boxes in A. The lines represent the direction of the estimated ϕ of each localization and are color-coded according to the estimated Ω. Scale bar: 100 nm. These data correspond to the fibril bundles shown in Figures.6.13A-D in the main text. Reprinted with permission from Ref. [138].

highly aligned β-sheets within the thin fibrils. We consistently observed similarly disordered ϕ orientations of NR on thicker aggregates compared to thinner structures (Figures 6.15 and 6.16). These disordered ϕ angles show that the β-sheets within bundles of amyloid fibrils exhibit a complex and heterogeneous architecture.

We note that the wobbling area Ω, which can indicate the binding strength between NR and the surrounding β-sheet grooves, also exhibits obvious differences between the two regions. We observed small Ω values on the thin fibril (Figures 6.13DI, 6.17A, and 6.17B) and large wobbling on the fibril bundle (Figures 6.13DII, 6.17A, and 6.17C) that represent tight and loose binding of NR molecules to each local region, respectively. From these measurements, we speculate that fibril bundling not only produces relatively disordered β-sheet orientations due to the entwining of multiple fibers but also increases dramatically the local density of binding sites for NR, thereby causing large NR wobbling during a single fluorescence burst. Note that we did not observe significantly different burst times for NR on thin fibers ($\tau_{\text{on}} = 13$ ms in Figure 6.13BI) versus disordered fibrillar bundles ($\tau_{\text{on}} = 11$ ms in Figure 6.13BII).

Interestingly, the local structural heterogeneity in amyloid fibrils detected by SMOLM is not always associated with thicker fibrils in standard SMLM. We observed similar disordered ϕ values and large Ω estimates from a fibril in another field of view (Figure 6.13E). Although the two fibril strands have similar thickness, the estimated ϕ and Ω distributions show noticeable differences (Figure 6.13F-6.13H). These measurements suggest the fibril in Figure 6.13FII may consist of more disorganized assemblies of β-sheets compared to those of Figure 6.13FI. Similar to the small aggregates shown in Figure 6.10G, the local heterogeneity cannot be resolved by conventional SMLM.

6.3 Outlook

Here, we characterize and compare the CRB of various PSFs for measuring the orientation and wobble of dipole-like emitters. We discover that imaging dipoles near a refractive index interface enables the simple polarized standard PSF to robustly measure orientational dynamics, particularly within the xy plane, that cannot be detected in matched media. Our analysis also shows that no single PSF measures all combinations of orientational second moments with optimal precision. Therefore, selection of a suitable PSF based on *a prior* knowledge or adaptively optimizing PSFs during measurements is essential for practical simultaneous imaging of SM positions and orientations.

Using the polarized standard PSF, our SMOLM images of amyloid aggregates confirm that the main binding orientation of NR is mostly parallel to the long axis of the fibrils. In cases where multiple fibrils are intertwined, TAB SMOLM detects heterogeneities in the stacking of β-sheets via larger variations in NR orientations and increased wobbling areas. In particular, SMOLM detects structural disorder along the fibrillar network which cannot be resolved by simple SMLM analysis of fibrillar width or NR binding time.

Simultaneous imaging of SM positions and orientations in SMOLM allows scientists to quantify local structural features on a nanometer scale without ensemble averaging. In particular, measuring the full spatial configuration (i.e., positions and orientations) of molecules provides unprecedented insight into the density and orientations of binding sites for NR on aggregate surfaces that aren't revealed with location information alone. These distributions could be a signature of how the stacked β-sheets are organized within fibrils and other aggregate morphologies.

Currently, no methodology can visualize the nanoscale structural configuration of amyloid aggregates as they organize over time at the single particle level [121]. In the future, SMOLM combined with transient binding of amyloid-sensitive fluorogenic molecules could become a powerful tool for understanding how structure affects various aggregation processes, such as “stop-and-go” and polarized aggregation [133, 136, 251] as well as the switching of aggregation modes [277], with nanoscale resolution over periods of hours to days [125,264]. Time-lapse SMOLM imaging of amyloidophilic dye-binding sites on aggregate surfaces could provide insight into amyloid assembly mechanisms [131–133] by connecting the energy landscapes of these pathways to β-sheet organization over time (Figure 1.13). Finally, TAB SMOLM imaging of amyloid aggregates on model membranes and neurons may provide links between aggregate structure and toxicity necessary for developing effective therapeutics against amyloidosis.

References

[1] W. E. Moerner and L. Kador, “Optical detection and spectroscopy of single molecules in a solid,” *Physical Review Letters*, vol. 62, pp. 2535–2538, 5 1989.

[2] E. Betzig and R. J. Chichester, “Single Molecules Observed by Near-Field Scanning Optical Microscopy,” *Science*, vol. 262, pp. 1422–1425, 11 1993.

[3] X. S. Xie, “Single-Molecule Spectroscopy and Dynamics at Room Temperature,” *Accounts of Chemical Research*, vol. 29, pp. 598–606, 1 1996.

[4] W. E. Moerner and D. P. Fromm, “Methods of single-molecule fluorescence spectroscopy and microscopy,” *Review of Scientific Instruments*, vol. 74, pp. 3597–3619, 8 2003.

[5] O. L. J. Harriman and M. C. Leake, “Single molecule experimentation in biological physics: exploring the living component of soft condensed matter one molecule at a time,” *Journal of Physics: Condensed Matter*, vol. 23, p. 503101, 12 2011.

[6] H. Arjmandi-Tash, L. A. Belyaeva, and G. F. Schneider, “Single molecule detection with graphene and other two-dimensional materials: nanopores and beyond,” *Chemical Society Reviews*, vol. 45, no. 3, pp. 476–493, 2016.

[7] A. Ameur, W. P. Kloosterman, and M. S. Hestand, “Single-Molecule Sequencing: Towards Clinical Applications,” *Trends in Biotechnology*, vol. 37, pp. 72–85, 1 2019.

[8] M. A. Thompson, M. D. Lew, M. Badieirostami, and W. E. Moerner, “Localizing and Tracking Single Nanoscale Emitters in Three Dimensions with High Spatiotemporal Resolution Using a Double-Helix Point Spread Function,” *Nano Letters*, vol. 10, pp. 211–218, 1 2010.

[9] K. I. Mortensen, L. S. Churchman, J. A. Spudich, and H. Flyvbjerg, “Optimized localization analysis for single-molecule tracking and super-resolution microscopy,” *Nature Methods*, vol. 7, no. 5, pp. 377–381, 2010.

[10] A. Gahlmann and W. E. Moerner, “Exploring bacterial cell biology with single-molecule tracking and super-resolution imaging,” *Nature Reviews Microbiology*, vol. 12, no. 1, pp. 9–22, 2014.

[11] W. Liu, F. Yu, J. Yang, B. Xiang, P. Xiao, and L. Wang, “3D Single-Molecule Imaging of Transmembrane Signaling by Targeting Nanodiamonds,” *Advanced Functional Materials*, vol. 26, no. 3, pp. 365–375, 2016.

[12] C. J. Comerci, J. Herrmann, J. Yoon, F. Jabbarpour, X. Zhou, J. F. Nomellini, J. Smit, L. Shapiro, S. Wakatsuki, and W. E. Moerner, “Topologically-guided continuous protein crystallization controls bacterial surface layer self-assembly,” *Nature Communications*, vol. 10, p. 2731, 12 2019.

[13] S. A. McKinney, C. Joo, and T. Ha, “Analysis of single-molecule FRET trajectories using hidden Markov modeling,” *Biophysical Journal*, vol. 91, no. 5, pp. 1941–1951, 2006.

[14] R. Roy, S. Hohng, and T. Ha, “A practical guide to single-molecule FRET,” *Nature Methods*, vol. 5, pp. 507–516, 6 2008.

[15] T. Ha and P. Tinnefeld, “Photophysics of Fluorescent Probes for Single-Molecule Biophysics and Super-Resolution Imaging,” *Annual Review of Physical Chemistry*, vol. 63, pp. 595–617, 5 2012.

[16] K. C. Neuman and A. Nagy, “Single-molecule force spectroscopy: optical tweezers, magnetic tweezers and atomic force microscopy,” *Nature Methods*, vol. 5, pp. 491–505, 6 2008.

[17] J. L. Killian, F. Ye, and M. D. Wang, “Optical Tweezers: A Force to Be Reckoned With,” *Cell*, vol. 175, pp. 1445–1448, 11 2018.

[18] J. M. Brockman, A. T. Blanchard, V. Pui-Yan, W. D. Derricotte, Y. Zhang, M. E. Fay, W. A. Lam, F. A. Evangelista, A. L. Mattheyses, and K. Salaita, “Mapping the 3D orientation of piconewton integrin traction forces,” *Nature Methods*, vol. 15, pp. 115–118, 2 2018.

[19] J. van Mameren, K. Vermeulen, G. J. L. Wuite, and E. J. G. Peterman, “A polarized view on DNA under tension,” *The Journal of Chemical Physics*, vol. 148, p. 123306, 3 2018.

[20] A. S. Backer, A. S. Biebricher, G. A. King, G. J. L. Wuite, I. Heller, and E. J. G. Peterman, “Single-molecule polarization microscopy of DNA intercalators sheds light on the structure of S-DNA,” *Science Advances*, vol. 5, p. eaav1083, 3 2019.

[21] C. P. Toseland, “Fluorescent labeling and modification of proteins,” *Journal of Chemical Biology*, vol. 6, pp. 85–95, 7 2013.

[22] H. Li and J. C. Vaughan, “Switchable Fluorophores for Single-Molecule Localization Microscopy,” *Chemical Reviews*, vol. 118, pp. 9412–9454, 9 2018.

[23] E. Betzig, "Single Molecules, Cells, and Super-Resolution Optics (Nobel Lecture)," *Angewandte Chemie International Edition*, vol. 54, pp. 8034–8053, 7 2015.

[24] W. E. Moerner, "Single-Molecule Spectroscopy, Imaging, and Photocontrol: Foundations for Super-Resolution Microscopy (Nobel Lecture)," *Angewandte Chemie International Edition*, vol. 54, pp. 8067–8093, 7 2015.

[25] E. Abbe, "Beiträge zur Theorie des Mikroskops und der mikroskopischen Wahrnehmung," *Archiv für Mikroskopische Anatomie*, vol. 9, pp. 413–468, 12 1873.

[26] S. J. Sahl and W. E. Moerner, "Super-resolution fluorescence imaging with single molecules," *Current Opinion in Structural Biology*, vol. 23, no. 5, pp. 778–787, 2013.

[27] H. Deschout, F. Cella Zanacchi, M. Mlodzianoski, A. Diaspro, J. Bewersdorf, S. T. Hess, and K. Braeckmans, "Precisely and accurately localizing single emitters in fluorescence microscopy.," *Nature methods*, vol. 11, no. 3, pp. 253–66, 2014.

[28] B. Valeur, *Molecular Fluorescence: Principles and Applications.* Wiley-VCH, 2002.

[29] L. Novotny and B. Hecht, *Principles of Nano-Optics.* Cambridge University Press, 2007.

[30] A. Fürstenberg, M. D. Julliard, T. G. Deligeorgiev, N. I. Gadjev, A. A. Vasilev, and E. Vauthey, "Ultrafast Excited-State Dynamics of DNA Fluorescent Intercalators: New Insight into the Fluorescence Enhancement Mechanism," *Journal of the American Chemical Society*, vol. 128, pp. 7661–7669, 6 2006.

[31] V. I. Stsiapura, A. A. Maskevich, V. A. Kuzmitsky, V. N. Uversky, I. M. Kuznetsova, and K. K. Turoverov, "Thioflavin T as a Molecular Rotor: Fluorescent Properties of Thioflavin T in Solvents with Different Viscosity," *The Journal of Physical Chemistry B*, vol. 112, pp. 15893–15902, 12 2008.

[32] M. Biancalana and S. Koide, "Molecular mechanism of Thioflavin-T binding to amyloid fibrils," *Biochimica et Biophysica Acta - Proteins and Proteomics*, vol. 1804, no. 7, pp. 1405–1412, 2010.

[33] L.-M. Needham, J. Weber, J. A. Varela, J. W. B. Fyfe, D. T. Do, C. K. Xu, L. Tutton, R. Cliffe, B. Keenlyside, D. Klenerman, C. M. Dobson, C. A. Hunter, K. H. Müller, K. O'Holleran, S. E. Bohndiek, T. N. Snaddon, and S. F. Lee, "ThX – a next-generation probe for the early detection of amyloid aggregates," *Chemical Science*, vol. 11, no. 18, pp. 4578–4583, 2020.

[34] P. Greenspan and S. D. Fowler, "Spectrofluorometric studies of the lipid probe, nile red," *Journal of Lipid Research*, vol. 26, no. 7, pp. 781–789, 1985.

[35] D. L. Sackett and J. Wolff, "Nile red as a polarity-sensitive fluorescent probe of hydrophobic protein surfaces," *Analytical Biochemistry*, vol. 167, pp. 228–234, 12 1987.

[36] A. Sharonov and R. M. Hochstrasser, "Wide-field subdiffraction imaging by accumulated binding of diffusing probes.," *Proceedings of the National Academy of Sciences of the United States of America*, vol. 103, pp. 18911–6, 12 2006.

[37] C. E. Aitken, R. A. Marshall, and J. D. Puglisi, "An oxygen scavenging system for improvement of dye stability in single-molecule fluorescence experiments," *Biophysical Journal*, vol. 94, no. 5, pp. 1826–1835, 2008.

[38] M. T. Hoffman, J. Sheung, and P. R. Selvin, "Fluorescence Imaging with One Nanometer Accuracy: In Vitro and In Vivo Studies of Molecular Motors," in *Single Molecule Enzymology: Methods and Protocols*, vol. 778, pp. 33–56, Springer Nature, 2011.

[39] S. F. Lee, Q. Vérolet, and A. Fürstenberg, "Improved Super-Resolution Microscopy with Oxazine Fluorophores in Heavy Water," *Angewandte Chemie International Edition*, vol. 52, pp. 8948–8951, 8 2013.

[40] L. Nahidiazar, A. V. Agronskaia, J. Broertjes, B. van den Broek, and K. Jalink, "Optimizing Imaging Conditions for Demanding Multi-Color Super Resolution Localization Microscopy," *PLOS ONE*, vol. 11, p. e0158884, 7 2016.

[41] M. Sauer and M. Heilemann, "Single-Molecule Localization Microscopy in Eukaryotes," *Chemical Reviews*, vol. 117, pp. 7478–7509, 6 2017.

[42] H. Sosa, E. J. Peterman, W. E. Moerner, and L. S. Goldstein, "ADP-induced rocking of the kinesin motor domain revealed by single-molecule fluorescence polarization microscopy," *Nature Structural Biology*, vol. 8, no. 6, pp. 540–544, 2001.

[43] E. J. Peterman, H. Sosa, L. S. Goldstein, and W. Moerner, "Polarized Fluorescence Microscopy of Individual and Many Kinesin Motors Bound to Axonemal Microtubules," *Biophysical Journal*, vol. 81, pp. 2851–2863, 11 2001.

[44] L. G. Lippert, T. Dadosh, J. A. Hadden, V. Karnawat, B. T. Diroll, C. B. Murray, E. L. Holzbaur, K. Schulten, S. L. Reck-Peterson, and Y. E. Goldman, "Angular measurements of the dynein ring reveal a stepping mechanism dependent on a flexible stalk," *Proceedings of the National Academy of Sciences of the United States of America*, vol. 114, no. 23, pp. E4564–E4573, 2017.

[45] T. Ha, J. Glass, T. Enderle, D. S. Chemla, and S. Weiss, "Hindered Rotational Diffusion and Rotational Jumps of Single Molecules," *Physical Review Letters*, vol. 80, no. 10, pp. 2093–2096, 1998.

[46] A. S. Backer, M. Y. Lee, and W. E. Moerner, “Enhanced DNA imaging using super-resolution microscopy and simultaneous single-molecule orientation measurements,” *Optica*, vol. 3, p. 659, 6 2016.

[47] B. Dong, Y. Pei, N. Mansour, X. Lu, K. Yang, W. Huang, and N. Fang, “Deciphering nanoconfinement effects on molecular orientation and reaction intermediate by single molecule imaging,” *Nature Communications*, vol. 10, p. 4815, 12 2019.

[48] N. Karedla, S. C. Stein, D. Hähnel, I. Gregor, A. Chizhik, and J. Enderlein, “Simultaneous Measurement of the Three-Dimensional Orientation of Excitation and Emission Dipoles,” *Physical Review Letters*, vol. 115, p. 173002, 10 2015.

[49] R. Kumarasinghe, E. D. Higgins, T. Ito, and D. A. Higgins, “Spectroscopic and Polarization-Dependent Single-Molecule Tracking Reveal the One-Dimensional Diffusion Pathways in Surfactant-Templated Mesoporous Silica,” *The Journal of Physical Chemistry C*, vol. 120, pp. 715–723, 1 2016.

[50] W. R. Legant, L. Shao, J. B. Grimm, T. A. Brown, D. E. Milkie, B. B. Avants, L. D. Lavis, and E. Betzig, “High-density three-dimensional localization microscopy across large volumes.,” *Nature methods*, vol. 13, no. January, pp. 1–9, 2016.

[51] A.-K. Gustavsson, P. N. Petrov, M. Y. Lee, Y. Shechtman, and W. E. Moerner, “3D single-molecule super-resolution microscopy with a tilted light sheet,” *Nature Communications*, vol. 9, no. 1, p. 123, 2018.

[52] A.-K. Gustavsson, P. N. Petrov, and W. E. Moerner, “Light sheet approaches for improved precision in 3D localization-based super-resolution imaging in mammalian cells [Invited],” *Optics Express*, vol. 26, p. 13122, 5 2018.

[53] Y. Li, Y. Hu, and H. Cang, “Light Sheet Microscopy for Tracking Single Molecules on the Apical Surface of Living Cells,” *The Journal of Physical Chemistry B*, vol. 117, pp. 15503–15511, 12 2013.

[54] M. B. M. Meddens, S. Liu, P. S. Finnegan, T. L. Edwards, C. D. James, and K. A. Lidke, “Single objective light-sheet microscopy for high-speed whole-cell 3D super-resolution,” *Biomedical Optics Express*, vol. 7, p. 2219, 6 2016.

[55] A. Ponjavic, Y. Ye, E. Laue, S. F. Lee, and D. Klenerman, “Sensitive light-sheet microscopy in multiwell plates using an AFM cantilever,” *Biomedical Optics Express*, vol. 9, p. 5863, 12 2018.

[56] Y. S. Hu, M. Zimmerley, Y. Li, R. Watters, and H. Cang, “Single-Molecule Super-Resolution Light-Sheet Microscopy,” *ChemPhysChem*, vol. 15, pp. 577–586, 3 2014.

[57] J. Goodman, *Introduction to Fourier Optics*. Roberts & Company Publishers, 2005.

[58] B. E. A. Saleh and M. C. Teich, *Fundamentals of Photonics*. Wiley, 2007.

[59] Rayleigh, "XXXI. Investigations in optics, with special reference to the spectroscope," *The London, Edinburgh, and Dublin Philosophical Magazine and Journal of Science*, vol. 8, pp. 261–274, 10 1879.

[60] E. Hecht, *Optics*. Addison Wesley, 1998.

[61] M. J. Rust, M. Bates, and X. W. Zhuang, "Sub-diffraction-limit imaging by stochastic optical reconstruction microscopy (STORM)," *Nat Methods*, vol. 3, no. 10, pp. 793–795, 2006.

[62] E. Betzig, G. H. Patterson, R. Sougrat, O. W. Lindwasser, S. Olenych, J. S. Bonifacino, M. W. Davidson, J. Lippincott-Schwartz, and H. F. Hess, "Imaging Intracellular Fluorescent Proteins at Nanometer Resolution," *Science*, vol. 313, pp. 1642–1645, 9 2006.

[63] S. T. Hess, T. P. K. Girirajan, and M. D. Mason, "Ultra-high resolution imaging by fluorescence photoactivation localization microscopy.," *Biophysical journal*, vol. 91, pp. 4258–72, 12 2006.

[64] A. V. Abraham, S. Ram, J. Chao, E. S. Ward, and R. J. Ober, "Quantitative study of single molecule location estimation techniques," *Optics Express*, vol. 17, p. 23352, 12 2009.

[65] S. Stallinga and B. Rieger, "Accuracy of the Gaussian Point Spread Function model in 2D localization microscopy," *Optics Express*, vol. 18, p. 24461, 11 2010.

[66] S. Stallinga and B. Rieger, "Position and orientation estimation of fixed dipole emitters using an effective Hermite point spread function model," *Optics Express*, vol. 20, p. 5896, 3 2012.

[67] B. Rieger and S. Stallinga, "The lateral and axial localization uncertainty in super-resolution light microscopy," *ChemPhysChem*, vol. 15, no. 4, pp. 664–670, 2014.

[68] D. Sage, H. Kirshner, T. Pengo, N. Stuurman, J. Min, S. Manley, and M. Unser, "Quantitative evaluation of software packages for single-molecule localization microscopy," *Nature Methods*, vol. 12, pp. 717–724, 8 2015.

[69] J. Enderlein, E. Toprak, and P. R. Selvin, "Polarization effect on position accuracy of fluorophore localization," *Optics Express*, vol. 14, no. 18, p. 8111, 2006.

[70] J. Engelhardt, J. Keller, P. Hoyer, M. Reuss, T. Staudt, and S. W. Hell, "Molecular Orientation Affects Localization Accuracy in Superresolution Far-Field Fluorescence Microscopy," *Nano Letters*, vol. 11, pp. 209–213, 1 2011.

[71] M. D. Lew, M. P. Backlund, and W. E. Moerner, “Rotational mobility of single molecules affects localization accuracy in super-resolution fluorescence microscopy,” *Nano Letters*, vol. 13, no. 9, pp. 3967–3972, 2013.

[72] M. D. Lew and W. E. Moerner, “Azimuthal polarization filtering for accurate, precise, and robust single-molecule localization microscopy,” *Nano Letters*, vol. 14, no. 11, pp. 6407–6413, 2014.

[73] A. Burgert, S. Letschert, S. Doose, and M. Sauer, “Artifacts in single-molecule localization microscopy,” *Histochemistry and Cell Biology*, vol. 144, pp. 123–131, 8 2015.

[74] S. Hugelier, J. J. de Rooi, R. Bernex, S. Duwé, O. Devos, M. Sliwa, P. Dedecker, P. H. C. Eilers, and C. Ruckebusch, “Sparse deconvolution of high-density super-resolution images,” *Scientific Reports*, vol. 6, no. 1, p. 21413, 2016.

[75] H. Mazidi, J. Lu, A. Nehorai, and M. D. Lew, “Minimizing Structural Bias in Single-Molecule Super-Resolution Microscopy,” *Scientific Reports*, vol. 8, p. 13133, 12 2018.

[76] J. Chao, E. Sally Ward, and R. J. Ober, “Fisher information theory for parameter estimation in single molecule microscopy: tutorial,” *Journal of the Optical Society of America A*, vol. 33, p. B36, 7 2016.

[77] R. E. Thompson, D. R. Larson, and W. W. Webb, “Precise Nanometer Localization Analysis for Individual Fluorescent Probes,” *Biophysical Journal*, vol. 82, no. 5, pp. 2775–2783, 2002.

[78] E. Betzig, “Proposed method for molecular optical imaging,” *Optics Letters*, vol. 20, p. 237, 2 1995.

[79] G. T. Dempsey, J. C. Vaughan, K. H. Chen, M. Bates, and X. Zhuang, “Evaluation of fluorophores for optimal performance in localization-based super-resolution imaging,” *Nature Methods*, vol. 8, pp. 1027–1036, 11 2011.

[80] M. A. Thompson, M. D. Lew, and W. Moerner, “Extending Microscopic Resolution with Single-Molecule Imaging and Active Control,” *Annual Review of Biophysics*, vol. 41, pp. 321–342, 6 2012.

[81] M. Heilemann, S. van de Linde, M. Schüttpelz, R. Kasper, B. Seefeldt, A. Mukherjee, P. Tinnefeld, and M. Sauer, “Subdiffraction-Resolution Fluorescence Imaging with Conventional Fluorescent Probes,” *Angewandte Chemie International Edition*, vol. 47, pp. 6172–6176, 8 2008.

[82] I. Schoen, J. Ries, E. Klotzsch, H. Ewers, and V. Vogel, “Binding-activated localization microscopy of DNA l,” *Nano Letters*, vol. 11, no. 9, pp. 4008–4011, 2011.

[83] T. Chandler, H. Shroff, R. Oldenbourg, and P. La Rivière, "Spatio-angular fluorescence microscopy I Basic theory," *Journal of the Optical Society of America A*, vol. 36, p. 1334, 8 2019.

[84] B. Richards and E. Wolf, "Electromagnetic diffraction in optical systems, II. Structure of the image field in an aplanatic system," *Proceedings of the Royal Society of London. Series A. Mathematical and Physical Sciences*, vol. 253, pp. 358–379, 12 1959.

[85] M. A. Lieb, J. M. Zavislan, and L. Novotny, "Single-molecule orientations determined by direct emission pattern imaging," *Journal of the Optical Society of America B*, vol. 21, no. 6, p. 1210, 2004.

[86] D. Axelrod, "Fluorescence excitation and imaging of single molecules near dielectric-coated and bare surfaces: A theoretical study," *Journal of Microscopy*, vol. 247, no. 2, pp. 147–160, 2012.

[87] A. S. Backer and W. E. Moerner, "Extending single-molecule microscopy using optical fourier processing," *Journal of Physical Chemistry B*, vol. 118, no. 28, pp. 8313–8329, 2014.

[88] S. HELL, G. REINER, C. CREMER, and E. H. K. STELZER, "Aberrations in confocal fluorescence microscopy induced by mismatches in refractive index," *Journal of Microscopy*, vol. 169, pp. 391–405, 3 1993.

[89] S. H. Wiersma, P. Török, T. D. Visser, and P. Varga, "Comparison of different theories for focusing through a plane interface," *Journal of the Optical Society of America A*, vol. 14, p. 1482, 7 1997.

[90] S. R. P. Pavani, M. A. Thompson, J. S. Biteen, S. J. Lord, N. Liu, R. J. Twieg, R. Piestun, and W. E. Moerner, "Three-dimensional, single-molecule fluorescence imaging beyond the diffraction limit by using a double-helix point spread function," *Proceedings of the National Academy of Sciences of the United States of America*, vol. 106, no. 9, pp. 2995–2999, 2009.

[91] M. D. Lew, S. F. Lee, J. L. Ptacin, M. K. Lee, R. J. Twieg, L. Shapiro, and W. E. Moerner, "Three-dimensional superresolution colocalization of intracellular protein superstructures and the cell surface in live Caulobacter crescentus," *Proceedings of the National Academy of Sciences*, vol. 108, pp. E1102–E1110, 11 2011.

[92] M. D. Lew, S. F. Lee, M. Badieirostami, and W. E. Moerner, "Corkscrew point spread function for far-field three-dimensional nanoscale localization of pointlike objects," *Optics Letters*, vol. 36, p. 202, 1 2011.

[93] S. Jia, J. C. Vaughan, and X. Zhuang, "Isotropic three-dimensional super-resolution imaging with a self-bending point spread function," *Nature Photonics*, vol. 8, no. 4, pp. 302–306, 2014.

[94] Y. Shechtman, L. E. Weiss, A. S. Backer, M. Y. Lee, and W. E. Moerner, "Multicolour localization microscopy by point-spread-function engineering," *Nature Photonics*, vol. 10, no. August, pp. 1–6, 2016.

[95] E. Hershko, L. E. Weiss, T. Michaeli, and Y. Shechtman, "Multicolor localization microscopy and point-spread-function engineering by deep learning," *Optics Express*, vol. 27, p. 6158, 3 2019.

[96] A. S. Backer, M. P. Backlund, A. R. Von Diezmann, S. J. Sahl, and W. E. Moerner, "A bisected pupil for studying single-molecule orientational dynamics and its application to three-dimensional super-resolution microscopy," *Applied Physics Letters*, vol. 104, no. 19, 2014.

[97] O. Zhang, J. Lu, T. Ding, and M. D. Lew, "Imaging the three-dimensional orientation and rotational mobility of fluorescent emitters using the Tri-spot point spread function," *Applied Physics Letters*, vol. 113, p. 031103, 7 2018.

[98] A. S. Backer, M. P. Backlund, M. D. Lew, and W. E. Moerner, "Single-molecule orientation measurements with a quadrated pupil.," *Optics letters*, vol. 38, no. 9, pp. 1521–3, 2013.

[99] F. Balzarotti, Y. Eilers, K. C. Gwosch, A. H. Gynnå, V. Westphal, F. D. Stefani, J. Elf, and S. W. Hell, "Nanometer resolution imaging and tracking of fluorescent molecules with minimal photon fluxes," *Science*, vol. 355, pp. 606–612, 2 2017.

[100] P. J. Rothwell, S. Berger, O. Kensch, S. Felekyan, M. Antonik, B. M. Wohrl, T. Restle, R. S. Goody, and C. A. M. Seidel, "Multiparameter single-molecule fluorescence spectroscopy reveals heterogeneity of HIV-1 reverse transcriptase:primer/template complexes," *Proceedings of the National Academy of Sciences*, vol. 100, pp. 1655–1660, 2 2003.

[101] J. Widengren, V. Kudryavtsev, M. Antonik, S. Berger, M. Gerken, and C. A. M. Seidel, "Single-Molecule Detection and Identification of Multiple Species by Multiparameter Fluorescence Detection," *Analytical Chemistry*, vol. 78, pp. 2039–2050, 3 2006.

[102] K. Suhling, L. M. Hirvonen, J. A. Levitt, P.-H. Chung, C. Tregidgo, A. Le Marois, D. A. Rusakov, K. Zheng, S. Ameer-Beg, S. Poland, S. Coelho, R. Henderson, and N. Krstajic, "Fluorescence lifetime imaging (FLIM): Basic concepts and some recent developments," *Medical Photonics*, vol. 27, pp. 3–40, 5 2015.

[103] M. A. Haidekker, A. G. Tsai, T. Brady, H. Y. Stevens, J. A. Frangos, E. Theodorakis, and M. Intaglietta, "A novel approach to blood plasma viscosity measurement using fluorescent molecular rotors," *American Journal of Physiology-Heart and Circulatory Physiology*, vol. 282, pp. H1609–H1614, 5 2002.

[104] M. K. Kuimova, S. W. Botchway, A. W. Parker, M. Balaz, H. A. Collins, H. L. Anderson, K. Suhling, and P. R. Ogilby, "Imaging intracellular viscosity of a single cell during photoinduced cell death," *Nature Chemistry*, vol. 1, pp. 69–73, 4 2009.

[105] N. A. Hosny, G. Mohamedi, P. Rademeyer, J. Owen, Y. Wu, M.-X. Tang, R. J. Eckersley, E. Stride, and M. K. Kuimova, "Mapping microbubble viscosity using fluorescence lifetime imaging of molecular rotors," *Proceedings of the National Academy of Sciences*, vol. 110, pp. 9225–9230, 6 2013.

[106] E. A. Jares-Erijman and T. M. Jovin, "FRET imaging," *Nature Biotechnology*, vol. 21, pp. 1387–1395, 11 2003.

[107] H. Wallrabe and A. Periasamy, "Imaging protein molecules using FRET and FLIM microscopy," *Current Opinion in Biotechnology*, vol. 16, pp. 19–27, 2 2005.

[108] A. PIETRASZEWSKA-BOGIEL and T. GADELLA, "FRET microscopy: from principle to routine technology in cell biology," *Journal of Microscopy*, vol. 241, pp. 111–118, 2 2011.

[109] M. Krebs, E. Bromley, and A. Donald, "The binding of thioflavin-T to amyloid fibrils: localisation and implications," *Journal of Structural Biology*, vol. 149, pp. 30–37, 1 2005.

[110] G. Steinbach, I. Pomozi, D. P. Jánosa, J. Makovitzky, and G. Garab, "Confocal Fluorescence Detected Linear Dichroism Imaging of Isolated Human Amyloid Fibrils. Role of Supercoiling," *Journal of Fluorescence*, vol. 21, pp. 983–989, 5 2011.

[111] J. Duboisset, P. Ferrand, W. He, X. Wang, H. Rigneault, and S. Brasselet, "Thioflavine-T and Congo Red reveal the polymorphism of insulin amyloid fibrils when probed by polarization-resolved fluorescence microscopy," *Journal of Physical Chemistry B*, vol. 117, no. 3, pp. 784–788, 2013.

[112] G. Diaz, M. Melis, B. Batetta, F. Angius, and A. M. Falchi, "Hydrophobic characterization of intracellular lipids in situ by Nile Red red/yellow emission ratio," *Micron*, vol. 39, pp. 819–824, 10 2008.

[113] O. A. Kucherak, S. Oncul, Z. Darwich, D. A. Yushchenko, Y. Arntz, P. Didier, Y. Mely, and A. S. Klymchenko, "Switchable Nile Red-Based Probe for Cholesterol and Lipid Order at the Outer Leaflet of Biomembranes," *Journal of the American Chemical Society*, vol. 132, pp. 4907–4916, 4 2010.

[114] W. Xu, J. S. Kong, Y. T. E. Yeh, and P. Chen, "Single-molecule nanocatalysis reveals heterogeneous reaction pathways and catalyticdynamics," *Nature Materials*, vol. 7, no. 12, pp. 992–996, 2008.

[115] J. B. Sambur, T.-Y. Chen, E. Choudhary, G. Chen, E. J. Nissen, E. M. Thomas, N. Zou, and P. Chen, "Sub-particle reaction and photocurrent mapping to optimize catalyst-modified photoanodes," *Nature*, vol. 530, pp. 77–80, 2 2016.

[116] M. Shen, T. Ding, J. Luo, C. Tan, K. Mahmood, Z. Wang, D. Zhang, R. Mishra, M. D. Lew, and B. Sadtler, "Competing Activation and Deactivation Mechanisms in Photodoped Bismuth Oxybromide Nanoplates Probed by Single-Molecule Fluorescence Imaging," *The Journal of Physical Chemistry Letters*, pp. 5219–5227, 6 2020.

[117] M. N. Bongiovanni, J. Godet, M. H. Horrocks, L. Tosatto, A. R. Carr, D. C. Wirthensohn, R. T. Ranasinghe, J.-E. Lee, A. Ponjavic, J. V. Fritz, C. M. Dobson, D. Klenerman, and S. F. Lee, "Multi-dimensional super-resolution imaging enables surface hydrophobicity mapping," *Nature Communications*, vol. 7, p. 13544, 12 2016.

[118] J.-E. Lee, J. C. Sang, M. Rodrigues, A. R. Carr, M. H. Horrocks, S. De, M. N. Bongiovanni, P. Flagmeier, C. M. Dobson, D. J. Wales, S. F. Lee, and D. Klenerman, "Mapping Surface Hydrophobicity of α-Synuclein Oligomers at the Nanoscale," *Nano Letters*, vol. 18, pp. 7494–7501, 12 2018.

[119] T. Cordes and S. A. Blum, "Opportunities and challenges in single-molecule and single-particle fluorescence microscopy for mechanistic studies of chemical reactions," *Nature Chemistry*, vol. 5, pp. 993–999, 12 2013.

[120] T. Chen, B. Dong, K. Chen, F. Zhao, X. Cheng, C. Ma, S. Lee, P. Zhang, S. H. Kang, J. W. Ha, W. Xu, and N. Fang, "Optical Super-Resolution Imaging of Surface Reactions," *Chemical Reviews*, vol. 117, pp. 7510–7537, 6 2017.

[121] M. G. Iadanza, M. P. Jackson, E. W. Hewitt, N. A. Ranson, and S. E. Radford, "A new era for understanding amyloid structures and disease," *Nature Reviews Molecular Cell Biology*, vol. 19, pp. 755–773, 12 2018.

[122] C. Haass and D. J. Selkoe, "Soluble protein oligomers in neurodegeneration: lessons from the Alzheimer's amyloid beta-peptide.," *Nature reviews. Molecular cell biology*, vol. 8, no. 2, pp. 101–12, 2007.

[123] J. Bieschke, J. Russ, R. P. Friedrich, D. E. Ehrnhoefer, H. Wobst, K. Neugebauer, and E. E. Wanker, "EGCG remodels mature α-synuclein and amyloid-β fibrils and reduces cellular toxicity," *Proceedings of the National Academy of Sciences*, vol. 107, pp. 7710–7715, 4 2010.

[124] K. Andrich, U. Hegenbart, C. Kimmich, N. Kedia, H. R. Bergen, S. Schönland, E. Wanker, and J. Bieschke, "Aggregation of full-length immunoglobulin light chains from systemic light chain amyloidosis (AL) patients is remodeled by epigallocatechin-3-gallate," *Journal of Biological Chemistry*, vol. 292, no. 6, pp. 2328–2344, 2017.

[125] K. Spehar*, T. Ding*, Y. Sun, N. Kedia, J. Lu, G. R. Nahass, M. D. Lew, and J. Bieschke, "Super-resolution Imaging of Amyloid Structures over Extended Times by Using Transient Binding of Single Thioflavin T Molecules," *ChemBioChem*, vol. 19, pp. 1944–1948, 9 2018.

[126] A. T. Petkova, Y. Ishii, J. J. Balbach, O. N. Antzutkin, R. D. Leapman, F. Delaglio, and R. Tycko, "A structural model for Alzheimer's -amyloid fibrils based on experimental constraints from solid state NMR," *Proceedings of the National Academy of Sciences*, vol. 99, pp. 16742–16747, 12 2002.

[127] L. M. Young, L.-H. Tu, D. P. Raleigh, A. E. Ashcroft, and S. E. Radford, "Understanding co-polymerization in amyloid formation by direct observation of mixed oligomers," *Chemical Science*, vol. 8, no. 7, pp. 5030–5040, 2017.

[128] E. Cohen, J. Bieschke, R. M. Perciavalle, J. W. Kelly, and A. Dillin, "Opposing Activities Protect Against Age-Onset Proteotoxicity," *Science*, vol. 313, pp. 1604–1610, 9 2006.

[129] M. Serra-Batiste, M. Ninot-Pedrosa, M. Bayoumi, M. Gairí, G. Maglia, and N. Carulla, "Aβ42 assembles into specific β-barrel pore-forming oligomers in membrane-mimicking environments," *Proceedings of the National Academy of Sciences*, vol. 113, pp. 10866–10871, 9 2016.

[130] G. Fusco, S. W. Chen, P. T. F. Williamson, R. Cascella, M. Perni, J. A. Jarvis, C. Cecchi, M. Vendruscolo, F. Chiti, N. Cremades, L. Ying, C. M. Dobson, and A. De Simone, "Structural basis of membrane disruption and cellular toxicity by α-synuclein oligomers," *Science*, vol. 358, pp. 1440–1443, 12 2017.

[131] F. U. Hartl and M. Hayer-Hartl, "Converging concepts of protein folding in vitro and in vivo," *Nature Structural & Molecular Biology*, vol. 16, pp. 574–581, 6 2009.

[132] T. Eichner and S. E. Radford, "A Diversity of Assembly Mechanisms of a Generic Amyloid Fold," *Molecular Cell*, vol. 43, pp. 8–18, 7 2011.

[133] A. K. Buell, "The growth of amyloid fibrils: rates and mechanisms," *Biochemical Journal*, vol. 476, pp. 2677–2703, 10 2019.

[134] D. E. Ehrnhoefer, J. Bieschke, A. Boeddrich, M. Herbst, L. Masino, R. Lurz, S. Engemann, A. Pastore, and E. E. Wanker, "EGCG redirects amyloidogenic polypeptides into unstructured, off-pathway oligomers.," *Nature structural & molecular biology*, vol. 15, no. 6, pp. 558–66, 2008.

[135] G. S. Kaminski Schierle, S. van de Linde, M. Erdelyi, E. K. Esbjorner, T. Klein, E. Rees, C. W. Bertoncini, C. M. Dobson, M. Sauer, and C. F. Kaminski, "In Situ Measurements of the Formation and Morphology of Intracellular β-Amyloid Fibrils by Super-Resolution Fluorescence Imaging," *Journal of the American Chemical Society*, vol. 133, pp. 12902–12905, 8 2011.

[136] L. J. Young, G. S. Kaminski Schierle, and C. Kaminski, "Imaging Aβ(1–42) fibril elongation reveals strongly polarised growth and growth incompetent states," *Phys. Chem. Chem. Phys.*, vol. 19, pp. 27987–27996, 2017.

[137] A. S. Backer and W. E. Moerner, "Determining the rotational mobility of a single molecule from a single image: a numerical study.," *Optics express*, vol. 23, no. 4, pp. 4255–76, 2015.

[138] T. Ding*, T. Wu*, H. Mazidi, O. Zhang, and M. D. Lew, "Single-molecule orientation localization microscopy for resolving structural heterogeneities between amyloid fibrils," *Optica*, vol. 7, p. 602, 6 2020.

[139] S. Stallinga, "Effect of rotational diffusion in an orientational potential well on the point spread function of electric dipole emitters," *J. Opt. Soc. Am. A*, vol. 32, no. 2, pp. 213–223, 2015.

[140] M. Shen*, T. Ding*, S. T. Hartman, F. Wang, C. Krucylak, Z. Wang, C. Tan, B. Yin, R. Mishra, M. D. Lew, and B. Sadtler, "Nanoscale Colocalization of Fluorogenic Probes Reveals the Role of Oxygen Vacancies in the Photocatalytic Activity of Tungsten Oxide Nanowires," *ACS Catalysis*, vol. 10, pp. 2088–2099, 2 2020.

[141] M. P. Backlund, M. D. Lew, A. S. Backer, S. J. Sahl, G. Grover, A. Agrawal, R. Piestun, and W. E. Moerner, "Simultaneous, accurate measurement of the 3D position and orientation of single molecules," *Proceedings of the National Academy of Sciences*, vol. 109, no. 47, pp. 19087–19092, 2012.

[142] A. Agrawal, S. Quirin, G. Grover, and R. Piestun, "Limits of 3D dipole localization and orientation estimation for single-molecule imaging: towards Green's tensor engineering," *Optics Express*, vol. 20, p. 26667, 11 2012.

[143] J. Otón, P. Ambs, M. S. Millán, and E. Pérez-Cabré, "Multipoint phase calibration for improved compensation of inherent wavefront distortion in parallel aligned liquid crystal on silicon displays," *Applied Optics*, vol. 46, p. 5667, 8 2007.

[144] H. Levine, "Thioflavine T interaction with synthetic Alzheimer's disease β-amyloid peptides: Detection of amyloid aggregation in solution," *Protein Science*, vol. 2, pp. 404–410, 12 1993.

[145] G.-f. Chen, T.-h. Xu, Y. Yan, Y.-r. Zhou, Y. Jiang, K. Melcher, and H. E. Xu, "Amyloid beta: structure, biology and structure-based therapeutic development," *Acta Pharmacologica Sinica*, vol. 38, pp. 1205–1235, 9 2017.

[146] H. T. Lam, M. C. Graber, K. A. Gentry, and J. Bieschke, "Stabilization of α-Synuclein Fibril Clusters Prevents Fragmentation and Reduces Seeding Activity and Toxicity," *Biochemistry*, vol. 55, pp. 675–685, 2 2016.

[147] H. J. Wobst, A. Sharma, M. I. Diamond, E. E. Wanker, and J. Bieschke, "The green tea polyphenol (-)-epigallocatechin gallate prevents the aggregation of tau protein into toxic oligomers at substoichiometric ratios," *FEBS Letters*, vol. 589, no. 1, pp. 77–83, 2015.

[148] B. B. Holmes, S. L. DeVos, N. Kfoury, M. Li, R. Jacks, K. Yanamandra, M. O. Ouidja, F. M. Brodsky, J. Marasa, D. P. Bagchi, P. T. Kotzbauer, T. M. Miller, D. Papy-Garcia, and M. I. Diamond, "Heparan sulfate proteoglycans mediate internalization and propagation of specific proteopathic seeds," *Proceedings of the National Academy of Sciences*, vol. 110, pp. E3138–E3147, 8 2013.

[149] A. Buades, B. Coll, and J.-M. Morel, "A Non-Local Algorithm for Image Denoising," in *2005 IEEE Computer Society Conference on Computer Vision and Pattern Recognition (CVPR'05)*, vol. 2, pp. 60–65, IEEE, 2005.

[150] J. Canny, "A Computational Approach to Edge Detection," *IEEE Transactions on Pattern Analysis and Machine Intelligence*, vol. PAMI-8, pp. 679–698, 11 1986.

[151] E. Hoogendoorn, K. C. Crosby, D. Leyton-Puig, R. M. P. Breedijk, K. Jalink, T. W. J. Gadella, and M. Postma, "The fidelity of stochastic single-molecule super-resolution reconstructions critically depends upon robust background estimation," *Scientific Reports*, vol. 4, p. 3854, 5 2015.

[152] Sternberg, "Biomedical Image Processing," *Computer*, vol. 16, pp. 22–34, 1 1983.

[153] I. Izeddin, J. Boulanger, V. Racine, C. Specht, A. Kechkar, D. Nair, A. Triller, D. Choquet, M. Dahan, and J. Sibarita, "Wavelet analysis for single molecule localization microscopy," *Optics Express*, vol. 20, p. 2081, 1 2012.

[154] M. Ovesný, P. Křížek, J. Borkovec, Z. Švindrych, and G. M. Hagen, "ThunderSTORM: A comprehensive ImageJ plug-in for PALM and STORM data analysis and super-resolution imaging," *Bioinformatics*, vol. 30, no. 16, pp. 2389–2390, 2014.

[155] C. A. Schneider, W. S. Rasband, and K. W. Eliceiri, "NIH Image to ImageJ: 25 years of image analysis," *Nature Methods*, vol. 9, no. 7, pp. 671–675, 2012.

[156] M. Bates, G. T. Dempsey, K. H. Chen, and X. Zhuang, "Multicolor super-resolution fluorescence imaging via multi-parameter fluorophore detection," *ChemPhysChem*, vol. 13, no. 1, pp. 99–107, 2012.

[157] H. Mazidi, E. S. King, O. Zhang, A. Nehorai, and M. D. Lew, "Dense Super-Resolution Imaging of Molecular Orientation Via Joint Sparse Basis Deconvolution and Spatial Pooling," in *2019 IEEE 16th International Symposium on Biomedical Imaging (ISBI 2019)*, pp. 325–329, IEEE, 4 2019.

[158] C. Steger, "An unbiased detector of curvilinear structures," *IEEE Transactions on Pattern Analysis and Machine Intelligence*, vol. 20, no. 2, pp. 113–125, 1998.

[159] S. Malkusch, U. Endesfelder, J. Mondry, M. Gelléri, P. J. Verveer, and M. Heilemann, "Coordinate-based colocalization analysis of single-molecule localization microscopy data," *Histochemistry and Cell Biology*, vol. 137, pp. 1–10, 1 2012.

[160] Y. P. Xie, G. Liu, L. Yin, and H.-M. Cheng, "Crystal facet-dependent photocatalytic oxidation and reduction reactivity of monoclinic WO3 for solar energy conversion," *Journal of Materials Chemistry*, vol. 22, no. 14, p. 6746, 2012.

[161] R. Li, H. Han, F. Zhang, D. Wang, and C. Li, "Highly efficient photocatalysts constructed by rational assembly of dual-cocatalysts separately on different facets of BiVO 4," *Energy Environ. Sci.*, vol. 7, no. 4, pp. 1369–1376, 2014.

[162] X. Chen, L. Liu, P. Y. Yu, and S. S. Mao, "Increasing Solar Absorption for Photocatalysis with Black Hydrogenated Titanium Dioxide Nanocrystals," *Science*, vol. 331, pp. 746–750, 2 2011.

[163] F. Lei, Y. Sun, K. Liu, S. Gao, L. Liang, B. Pan, and Y. Xie, "Oxygen Vacancies Confined in Ultrathin Indium Oxide Porous Sheets for Promoted Visible-Light Water Splitting," *Journal of the American Chemical Society*, vol. 136, pp. 6826–6829, 5 2014.

[164] J. Yan, T. Wang, G. Wu, W. Dai, N. Guan, L. Li, and J. Gong, "Tungsten Oxide Single Crystal Nanosheets for Enhanced Multichannel Solar Light Harvesting," *Advanced Materials*, vol. 27, pp. 1580–1586, 3 2015.

[165] Z.-F. Huang, J. Song, L. Pan, X. Zhang, L. Wang, and J.-J. Zou, "Tungsten Oxides for Photocatalysis, Electrochemistry, and Phototherapy," *Advanced Materials*, vol. 27, pp. 5309–5327, 9 2015.

[166] G. Xi, S. Ouyang, P. Li, J. Ye, Q. Ma, N. Su, H. Bai, and C. Wang, "Ultrathin W18O49 Nanowires with Diameters below 1 nm: Synthesis, Near-Infrared Absorption, Photoluminescence, and Photochemical Reduction of Carbon Dioxide," *Angewandte Chemie International Edition*, vol. 51, pp. 2395–2399, 3 2012.

[167] X. Chen, Y. Zhou, Q. Liu, Z. Li, J. Liu, and Z. Zou, "Ultrathin, Single-Crystal WO 3 Nanosheets by Two-Dimensional Oriented Attachment toward Enhanced Photocatalystic Reduction of CO 2 into Hydrocarbon Fuels under Visible Light," *ACS Applied Materials & Interfaces*, vol. 4, pp. 3372–3377, 7 2012.

[168] L. Liang, X. Li, Y. Sun, Y. Tan, X. Jiao, H. Ju, Z. Qi, J. Zhu, and Y. Xie, "Infrared Light-Driven CO2 Overall Splitting at Room Temperature," *Joule*, vol. 2, pp. 1004–1016, 5 2018.

[169] N. Zhang, X. Li, H. Ye, S. Chen, H. Ju, D. Liu, Y. Lin, W. Ye, C. Wang, Q. Xu, J. Zhu, L. Song, J. Jiang, and Y. Xiong, "Oxide Defect Engineering Enables to Couple Solar Energy into Oxygen Activation," *Journal of the American Chemical Society*, vol. 138, pp. 8928–8935, 7 2016.

[170] N. Zhang, X. Li, Y. Liu, R. Long, M. Li, S. Chen, Z. Qi, C. Wang, L. Song, J. Jiang, and Y. Xiong, "Defective Tungsten Oxide Hydrate Nanosheets for Boosting Aerobic Coupling of Amines: Synergistic Catalysis by Oxygen Vacancies and Brønsted Acid Sites," *Small*, vol. 13, p. 1701354, 8 2017.

[171] K. Villa, S. Murcia-López, T. Andreu, and J. R. Morante, "Mesoporous WO3 photocatalyst for the partial oxidation of methane to methanol using electron scavengers," *Applied Catalysis B: Environmental*, vol. 163, pp. 150–155, 2 2015.

[172] W. Zhu, M. Shen, G. Fan, A. Yang, J. R. Meyer, Y. Ou, B. Yin, J. Fortner, M. Foston, Z. Li, Z. Zou, and B. Sadtler, "Facet-Dependent Enhancement in the Activity of Bismuth Vanadate Microcrystals for the Photocatalytic Conversion of Methane to Methanol," *ACS Applied Nano Materials*, vol. 1, pp. 6683–6691, 12 2018.

[173] R. A. Pala, A. J. Leenheer, M. Lichterman, H. A. Atwater, and N. S. Lewis, "Measurement of minority-carrier diffusion lengths using wedge-shaped semiconductor photoelectrodes," *Energy Environ. Sci.*, vol. 7, no. 10, pp. 3424–3430, 2014.

[174] F. F. Abdi, T. J. Savenije, M. M. May, B. Dam, and R. van de Krol, "The Origin of Slow Carrier Transport in BiVO 4 Thin Film Photoanodes: A Time-Resolved Microwave Conductivity Study," *The Journal of Physical Chemistry Letters*, vol. 4, pp. 2752–2757, 8 2013.

[175] H. Cheng, T. Kamegawa, K. Mori, and H. Yamashita, "Surfactant-Free Nonaqueous Synthesis of Plasmonic Molybdenum Oxide Nanosheets with Enhanced Catalytic Activity for Hydrogen Generation from Ammonia Borane under Visible Light," *Angewandte Chemie International Edition*, vol. 53, pp. 2910–2914, 3 2014.

[176] T. R. Gordon, M. Cargnello, T. Paik, F. Mangolini, R. T. Weber, P. Fornasiero, and C. B. Murray, "Nonaqueous Synthesis of TiO 2 Nanocrystals Using TiF 4 to Engineer

Morphology, Oxygen Vacancy Concentration, and Photocatalytic Activity," *Journal of the American Chemical Society*, vol. 134, pp. 6751–6761, 4 2012.

[177] J. Wang, Z. Wang, B. Huang, Y. Ma, Y. Liu, X. Qin, X. Zhang, and Y. Dai, "Oxygen Vacancy Induced Band-Gap Narrowing and Enhanced Visible Light Photocatalytic Activity of ZnO," *ACS Applied Materials & Interfaces*, vol. 4, pp. 4024–4030, 8 2012.

[178] N. Zhang, A. Jalil, D. Wu, S. Chen, Y. Liu, C. Gao, W. Ye, Z. Qi, H. Ju, C. Wang, X. Wu, L. Song, J. Zhu, and Y. Xiong, "Refining Defect States in W 18 O 49 by Mo Doping: A Strategy for Tuning N 2 Activation towards Solar-Driven Nitrogen Fixation," *Journal of the American Chemical Society*, vol. 140, pp. 9434–9443, 8 2018.

[179] Y. Zhao, S. Balasubramanyam, R. Sinha, R. Lavrijsen, M. A. Verheijen, A. A. Bol, and A. Bieberle-Hütter, "Physical and Chemical Defects in WO 3 Thin Films and Their Impact on Photoelectrochemical Water Splitting," *ACS Applied Energy Materials*, vol. 1, pp. 5887–5895, 11 2018.

[180] K. Manthiram and A. P. Alivisatos, "Tunable Localized Surface Plasmon Resonances in Tungsten Oxide Nanocrystals," *Journal of the American Chemical Society*, vol. 134, pp. 3995–3998, 3 2012.

[181] X. Zhou, N. M. Andoy, G. Liu, E. Choudhary, K. S. Han, H. Shen, and P. Chen, "Quantitative super-resolution imaging uncovers reactivity patterns on single nanocatalysts," *Nature Nanotechnology*, vol. 7, no. 4, pp. 237–241, 2012.

[182] N. M. Andoy, X. Zhou, E. Choudhary, H. Shen, G. Liu, and P. Chen, "Single-Molecule Catalysis Mapping Quantifies Site-Specific Activity and Uncovers Radial Activity Gradient on Single 2D Nanocrystals," *Journal of the American Chemical Society*, vol. 135, pp. 1845–1852, 2 2013.

[183] X. Zhou, E. Choudhary, N. M. Andoy, N. Zou, and P. Chen, "Scalable parallel screening of catalyst activity at the single-particle level and subdiffraction resolution," *ACS Catalysis*, vol. 3, no. 7, pp. 1448–1453, 2013.

[184] Y. Du, X. He, Y. Zhan, S. Li, Y. Shen, F. Ning, L. Yan, and X. Zhou, "Imaging the Site-Specific Activity and Kinetics on a Single Nanomaterial by Microchamber Array," *ACS Catalysis*, vol. 7, pp. 3607–3614, 5 2017.

[185] N. Zou, G. Chen, X. Mao, H. Shen, E. Choudhary, X. Zhou, and P. Chen, "Imaging Catalytic Hotspots on Single Plasmonic Nanostructures via Correlated Super-Resolution and Electron Microscopy," *ACS Nano*, vol. 12, pp. 5570–5579, 6 2018.

[186] A. J. Wilson and K. A. Willets, "Visualizing Site-Specific Redox Potentials on the Surface of Plasmonic Nanoparticle Aggregates with Superlocalization SERS Microscopy," *Nano Letters*, vol. 14, pp. 939–945, 2 2014.

[187] M. L. Weber, A. J. Wilson, and K. A. Willets, “Characterizing the Spatial Dependence of Redox Chemistry on Plasmonic Nanoparticle Electrodes Using Correlated Super-Resolution Surface-Enhanced Raman Scattering Imaging and Electron Microscopy,” *The Journal of Physical Chemistry C*, vol. 119, pp. 18591–18601, 8 2015.

[188] T. Chen, S. Chen, P. Song, Y. Zhang, H. Su, W. Xu, and J. Zeng, “Single-Molecule Nanocatalysis Reveals Facet-Dependent Catalytic Kinetics and Dynamics of Pallidium Nanoparticles,” *ACS Catalysis*, vol. 7, no. 4, pp. 2967–2972, 2017.

[189] M. B. J. Roeffaers, B. F. Sels, H. Uji-i, F. C. De Schryver, P. A. Jacobs, D. E. De Vos, and J. Hofkens, “Spatially resolved observation of crystal-face-dependent catalysis by single turnover counting,” *Nature*, vol. 439, pp. 572–575, 2 2006.

[190] M. B. Roeffaers, G. De Cremer, J. Libeert, R. Ameloot, P. Dedecker, A. J. Bons, M. Bückins, J. A. Martens, B. F. Sels, D. E. De Vos, and J. Hofkens, “Super-resolution reactivity mapping of nanostructured catalyst particles,” *Angewandte Chemie - International Edition*, vol. 48, no. 49, pp. 9285–9289, 2009.

[191] R. Han, J. W. Ha, C. Xiao, Y. Pei, Z. Qi, B. Dong, N. L. Bormann, W. Huang, and N. Fang, “Geometry-Assisted Three-Dimensional Superlocalization Imaging of Single-Molecule Catalysis on Modular Multilayer Nanocatalysts,” *Angewandte Chemie International Edition*, vol. 53, pp. 12865–12869, 11 2014.

[192] W. Xu, P. K. Jain, B. J. Beberwyck, and A. P. Alivisatos, “Probing redox photocatalysis of trapped electrons and holes on single Sb-doped titania nanorod surfaces,” *Journal of the American Chemical Society*, vol. 134, no. 9, pp. 3946–3949, 2012.

[193] T. Tachikawa, S. Yamashita, and T. Majima, “Evidence for Crystal-Face-Dependent TiO 2 Photocatalysis from Single-Molecule Imaging and Kinetic Analysis,” *Journal of the American Chemical Society*, vol. 133, pp. 7197–7204, 5 2011.

[194] J. B. Sambur and P. Chen, “Distinguishing Direct and Indirect Photoelectrocatalytic Oxidation Mechanisms Using Quantitative Single-Molecule Reaction Imaging and Photocurrent Measurements,” *The Journal of Physical Chemistry C*, vol. 120, pp. 20668–20676, 9 2016.

[195] X. Mao, C. Liu, M. Hesari, N. Zou, and P. Chen, “Super-resolution imaging of non-fluorescent reactions via competition,” *Nature Chemistry*, vol. 11, pp. 687–694, 8 2019.

[196] M. Hesari, X. Mao, and P. Chen, “Charge Carrier Activity on Single-Particle Photo(electro)catalysts: Toward Function in Solar Energy Conversion,” *Journal of the American Chemical Society*, vol. 140, pp. 6729–6740, 6 2018.

[197] T. Tachikawa, T. Yonezawa, and T. Majima, “Super-Resolution Mapping of Reactive Sites on Titania-Based Nanoparticles with Water-Soluble Fluorogenic Probes,” *ACS Nano*, vol. 7, pp. 263–275, 1 2013.

[198] J. W. Ha, T. P. A. Ruberu, R. Han, B. Dong, J. Vela, and N. Fang, “Super-Resolution Mapping of Photogenerated Electron and Hole Separation in Single Metal–Semiconductor Nanocatalysts,” *Journal of the American Chemical Society*, vol. 136, pp. 1398–1408, 1 2014.

[199] Y. Li, Y. Bando, and D. Golberg, “Quasi-Aligned Single-Crystalline W18O49 Nanotubes and Nanowires,” *Advanced Materials*, vol. 15, pp. 1294–1296, 8 2003.

[200] C. Guo, S. Yin, M. Yan, M. Kobayashi, M. Kakihana, and T. Sato, “Morphology-Controlled Synthesis of W 18 O 49 Nanostructures and Their Near-Infrared Absorption Properties,” *Inorganic Chemistry*, vol. 51, pp. 4763–4771, 4 2012.

[201] J. Kim, C. W. Lee, and W. Choi, “Platinized WO 3 as an Environmental Photocatalyst that Generates OH Radicals under Visible Light,” *Environmental Science & Technology*, vol. 44, pp. 6849–6854, 9 2010.

[202] J. Zhang and Y. Nosaka, “Mechanism of the OH Radical Generation in Photocatalysis with TiO 2 of Different Crystalline Types,” *The Journal of Physical Chemistry C*, vol. 118, pp. 10824–10832, 5 2014.

[203] C. Lops, A. Ancona, K. Di Cesare, B. Dumontel, N. Garino, G. Canavese, S. Hérnandez, and V. Cauda, “Sonophotocatalytic degradation mechanisms of Rhodamine B dye via radicals generation by micro- and nano-particles of ZnO,” *Applied Catalysis B: Environmental*, vol. 243, pp. 629–640, 4 2019.

[204] A. Gomes, E. Fernandes, and J. L. Lima, “Fluorescence probes used for detection of reactive oxygen species,” *Journal of Biochemical and Biophysical Methods*, vol. 65, pp. 45–80, 12 2005.

[205] D. G. Barton, S. L. Soled, and E. Iglesia, “Solid acid catalysts based on supported tungsten oxides,” *Topics in Catalysis*, vol. 6, no. 1-4, pp. 87–99, 1998.

[206] J. González, J. A. Wang, L. F. Chen, M. E. Manríquez, and J. M. Dominguez, “Structural Defects, Lewis Acidity, and Catalysis Properties of Mesostructured WO 3 /SBA-15 Nanocatalysts,” *The Journal of Physical Chemistry C*, vol. 121, pp. 23988–23999, 11 2017.

[207] Y. Xu and M. A. Schoonen, “The absolute energy positions of conduction and valence bands of selected semiconducting minerals,” *American Mineralogist*, vol. 85, pp. 543–556, 3 2000.

[208] X. Chan, W. Nan, D. Mahajan, and T. Kim, "Comprehensive investigation of the biomass derived furfuryl alcohol oligomer formation over tungsten oxide catalysts," *Catalysis Communications*, vol. 72, pp. 11–15, 12 2015.

[209] T. Kim, R. S. Assary, C. L. Marshall, D. J. Gosztola, L. A. Curtiss, and P. C. Stair, "Acid-Catalyzed Furfuryl Alcohol Polymerization: Characterizations of Molecular Structure and Thermodynamic Properties," *ChemCatChem*, vol. 3, pp. 1451–1458, 9 2011.

[210] M. Choura, N. M. Belgacem, and A. Gandini, "Acid-Catalyzed Polycondensation of Furfuryl Alcohol: Mechanisms of Chromophore Formation and Cross-Linking," *Macromolecules*, vol. 29, pp. 3839–3850, 1 1996.

[211] Y. Ping, R. Sundararaman, and W. A. Goddard III, "Solvation effects on the band edge positions of photocatalysts from first principles," *Physical Chemistry Chemical Physics*, vol. 17, no. 45, pp. 30499–30509, 2015.

[212] L. Zhang, B. Wen, Y.-N. Zhu, Z. Chai, X. Chen, and M. Chen, "First-principles calculations of water adsorption on perfect and defect WO3(0 0 1)," *Computational Materials Science*, vol. 150, pp. 484–490, 7 2018.

[213] R. Kishore, X. Cao, X. Zhang, and A. Bieberle-Hütter, "Electrochemical water oxidation on WO3 surfaces: A density functional theory study," *Catalysis Today*, vol. 321-322, pp. 94–99, 2 2019.

[214] J. Hu, X. Zhao, W. Chen, H. Su, and Z. Chen, "Theoretical Insight into the Mechanism of Photoelectrochemical Oxygen Evolution Reaction on BiVO 4 Anode with Oxygen Vacancy," *The Journal of Physical Chemistry C*, vol. 121, pp. 18702–18709, 8 2017.

[215] M. Pattanaik and S. K. Bhaumik, "Adsorption behaviour of polyvinyl pyrrolidone on oxide surfaces," *Materials Letters*, vol. 44, pp. 352–360, 7 2000.

[216] K. M. Koczkur, S. Mourdikoudis, L. Polavarapu, and S. E. Skrabalak, "Polyvinylpyrrolidone (PVP) in nanoparticle synthesis," *Dalton Transactions*, vol. 44, no. 41, pp. 17883–17905, 2015.

[217] J. Wei, X. Jiao, T. Wang, and D. Chen, "Electrospun Photochromic Hybrid Membranes for Flexible Rewritable Media," *ACS Applied Materials & Interfaces*, vol. 8, pp. 29713–29720, 11 2016.

[218] X. Zhou, Y. Qiu, J. Yu, J. Yin, and X. Bai, "High electrochemical activity from hybrid materials of electrospun tungsten oxide nanofibers and carbon black," *Journal of Materials Science*, vol. 47, pp. 6607–6613, 9 2012.

[219] H. Zhang, C. Huang, R. Tao, Y. Zhao, S. Chen, Z. Sun, and Z. Liu, "One-pot solvothermal method to synthesize platinum/W18O49 ultrafine nanowires and their catalytic performance," *Journal of Materials Chemistry*, vol. 22, no. 8, p. 3354, 2012.

[220] T. T. Mills, G. E. Toombes, S. Tristram-Nagle, D.-M. Smilgies, G. W. Feigenson, and J. F. Nagle, "Order Parameters and Areas in Fluid-Phase Oriented Lipid Membranes Using Wide Angle X-Ray Scattering," *Biophysical Journal*, vol. 95, pp. 669–681, 7 2008.

[221] S. Frey and L. Tamm, "Orientation of melittin in phospholipid bilayers. A polarized attenuated total reflection infrared study," *Biophysical Journal*, vol. 60, pp. 922–930, 10 1991.

[222] L. S. Vermeer, B. L. de Groot, V. Réat, A. Milon, and J. Czaplicki, "Acyl chain order parameter profiles in phospholipid bilayers: computation from molecular dynamics simulations and comparison with 2H NMR experiments," *European Biophysics Journal*, vol. 36, pp. 919–931, 11 2007.

[223] S. Jen, N. A. Clark, P. S. Pershan, and E. B. Priestley, "Polarized Raman scattering studies of orientational order in uniaxial liquid crystalline phases," *The Journal of Chemical Physics*, vol. 66, pp. 4635–4661, 5 1977.

[224] H.-F. Wang, W. Gan, R. Lu, Y. Rao, and B.-H. Wu, "Quantitative spectral and orientational analysis in surface sum frequency generation vibrational spectroscopy (SFG-VS)," *International Reviews in Physical Chemistry*, vol. 24, pp. 191–256, 4 2005.

[225] B. R. Lentz, "Use of fluorescent probes to monitor molecular order and motions within liposome bilayers," *Chemistry and Physics of Lipids*, vol. 64, pp. 99–116, 9 1993.

[226] C.-P. Lafrance, A. Nabet, R. E. Prud'homme, and M. Pézolet, "On the relationship between the order parameter and the shape of orientation distributions," *Canadian Journal of Chemistry*, vol. 73, pp. 1497–1505, 9 1995.

[227] J. E. T. Corrie, B. D. Brandmeier, R. E. Ferguson, D. R. Trentham, J. Kendrick-Jones, S. C. Hopkins, U. A. v. d. Heide, Y. E. Goldman, C. Sabido-David, R. E. Dale, S. Criddle, and M. Irving, "Dynamic measurement of myosin light-chain-domain tilt and twist in muscle contraction," *Nature*, vol. 400, pp. 425–430, 7 1999.

[228] S. R. Adams, R. E. Campbell, L. A. Gross, B. R. Martin, G. K. Walkup, Y. Yao, J. Llopis, and R. Y. Tsien, "New Biarsenical Ligands and Tetracysteine Motifs for Protein Labeling in Vitro and in Vivo: Synthesis and Biological Applications," *Journal of the American Chemical Society*, vol. 124, pp. 6063–6076, 5 2002.

[229] S. A. Rosenberg, M. E. Quinlan, J. N. Forkey, and Y. E. Goldman, "Rotational Motions of Macro- molecules by Single-Molecule Fluorescence Microscopy," *Accounts of Chemical Research*, vol. 38, pp. 583–593, 7 2005.

[230] T. Ha, T. A. Laurence, D. S. Chemla, and S. Weiss, "Polarization Spectroscopy of Single Fluorescent Molecules," *The Journal of Physical Chemistry B*, vol. 103, pp. 6839–6850, 8 1999.

[231] J. N. Forkey, M. E. Quinlan, and Y. E. Goldman, "Measurement of Single Macromolecule Orientation by Total Internal Reflection Fluorescence Polarization Microscopy," *Biophysical Journal*, vol. 89, pp. 1261–1271, 8 2005.

[232] C. A. Valades Cruz, H. A. Shaban, A. Kress, N. Bertaux, S. Monneret, M. Mavrakis, J. Savatier, and S. Brasselet, "Quantitative nanoscale imaging of orientational order in biological filaments by polarized superresolution microscopy," *Proceedings of the National Academy of Sciences*, vol. 113, pp. E820–E828, 2 2016.

[233] D. Patra, I. Gregor, and J. Enderlein, "Image analysis of defocused single molecule images for three dimensional molecular orientation studies," *J. Phys. Chem. A*, vol. 108, pp. 6836–6841, 2004.

[234] F. Aguet, S. Geissbühler, I. Märki, T. Lasser, and M. Unser, "Super-resolution orientation estimation and localization of fluorescent dipoles using 3-D steerable filters," *Optics Express*, vol. 17, p. 6829, 4 2009.

[235] J. Lu, H. Mazidi, T. Ding, O. Zhang, and M. D. Lew, "Single-Molecule 3D Orientation Imaging Reveals Nanoscale Compositional Heterogeneity in Lipid Membranes," *Angewandte Chemie International Edition*, p. anie.202006207, 8 2020.

[236] T. K. Moon and W. C. Stirling, *Mathematical methods and algorithms for signal processing.* Prentice Hall, 2000.

[237] G. Marsaglia, "Choosing a Point from the Surface of a Sphere," *The Annals of Mathematical Statistics*, vol. 43, pp. 645–646, 4 1972.

[238] R. J. Ober, S. Ram, and E. S. Ward, "Localization accuracy in single-molecule microscopy.," *Biophysical journal*, vol. 86, no. 2, pp. 1185–200, 2004.

[239] Megha and E. London, "Ceramide Selectively Displaces Cholesterol from Ordered Lipid Domains (Rafts)," *Journal of Biological Chemistry*, vol. 279, pp. 9997–10004, 3 2004.

[240] Ira and L. J. Johnston, "Ceramide Promotes Restructuring of Model Raft Membranes," *Langmuir*, vol. 22, pp. 11284–11289, 12 2006.

[241] B. Stancevic and R. Kolesnick, "Ceramide-rich platforms in transmembrane signaling," *FEBS Letters*, vol. 584, pp. 1728–1740, 5 2010.

[242] S. Chiantia, N. Kahya, J. Ries, and P. Schwille, “Effects of Ceramide on Liquid-Ordered Domains Investigated by Simultaneous AFM and FCS,” *Biophysical Journal*, vol. 90, pp. 4500–4508, 6 2006.

[243] Ira and L. J. Johnston, “Sphingomyelinase generation of ceramide promotes clustering of nanoscale domains in supported bilayer membranes,” *Biochimica et Biophysica Acta (BBA) - Biomembranes*, vol. 1778, pp. 185–197, 1 2008.

[244] B. M. Hanser, M. G. L. Gustafsson, D. A. Agard, and J. W. Sedat, “Phase-retrieved pupil functions in wide-field fluorescence microscopy,” *Journal of Microscopy*, vol. 216, pp. 32–48, 10 2004.

[245] E. Nehme, L. E. Weiss, T. Michaeli, and Y. Shechtman, “Deep-STORM: super-resolution single-molecule microscopy by deep learning,” *Optica*, vol. 5, p. 458, 4 2018.

[246] J. D. Harper and P. T. Lansbury, “MODELS OF AMYLOID SEEDING IN ALZHEIMER'S DISEASE AND SCRAPIE:Mechanistic Truths and Physiological Consequences of the Time-Dependent Solubility of Amyloid Proteins,” *Annual Review of Biochemistry*, vol. 66, pp. 385–407, 6 1997.

[247] C. L. Masters, G. Simms, N. A. Weinman, G. Multhaup, B. L. McDonald, and K. Beyreuther, “Amyloid plaque core protein in Alzheimer disease and Down syndrome.,” *Proceedings of the National Academy of Sciences*, vol. 82, pp. 4245–4249, 6 1985.

[248] K. Beyreuther and C. L. Masters, “Amyloid Precursor Protein (APP) and BZA4 Amyloid in the Etiology of Alzheimer's Disease: Precursor-Product Relationships in the Derangement of Neuronal Function,” *Brain Pathology*, vol. 1, pp. 241–251, 7 1991.

[249] T. Ban, D. Hamada, K. Hasegawa, H. Naiki, and Y. Goto, “Direct Observation of Amyloid Fibril Growth Monitored by Thioflavin T Fluorescence,” *Journal of Biological Chemistry*, vol. 278, pp. 16462–16465, 5 2003.

[250] T. Ban and Y. Goto, “Direct Observation of Amyloid Growth Monitored by Total Internal Reflection Fluorescence Microscopy,” in *Methods in Enzymology*, vol. 413, pp. 91–102, Elsevier Inc, 2006.

[251] C. B. Andersen, H. Yagi, M. Manno, V. Martorana, T. Ban, G. Christiansen, D. E. Otzen, Y. Goto, and C. Rischel, “Branching in Amyloid Fibril Growth,” *Biophysical Journal*, vol. 96, pp. 1529–1536, 2 2009.

[252] M. M. Wördehoff, O. Bannach, H. Shaykhalishahi, A. Kulawik, S. Schiefer, D. Willbold, W. Hoyer, and E. Birkmann, “Single Fibril Growth Kinetics of α-Synuclein,” *Journal of Molecular Biology*, vol. 427, pp. 1428–1435, 3 2015.

[253] D. Ozawa, H. Yagi, T. Ban, A. Kameda, T. Kawakami, H. Naiki, and Y. Goto, "Destruction of Amyloid Fibrils of aβ2 -Microglobulin Fragment by Laser Beam Irradiation," *Journal of Biological Chemistry*, vol. 284, pp. 1009–1017, 1 2009.

[254] H. Yagi, D. Ozawa, K. Sakurai, T. Kawakami, H. Kuyama, O. Nishimura, T. Shimanouchi, R. Kuboi, H. Naiki, and Y. Goto, "Laser-induced Propagation and Destruction of Amyloid β Fibrils," *Journal of Biological Chemistry*, vol. 285, pp. 19660–19667, 6 2010.

[255] S. W. Hell, "Nanoscopy with Focused Light (Nobel Lecture)," *Angewandte Chemie International Edition*, vol. 54, pp. 8054–8066, 7 2015.

[256] C. Eggeling and M. Heilemann, "Editorial overview: Molecular imaging," *Current Opinion in Chemical Biology*, vol. 20, no. 1, pp. v–vii, 2014.

[257] D. Pinotsi, G. S. K. Schierle, and C. F. Kaminski, "Optical Super-Resolution Imaging of β-Amyloid Aggregation In Vitro and In Vivo: Method and Techniques," in *Systems Biology of Alzheimer's Disease* (J. I. Castrillo and S. G. Oliver, eds.), vol. 1303 of *Methods in Molecular Biology*, pp. 125–141, New York, NY: Springer New York, 2016.

[258] H. A. Shaban, C. A. Valades-Cruz, J. Savatier, and S. Brasselet, "Polarized super-resolution structural imaging inside amyloid fibrils using Thioflavine T," *Scientific Reports*, vol. 7, p. 12482, 12 2017.

[259] H. Shroff, C. G. Galbraith, J. A. Galbraith, and E. Betzig, "Live-cell photoactivated localization microscopy of nanoscale adhesion dynamics," *Nature Methods*, vol. 5, pp. 417–423, 4 2008.

[260] R. P. J. Nieuwenhuizen, K. A. Lidke, M. Bates, D. L. Puig, D. Grünwald, S. Stallinga, and B. Rieger, "Measuring image resolution in optical nanoscopy," *Nature Methods*, vol. 10, pp. 557–562, 6 2013.

[261] J. Ries, V. Udayar, A. Soragni, S. Hornemann, K. P. R. Nilsson, R. Riek, C. Hock, H. Ewers, A. A. Aguzzi, and L. Rajendran, "Superresolution Imaging of Amyloid Fibrils with Binding-Activated Probes," *ACS Chemical Neuroscience*, vol. 4, pp. 1057–1061, 7 2013.

[262] R. Jungmann, M. S. Avendaño, J. B. Woehrstein, M. Dai, W. M. Shih, and P. Yin, "Multiplexed 3D cellular super-resolution imaging with DNA-PAINT and Exchange-PAINT," *Nature Methods*, vol. 11, pp. 313–318, 2 2014.

[263] J. Molle, M. Raab, S. Holzmeister, D. Schmitt-Monreal, D. Grohmann, Z. He, and P. Tinnefeld, "Superresolution microscopy with transient binding," *Current Opinion in Biotechnology*, vol. 39, pp. 8–16, 2016.

[264] T. Ding, K. Spehar, J. Bieschke, and M. D. Lew, "Long-term, super-resolution imaging of amyloid structures using transient amyloid binding microscopy," in *Single Molecule Spectroscopy and Superresolution Imaging XII* (I. Gregor, Z. K. Gryczynski, and F. Koberling, eds.), p. 19, SPIE, 2 2019.

[265] A. I. Sulatskaya, I. M. Kuznetsova, M. V. Belousov, S. A. Bondarev, G. A. Zhouravleva, and K. K. Turoverov, "Stoichiometry and Affinity of Thioflavin T Binding to Sup35p Amyloid Fibrils," *PLOS ONE*, vol. 11, p. e0156314, 5 2016.

[266] A. E. Roher, M. O. Chaney, Y.-m. Kuo, S. D. Webster, W. B. Stine, L. J. Haverkamp, A. S. Woods, R. J. Cotter, J. M. Tuohy, G. a. Krafft, B. S. Bonnell, and M. R. Emmerling, "Morphology and Toxicity of Aβ-(1-42) Dimer Derived from Neuritic and Vascular Amyloid Deposits of Alzheimer's Disease," *Journal of Biological Chemistry*, vol. 271, pp. 20631–20635, 8 1996.

[267] Y. Hu, T. Guo, X. Ye, Q. Li, M. Guo, H. Liu, and Z. Wu, "Dye adsorption by resins: Effect of ionic strength on hydrophobic and electrostatic interactions," *Chemical Engineering Journal*, vol. 228, pp. 392–397, 7 2013.

[268] C. Wu, M. Biancalana, S. Koide, and J.-E. Shea, "Binding Modes of Thioflavin-T to the Single-Layer β-Sheet of the Peptide Self-Assembly Mimics," *Journal of Molecular Biology*, vol. 394, pp. 627–633, 12 2009.

[269] A. J. Baldwin, T. P. J. Knowles, G. G. Tartaglia, A. W. Fitzpatrick, G. L. Devlin, S. L. Shammas, C. A. Waudby, M. F. Mossuto, S. Meehan, S. L. Gras, J. Christodoulou, S. J. Anthony-Cahill, P. D. Barker, M. Vendruscolo, and C. M. Dobson, "Metastability of Native Proteins and the Phenomenon of Amyloid Formation," *Journal of the American Chemical Society*, vol. 133, pp. 14160–14163, 9 2011.

[270] M. P. Backlund, M. D. Lew, A. S. Backer, S. J. Sahl, and W. E. Moerner, "The role of molecular dipole orientation in single-molecule fluorescence microscopy and implications for super-resolution imaging," *ChemPhysChem*, vol. 15, no. 4, pp. 587–599, 2014.

[271] G. Grover, K. DeLuca, S. Quirin, J. DeLuca, and R. Piestun, "Super-resolution photon-efficient imaging by nanometric double-helix point spread function localization of emitters (SPINDLE)," *Optics Express*, vol. 20, p. 26681, 11 2012.

[272] Y. Shechtman, S. J. Sahl, A. S. Backer, and W. E. Moerner, "Optimal point spread function design for 3D imaging," *Physical Review Letters*, vol. 113, no. 3, 2014.

[273] T. Chandler, H. Shroff, R. Oldenbourg, and P. L. Rivière, "Spatio-angular fluorescence microscopy II Paraxial 4f imaging," *Journal of the Optical Society of America A*, vol. 36, p. 1346, 8 2019.

[274] M. Böhmer and J. Enderlein, “Orientation imaging of single molecules by wide-field epifluorescence microscopy,” *Journal of the Optical Society of America B*, vol. 20, p. 554, 3 2003.

[275] O. Zhang and M. D. Lew, “Fundamental Limits on Measuring the Rotational Constraint of Single Molecules Using Fluorescence Microscopy,” *Physical Review Letters*, vol. 122, p. 198301, 5 2019.

[276] J. A. Varela, M. Rodrigues, S. De, P. Flagmeier, S. Gandhi, C. M. Dobson, D. Klenerman, and S. F. Lee, “Optical Structural Analysis of Individual α-Synuclein Oligomers,” *Angewandte Chemie - International Edition*, vol. 57, no. 18, pp. 4886–4890, 2018.

[277] T. Watanabe-Nakayama, K. Ono, M. Itami, R. Takahashi, D. B. Teplow, and M. Yamada, “High-speed atomic force microscopy reveals structural dynamics of amyloid β 1–42 aggregates,” *Proceedings of the National Academy of Sciences*, vol. 113, pp. 5835–5840, 5 2016.

Vita

Tianben Ding

Degrees

Ph.D., Electrical Engineering
Washington University in St. Louis, August 2020

M.Eng., Electrical Engineering and Information Systems
The University of Tokyo, March 2014

B.Eng., Physics
Yokohama National University, March 2012

Publications

Journal Publications: *equal contribution

H. Mazidi, **T. Ding**, A. Nehorai and M. D. Lew, "Measuring localization confidence for quantifying accuracy and heterogeneity in single-molecule super-resolution microscopy," under revision for *Nature Communications*.

J. Lu, H. Mazidi, **T. Ding**, O. Zhang and M. D. Lew, "Single-molecule 3D orientation imaging reveals nanoscale compositional heterogeneity in lipid membranes," to appear in *Angewandte Chemie International Edition*.

M. Shen, **T. Ding**, J. Luo, C. Tan, K. Mahmood, Z. Wang, D. Zhang, R. Mishra, M. D. Lew and B. Sadtler, "Competing activation and deactivation mechanisms in photodoped bismuth oxybromide nanoplates probed by single-molecule fluorescence imaging," *Journal of Physical Chemistry Letters*, **11**, 13, 5219-5227 (2020).

T. Ding*, T. Wu*, H. Mazidi, O. Zhang, and M. D. Lew, "Single-molecule orientation localization microscopy for resolving structural heterogeneities between amyloid fibrils," *Optica*, **7**, 6, 602-607 (2020).

M. Shen*, **T. Ding***, S. T. Hartman, F. Wang, C. Krucylak, Z. Wang, C. Tan, B. Yin, R. Mishra, M. D. Lew, and B. Sadtler, "Nanoscale colocalization of fluorogenic probes reveals role of oxygen vacancies in the photocatalytic activity of tungsten oxide nanowires," *ACS Catalysis* **10**, 3, 2088-2099 (2020).

K. Spehar*, **T. Ding***, Y. Sun, N. Kedia, J. Lu, G. R. Nehass, M. D. Lew, and J. Bieschke, "Super-resolution imaging of amyloid structures over extended times using transient binding of single thioflavin T molecules," *ChemBioChem* **19**, 18, 1944-1948 (2018).

O. Zhang, J. Lu, **T. Ding**, and M. D. Lew, "Imaging the three-dimensional orientation and rotational mobility of fluorescent emitters using the Tri-spot point spread function," *Applied Physics Letters* **113**, 031103, (2018).

T. Ding and A. Hirose, "Fading channel prediction based on combination of complex-valued neural networks and chirp z-transform," *IEEE Transactions on Neural Networks and Learning Systems* **25**, 9, 1686-1695, (2014).

Other Publications:

T. Wu, **T. Ding**, H. Mazidi, O. Zhang, and M. D. Lew, "A computationally-efficient bound for the variance of measuring the orientation of single molecules," *Proc. SPIE, the International Society for Optics and Photonics* **11246** 1124616 (2020).

H. Mazidi, **T. Ding**, A. Nehorai, and M. D. Lew, "Measuring localization confidence for quantifying accuracy and heterogeneity in single-molecule super-resolution microscopy," *Proc. SPIE, the International Society for Optics and Photonics* **11246** 1124611 (2020).

T. Ding and A. Hirose, "Proposal of Online Regularization for Dynamical Structure Optimization in Complex-Valued Neural Networks," *in Neural Information Processing. International Conference on Neural Information Processing (ICONIP) 2019. Lecture Notes in Computer Science* **11954**, Springer, 407-418 (2019).

T. Ding, K. Spehar, J. Bieschke, and M. D. Lew, “Long-term, super-resolution imaging of amyloid structures using transient amyloid binding microscopy,” *Proc. SPIE, the International Society for Optics and Photonics* **10884**, 108840J (2019).

O. Zhang, **T. Ding**, J. Lu, H. Mazidi, and M. D. Lew, “Measuring 3D molecular orientation and rotational mobility using a Tri-spot point spread function,” *Proc. SPIE, the International Society for Optics and Photonics* **10500**, 10500B (2018).

M. Hikosaka, **T. Ding**, and A. Hirose, “Proposal of polarization state prediction using quaternion neural networks for fading channel prediction in mobile communications,” *Proc. 2016 International Joint Conference on Neural Networks (IJCNN)* Vancouver, BC, 4105-4111 (2016).

A. Hirose and **T. Ding**, “Neural networks to deal with complex amplitude and its strength in electronics,” *C - Abstracts of IEICE Transactions on Electronics (Japanese Edition)* **J98-C**, 10, 184-192 (2015).

T. Murata, **T. Ding**, and A. Hirose, “Proposal of channel prediction by complex-valued neural networks that deals with polarization as a transverse wave entity,” *in Neural Information Processing. International Conference on Neural Information Processing (ICONIP) 2015. Lecture Notes in Computer Science* **9491**, Springer, 541-549 (2015).

T. Murata, **T. Ding**, and A. Hirose, “Polarization combination using complex-valued neural networks in channel prediction [in Japanese],” *IEICE technical report* **115**, 83, 31-35 (2015).

T. Ding and A. Hirose, “Fading channel prediction based on self-optimizing neural networks,” *in Neural Information Processing. International Conference on Neural Information Processing (ICONIP) 2014. Lecture Notes in Computer Science* **8834**, 175-182 (2014).

T. Ding and A. Hirose, “Sparsity of complex-valued neural networks in fading channel prediction [in Japanese],” *IEICE technical report. Neurocomputing* **113**, 500, 103-108 (2014).

T. Ding and A. Hirose, “Fading channel prediction based on complex-valued neural networks in frequency domain,” *Proc. of 2013 URSI International Symposium on Electromagnetic Theory (EMTS)* 640-643 (2013).

August 2020